UNIVERSITÉ DE STRASBOURG

ÉCOLE DOCTORALE physique et chimie-physique (ED 182)

Institut de Physique et Chimie des Matériaux de Strasbourg

THÈSE présentée par :

[Md Samiul Islam]

soutenue le : **13 November, 2024**

pour obtenir le grade de : **Docteur de l'université de Strasbourg**

Discipline/ Spécialité : Nanophysique

Coherent ultrafast spectroscopy of excitons in Van der Waals materials

THÈSE dirigée par :

[M. BARSELLA Alberto]	Maitre de conférences, Université de Strasbourg
[M. Francois Fras]	Maitre de conférences, Université de Strasbourg

RAPPORTEURS :

[Mme CHAMARRO Maria]	Professeur, INSP-CNRS Sorbonne Université
[M. GUILLET Thierry]	Professeur, L2C-CNRS Université de Montpellier

---

AUTRES MEMBRES DU JURY :

[Mme HALTÉ-FILIPPI Valérie]	Professeur, IPCMS-CNRS, Université de Strasbourg
[M. DELTEIL Aymeric]	Chargé de recherches, GEMAC-CNRS, Université Versailles Saint-Quentin-en-Yvelines

Acknowledgements

I would like to sincerely thank Prof. Maria Chamarro, Prof. Thierry Guillet, Prof. Valerie Halte-Filippi and Prof. Aymeric Delteil, for agreeing to be part of the Jury for my thesis. Their effort and suggestions will be very helpful for the successful completion of my thesis.

I thank Prof. Francois Fras for supervising me throughout my master internship and my PhD thesis. The project I was a part of was long and ambitious. But I think it was worth the effort. During all these years, I learned a lot from Francois, through numerous discussions. I am grateful for his help in the lab, specially during the FWM experimental setup development and for his advice. He never seems to run out of ideas about anything. I am grateful for his help in reviewing my thesis manuscript. I thank Prof. Alberto Barsella for his supervision throughout my PhD. Specially, his efforts for reviewing my thesis manuscript was very helpful. I thank Prof. Marie Barthelemy for helping me in the lab and for the scientific discussions. Her help was valuable in the successful development of the experiment. I would like to thank Nicolas Beyer for his help with any practical problem in our lab. No matter the nature of the problem, from mechanical problem to electrical, electronic, cryogenic and even safety protocols, Nicolas always gave his best effort for us. I thank Rup Kumar Chowdhury for his contribution in our project, specially in the sample preparation and massive amount of data analysis. I learnt many things through working with him, as well as through scientific discussions and debates.

Outside or research group, a lot of people from IPCMS and beyond helped me a great deal during my thesis. Among them is Prof. Stephane Berciaud, who has helped and advised me since I came to IPCMS for my master. I am grateful for his help in my master internship and providing a very interesting sample for my thesis. The discussions we had with him regarding this sample and the subsequent results were highly productive. I would also like to thank Thibault Chervy for his collaboration with us and sending us a highly advanced 2D structure. I thank Prof. Pascal hebraud and Prof. Mircea Rastei, whose collaborative work with our project, helped me greatly. I thank Prof. Loic Mager for helping me with sample preparation.

I would also like to thank Bruno Michel and Lorry Engel for their assistance with the complicated electronic requirement in our lab. I am grateful to Olivier Cregut for

his help in the lab, specially with the autocorrelator. I thank Marie-Noelle Lalloz for helping me with any chemistry related problem and Gilles Versini for his help with sample preparation, as well as vacuum and cryogenics maintenance. I would like to thank Romain Bernard and Hicham Majjad for training me on how to use the clean room and all the subsequent help with my sample preparation.

Besides the academic help, all my friends in IPCMS helped make an enjoyable environment and make the journey easier. I thank all of them, specially Ilias, Amira, Moahmmed Soliman, Mohammed Guerboub, Krystyna, Gabe, Denis, Laurianne, Adrian, Vincent, Matthew, Daniel, Saeel, Hussain and Ashfaq.

I will always be grateful to my family, specially my parents for always standing by me and supporting me throughout all my life. And finally, I would like to thank Faria for being with me through the last year, even on the days when I was insufferable. The most difficult year became the best year of my life. Thank you.

Résumé

Introduction

Les matériaux de Van der Waals (vdW), sont devenus un pilier de la physique moderne des solides depuis l'isolement du graphène monocouche en 2004. Cette découverte a mis en évidence des propriétés radicalement différentes dans la forme bidimensionnelle d'un matériau comparé à sa forme volumique, ce qui a catalysé les recherches sur les "matériaux 2D". Parmi eux, les dichalcogénures de métaux de transition (TMD) se distinguent par leurs propriétés électroniques et optiques modulables, leur couplage efficace à la lumière, et leurs comportements excitoniques uniques, tels que les propriétés de spin-vallée et une grande énergie de liaison des excitons. La possibilité de créer des hétérostructures en empilant des couches de différents matériaux 2D élargit encore leur potentiel pour la recherche fondamentale et les applications en optoélectronique, en valleytronique et en technologies quantiques. Malgré des progrès substantiels, des questions clés subsistent concernant la cohérence excitonique et les dynamiques de population dans les TMD et leurs hétérostructures. Par exemple, le disulfure de rhénium (ReS_2), un TMD du groupe 7 avec des excitons anisotropes et un faible couplage inter-couche, reste en grande partie inexploré en ce qui concerne la dynamique des excitons. De même, pour des TMD largement plus étudiés comme le diséléniure de molybdène ($MoSe_2$), des mécanismes critiques tels que la décroissance radiative des excitons et leur diffusion vers des états sombres nécessitent des investigations supplémentaire. Les hétérostructures introduisent une complexité supplémentaire, où les interactions inter-couches influencent de manière significative les propriétés excitoniques, offrant à la fois des défis et des opportunités pour les applications dans les dispositifs.

Cette thèse explore les propriétés dynamiques des excitons dans les matériaux vdW, en se concentrant sur la cohérence, les dynamiques de population, et leur dépendance aux facteurs environnementaux tels que la température, la puissance d'excitation et l'environnement cristallographique. Des stratégies pour moduler les

propriétés excitoniques à des fins d'applications avancées sont également explorées. Dans ce but, une configuration originale de spectroscopie de mélange à quatre ondes à l'état de l'art a été développée, combinant une résolution temporelle ultrarapide, une résolution spatiale limitée par diffraction et une grande résolution spectrale, à résonance optique. Ce cadre expérimental permet des mesures précises des dynamiques des excitons.

Le chapitre 1 introduit les concepts fondamentaux des matériaux vdW, en mettant l'accent sur les propriétés électronique et excitonique du graphène, des TMD du groupe 6 et du ReS_2, ainsi que sur les enjeux de ce travail de thèse. Le chapitre 2 détaille la méthodologie expérimentale, en se concentrant sur le développement de la configuration spectroscopique FWM, et les méthodes théoriques sous-jacentes à l'analyse des données.

Les chapitres suivants présentent les résultats principaux :

- **Chapitre 3:** Analyse des dynamiques de cohérences de populations des excitons anisotropes dans le ReS_2 à résonance optiques, révélant leur robustesse en fonction de la puissance d'excitation optique, la température et le nombre de couches.

- **Chapitre 4:** Explore la dynamique des excitons dans une hétérostructure $MoSe_2$-graphène, démontrant des changements significatifs dans le comportement des excitons dus à l'influence du graphène. Notamment une influence sur es des dynamiques de population, des échelles de temps de mécanisme de diffusion et de transfert excitonique, ainsi et une augmentation du désordre dans l'environnement excitonique.

- **Chapitre 5:** Se concentre sur les excitons localisés dans le nitrure de bore hexagonal (hBN), réalisant une analyse statistique à grande échelle des spectres de photoluminescence liés aux défauts. Les résultats révèlent des familles spectrales distinctes pour les émissions de défauts et démontrent une méthode pour contrôler la formation des défauts avec des propriétés d'émission spécifiques via uen sélection de la morphologie des feuillets bidimensionnels.

En explorant les propriétés excitoniques des matériaux vdW et des hétérostructures à l'échelle microscopique, cette thèse apporte une contribution significative à la compréhension fondamentale des systèmes semi-conducteurs 2D

tout en ouvrant de nouvelles perspectives pour des applications potentielles en optoélectronique et en technologies quantiques. Les prochains défis à relever grâce à cette configuration expérimentale unique, développée dans le cadre de ce travail, concernent l'étude approfondie des systèmes localisés présents dans les hôtes bidimensionnels semi-conducteurs.

Structure de bande et excitons dans les matériaux van der Waals

---

Matériaux de Van der Waals

Les matériaux bidimensionnels (2D) de Van der Waals (vdW) sont constitués de couches atomiquement fines avec des liaisons covalentes fortes dans le plan et des liaisons vdW faibles entre les couches successives [1]. Cette liaison inter-couches faible permet d'extraire des monocouches thermodynamiquement stables. Le graphène, premier matériau 2D découvert, a ouvert la voie à des recherches approfondies et à la découverte de matériaux tels que les dichalcogénures de métaux de transition (TMDs, de formule générale MX_2, où M = Mo, W, et X = S, Se), le phosphore noir, le nitrure de bore hexagonal (hBN) et le silicène. Les propriétés de ces matériaux dépendent du nombre de couches ; par exemple, le MoS_2 passe d'un gap indirect à un gap direct sous forme de monocouche [2, 3]. L'empilement de matériaux vdW permet de former des hétérostructures avec des propriétés électroniques et optiques modulables. Cette thèse s'intéresse particulièrement au hBN, au disulfure de rhénium (ReS_2) et à des structures vdW avancées comme les hétérostructures $MoSe_2$-graphène.

Le graphène

Le graphène est une monocouche d'atomes de carbone arrangés dans une structure en nid d'abeilles. L'hybridation sp_2 des orbitales 2s, $2p_x$ et $2p_y$ du carbone forme des liaisons σ, tandis que les orbitales $2p_z$ restantes forment des liaisons π. Les propriétés électroniques clés du graphène découlent des bandes π [4–6]. La maille cristalline du graphène comprend deux sous-réseaux (A et B), avec des voisins les

plus proches séparés par $a = 1.42\,\text{Å}$. La cellule unitaire contient deux atomes de carbone, conduisant à un réseau de Bravais hexagonal. La structure du réseau génère une première zone de Brillouin hexagonale avec des points de haute symétrie tels que K, K' et Γ. Ces points jouent un rôle central dans les propriétés électroniques du graphène. La structure de bande d'énergie du graphène présente une forme conique près des points K, où les électrons se comportent comme des fermions de Dirac sans masse. Ce comportement unique confère au graphène une conductivité électrique et thermique extrêmement élevée, une grande résistance mécanique et une transparence pour la lumière dans le spectre optique [5–7].

Les dichalcogénures de métaux de transition (TMDs)

Les TMDs ont pour formule générale MX_2, où M est un métal de transition (par ex: Mo, W) et X un chalcogène (par ex: S, Se). Leur structure en couches se caractérise par des liaisons covalentes fortes dans le plan et des interactions vdW faibles entre les couches [8]. Une monocouche est composée d'un réseau hexagonal d'atomes métalliques de transition pris en sandwich entre deux couches d'atomes de chalcogène. La structure cristalline peut être prismatique trigonale (phase H) ou octaédrique (phase T) [8]. Les séquences d'empilement définissent des polymorphes comme 2H (AbA bAb) ou 1T′ (octaédrique déformée) [9].

TMDs du groupe 6

Les TMDs du groupe 6, tels que MoS_2, $MoSe_2$, WS_2 et WSe_2, suscitent un intérêt particulier en raison de leurs propriétés semi-conductrices et de leurs caractéristiques électroniques modulables. Les monocouches de ces matériaux présentent un gap direct, avec des valeurs de gap comprises entre 1.1 eV et 2.0 eV selon le matériau et le degré de contrainte [10]. Ces matériaux sont particulièrement attrayants pour les applications optoélectroniques en raison de leur forte interaction lumière-matière et de la grande énergie de liaison excitonique, pouvant dépasser plusieurs centaines de meV. La nature du gap électcronique est très sensible au nombre de couches, devenant indirect dans les formes bi-couches ou massives. Dans les monocouches, le fort couplage spin-orbite entraîne une division significative de la bande de valence aux points K, induisant un effet de verrouillage spin-valléee [11]. Cette propriété à ouvert la voire à l'émergence de la valleytronique.

De plus, ces TMDs présentent de hauts rendements quantiques de photoluminescence, les rendant adaptés aux dispositifs émetteurs de lumière. La présence de différents états excitoniques, y compris les excitons neutres (X^0), les excitons chargés (trions, X^-) et les biexcitons (XX), enrichit davantage leur photophysique [12]. Le dopage, les contraintes et les champs électriques peuvent être utilisés pour moduler ces propriétés excitoniques, offrant une grande polyvalence pour l'ingénierie des dispositifs.

Les excitons dans les TMDs du groupe 6 : Polarisation des vallées et couplage spin-orbite

Les monocouches de TMDs, telles que MoX_2 et WX_2, présentent une symétrie réduite par rapport à leurs homologues massifs. En particulier, l'absence de symétrie d'inversion entraîne la formation de deux vallées distinctes dans la zone de Brillouin : les vallées K_+ et K_-. Ces vallées sont cruciales pour la formation des excitons dans ces matériaux. Les excitons dans les TMDs sont fortement influencés par la polarisation de la lumière incidente. Une lumière polarisée circulairement à droite excite les excitons dans la vallée K_+, tandis qu'une lumière polarisée circulairement à gauche excite ceux de la vallée K_-. Cette excitation sélective des vallées permet de préserver la polarisation des vallées lors de la recombinaison des excitons, ce qui a des implications importantes pour la valleytronique, exploitant les degrés de liberté des vallées pour le traitement de l'information [8, 12–16].

Un aspect important des monocouches de TMDs est le couplage spin-orbite (SOC). L'intensité du SOC est beaucoup plus élevée dans les TMDs que dans des matériaux comme le graphène, en raison de la présence d'atomes métalliques de transition lourds et d'orbitales d. Ce couplage entre les degrés de liberté spin et vallée conduit à des comportements excitoniques et des transitions optiques uniques [12, 13].

Disulfure de rhénium (ReS_2)

Contrairement aux TMDs du groupe 6, le disulfure de rhénium (ReS_2) est un TMD du groupe 7 encore peu étudié, mais qui suscite un intérêt croissant en raison de ses propriétés anisotropes uniques et de son faible couplage inter-couches. À la différence des TMDs du groupe 6, le ReS_2 présente une structure cristalline haute-

ment anisotrope. Cette anisotropie provient de sa structure cristalline octaédrique déformée, qui entraîne des dipôles excitoniques orientés dans différentes directions du plan. Cette structure confère des caractéristiques unidimensionnelles remarquables aux excitons le long des chaînes de rhénium. Les propriétés structurales uniques du ReS_2 en font un matériau intéressant pour explorer de nouveaux phénomènes optiques et électroniques, et son faible couplage inter-couches en fait un excellent candidat pour l'étude des dynamiques excitoniques dans les systèmes 2D multifeuillets [17–21].

Expérience de microscopie par mélange à quatre ondes (FWM)

Configuration expérimentale

Une configuration expérimentale originale de microscopie ultrarapide cohérente par mélange à quatre ondes (FWM) a été développée dans cette thèse pour étudier la dynamique des excitons dans les matériaux vdW. Cette configuration combine une résolution spatiale limitée par la diffraction (typiquement $\leq 1\ \mu m$), une résolution temporelle ultrarapide (environ 100 femtosecondes) et une résolution spectrale d'environ 30 μeV. Les techniques classiques non résonnantes de résolution temporelle, comme la photoluminescence résolue en temps (PL), souffrent de canaux de décroissance complexes en raison de leur nature non résonnante. Les techniques non linéaires du troisième ordre, telles que la spectroscopie FWM résonnante, permettent de surmonter ces limitations. Cependant, la spectroscopie FWM conventionnelle est souvent limitée en résolution spatiale en raison de la sélection directionnelle, nécessitant la récupération des phases spatiales. Pour résoudre ce problème, une méthode novatrice a été développée, impliquant une modulation temporelle de la phase optique des impulsions d'excitation, à l'aide de la méthode d'hétérodynage optique combinée à l'interférométrie spectrale (SI). Cette technique permet l'utilisation d'un objectif de microscope en géométrie colinéaire, atteignant une résolution spatiale microscopique imitée par la diffraction.

Modélisation du signal et hypothèses clés

Le mélange à quatre ondes (FWM) correspond, au plus bas ordre, à une réponse non linéaire du troisième ordre d'un système excité par des impulsions optiques. La séquence d'interaction entre le système, considéré pour simplifier comme un système à deux niveaux, et les impulsions optiques est la suivante : la première interaction optique génère une polarisation (ou cohérence) dans le système. La deuxième impulsion, retardée par rapport à la première, induit une population proportionnelle à la polarisation générée par la première interaction. Enfin, la troisième interaction avec cette population donne naissance au signal FWM. Le signal de FWM est ici décrit à l'aide du formalisme de la matrice densité, en considérant d'une part l'interaction entre un système à deux niveaux et une impulsion optique, et d'autre part la dissipation et la relation due au couplage entre le système et son environnement via l'équation de Liouville-von Neumann. Dans ce formalisme, les éléments diagonaux représentent la population des états du système, tandis que les éléments hors-diagonaux décrivent la superposition cohérente (cohérence) entre les états, prenant la forme des équations de Bloch optiques (OBE). Les solutions des OBE peuvent être obtenues par une approche perturbative, où la matrice densité est développée en série en puissances (expansion perturbative) du champ d'excitation. Le champ optique peut être exprimé en termes de champ électrique. Du point de vue macroscopique (ou de l'optique non linéaire), l'observable d'intérêt est la polarisation macroscopique. Cette grandeur est liée aux variables microscopiques, par la valeur moyenne de l'opérateur dipolaire. Enfin, les composantes linéaires de la polarisation non linéaire du troisième ordre contribuent à la réponse du système d'ordre supérieur, formant le signal FWM. La solution générale complexe des OBE peut être simplifiée en utilisant plusieurs hypothèses clés. Tout d'abord, un ordre temporel strict des impulsions est supposé, avec un certain délai entre chaque paire d'impulsions. Ces impulsions ne se superposent pas, et chaque interaction à un moment donné n'implique que l'impulsion correspondante. Deuxièmement, la limite de l'interaction quasi-instantanée est utilisée, où les impulsions sont modélisées comme des fonctions delta en temps, avec un facteur de phase correspondant à la fréquence et au vecteur d'onde appropriés. Cette approximation fonctionne bien pour les systèmes où la durée de l'impulsion est bien plus courte que le temps de déclin du système. Troisièmement, l'approximation des ondes tournantes (RWA) est appliquée, ou seulement la contribution résonnante est considérée. La

décroissance du signal FWM peut ainsi être analysée en intégrant la polarisation du système dans le temps et en traçant son évolution en fonction des délais entre les impulsions. En analysant la dynamique, les taux de décroissance i) de la superposition cohérente γ (ou T_2, temps de cohérence) et ii) de la population Γ (ou T_1, temps de vie) peuvent être retrouvés. Dans cette approche, nous considérons également une distribution inhomogène d'excitons, où la réponse du troisième ordre conduit à un élargissement inhomogène, dont la caractéristique est également étudiée.

Dynamique des excitons anisotropes dans le disulfure de rhénium (ReS_2)

Ce chapitre décrits les résultats expérimentaux obtenus par microscopie de mélange à quatre ondes sur les excitons dans le disulfure de rhénium (ReS_2). Comment mentionnée dans le chapitre 2 le ReS_2, un dichalcogénure de métal de transition du groupe 7 (TMD), présente une forte anisotropie dans le plan en raison de sa phase octaédrique déformée (1T′) et de la structure en chaîne zigzag Re-Re le long de l'axe cristallographique b [20, 22–24]. Cette configuration unique du réseau engendres des excitons anisotropes aux caractéristiques quasi-unidimensionnelles sans e ingénierie externe des contraintes. Contrairement au phosphore noir, le ReS_2 reste stable dans des conditions ambiantes, ce qui en fait un candidat prometteur pour les dispositifs optoélectroniques sensibles à la polarisation [25–27]. De plus, le ReS_2 conserve sa réponse optique excitonique même sous forme de multicouches en raison d'un faible couplage inter-couches, qui préserve sa structure électronique indépendamment du nombre de couche. Cependant, des débats persistent concernant la nature de son gap de bande diret l'origine précise de ses propriétés anisotropes [17, 18].

Les études résolues en temps permettent d'apporter des réponses clés sur ces enjeux. Les études précédentes réalisées hors résonance, basées sur la photoluminescence résolue en temps et la spectroscopie de pompe-sonde, ont fourni des échelles de temps de décroissance des excitons de 10 à 100 ps. Cependant ces approches, non

résonnantes sont limitées par leur résolution temporelle et l'engagement d'autres dynamiques de relaxation pour la formation de l'exciton, masquant ainsi les dynamiques intrinsèques de l'exciton. Également, dans les TMD de type MX_2, l'élargissement inhomogène dû à la contrainte à l'échelle nanométrique ou au désordre diélectrique domine la largeur de raie des excitons. L'étendue de ce désordre et les propriétés de cohérence des excitons dans le ReS_2 n'avaient pas, avant nos études, été étudiées. La configuration de microscopie FWM développée lors de cette thèse est particulièrement adaptée pour répondre à ces questions.

En utilisant la microscopie de FWM, nous étudions la dynamique de cohérence et de population des excitons anisotropes dans le ReS_2 en focntion de différents paramètres tels que la température, la puissance d'excitation et l'épaisseur de l'échantillon (nombre de feuillets). En premier lieu, nous avons observé un temps de cohérence (T_2) des excitons de l'ordre des centaines de femtosecondes. De plus, les largeurs de raies des excitons étaient principalement élargies de manière homogène, indiquant un désordre négligeable dans le ReS_2 nu. Ensuite, nous explorons l'évolution de la largeur de raie homogène (γ) sous différentes conditions. Tout d'abord, en fonction de la température, la cohérence des excitons dans le ReS_2 montre une remarquable résistance aux augmentations de température, avec une dynamique de cohérence qui reste observable même à température ambiante. Nous observons également une dépendance linéaire de γ avec la température, ce qui signifie que l'augmentation de la décohérence induite par la température a une très faible contribution des phonons optiques et est plutôt dominée par la diffusion des phonons acoustiques. Ces comportements inhabituels contrastent fortement avec les systèmes MX_2, où la cohérence devient indétectable au-dessus de 120 K dans des conditions similaires et où) en fonction de la température montre une contribution significative des phonons optiques. Nos résultats concluent à une robustesse particulière des excitons de ReS_2 face à la décohérence induite par la température.

Parallèlement, nous observons un très faible déphasage induit par l'excitation (EID), à mesure que la puissance d'excitation augmente. D'après nos résultats obtenus à une température de 4 K, nous déduisons un EID d'un ordre de grandeur plus petit dans le ReS_2, par rapport aux autres TMD de type MX_2 [28–31]. De plus, les valeurs extraites de γ montrent un très faible changement en fonction du nombre de couche ReS_2.

D'autre part, la dynamique de décroissance de la population (obtenue cette fois

à partir de mesures FWM à trois impulsions) présente un comportement complexe multi-exponentiel, avec des échelles de temps variant de 150 fs à plusieurs nanosecondes. Une telle dynamique complexe est due à une combinaison de l'émission radiative des excitons dans l'état fondamental et de la diffusion avec des états excitoniques noires. Nous observons une réduction des trois échelles de temps avec l'augmentation de la température et de la puissance d'excitation. Cependant, très peu de changement est observé avec l'épaisseur variable du feuillet, confirmant que la structure de bande du ReS_2 n'est pas ou peu dépendant du nombre de couche atomique.

Pour conclure, nos résultats indiquent que le ReS2 multicouche présente des valeurs de T1 et T2 similaires à celles des monolayers MX_2 à gap direct (à basse température et faible puissance). À l'inverse, le système multicouche de MX_2 tel que $MoSe_2$, montre des durées de vie et de cohérence d'un ordre de grandeur plus courtes en raison du couplage inter-couches. Nos observations soutiennent donc l'hypothèse que ReS_2 possède une structure à gap direct, et ce, indépendamment du nombre de couches [20, 32]. Nos résultats confirment également le potentiel du ReS_2 pour des applications optoélectroniques et la photonique ultrarapides, où la stabilité et le faible désordre sont essentiels.

Dynamiques des excitons dans les hétérostructures $MoSe_2$-graphène

Le $MoSe_2$, un matériau vdW largement étudié, présente un gap direct et des excitons brillants avec de fortes énergies de liaison dans sa forme monomono-couche [8, 12–16]. Sa compatibilité d'assembalge avec d'autres matériaux vdW permet la formation d'hétérostructures, offrant ainsi des opportunités pour explorer de nouvelles propriétés excitoniques [9, 12, 13, 33]. Ce chapitre examine les dynamiques des excitons dans une hétérostructure $MoSe_2$-graphène.

L'échantillon étudié, préparé par nos collaborateurs (le groupe de Stéphane Berciaud) à l'IPCMS de Strasbourg, consiste en un monomono-couche de $MoSe_2$ encapsulé dans du hBN et partiellement empilé avec du graphène. Les propriétés excitoniques de l'hétérostructure sont influencées par les interactions aux interfaces dues à l'échelle

atomique des couches et à la distance inter-couche sub-nanométrique [5]. Nous examinons les effets de couplage entre le graphène et le $MoSe_2$ sur les dynamiques des excitons, en nous concentrant sur les échelles de temps et la nature des mécanismes de couplage dominants. L'interaction entre le graphène et le $MoSe_2$ peut être statique ou dynamique (induite par photon). Le graphène introduit un canal de décroissance non radiatif (τ_G) pour les excitons dans l'hétérostructure, via des processus dynamiques tels que le transfert de charge ou d'énergie [5,33–36]. Des études antérieures, y compris des mesures de photoluminescence résolue en temps (TRPL) sur le même échantillon, estiment que l'échelle de temps de transfert d'énergie vers le graphène est d'environ 2.5 ps [5], ce qui est cohérent avec d'autres rapports [33–35]. Cependant, l'excitation non résonante dans ces étudesne permat pas d'explorer les dynamiques ultrarapides (inférieures à 1 ps).

Dans cette étude, nous comparons deux emplacements sur l'échantillon : Gr-1L (MoSe2 - monomono-couche de graphène) et Gr-2L ($MoSe_2$ - bilayer de graphène) avec un emplacement de référence (uniquement $MoSe_2$). Les mesures de PL effectuées sur ces emplacements montrent immédiatement des changements significatifs en présence de graphène : absence de trion, décalage vers le rouge du pic des excitons (de 10 meV) et une quenching (réduction) de l'intensité de la PL des excitons d'un facteur ≈ 20. Ces effets sont cohérents avec des mesures précédentes effectuées sur des hétérostructures TMD-graphène similaires [5, 6, 33–37]. La réduction de l'intensité de la PL des excitons est causée par un processus dynamique de transfert d'exciton ou transfert de charge net vers le graphène [5, 33, 34].

Suite à la caractérisation par photoluminescence (PL), nous effectuons des mesures de mélange de quatre ondes résonantes (FWM) à trois endroits distincts de l'échantillon. L'analyse des données FWM (à deux impulsions) nous permet d'extraire à la fois la largeur de raie homogène (γ) et la largeur de raie inhomogène (σ) en utilisant la méthodologie décrite dans les sections précédentes. Nos résultats indiquent que l'élargissement inhomogène joue un rôle clé dans la dynamique des excitons au sein de cette hétérostructure. Notamment, le comportement de σ en fonction de la puissance d'excitation diffère considérablement entre l'emplacement de référence et les deux autres emplacements (avec graphène). À l'emplacement de référence, σ diminue légèrement avec l'augmentation de la puissance, tandis qu'en présence de graphène, σ montre une augmentation prononcée. Fait intéressant, cette variation de σ est corrélée au changement des es dynamiques excitoniques observées dans l'échantillon.

À partir des mesures FWM à trois impulsions, nous identifions trois échelles de temps de décroissance distinctes : T_{11} (allant de 370 fs à 1.5 ps), T_{12} (5 à 30 ps) et T_{13} (50 à 830 ps). Ces échelles de temps de décroissance de la population sont principalement en accord avec des études précédentes sur les excitons dans les monocouches de $MoSe_2$ [28, 31, 38, 39]. Nos résultats montrent que la présence de graphène affecte principalement la composante de décroissance longue (T_{13}), qui diminue d'environ la moitié par rapport à l'emplacement de référence, tandis que les échelles de temps plus courtes (T_{11} et T_{12}) restent inchangées. Cela met en évidence une échelle de temps de couplage longue (≈ 100 ps) entre les excitons dans $MoSe_2$ et le graphène, qui pourrait être attribuée à un transfert de charge net plutôt qu'au transfert d'énergie de quelques picosecondes rapporté dans des études précédentes [5, 33–35, 40]. La différence entre nos résultats et les études précédentes peut s'expliquer de la manière suivante. L'excitation résonnante utilisée dans notre étude implique principalement des excitons liés au niveau de transition fondamental, excluant les paires électron-trou libres et les "excitons chauds". Dans ce régime, les mécanismes de diffusion exciton-exciton dominent les dynamiques de population, pouvant prévenir l'observation d'éventuels processus de couplage à court terme avec le graphène. En revanche, les expériences non résonantes excitent des "excitons chauds", qui se relaxent et peuplent des états d'excitons sombres, réduisant la densité d'excitons brillants au niveau fondamental et laissant ouverte la possibilité d'un transfert rapide vers le graphène. Pour mieux résoudre ces mécanismes, une spectroscopie Raman résonante résolue netemps pourrait être employée pour surveiller les niveaux de dopage dans le graphène à des échelles de temps de dizaines de picosecondes, offrant plus de clarté sur les dynamiques de couplage dans de telles hétérostructures.

En parallèle de l'effet du graphène sur T_{13}, la décroissance la plus rapide, T11 montre un comportement intéressant avec la puissance d'excitation (P). T_{11} en fonction de P reflète la tendance observée pour σ : T_{11} diminue avec P à l'emplacement de référence, mais augmente à Gr-1L et Gr-2L. Cela peut être expliqué par la localisation des excitons, ce qui ralentit le processus de décroissance radiative [30, 41]. En effet un désordre plus élevé du potentiel perçu par les excitons, reflété par une augmentation de σ, induit une localisation spatiale de ces derniers, et ainsi un temps de vie T_{11} plus long. De plus, le comportement de la largeur de raie homogène γ avec la puissance d'excitation suit également les changements de σ et T_{11}. À des puissances plus élevées, γ augmente pour tous les emplacements, mais à l'emplacement de référence,

γ augmente plus rapidement qu'à Gr-1L et Gr-2L. À l'emplacement de référence, le temps de décohérence, T_2, est limité par la durée de vie. L'augmentation de γ avec une puissance plus élevée, à cet emplacement, est causée par une diminution de T_{11}, en raison d'une réduction de σ. À Gr-1L et Gr-2L, cependant, la décohérence est gouvernée par des mécanismes de dépahsage, tels que la diffusion exciton-exciton, entraînant un taux d'augmentation de γ avec la puissance plus élevé.

Cette étude est la première à utiliser une excitation résonante avec une résolution temporelle de $\approx$ 100 fs et une détection sensible à la phase sur une hétérostructure $MoSe_2$-graphène, fournissant de nouvelles perspectives sur la dynamique des excitons et des interactions exciton-graphène.

Analyse statistique de l'émission des défauts quantiques dans le hBN: familles spectrale et influence de la morphologie des feuillets

---

Ce chapitre se concentre sur les propriétés optiques des systèmes confinés zéro-dimensionnels (0D), spécifiquement les émetteurs de photons uniques (SPEs) dans le nitrure de bore hexagonal (hBN). Le hBN a suscité une grande attention ces dernières années abritant des émetteurs quantiques photostables à température ambiante avec une émission sur une large plage de longueurs d'onde. Cependant, l'identification des défauts responsables de ces émissions reste un défi en raison de la dispersion spectrale et de la nature complexe des raies d'émission des défauts.

Cette étude aborde l'identification spectrale des familles d'émission de défauts dans des nanofeuillets de hBN exfoliés en phase liquide. Un ensemble de données de 87421 spectres PL a révélé 8307 raies zéro-phonon (ZPL), permettant l'identification de 11 clusters d'émission spectrale ZPL distincts. Ces résultats contredisent l'hypothèse d'une distribution continue des énergies de défauts, fournissant de nouvelles perspectives sur les origines microscopiques des émetteurs. De plus, l'étude

démontre comment la morphologie des nanofeuillets de hBN influence la formation des défauts, permettant un contrôle précis des espèces de défauts.

Les échantillons de cette étude ont été préparés à partir de nanofeuillets de hBN exfoliés en phase liquide, suspendus dans une solution eau-éthanol, puis déposés sur des substrats Si/SiO_2 après traitement par ultrason et centrifugation. Une caractérisation par diffusion dynamique de la lumière (DLS) a été réalisée pour déterminer la distribution de taille des feuillets avant le dépôt. Deux échantillons ont été préparés : l'échantillon A (taille des feuillets variant de 80 à 160 nm) et l'échantillon B (taille des feuillets variant de 130 à 250 nm et de 9 à 14 μm). Un système micro-PL confocal maison (NA de 0.6, objectif 50×, excitation laser continu à 532 nm) a été utilisé pour obtenir des cartes PL hyperspectrales, avec un pas de 1 μm. Les cartes ont été analysées à l'aide d'un algorithme de détection de pics développé lors de cette thèse. Cet algorithme permet de classer automatiquement les spectres de raies zéro-phonon (ZPLs) et ceux des bandes latérales de phonons (PSBs). Un histogramme de 8307 ZPLs de défauts identifiés a révélé une distribution énergétique discrète, contrairement aux hypothèses précédentes d'un spectre d'émission continu et aléatoire. Onze familles distinctes de défauts, étiquetées F1 à F11, ont été identifiées dans la plage de 1.6 à 2.2 eV. Notre approche statistique nous a également permis d'extraire des paramètres clés des défauts, tels que les largeurs de raies d'émission, la densité spatiale des défauts, et les facteurs de Franck-Condon. Après avoir identifié les familles spectrales, nous avons exploré la possibilité de contrôler la formation des défauts en ajustant les paramètres relatifs à la morphologie des feuillets : la densité d'agglomération des feuillets et la taille des feuillets. La distribution spectrale de l'énergie des défauts en fonction de ces paramètres a révélé des différences distinctes, démontrant ainsi la formation sélective des familles de défauts.

Nos résultats offrent des informations clés sur les origines microscopiques des émetteurs dans les hôtes hBN. Nous mettons en évidence l'espacement spectral entre les familles de défauts comme un paramètre crucial pour les études théoriques, offrant une approche plus fiable que les valeurs d'énergie absolues, qui sont difficiles à déterminer. De plus, nous démontrons que la morphologie des hôtes hBN influence fortement la distribution spectrale des familles de défauts. En contrôlant la taille et l'agencement des feuillets par des méthodes simples comme la centrifugation et le dépôt par gouttelette, nous montrons qu'une variété de défauts peut être générée sélectivement tout en maintenant une densité de défauts élevée, offrant une alternative

évolutive aux techniques coûteuses d'ingénierie des défauts.

Conclusion

Cette thèse explore les dynamiques intrinsèques des excitons dans les matériaux de van der Waals , en se concentrant sur les TMDs et les hétérostructures à base de TMDs. Grâce à une technique originale résolue en temps de microscopie cohérente de mélange à quatre ondes, nous avons étudié les excitons dans le ReS_2, mettant en évidence une dynamique excitonique cohérente homogène, et particulièrement robuste en fonction de la température, de l'excitation optique et du nombre de feuillets. Dans une hétérostructure $MoSe_2$-graphène, nous avons identifié un processus de transfert de charges à long terme vers le graphène, ainsi qu'un effet inédit, dépendant de la puissance, du graphène sur l'élargissement inhomogène des excitons. Cela a conduit à des modifications des échelles de temps rapides de décroissance de population et de l'élargissement homogène. En outre, nous avons réalisé une analyse statistique des émissions de défauts dans le hBN à l'aide de la spectroscopie de microphotoluminescence. Nos résultats remettent en question l'idée d'une distribution aléatoire des énergies spectrales, révélant une discrétisation claire des distributions d'énergie d'émission. Par ailleurs, ces travaux fournissent des informations sur les origines microscopiques des défauts et une méthode intéressante pour fabriquer des défauts avec une énergie d'émission définie.

List of publications

Journal publications

1. Md Samiul Islam, Rup Kumar Chowdhury, Marie Barthelemy, Loic Moczko, Pascal Hebraud, Stephane Berciaud, Alberto Barsella and Francois Fras. Large-Scale Statistical Analysis of Defect Emission in hBN: Revealing Spectral Families and Influence of Flakes Morphology, ACS Nano 2024, 18, 32, 20980–20989.

2. Rup Kumar Chowdhury, Md Samiul Islam, Marie Barthelemy, Nicolas Beyer, Lorry Engel, Jean-Sebastien Pelle, Mircea Rastei, Alberto Barsella, Francois Fras. Robust coherent dynamics of homogeneously limited anisotropic excitons in two-dimensional layered ReS2. [Submitted in Nature Physics]

3. Md Samiul Islam, Luis E Parra Lopez, Rup K. Chowdhury, Marie Barthelemy, Stephane Berciaud and Francois Fras. Long timescale coupling and effect of inhomogeneous broadening on exciton dynamics in MoSe2 - graphene heterostructure. [Manuscript in preparation]

4. Md Samiul Islam, Rup K. Chowdhury, Thibault Chervy, Marie Barthelemy and Francois Fras. Effect of out of plane and in-plane electric field on the coherence dynamics of excitons in MoSe2 monolayer. [Manuscript in preparation]

Conference proceedings and contributions

1. Md Samiul Islam, Rup K. Chowdhury, Marie Barthelemy, Stephane Berciaud, Alberto Barsella and Francois Fras. Large-Scale Statistical Analysis of Defect Emission in hBN: Revealing Spectral Families and Influence of Flakes Morphology. Oral presentation. SPIE Photonics Europe - Quantum Technologies. Strasbourg (France), April 2024.

2. Rup K. Chowdhury, Md Samiul Islam, Marie Barthelemy, and Francois Fras. Layer independent lifetime and coherence of anisotropic excitons in ReS2. Oral presentation, SPIE Photonics Europe - Advances in Ultrafast Condensed Phase Physics IV. Strasbourg (France), April 2024.

3. Md Samiul Islam, Rup Kumar Chowdhury, Marie Barthelemy, Francois Fras. Coherent ultrafast spectroscopy of excitons in Van der Waals materials. Poster and verbal presentation. QUSTEC (Quantum Science and Technologies at the European Campus) closing conference. Strasourg (France), April 2024.

4. Md Samiul Islam, Rup K. Chowdhury, Marie Barthelemy, Stephane Berciaud, Alberto Barsella and Francois Fras. Large-Scale Statistical Analysis of Defect Emission in hBN: Revealing Spectral Families and Influence of Flakes Morphology. Poster presentation. Nanophotonics and Micro/Nano Optics International Conference. Barcelona (Spain), November 2023.

5. Md Samiul Islam, Romain Parret, Stephane Berciaud and Francois Fras. Quantum properties of singe photon emitters in hBN : micro Photoluminescence characterization toward ultrafast coherent spectroscopy. Poster presentation. Quantum Technologies with Light and Matter summer school, Les Houches (France), September 2020.

Contents

Introduction

Van der Waals (vdW) materials consist of covalently bonded atomic layers, connected by weak vdW force. Although these materials have been known to scientists for a long time, it wasn't known whether it is possible to isolate individual layers of such materials. This changed in 2004, when Novoselov et. al. [42] managed to isolate a single layer of graphite (named graphene), using the now famous "scotch tape" technique. He showed that such monolayer is not only thermodynamically stable, but gives rise to drastically different properties compared to the bulk form of the same material. This discovery launched a subfield of solid state physics known today as "2D materials" and led to the discovery of a plethora of such materials. Among these, Transition metal dichalcogenides (TMDs) have garnered a particularly striking amount of scientific curiosity and effort. This is due, among other factors, to its unique flexibility and tunability, and, from an optical standpoint, efficient light-matter coupling and exceptionally high exciton binding energy. Additionally, it offers unique control over excitons through spin-valley locking and enables single-photon emission from defects and bound excitons [11, 43]. Moreover, such 2D systems allow the formation of heterostructures consisting of stacked monolayers or few layers from different 2D materials, exhibiting unique properties, not found in the individual constituent materials. These heterostructures offer unprecedented possibilities for enginnering the electronic and optical properties of vdW materials. In addition to offering significant opportunities for fundamental research into excitonic properties, vdW materials present possess potential for applications in optoelectronics, valleytronics, and quantum technologies [13, 43–45].

Despite significant research efforts aimed at understanding the excitonic properties in vdW materials, many questions remain unanswered. In particular, the coherence and population dynamics of excitons in TMDs continue to be the subject of ongoing debates. A notable example is rhenium disulfide (ReS_2), a group 7 TMD, which exhibits anisotropic excitons and features weak interlayer coupling, making it a highly promising candidate for device applications [17–21]. However, the dynamic properties of excitons in ReS_2 are still largely unexplored. Even for a more extensively studied TMD like molybdenum disulfide ($MoSe_2$), key aspects of exciton dynamics such as, the timescale of radiative decay of excitons and the mechanisms underlying exci-

ton scattering into dark states, require further investigation. Furthermore, excitonic properties in vdW heterostructures present a fascinating area of study with numerous opportunities for fundamental research and device integration [5, 33, 35, 37, 40, 46, 47]. The excitonic properties in these advanced structures have not been extensively studied, offering considerable potential for further investigation. In particular, the interaction between excitons in TMD layers and adjacent layers in a vdW heterostructure, and the resulting impact on excitonic dynamics, warrants more in-depth investigation. This will not only deepen our understanding of these systems but also enable fine-tuning of excitonic properties, unlocking the potential of these structures for applications in optoelectronics, photonics, and valleytronics.

In both bare vdW materials and their heterostructures, the interactions of bright excitons with phonons, other excitons, and local disorder centers at the microscopic or even single-system level play a critical role in shaping the excitonic properties [29, 30, 38, 48, 49]. To address these questions, resonant optical techniques, such as four-wave mixing (FWM) spectroscopy, are particularly suitable [28, 50, 51], as they provide a direct method for investigating exciton coherence and population dynamics at the resonant level. However, sample parameters such as strain, local doping, number of layers, and mechanical defects can vary significantly on a microscopic scale. Therefore, a microscopic approach is essential to tackle these questions. However, coupling resonant spectroscopy with a microscopic approach is quite a challenge, and this forms the core of the work presented here.

The primary objective of this thesis is to study the dynamic properties of excitons in vdW materials. We study the coherence and population dynamics of excitons in such materials as a function of various environmental parameters like excitation power density, temperature and crystallographic environment. We also investigate the possibility of engineering the properties of excitonic systems in these materials. Through this investigation, this thesis aims to answer questions regarding the fundamental properties of the studied materials and at the same time, reveal their potential for application. In order to study the exciton dynamics, we have developed a state of the art resonant four wave mixing (FWM) experimental setup, combining ultrafast temporal resolution, diffraction limited spatial resolution and 300 μeV spectral resolution. This setup utilizes optical heterodyne detection and spectral interferometry. It allows us to extract both the coherence and population dynamics of excitons in vdW materials.

In chapter 1, some fundamental excitonic properties in vdW materials will be provided. The will focus on the properties of vdW materials that are relevant for this thesis and will give the readers the concepts necessary to follow the work in this thesis. These materials are: graphene, group-6 TMDs and one particular group-7 TMD: rhenium di-sulfide (ReS_2). This chapter will also provide an idea about the underlying motivation behind this work.

Chapter 2 will provide the essential concepts and experimental methodology required to fully grasp the findings presented in later chapters. While the more traditional and straightforward aspects such as the sample preparation methods and initial characterization technique will be briefly covered, the chapter's primary focus will be on the development of a state of the art FWM microscopy experimental setup. The theoretical foundation supporting this technique will be explained in detail, including the derivation of key equations used to fit the data in subsequent chapters. A full discussion of the experimental setup design, with all its details, falls beyond the scope of this thesis. Instead, a practical overview will be provided, focusing on the key aspects necessary to understand how the time-resolved measurements are conducted and how to interpret the results.

The three subsequent chapters will describe in detail the obtained results in this work. The coherence and population dynamics of anisotropic excitons in ReS_2 will be presented in chapter 3. The associated discussion will highlight the exceptional robustness of the dynamic properties with respect to optical power, temperature, and the number of layers, with the latter offering significant insights into the nature of the electronic bandgap of such materials.

Chapter 4 will present the results obtained from a molybdenum di-selenide ($MoSe_2$) - graphene heterostructure. This chapter will demonstrate the changes in the dynamic properties of excitons in a $MoSe_2$ monolayer, due to the presence of graphene in the local environment. We observe clear changes in the exciton population dynamics as a result of interaction between the excitons in $MoSe_2$ and graphene. We also estimate a timescale characterizing this interaction and discuss our results in contrast to previous studies on similar heterostructures. In addition, we observe a novel effect of graphene on the local disorder in the exciton environment.

The results presented in chapter 5 is somewhat different compared to the preceding chapters, as it focuses on localized excitons, and addresses the last stated objective of this thesis: engineering the properties of excitonic systems in vdW materials. This

chapter concentrates on a large scale statistical analysis of photoluminescence (PL) spectra from defects in hexagonal boron nitride (hBN). The findings reveal that the defects appear to form narrow set of spectral families distributed within the 1.6 to 2.2 eV energy range. The findings reveal a departure from a continuous distribution of defect emission energies when the number of defects becomes statistically significant. Additionally, a method is demonstrated to control the formation of defects with specific emission energies using relatively simple sample preparation techniques.

1 Bandstructure and excitons in van der Waals materials

In this chapter, some background context to the systems of interest for this thesis is provided. Van der Waals (vdW) materials will be introduced first, followed by a description of the first 2 dimensional vdW material ever discovered: graphene. The properties of excitons in semiconductors will then be described, followed by an exploration of excitonic properties in some specific vdW materials studied in this thesis.

1.1 Van der Waals materials

Two-dimensional (2D) vdW materials consist of atomically thin layers with strong in-plane covalent bonds and weak van der Waals bonds between successive layers [1]. This characteristic property of weak interlayer bonding makes it possible to extract very thin layers of such materials, even one-atom-thick monolayers from the bulk crystal. These monolayers are thermodynamically stable. The most well-known material of this type is graphene. Since the discovery of graphene in 2004, using the now famous "scotch tape" technique [42], a significant amount of research has been done on this topic, which led to the discovery of a whole library of such materials. These include transition metal dichalcogenides (TMDs) of the form MX_2, where M= molybdenum (Mo), tungsten (W), and X= sulfur (S), selenium (Se), and other materials like black phosphorus, hexagonal boron nitride (hBN), silicene, etc. The properties of these materials are largely dependent on the number of layers. For example, molybdenum disulfide (MoS_2) and molybdenum diselenide ($MoSe_2$) in their bulk form are indirect bandgap semiconductors, but they transition from indirect to direct bandgap semiconductors as the number of layers is reduced down to a monolayer [2, 3]. Furthermore, it's possible to stack multiple monolayers or multilayers of different vdW materials to design heterostructures, which effectively opened up a tremendous number of possibilities in terms of tunability of electronic and optical properties. The work in this thesis is focused on hexagonal boron nitride (hBN), rhenium disulfide (ReS_2), and advanced vdW structures such as $MoSe_2$-graphene heterostructures. In

the following sections, graphene will first be introduced to establish a foundational understanding of 2D van der Waals (vdW) materials and to explain its relevance as part of a heterostructure. Next, we will briefly discuss the general properties of transition metal dichalcogenides (TMDs). This will be followed by an overview of excitons, with particular attention to their properties in TMDs. Finally, a more detailed discussion of the properties of $MoSe_2$ and ReS_2 will be provided.

1.2 Graphene

Graphene is a monolayer of graphite. It is an allotrope of carbon (C), consisting of a single layer of C atoms arranged in a honeycomb pattern. The 2s, $2p_x$, and $2p_y$ orbitals hybridize to form three sp^2 hybrid orbitals. In graphene, each C atom forms a σ bond with its neighboring C atom through these sp^2 orbitals. The remaining unhybridized $2p_z$ orbitals of neighboring C atoms form π bonds between each other. In the bandstructure picture, the σ energy bands (bonding and antibonding) are significantly far away from the Fermi energy level. The key electronic properties of graphene are determined by the π energy bands [4–6].

1.2.1 Crystal structure

Graphene's lattice structure can be considered triangular with a two-atom basis. In other words, graphene's lattice consists of two sublattices of one atom basis each, referred to as A and B atoms. Figure 1.1a shows this crystal structure, with the lattice vectors and the unit cell (shaded). Two neighboring A and B atoms are separated from each other by a distance, $a = 1.42\,\text{Å}$. The lattice basis vectors are given by $a_1 = \frac{a}{2}(3, \sqrt{3})$ and $a_2 = \frac{a}{2}(3, -\sqrt{3})$. As shown in Figure 1.1a, the vectors $\delta_1 = \frac{a}{2}(1, \sqrt{3})$, $\delta_2 = \frac{a}{2}(1, -\sqrt{3})$, and $\delta_3 = -a(1, 0)$ connect each atom (A or B) to its next nearest neighbor. Figure 1.1b demonstrates the hexagonal first Brillouin zone (BZ) of graphene, with reciprocal lattice vectors $b_1 = \frac{2\pi}{3a}(1, \sqrt{3})$ and $b_2 = \frac{2\pi}{3a}(1, -\sqrt{3})$ [6].

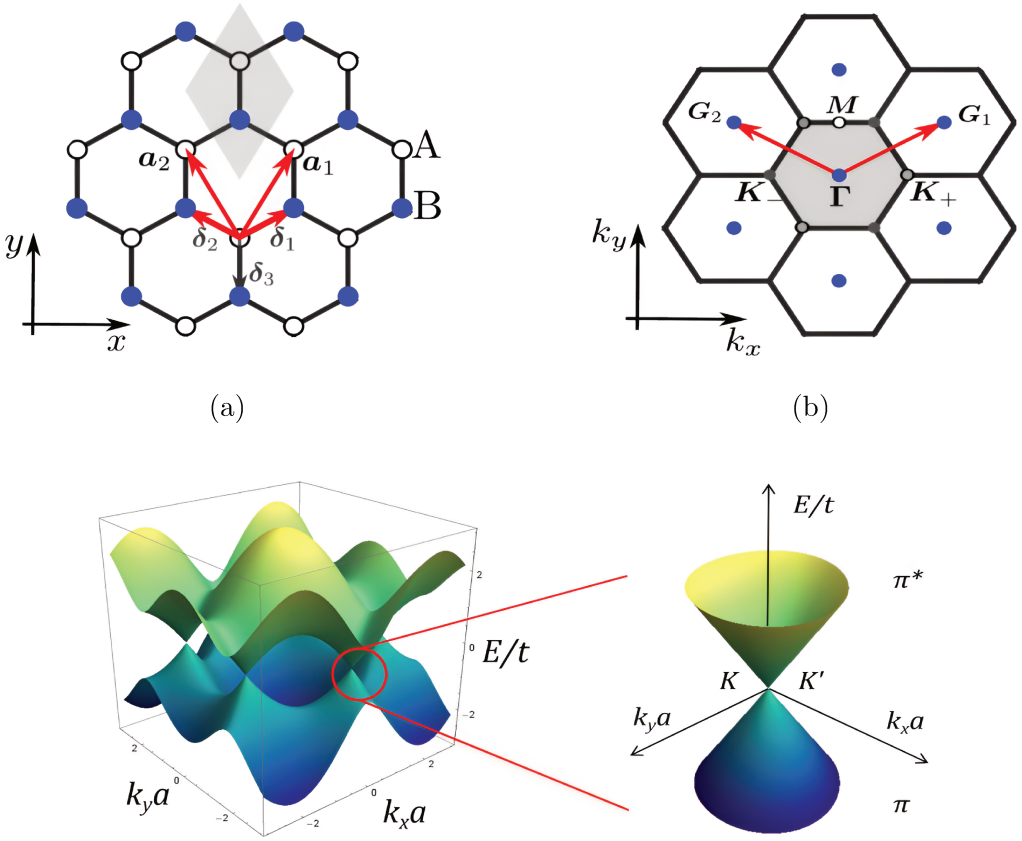

(a) (b)

(c)

Figure 1.1: (a) Crystal structure of Graphene, shown with the lattice vectors a_1, a_2 and nearest neighbor vectors δ_1, δ_2 and δ_3. The shaded region is the unit cell. (b) First Brilluoin zone of Graphene, with the inequivalent high symmetry points K_+ and K_-.(c) Graphene's energy dispersion relation calculated using the Tight Binding model. The dispersion near the K point is enhanced for clarity [4, 6].

1.2.2 Energy bandstructure and key properties

The bandstructure of Graphene can be described using the Tight binding model. The resulting energy dispersion relation can be written as:

$$E_{\pm}(k_x, k_y) = \pm t\sqrt{3 + 2cos(\sqrt{3}k_y a) + 4cos(\frac{\sqrt{3}}{2}k_y a)cos(\frac{\sqrt{3}}{2}k_x a)} \tag{1.2.1}$$

Here, the + and - correspond to the completely filled valence band (π) and completely empty conduction band (π^*), respectively. k is the electron wavevector and $\hbar$ is taken

to be equal to 1 [52]. The energy dispersion is shown in figure 1.1c. The Fermi energy (E_F) is located where the valence and conduction bands meet, giving graphene semi-metallic properties. The energy dispersion has a conical shape near E_F and is also symmetric around the $K_{\pm}$points of the first BZ [4, 53]. Figure 1.1c shows an enhanced view of the dispersion near these two inequivalent points (K_+ and K_-). The dispersion relation is identical at these two points and an electron can occupy any of these two degenerate states. These two points are referred to as K_+ and K_- valleys. So, in addition to the spin, graphene provides a new degree of freedom for the electron: valley degree of freedom. Near the $K_{\pm}$ points, the electron wavevector can be expressed as $\boldsymbol{k} = \boldsymbol{K_{\pm}} + \boldsymbol{\kappa}$, where $\mid \boldsymbol{\kappa} \mid < \mid \boldsymbol{K_{\pm}} \mid$. A Taylor expansion of the energy dispersion with this wavevector definition gives the following expression (including $\hbar$ in the expression) [5]:

$$E_{\pm} = \pm \hbar v_F \mid \boldsymbol{\kappa} \mid \tag{1.2.2}$$

where $v_F = \frac{3ta}{2} = (1 \times 10^6)$ ms^{-1} is known as the Fermi velocity. This linear relation between the energy of the electron near the $K_{\pm}$ and the wavevector gives rise to the conical shape of the dispersion shown in figure 1.1c. They are known as the "Dirac cones", and the two points $K_{\pm}$ are called Dirac points. The name originates from the fact that the energy of the electrons at this point does not follow the usual quadratic dispersion relation like in most solids. Instead, the energy dispersion relation is linear, similar to that of relativistic particles with zero rest mass, mimicking the equation: $E = \sqrt{p^2c^2 + m^2c^4}$, with $m = 0$. The wavefunction of the electrons at the $K_{\pm}$ also obeys the Dirac equation for massless Fermions, instead of the Schrödinger equation [4–6, 52].

The Dirac Hamiltonians near the $K_{\pm}$ points:

$$H_{K_+} = v_F \boldsymbol{\sigma} \cdot \boldsymbol{p} \tag{1.2.3}$$

$$H_{K_-} = v_F \boldsymbol{\sigma^*} \cdot \boldsymbol{p} \tag{1.2.4}$$

where $\boldsymbol{p} = \hbar \boldsymbol{\kappa}$ and $\boldsymbol{\sigma} = (\sigma_x \sigma_y)$ is a vector, with Pauli matrices as its components. This two-component Pauli vector $\boldsymbol{\sigma}$ does not operate on the real spin; rather, it operates on the sublattice degree of freedom (A atoms or B atoms). This is referred to as the "pseudospin" degree of freedom. This is just an alternate way to refer to a specific lattice site, with pseudospin up referring to sublattice A and pseudospin down to sublattice B.

Electrons behaving as massless Dirac Fermions give rise to some highly unusual properties in graphene. For example, graphene has remarkably high conductivity with electron mobility of 10^4 $cm^2V^{-1}s^{-1}$ at room temperature [5], extremely high thermal conductivity (up to 5000 Wm/K) and mechanical strength (Young's Modulus 1 TPa). Additionally, graphene is highly transparent, transmitting about 97.4% of incident light in the optical range. The high conductivity and transparency together make graphene an ideal material for use as gate electrodes in solid-state optical devices. Moreover, graphene is an attractive choice for use in vdW heterostructures, where its unique properties can significantly influence the behavior of the adjacent materials. For instance, graphene's Fermi level E_F lies within the bandgap of many transition metal dichalcogenides (TMDs), enabling it to efficiently function as an electron acceptor in a TMD-graphene heterostructure. This interaction has the potential to give rise to remarkable electronic and optoelectronic phenomena [5–7].

1.3 Transition metal dichalcogenide (TMD)

Transition metal dichalcogenides (TMDs) refer to a group of 60 materials. Most of these materials have a layered structure with strong in-plane covalent bonds and a weak out-of-plane van der Waals (vdW) force connecting the layers. The general chemical formula of TMDs is MX_2, where M represents a transition metal atom and X refers to chalcogen atoms. According to the definition from the International Union of Pure and Applied Chemistry (IUPAC), a transition metal atom has a partially filled d orbital or can lead to a cation with a partially filled d orbital. Examples of transition metals include Mo, W and Re. Whereas, the chemical elements in group 16 of the periodic table are known as chalcogens (six valence electrons, s^2p^4), S and Se.

1.3.1 Crystal structure

A single layer of a layered TMD material features transition metal atoms typically arranged in a hexagonal pattern, positioned between two layers of chalcogen atoms. However, variations in atomic arrangements can occur depending on the specific TMD. The thickness of a typical monolayer is on the order of a few angstroms. For instance, a $MoSe_2$ monolayer measures approximately 6–7 Å [10]. The transition metal atom contributes 4 electrons from its partially filled d orbital to the in-plane covalent

bond with the chalcogen atoms, while the lone pair electrons from the chalcogen atom provide surface termination. Such a single layer of TMD is thermodynamically stable because of the absence of dangling bonds [8].

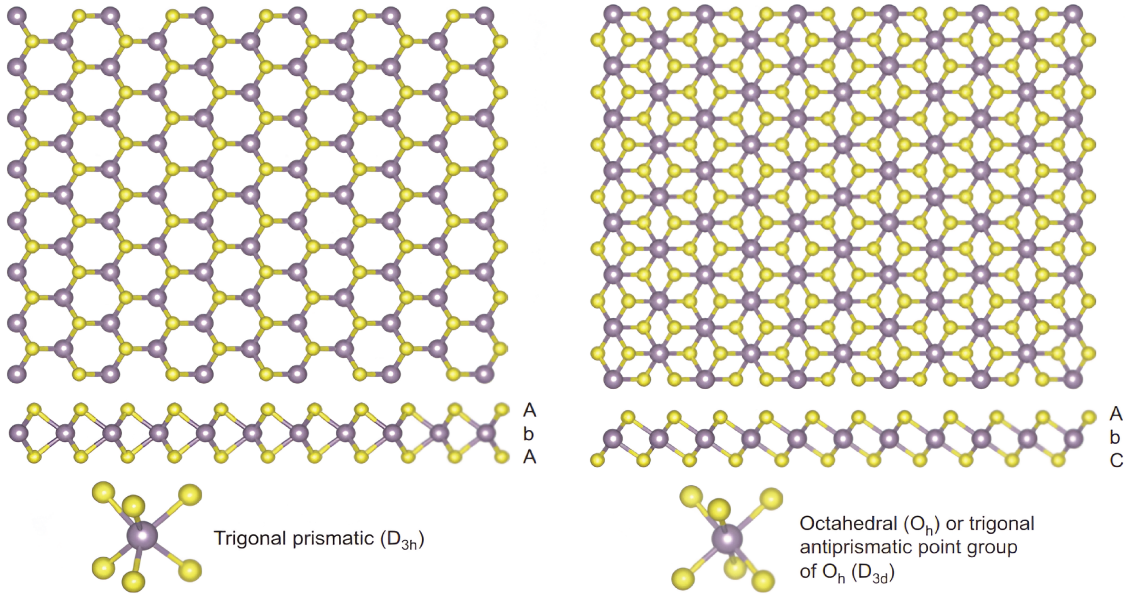

Figure 1.2: Crystal structure of layered TMD (Top view and side view): (a) Trigonal prismatic or H phase (b) Octahedral or T phase [8].

Depending on the atomic arrangement, most MX_2 exhibit one of two types of crystal structures: trigonal prismatic (H phase) and octahedral (T phase). Figure 1.2 shows these two types of crystal structure. In the H phase, the atoms in the two chalcogen layers above and below the metal atomic layer are aligned with respect to each other, whereas in the T phase, the two layers are 180^0 shifted from one another [9]. The T phase is also known as the trigonal antiprismatic phase. These two crystal structures belong to the hexagonal D_{3d} and tetragonal D_{3h} point group symmetry, respectively [8, 54].

The properties of layered TMD are also heavily influenced by how many X-M-X unit layers constitute a unit cell and what the stacking sequence of these constituent unit layers is. These factors give rise to many different polymorphs of layered TMD materials. Different stacking sequences of the layers are also known as polytypes. Two of the most common types of polymorphs found in TMD are 1T and 2H. Here,

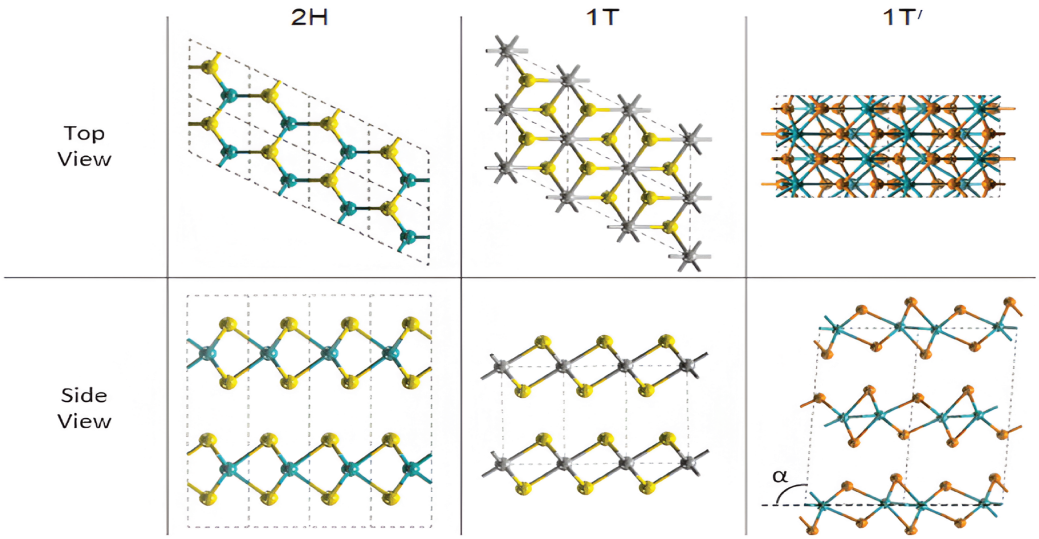

Figure 1.3: Different types of stacking sequence of layered TMD: Trigonal prismatic 2H, octahedral 1T and distorted octahedral 1T′ [9]

the number refers to the number of unit layers that make up the unit cell [8]. Figure 1.3 shows the top view and side view of trigonal prismatic 2H, octahedral 1T, and distorted octahedral 1T′ polymorphs. The stacking sequence of the 2H polymorph is AbA bAb, where the upper and lower case letters refer to metal and chalcogen atoms, respectively. The 1T′ polymorph is a distorted 1T polymorph, where the chalcogen atoms are shifted in the out-of-plane direction as a result of dimerization [8, 9]. Molybdenum diselenide ($MoSe_2$) and rhenium disulfide (ReS_2) are examples of 2H and 1T′ polymorphs, respectively. An interesting aspect of TMD is the change in crystal symmetry depending on the number of layers. For example, for 2H phase TMD, the bulk unit cell is made of two MX_2 molecules (six atoms) which gives D_{6h} symmetry with an inversion center. However, the monolayer unit cell consists of one MX_2 molecule and lacks an inversion center, resulting in D_{3h} symmetry [14].

The electronic bandstructure of solids is strongly correlated to their crystal structure and the electronic configuration of the constituent atoms. In layered TMD, the chalcogen atom s and p orbital energy lies much below the Fermi level [9, 54]. The bandstructure and the electronic properties of TMD are mostly determined by the

coordination of transition metal atoms and the number of d orbital electrons [8]. In both 1H and 1T phases, the nonbonding d orbitals lie between the bonding and the antibonding orbitals. Partially filled nonbonding d orbitals can lead to metallic behavior for a TMD, whereas completely filled d orbitals result in semiconducting properties [54]. For example, $MoSe_2$ and MoS_2 show semiconducting properties in their 2H phase but transition to metallic behavior when their phases change to 1T [55, 56]. The 1H phase leads to a splitting of the d orbitals into three sets of degenerate energy levels: d_{z^2} (a_1), $d_{x^2\text{-}y^2,xy}$ (e), and $d_{xz,yz}$ (e'). In contrast, the 1T phase or octahedral coordination gives rise to two sets of degenerate levels: $d_{z^2,x^2\text{-}y^2}$ (e_g) and $d_{yz,xz,xy}$ (t_{2g}). As for the effect of the chalcogen atoms, there is a general trend of TMD bandgap decreasing with an increase in the atomic number of the constituent chalcogen atoms [8, 12, 54].

1.3.2 Group 6 TMD: MoX_2, WX_2

Among the different materials in the TMD family, some of the most prominent and well-studied ones are those originating from group 6 transition metals (Mo, W). Since the emergence of 2D materials, these group 6 TMDs have garnered considerable attention due to their diverse properties and potential applications in optoelectronic and valleytronic devices. A significant part of the results presented in this thesis concerns this type of TMD. Group-6 TMDs are indirect semiconductors in their bulk form. Examples include molybdenum disulfide (MoS_2), molybdenum diselenide ($MoSe_2$), tungsten diselenide (WSe_2), etc. These TMDs are usually stable in the 2H-phase (trigonal prismatic), with a hexagonal crystal structure. They have the chalcogen atom p_z orbital and the transition metal atom d_z^2 orbital providing the electronic states at the Γ point of the hexagonal Brillouin zone. The valence band maximum (VBM) is located at this point, with strong out-of-plane electronic state contribution and strongly affected by inter-layer interaction. The conduction band minimum (CBM) is located halfway between Γ and K points ($\Gamma - K$). On the other hand, the $K_\pm$ points have their electronic states mostly localized in-plane, contributed largely by transition metal $d_{x^2-y^2,xy}$ orbitals and chalcogen atom $p_{x,y}$ orbitals. There is a direct transition at the K points, with a larger gap than the indirect gap between the aforementioned VBM and CBM [14, 15]. If the number of layers is reduced, the in-plane electronic states near the K remain more or less the same. But the energy

gap between VBM and CBM at the Γ point and halfway along $\Gamma - K$ keeps increasing because of the aforementioned strong out-of-plane overlap of the corresponding orbitals. Eventually, at the monolayer (ML) limit, the energy gap at the K point becomes the lowest in the Brillouin zone, and so it hosts the new VBM and CBM. This leads to the ML TMD becoming a direct bandgap semiconductor, with excitonic emission getting stronger by orders of magnitude compared to bulk TMD [11,14,15].

1.4 Excitons

Excitons are a central concept in the work presented in this thesis. It is the relevant optical signatures that we will follow in our experimental investigations of 2D systems. The upcoming parts will be dedicated to introducing some key ideas and properties associated with them.

Excitons are the primary or lowest electronic excitation in a semiconductor. In the most simplified picture, if enough energy is provided to the semiconductor, an electron will absorb the energy and jump to the conduction band, leaving behind an empty "hole" (absence of electron) in the filled valence band. A hole has the opposite charge (+1) compared to an electron. The wavevectors of an electron and hole are expressed with opposite signs as well. An exciton is an electron-hole pair bound by Coulomb interaction. Because they are bound by the Coulomb interaction, they are described as not two different independent particles, but as a single bosonic quasiparticle with slightly lower energy than the bandgap (E_g) [57]. The energy difference between the exciton energy and the bandgap E_g is called the exciton binding energy. An exciton can be considered a hydrogen-like system. Using the effective mass approximation, the binding energy of an exciton in a 3-dimensional solid can be expressed as:

$$E_{b(3D)} = \frac{\mu q^4}{2(4\pi\epsilon)^2\hbar^2}(-\frac{1}{n^2}) \ ; \ n = 1, 2, 3, ... \tag{1.4.1}$$

where, ϵ is the dielectric constant of the medium, q is the charge of an electron and $\hbar$ is the reduced Planck constant. If we denote the center of mass motion wavevector of the exciton as $\boldsymbol{K}$, we can write the total energy of an exciton as:

$$E = \frac{\hbar^2 K^2}{2M} + E_{b(3D)} + E_g \tag{1.4.2}$$

with,

$$M = m_e + m_h \tag{1.4.3}$$

Here, m_e and m_h are the electron and hole effective masses and $K = \mid \boldsymbol{K} \mid$. The first term on the right side of equation 1.4.2 corresponds to the kinetic energy of the exciton. It is characterized by the center of mass wavevector $\boldsymbol{K}$. For optical wavelengths, the excitation light wavelength, λ, is much larger than the size of the exciton, a_X. Thus, the photon momentum $\frac{2\pi}{\lambda}$ is not large enough to cause a significant change in K. Hence, K can be approximated as 0. On the other hand, the binding energy, $E_{b(3D)}$, stems from the Coulomb interaction between the electron and hole, leading to a series of transitions for the exciton similar to an electron in a hydrogen atom. In equation 1.4.1, $n = 1$ corresponds to the ground state of the exciton, and $n = 2, 3, 4, \ldots$ are the higher energy states [57, 58].

There are three different types of excitons in general: Frenkel excitons, charge transfer excitons, and Wannier excitons. Among them, Wannier excitons are found in most semiconductors and many van der Waals materials like TMDs. Wannier excitons are excitons with weakly bound electron-hole pairs. These excitons have a large Bohr radius, meaning their wavefunction is strongly delocalized and spread over several lattice constants. For example, the exciton Bohr radius in gallium arsenide (GaAs) is ≈ 13 nm [57], which is ≈ 23 times larger than the lattice constant.

There are several types of new quasiparticles that can originate from excitons under certain conditions. One such quasiparticle that will be relevant for this thesis is the trion. These quasiparticles consist of two electrons and one hole or two holes and one electron. In other words, trions are fermions formed by an exciton interacting with an electron (negative trion) or a hole (positive trion) [13].

1.5 Excitons in TMD

In a 2-dimensional solid, the confinement of electron motion in one direction leads to a density of states (DOS) with steplike features, corresponding to discrete subband edges. If we use a hydrogen-like model (similar to the case for a 3-dimensional solid), we can write the binding energy expression as [5]:

$$E_{b(2D)} = \frac{E_{b(3D)}}{(n - \frac{1}{2})^2} \; ; \; n = 1, 2, 3, \ldots \tag{1.5.1}$$

However, for a 2D system like a monolayer of TMD, the hydrogen model cannot accurately predict the full Rydberg series of an exciton, particularly the lower energy states ($n < 3$) in the series. Principally, the hydrogen model does not take into

account the electric field permeation out of the monolayer and does not consider the different dielectric constant of TMD and the surrounding environment [59].

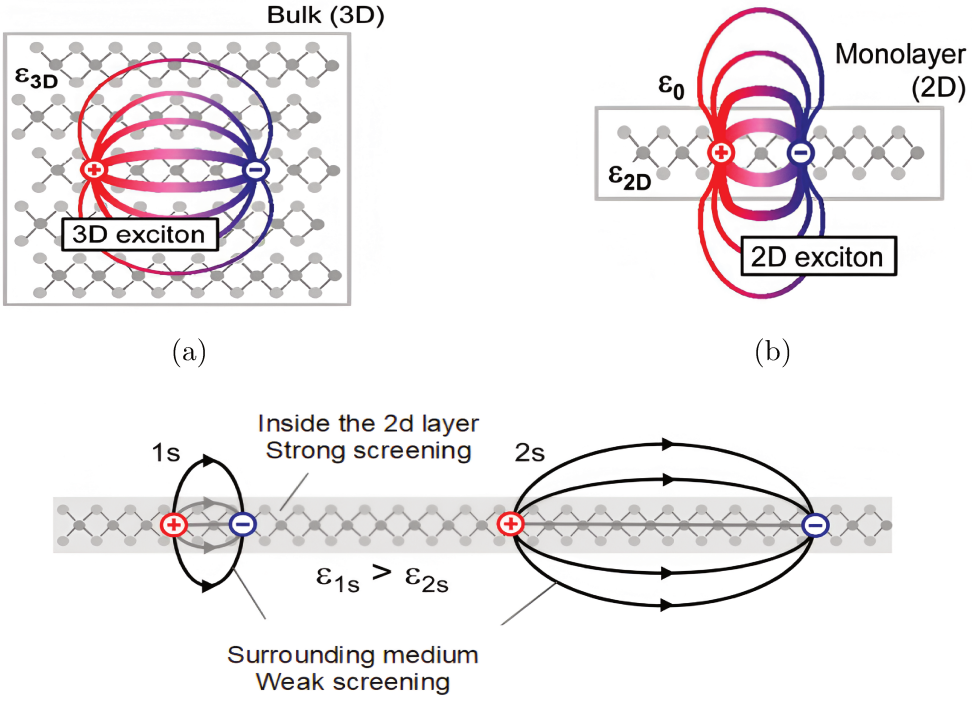

Figure 1.4: (a) Electric field lines for an exciton in a 3d medium. (b) Electric field lines for an exciton in 2d material. Exciton feels more the effect of the surrounding dielectric environment, compared to exciton in 3d medium (b) effective screening for 1s and 2s excitons. For 2s exciton (larger n), most of the lines permeate outside of the 2d layer, leading to weaker screening [59].

Figure 1.4a and 1.4b show a schematic picture of electric field lines for an exciton in a 3D system and a 2D system, respectively. As shown in these figures, the electric field lines in a 2D system permeate out of the 2D layer and into the surrounding medium. Thus, the difference in dielectric constant between the two media plays an important role in determining the electron-hole interaction and the exciton energy. To accurately describe the excitonic states in a 2D system, the so-called "effective medium" model can be used. This model considers a strong effective dielectric screening of the exciton at short range ($n < 3$) and a relatively weak effective screening at long range ($n = 3, 4, 5, \ldots$) [5,59]. Instead of a Coulomb potential ($\propto \frac{1}{r}$), this model uses the "Keldysh"

potential, which can be written in a simplified form as [60]:

$$V_{eff}(r) \;=\; -\frac{1}{r_0}\,[ln(\frac{r}{r+r_0}) + (0.5772 - ln\ 2)e^{-\frac{r}{r_0}}] \tag{1.5.2}$$

$$r_0 \;=\; 2\pi\alpha_{2D} \tag{1.5.3}$$

Here, r is the electron-hole distance, r_0 is the dielectric screening length, and α_{2D} is the 2-dimensional polarizability. This form of potential introduces r_0 as a cut-off length and correctly represents the dielectric screening in a 2D material. Figure 1.4c shows the comparative effective screening for short and long ranges. For $r < r_0$, or in other words, when n is small and the electron-hole distance is smaller than the screening length, a large portion of the exciton's electric field stays inside the 2D plane. The effective screening is strong in this case, and the exciton's behavior deviates from the hydrogen model. In contrast, for $r > r_0$, most of the electric field permeates outside the 2D layer, and the effective screening is weak, leading to excitonic behavior similar to the hydrogen model [5, 59, 60].

Exciton binding energy in monolayer TMDs increases, reaching values up to 0.9 eV, due to quantum confinement in one direction and reduced dielectric screening. Because of such high binding energy, the optical signature of the excitons is visible even at room temperature [11]. Furthermore, light-matter interactions in these materials are particularly efficient compared to traditional semiconductors, leading to an absorption of about 10% [61].

1.6 Excitons in Group-6 TMD: Valley Polarization and Spin-Orbit Coupling

As mentioned before, ML TMDs have reduced symmetry compared to bulk TMDs. Particularly, the lack of inversion symmetry in ML TMDs leads to some very unique properties. Because of this missing symmetry, the six corners of the hexagon-shaped first Brillouin zone become divided into two distinct and inequivalent groups: K_+ and K_- points. Due to the momentum conservation law and the weak momentum imparted by the photon, the interband transitions in Group-6 TMDs are almost vertical from the valence to the conduction band. This, among other arguments, leads to the formation of excitons around the minimum of the dispersion band, namely the $K_\pm$ points. They are also known as K_+ and K_- valleys [8, 14, 15]. The formation of

excitons in the K_+ and K_- valleys depends on the incident light polarization. Right circularly polarized (σ^+) light leads to the formation of excitons in the K_+ valley, and left circularly polarized (σ^-) light leads to excitons in the K_- valley. When these excitons recombine, they emit the corresponding polarized light as well, preserving its valley polarization. An electron in a ML TMD can be associated with the so-called valley quantum number or valley pseudospin, which expresses the electron's momentum and specifically designates its corresponding valley polarization.

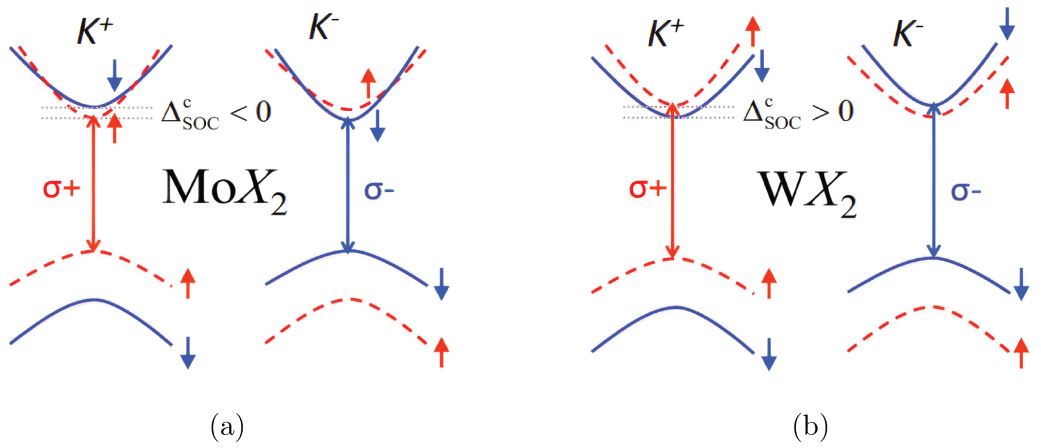

(a) (b)

Figure 1.5: Simplified bandstructure of group 6 TMD at the $\pm K$ valleys: (a) MoX_2 (b) WX_2. The spin splitting direction at each valley is opposite between these two materials [62].

Another important aspect to consider when discussing TMD ML properties is spin-orbit coupling (SOC), or in other words, the interaction between the electron orbital angular momentum ($\boldsymbol{L}$) and spin angular momentum ($\boldsymbol{S}$). SOC gives rise to an extra term ($\boldsymbol{L} \cdot \boldsymbol{S}$) in the electron Hamiltonian and causes a splitting of electron energy levels based on their spin [13]. It is a general consequence of inversion symmetry breaking [63]. In TMD MLs, the SOC is much stronger than in graphene, because of the presence of the heavy transition metal atom and d orbitals. The value of the spin splitting in the valence band (VB) in both valleys has been reported to be 200 meV for Mo-based TMDs and 400 meV for W-based TMDs [12]. The excitons that can form in these two spin-split valence subbands are denoted as A and B excitons, corresponding to the higher and lower energy subbands, respectively. Moreover, time reversal symmetry dictates that the sign of spin splitting in the K_+ and K_- valleys are opposite to each other (the sign of the energy shift is opposite) [63]. As a consequence,

the spin and valley degrees of freedom are essentially coupled to each other, and the opposite spin splitting at the two valleys give rise to unique transitions at each valley. In contrast, the spin splitting in the conduction band is relatively small [8, 12–16].

Figure 1.5 shows a schematic diagram of the two valleys with their corresponding spin splitting for MoX_2 and WX_2. It shows the opposite spin configuration at the K_+ and K_- valleys. It also highlights that because of the opposite direction of spin splitting in the conduction band for MoX_2 and WX_2, the allowed spin at the CBM for these two types of TMDs is opposite to each other. The relative energy levels between bright excitons and dark excitons (spin-forbidden transitions) depend on the material, for example, in MoX_2, the lowest energy transition (A exciton) is optically bright, whereas the A excitons in WX_2 are optically dark, and the opposite is true for B excitons in both types of TMDs [11, 15]. These interesting properties of TMDs have attracted a lot of research, with important implications for valleytronics and spintronics applications [44].

1.6.1 Exciton Dynamics in Group-6 TMDs

An exciton can be annihilated or lose its energy in a process called exciton relaxation or recombination. This can be accompanied by the emission of a photon with the same energy as the exciton energy. This is referred to as radiative recombination. This is a spontaneous decay process, with a timescale (radiative lifetime) that depends on the coupling between the exciton and the electromagnetic field of the photon and on the Coulomb interaction between the electron and hole. On the other hand, excitons can lose their energy without emitting a photon in a nonradiative recombination process. This can happen as a result of the exciton's interaction with the environment, each type of interaction giving rise to a new decay channel with its own decay timescale. For example, excitons can be scattered by interaction with phonons, other excitons, defects, or local disorder centers. These nonradiative decay channels can have relatively longer decay timescales compared to radiative decay [5, 28]. More specifically for Group-6 TMDs, the population decay also depends on intervalley and intravalley exciton scattering. The overall exciton population dynamics is dependent on the interaction between radiative and non-radiative decay channels.

There has been a significant number of studies on the dynamic properties of excitons in Group-6 TMDs, owing to their efficient light-matter coupling, spin-valley

polarization, and high oscillator strength among other reasons [12]. However, key questions about exciton dynamics in these materials remain unanswered, including the interplay between radiative and non-radiative decay channels, and how these intrinsic times are influenced by the surrounding environment (including in novel heterostructures). One of the objectives of this thesis, relying on the particular spectroscopy presented in the next chapter, is specifically to address these dynamic properties at optical resonance with approximately 100 fs temporal resolution, combined with a microscopic approach.

1.7 Rhenium Disulfide (ReS_2)

In contrast to the more prominent Group-6 TMDs, a relatively less studied Group-7 TMD is rhenium disulfide (ReS_2). This material is one of the focuses of this thesis due notably to its anisotropic properties and particularly weak interlayer bonding. As mentioned before, TMD monolayers have reduced structural symmetry compared to their bulk form. Such is the case for Group-6 TMD monolayers, as described in the previous section. Despite this, they retain sufficient symmetry to prevent any in-plane anisotropic properties. In contrast, this is not the case for the ReX_2 (X=S, Se, ...) family, which exhibits lower symmetry than Group-6 TMDs, resulting in pronounced in-plane anisotropy. The cause of this further reduced symmetry can be understood in terms of its crystal structure.

ReS_2 is a diamagnetic semiconductor with a bandgap of 1.4 eV [64]. The crystal structure of ReS_2 is a distorted octahedral or 1T′ phase. Figure 1.6 shows a comparative view of the octahedral 1T and distorted octahedral 1T′ crystal structures, with top and side views along the crystallographic axis b. As shown in this figure, the chalcogen atoms surround the metal atom in an octahedral or trigonal antiprismatic configuration in the undistorted 1T phase. However, in the case of Re-based TMDs, like ReS_2, each Re atom has d^3 electrons that allow it to bond with three nearby Re atoms, forming a diamond chain (DC). The DC forms along the crystallographic b axis, giving rise to a zigzag structure and also an out-of-plane bending of the chalcogen atoms. This distorted 1T′ structure results in a triclinic symmetry, leading to some interesting properties. For example, it causes higher electron mobility along the b axis. Due to the strong Re-Re bond, the crystal preferentially breaks along this axis as well. The in-plane unit vectors get larger by a factor of 2. Finally, this distortion

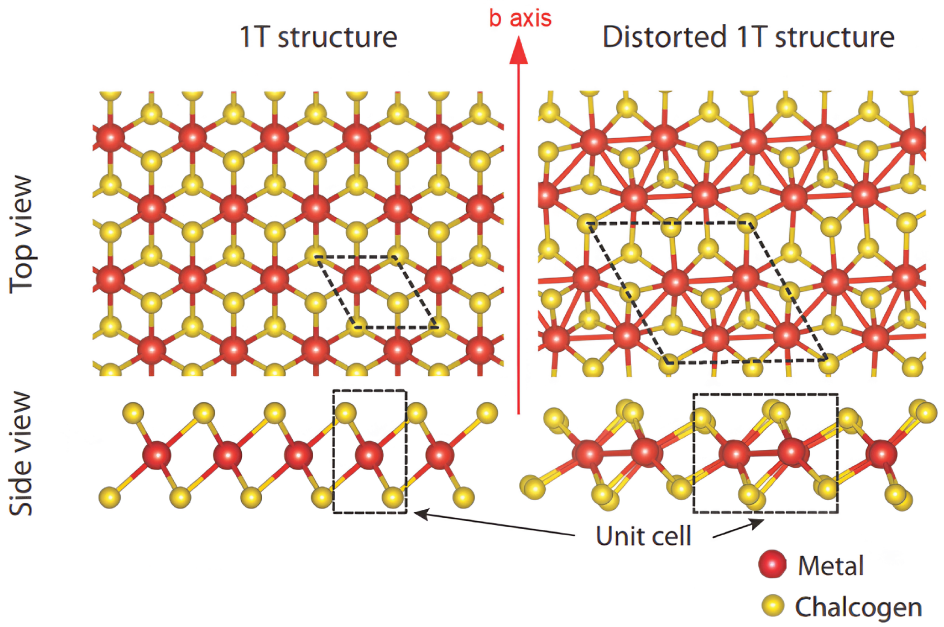

Figure 1.6: Comparison between octahedral 1T and distorted octahedral 1T′ crystal structure (top view and side view). The unit cell is shown with a dashed line for both cases. The crystallographic axis is denoted as b axis [20].

causes the TMD to lose the threefold rotational symmetry observed in the undistorted 1T structure. The loss of symmetry manifests itself as anisotropy in the electronic band structure, resulting in excitons with dipoles oriented in different in-plane directions. These excitons can be selectively excited by using light that is linearly polarized along the exciton dipole direction [17–21]. Among the five excitons identified in ReS_2 so far, the two lowest energy excitons have their dipoles oriented parallel and perpendicular to the crystallographic axis b, respectively [17]. Such strong anisotropic structural properties have even imparted a notable one-dimensional character to the excitons along the Re chains [20, 65].

An important distinction between Group-6 TMDs and ReS_2 is the particularly weak interlayer coupling in the latter. As a result, the bulk material has a crystal structure similar to that of a monolayer TMD [20]. The band structure does not show a drastic change in the electronic structure when going from bulk to monolayer, as is observed for Group-6 TMDs [66]. A photoluminescence (PL) measurement-based study of the brightest exciton in ReS_2 (transition energy 1.59 eV for monolayer) shows

very small change in transition energy as the number of layers is increased (less than 100 meV redshift from monolayer to 11 layers) [67]. The emission intensity from ReS_2 excitons is enhanced when the number of layers is increased from monolayer, in sharp contrast with Group-6 TMDs. This leads to the consideration of a few or multiple layers of ReS_2 as quasi-independent monolayers, combining the advantages of monolayers with the robustness of the multilayer form. Combined with the degrees of freedom arising from the in-plane optical anisotropy, this makes ReS_2 a strong candidate for multilayer device applications such as polarization-controlled optical switches, transistors, photodetectors, and LEDs [18, 64].

Despite the potential for applications, many fundamental properties of ReS_2 remain either unknown or under debate. For example, the nature of the fundamental bandgap (direct vs indirect) of ReS_2 is not yet fully agreed upon. A combined PL, Raman spectroscopy, and reflectivity study claims an indirect bandgap for ReS_2 [66]. Absorption edge measurements also support this hypothesis [21]. On the other hand, a study using Angle-Resolved Photoemission Spectroscopy (ARPES) and Density Functional Theory (DFT) calculations suggests the presence of a direct bandgap located at the Z point (k_z direction) of the hexagonal Brillouin zone [20]. Additionally, a study combining transmission electron microscopy (TEM) and DFT calculations also supports the possibility of a direct bandgap in ReS_2 [67]. Figure **??** shows the theoretically calculated (DFT) electronic band structure of ReS_2 for both bulk and monolayer, as reported in [20].

Similarly, the origin of the anisotropic properties continues to be the subject of investigations, whether the excitonic species originate from a single high-symmetry point of the Brillouin zone or from two different valleys related by space inversion [67–69]. In this context, time-resolved experiments can provide valuable insight and help determine the nature of the band structure in ReS_2.

The dynamic properties of excitons in ReS_2 are not very well known as well. Non-resonant macroscopic transient absorption measurements suggest hot exciton relaxation and exciton formation timescales on the order of 10 ps and exciton lifetimes of 86 ps for few-layer ReS_2. For monolayer ReS_2, a similar exciton formation time and a lifetime of ≈ 40 ps have been reported [70, 71]. Non-resonant excitation of the exciton generates a number of dynamic processes in addition to the intrinsic exciton formation or population relaxation. A macroscopic resolution does not allow for the dynamic properties of a single exciton to be studied independently of inhomogeneous

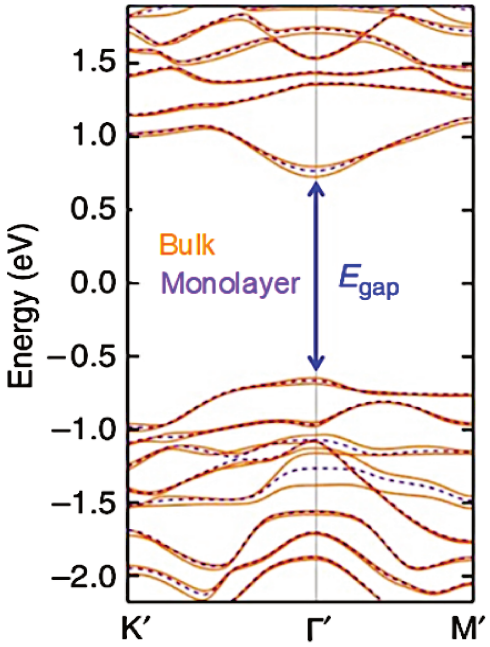

Figure 1.7: Theoretically calculated electronic bandstructure of ReS_2 bulk (orange solid curve) and monolayer (purple dashed curve), using density functional theorey (DFT) [20].

broadening effects as well. As a result, the fundamental coherence and population dynamics properties of excitons in monolayer and bulk ReS_2 are still unknown. We will use our experimental tools to explore the intrinsic coherence times and population dynamics at optical resonance, with microscopic and ultrafast resolutions.

2 Experimental and analysis methods

In this chapter, the experimental techniques utilized in this thesis will be outlined. The discussion will begin with the methods used for sample preparation. Two experimental setups were developed for the work in this thesis: micro-photoluminscence (μPL) spectroscopy and four wave mixing (FWM) microscopy. The basic principles of photoluminescence will be discussed, followed by a description of the PL experimental setup. Following this, a comprehensive theoretical overview of four-wave mixing (FWM) spectroscopy will be provided. The chapter will conclude with a detailed description of the developed FWM microscopy setup.

2.1 Sample preparation

Some of the most prominent methods for preparing 2D vdW materials are mechanical exfoliation, chemical exfoliation, chemical vapor deposition and molecular beam epitaxy. For this thesis, mechanical exfoliation was used to prepare samples of TMD: $MoSe_2$ and ReS_2. On the other hand, hBN samples were prepared with commercially available liquid exfoliated flakes. Both methods of sample preparation will described briefly.

2.1.1 Mechanical Exfoliation

Mechanical exfoliation and transfer is a well known method to separate one atom thick monolayer or a few atom thick multilayer flakes of vdW materials from their respective bulk form. This method is very convenient offering a relatively low cost process, which is easy to implement in practice and provides high quality 2D layers. Thin flakes fabricated in this way are stable in ambient condition and continuous on a macroscopic scale, upto the order of millimeters [72]. The identification of 2D layers deposited on a oxidized Silicon substrate is readily possible with an optical microscope due to the fact that even a monolayer causes a noticeable change in the optical contrast. This method allows for the combination of different 2D layered materials without stringent requirements for lattice matching, enabling the creation

of unique heterostructures with novel properties. These heterostructures will be the subject of Chapter 4.

Mechanical Exfoliation is done using the "scotch tape" technique, as mentioned before [42]. It was used to fabricate the first ever discovered 2D material, Graphene. This process involves applying a peeling force with a tape causing tearing of the layers of the bulk material. The material properties, geometry and exfoliation kinetics control the strength of peeling and tearing. First, the bulk material crystal is placed on a long piece of tape with a tweezer. The empty part of the tape is then folded around to make contact with the bulk crystal slowly and subsequently pulled off contact very fast, to provide the peeling force. This process is repeated multiple times with different parts of the tape until the bulk material visibly looks thin (can be estimated based on light reflection from the material). The next part of the process is to transfer the thin flakes onto a substrate. For this thesis, two types of substrates were used: Silicon with a thin layer of Silicon di-oxide (Si/SiO_2) and quartz. The substrates are cleaned with Acetone, Ethanol and Isopropanol, followed by oxygen plasma cleaning. The part of the tape with the thin material is put into contact slowly on a substrate of choice and rubbed on it without applying any considerable force. Finally the tape is removed from the substrate extremely slowly, to ensure the transfer of continuous thin flakes. The whole process was done in a clean room dedicated for 2D material sample preparation. The transfer of the flakes onto the substrate can also be done with a transfer machine available in the Stnano cleanroom of the laboratory dedicated for this purpose. But most of the samples for the work in this thesis is done with by hand transfer.

2.1.2 Deposition of liquid exfoliated flakes

Chapter 5 is dedicated to the study of quantum defects hosted in hexagonal Boron Nitride (hBN). The samples for this study were prepared using liquid exfoliated hBN nanoflakes. Basic information about this type of sample preparation is provided here. More detailed explanations are available in Chapter 5. The liquid exfoliated hBN flakes are commercially available as suspended in a water-ethanol ($50\% - 50\%$) solution. In order to deposit these flakes on a substrate, first the substrate was cleaned as mentioned before: with Acetone, Ethanol and Isopropanol, followed by Oxygen plasma cleaning. The solution containing the flakes were sonicated in a ultrasonication

bath to break any agglomeration. Then the flakes were centrifuged at high rotation speed (usually 8000 rpm), to isolate small flakes of roughly uniform size, on the top part of the solution (supernatant) and the larger size flakes of mixed size at the bottom part of the solution (precipitate). These two parts were separately extracted. Depending on the motivation behind the sample preparation, either supernatant or precipitated part of the solution was used. To deposit the flakes on the cleaned substrate, three different types of deposition were used. The simplest deposition method was to dropcast the solution onto the substrate and dry the solution. This kind of deposition usually leads to large agglomeration of flakes on the substrate. The second method involved the use of a simple stage (to hold the sample in place) and motor. This "shaker" was used to introduce some rotational motion of the substrate when the solution was dropped onto it. The motion helped disperse the solution more uniformly, leading to less agglomeration of flakes compared to simple dropcasting. The third method that was used was spin coating. The spin coating machine provided the added benefit of offering different speed and acceleration of rotational motion. Using spin coating to disperse the solution onto the substrate at high speed, provided the least amount of flake agglomeration. However, almost 90% of the solution would be lost in the process simply because the solution would be thrown out of the substrate surface at high speed.

2.2 μ-Photoluminescence spectroscopy

2.2.1 Principles of Photoluminescence Spectroscopy

The micro-photoluminescence experiment played a significant role in this thesis. It was used either to optically characterize the samples before conducting time-resolved experiments or for self-consistent studies, such as the one on quantum defects in hBN (Chapter 5). The principles of such spectroscopy is described in short here. Photoluminescence spectroscopy is a contactless, nondestructive process to analyze the electronic structure of materials, in particular the lowest optical transitions. In such an experiment, the system under study is excited with photons, which are absorbed by the material in a process called photo-excitation. In the electron picture in vdW material, an incident photon promotes an electron to a higher energy state in the conduction bands. The electron then relaxes or thermalizes (generally by emitting phonons) to the lowest excited state, forming an exciton. The exciton can release

this excess energy by emitting a photon and relaxing back to the ground state, in a radiative recombination process. The collection and analysis of these emitted photons is at the core of PL spectroscopy. Once spectrally resolved, the PL experiment allows then the identification of the energy of the exciton (or the lowest optical transition). On the other hand, the intensity of the collected photons provides information about the strength of the optical transitions. Other more subtle information can also be deciphered, such as the spectral and temporal stability of the system.

2.2.2 Micro-photoluminescence Setup

The μPL setup that was developed during this thesis is shown schematically in figure 2.1. In the presented work, the primary light source used for the PL experiment is a continuous-wave laser with a wavelength of 532 nm. The light from the source is directed towards the sample with a series of optical components. A dichroic mirror on the laser path ensures that a part of the excitation laser at 532 nm is reflected. At the same time, the PL signal from the sample (emitted at a higher wavelength) is transmitted through the dichroic mirror almost completely ($\approx 90\%$) and goes to the detection line. A set of waveplates enable the control of excitation polarization. As mentioned before, the experimental setup involves microscopy. So the laser is focused onto the sample through a microscope objective lens. The spatial resolution is diffraction limited and depends on the numerical aperture (NA) of the objective. The setup provided options to use several NA objective (0.25, 0.5, 0.6, 0.75 and 0.9 NA). The sample is glued onto a metallic sample holder that is screwed on three-axis piezostages. The piezostages allow movement of the sample with nanometer scale accuracy. The sampleholder and the piezostages are housed inside a cryostat (details and pictures are provided in the section 2.4.2). The cryostat allows the use of liquid Nitrogen or liquid Helium as coolant and temperature control between 4K and room temperature.

The PL response from the sample is collected using reflection geometry. The PL signal (collinear with the reflected part of the excitation laser) transmits through the dichroic mirror to the detection line. A spectral filter cuts off the remaining excitation laser intensity accompanying the PL signal. After the PL signal is collected through a spatial filter and a focusing lens, it enters the monochromator slit of the spectrometer. After the monochromator grating spectrally resolves the PL signal, it is finally sent

to a CCD camera. With the correct calibration between the CCD camera pixels and wavelength, the PL spectrum then can be extracted. A home-made user interface developed with Python programming language allows the control of the necessary devices (piezostage, CCD camera, monochromator) for the measurement and PL signal extraction.

The μPL setup contains a branch built for imaging the sample. A white light source and a beamsplitter on a flip mount placed before the objective provides the option to send white light towards the sample. A flip mirror in the detection line is used to direct the white light image towards a dedicated imaging camera.

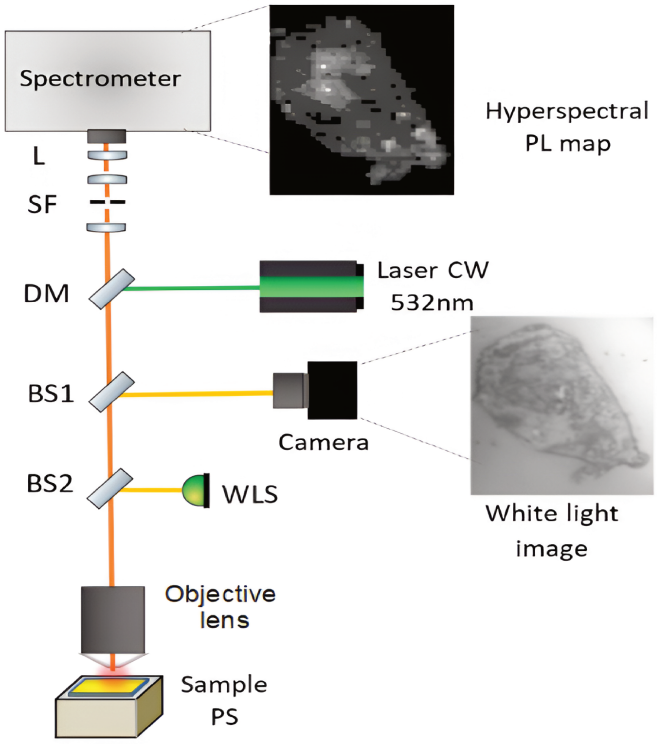

Figure 2.1: Schematic diagram of the homebuilt micro-photoluminescence (μPL) setup used in this thesis. An example white light image and a corresponding hyperspectral PL map (spectrally integrated) are shown in the inset. The optical components are designates as follows: lense (L), spatial filter (SF), dichroic mirror (DM), beam splitter (BS), white light source (WLS), piezo stages (PS). A waveplate placed in the laser path (not shown) controls the excitation polarization.

2.2.3 Hyperspectral Mapping

The experimental setup described above provides an opportunity to pinpoint a specific location on the sample and take the PL spectrum for that point. It is also possible to take a PL map of any area of the sample by automatically moving the piezo through the interface. In this kind of measurement, by moving the piezostage, a PL scan of a specified are of the sample is performed. A PL spectrum is taken periodically while the piezostage moves from one location to the next, with a pre-defined step size between them. This type of map is called hyperspectral PL map. Every point on the map has its own PL spectrum. So, the map contains four dimensional data, namely x, y position, wavelength and PL intensity. For convenient visualization, the PL spectrum can be integrated in wavelength and the integrated intensity can be shown in a color plot or grayscale. It allows fast and efficient identification of the locations of interest (excitons or defects). In the inset of figure 2.1, a white light image of liquid exfoliated hBN flakes and the corresponding hyperspectral PL map (integrated here over the entire PL spectral range, 1.65 - 2.25 eV) of the area is shown.

2.3 Theoretical description of FWM spectroscopy

In order to study the dynamics of excitons in VdW materials, a state of the art coherent ultrafast four wave mixing (FWM) microscopy experimental setup was developed in this thesis. This experimental setup combines a diffraction limited spatial resolution, ultrafast time resolution ($\approx$ 100 femtosecond) and $\approx$ 300 μeV spectral resolution. Non resonant time resolved techniques such as time resolved photoluminescence fail in measuring sub-ps phenomena and at the same time suffer from the presence of complex decay channels because of the nonresonant nature of the experiment. Third order nonlinear techniques like resonant FWM spectroscopy can circumvent these issues. However, directional selection used in traditional FWM sepctroscopy imposes a limited spatial resolution as it requires the recovery of the spatial phase [28, 73]. Here, a novel approach was developed based on the temporal modulation of the optical phase of the excitation pulses. Such modulation, assisted by heterodyne dual-balanced detection and spectral interferometry (SI) allows a collinear geometry and enables the use of a microscope objective, reaching the diffraction limit in spatial resolution. In this section, we will present a comprehensive theoretical framework required to understand such an experimental approach. The subsequent

sections will describe the experimental setup and how the spectral data is extracted and processed in order to measure the dynamic properties of excitons.

Four wave mixing (FWM) is a third order nonlinear response of a system driven by optical pulses. In order to provide an overview of FWM, let's consider the interaction between a two level system and three optical pulse delayed with respect to each other. The first pulse creates a polarization (coherence) in the system, which starts to decay immediately. The delayed second pulse generates a population from the remaining polarization, followed by the third pulse which interacts with the population and generates the FWM signal from the system as a third order response. The following sections will describe in details how these interactions occur and how the resulting FWM signal can be used to probe the dynamic properties of the system. To describe the FWM signal, we will proceed with the following steps. First, we will introduce a two-level system using the density matrix formalism in interaction with an optical pulse. Next, we will address dissipation effects by considering the environment through the Liouville-von Neumann equation, leading to the optical Bloch equations, which effectively express the time evolution of the density matrix elements. We will then develop solutions to the optical Bloch equations using a perturbative approach up to the third order in the electric field of the optical pulses. Finally, with the general solution in place, we will derive the specific solutions for the FWM signal. The derivation and description provided below, follows the references [74], [75], [76] and [77].

2.3.1 Optical Bloch Equations

Density matrix formalism

The interaction between a two level system and a resonant optical pulse can be described using the density matrix formalism. It leads to a set of equations that model the coherence and population dynamics of the two level system, known as the "Optical Bloch Equations" (OBE). This density matrix formalism enables us to consider open systems and account for dissipation processes affecting coherence and relaxation of energy (or population). It allows us to describe the system in terms of mixed states (as opposed to pure states described by wave functions), whether the system is a single entity or an ensemble of systems in contact with a dissipative environment.

Let's consider first a two level system in a pure state, with $|1\rangle$ and $|2\rangle$, being the Eigenstates of the unperturbed Hamiltonian, H_0, with energy eigenvalues $E_1 = \hbar\omega_1$ and $E_2 = \hbar\omega_2$, respectively. The wavefunction of this system can be written as:

$$|\Psi(t)\rangle = C_1(t)\,|1\rangle + C_2(t)\,|2\rangle \tag{2.3.1}$$

Here, $\mid C_1 \mid^2$ and $\mid C_2 \mid^2$ are the probabilities of finding the system in states $|1\rangle$ and $|2\rangle$, respectively. The density operator for the system in such a pure state is given by:

$$\rho = |\Psi\rangle\,\langle\Psi| \tag{2.3.2}$$

The density operator can also be expressed in matrix form:

$$\rho = \begin{bmatrix} \rho_{11} & \rho_{12} \\ \rho_{21} & \rho_{22} \end{bmatrix} = \begin{bmatrix} \mid C_1 \mid^2 & C_1 C_2^* \\ C_2 C_1^* & \mid C_2 \mid^2 \end{bmatrix} \tag{2.3.3}$$

The diagonal elements $\rho_{11} =\mid C_1 \mid^2$ and $\rho_{22} =\mid C_2 \mid^2$ represent the population of the two states. The off-diagonal terms represent the superposition of the states namely "the coherence" of the system. Using the density matrix, the expectation value of any operator M, associated with an observable can be calculated by taking the trace of the product of the operator M and the density matrix ρ:

$$\langle M\rangle = Tr\{M\rho\} \tag{2.3.4}$$

Next, we describe the case of a mixed state represented by a statistical average over an ensemble of two-level systems. Such states cannot be described by a wave function but only by a density matrix. One way to picture such a mixed state is to introduce the probability P_j of an individual system j being in the pure state $|\psi_j\rangle$. We can write $|\psi_j\rangle$ as:

$$|\Psi_j(t)\rangle = C_{1j}(t)\,|1\rangle + C_{2j}(t)\,|2\rangle \tag{2.3.5}$$

and the density operator for the ensemble as:

$$\rho = \sum_j P_j\,|\psi_j\rangle\,\langle\psi_j| \tag{2.3.6}$$

Note that this formalism also equally applies to a single system in a mixed state, for instance, due to coupling with a dissipative environment.

Coupling Hamiltonian with optical pulses

The full Hamiltonian, H has two contributions:

$$H = H_0 + H_L \tag{2.3.7}$$

where, H_0 is the Hamiltonian of the isolated two level system, H_L describes the interaction of the system with the electromagnetic field of the excitation pulse. In matrix form, H_0 can be expressed as:

$$H_0 = \begin{bmatrix} E_1 & 0 \\ 0 & E_2 \end{bmatrix} \tag{2.3.8}$$

We can consider the two level system interacting with an optical pulse of the form:

$$E(\omega, t) = E_0(t)(e^{i\omega t} + e^{-i\omega t}) \tag{2.3.9}$$

where $E_0(t)$ is the temporal envelope of the light field. The interaction part of the Hamiltonian can be written as $H_L = -E(t) \cdot \hat{\mu}$, where $\hat{\mu}$ is the transition dipole operator which connects the system states $|1\rangle$ and $|2\rangle$. The scalar dipole moment is given by: $\mu = \langle 1| q\boldsymbol{r} \cdot \epsilon |2\rangle$, where $\boldsymbol{r}$ is the position operator and ϵ is the unit vector of the electric field direction. For simplicity, we will discard the top hat notation and use the quantity μ in the subsequent description. So, the total Hamiltonian can be written as:

$$H = E_1 |1\rangle \langle 1| + E_2 |2\rangle \langle 2| - \mu \cdot E(t)(|1\rangle \langle 2| + |2\rangle \langle 1|) \tag{2.3.10}$$

or in matrix form:

$$H_0 = \begin{bmatrix} E_1 & -\mu E(t) \\ -\mu E(t) & E_2 \end{bmatrix} \tag{2.3.11}$$

The wavefunction of the system $|\Psi\rangle$ follows the Schrodinger equation:

$$\frac{d|\Psi(t)\rangle}{dt} = -\frac{i}{\hbar} H |\Psi(t)\rangle \tag{2.3.12}$$

However, the wavefunction and the Schrodinger equation can only be used as long as a pure state is considered. On the other hand, the density operator follows the Liouville-Von Neumann equation even for mixed states. This equation is written as:

$$i\hbar\frac{d\rho}{dt} = [H, \rho] \tag{2.3.13}$$

where, $[H, \rho] = H\rho - \rho H$ is the commutation relation. We can evaluate the commutation, by considering one part of the Hamiltonian at a time. For H_0,

$$\begin{bmatrix} \dot{\rho}_{11} & \dot{\rho}_{12} \\ \dot{\rho}_{21} & \dot{\rho}_{22} \end{bmatrix} = \begin{bmatrix} 0 & (E_1 - E_2)\rho_{12} \\ (E_2 - E_1)\rho_{21} & 0 \end{bmatrix} \tag{2.3.14}$$

We can rewrite it in the "Liouville representation", as:

$$\begin{bmatrix} \dot{\rho}_{12} \\ \dot{\rho}_{21} \\ \dot{\rho}_{11} \\ \dot{\rho}_{22} \end{bmatrix} = -\frac{i}{\hbar}\begin{bmatrix} E_1 - E_2 & 0 & 0 & 0 \\ 0 & E_2 - E_1 & 0 & 0 \\ 0 & 0 & 0 & 0 \\ 0 & 0 & 0 & 0 \end{bmatrix}\begin{bmatrix} \rho_{12} \\ \rho_{21} \\ \rho_{11} \\ \rho_{22} \end{bmatrix} \tag{2.3.15}$$

If we include the interaction part of the Hamiltonian (equation 2.3.7), we can write:

$$\begin{bmatrix} \dot{\rho}_{12} \\ \dot{\rho}_{21} \\ \dot{\rho}_{11} \\ \dot{\rho}_{22} \end{bmatrix} = -\frac{i}{\hbar}\begin{bmatrix} E_1 - E_2 & 0 & -\mu E(t) & \mu E(t) \\ 0 & E_2 - E_1 & \mu E(t) & -\mu E(t) \\ -\mu E(t) & \mu E(t) & 0 & 0 \\ \mu E(t) & -\mu E(t) & 0 & 0 \end{bmatrix} \tag{2.3.16}$$

Dissipation

At this point, we can introduce two relaxation mechanisms into the discussion: population decay and coherence decay, corresponding to the time evolution of the diagonal and non-diagonal elements of the density matrix, respectively. We can include the decay mechanisms phenomenologically into the equation by stating:

$$\frac{d\rho_{ii}}{dt} = -\frac{\rho_{ii}}{T_1} = -\Gamma\rho_{ii} \tag{2.3.17}$$

$$\frac{d\rho_{ik}}{dt} = -\frac{\rho_{ik}}{T_2} = \gamma\rho_{ik} \;\; ; \; i \neq k \tag{2.3.18}$$

where, the decay rate and the decay time constant corresponding to the population and coherence decay mechanisms are denoted as Γ, T_1 and γ, T_2, respectively. Similar expressions are applicable for the other two elements of the density matrix.

Finally, considering the full Hamiltonian and dissipation, we can write the time evolution of the density matrix elements as:

$$\begin{bmatrix} \dot{\rho}_{12} \\ \dot{\rho}_{21} \\ \dot{\rho}_{11} \\ \dot{\rho}_{22} \end{bmatrix} = -\frac{i}{\hbar} \begin{bmatrix} E_1 - E_2 & 0 & -\mu E(t) & \mu E(t) \\ 0 & E_2 - E_1 & \mu E(t) & -\mu E(t) \\ -\mu E(t) & \mu E(t) & 0 & 0 \\ \mu E(t) & -\mu E(t) & 0 & 0 \end{bmatrix} \begin{bmatrix} \rho_{12} \\ \rho_{21} \\ \rho_{11} \\ \rho_{22} \end{bmatrix} - \begin{bmatrix} \rho_{12}\gamma \\ \rho_{21}\gamma \\ \rho_{11}\Gamma \\ \rho_{22}\Gamma \end{bmatrix} \tag{2.3.19}$$

These coupled equations are known as the "Optical Bloch Equations" (OBE). These equations describe the coherence and population dynamics of a two level system under resonant excitation by optical field and form the basis for coherent time resolved spectroscopy.

2.3.2 General solutions of Optical Bloch Equations

In this section, we express the general solution to the solution to the OBE. Given that the optical field is typically much weaker than the intrinsic field of the material system (the electrostatic field acting on electron due to nucleus), the interaction between the two-level system and the optical field can be treated using perturbation theory. We start by writing the solution to the Liouville-Von Neumann equation (equation 2.3.13), as an expansion of $\rho(t)$:

$$\rho(t) = \rho^{(0)}(t_1) + \rho^{(1)}(t_2) + \rho^{(2)}(t_3) + \rho^{(3)}(t_4) + \cdots \tag{2.3.20}$$

where $\rho^{(0)}(t_1) = \rho(-\infty)$ is the initial steady state density matrix. Whereas, $\rho^{(1)}(t_2), \rho^{(2)}(t_3), \rho^{(3)}(t_4), \cdots$ are the higher order corrections, proportional to the corresponding power of the excitation optical field $(E, E^2, E^3, \cdots)$. The expression for the first, second and third order terms in this equation can be written by taking into account the interaction of the system with the optical field and dissipation:

$$\rho^{(1)}(t_2) = \int_{-\infty}^{t_2} -\frac{i}{\hbar}[H_L(t_1), \rho^{(0)}(t_1)]\ e^{(i\omega_0 + \gamma)(t_1 - t_2)} dt_1 \tag{2.3.21}$$

$$\rho^{(2)}(t_3) = \int_{-\infty}^{t_3} -\frac{i}{\hbar}[H_L(t_2), \rho^{(1)}(t_2)]\ e^{(i\omega_0 + \Gamma)(t_2 - t_3)} dt_2 \tag{2.3.22}$$

$$\rho^{(3)}(t_4) = \int_{-\infty}^{t_4} -\frac{i}{\hbar}[H_L(t_3), \rho^{(2)}(t_3)]\ e^{(i\omega_0 + \gamma)(t_3 - t_4)} dt_3 \tag{2.3.23}$$

The rest of the terms in equation 2.3.20 have similar forms, which can be used to write $\rho(t)$ as:

$$\rho(t) = \rho(-\infty) + \sum_{n=1}^{\infty} \rho^{(n)}(t) \tag{2.3.24}$$

where, the *n-th* order density operator is:

$$\begin{aligned} \rho^{(n)}(t) = \sum_{n=1}^{\infty} \left(\frac{i}{\hbar}\right)^n \int_{-\infty}^{t} dt_n \int_{-\infty}^{t_n} dt_{n-1} \cdots \int_{-\infty}^{t_2} dt_1 \\ \times [H_L(t_n), [H_L(t_{n-1}), \cdots [H_L(t_1), \rho(-\infty)] \cdots]] \\ \times\ e^{(i\omega_0 + \gamma)(t_1 - t_2 + t_3 - t_4 + \cdots \pm t_n - t)} \\ \times\ e^{(i\omega_0 + \Gamma)(t_2 - t_3 + t_4 - t_5 + \cdots \mp t_n - t)} \end{aligned} \tag{2.3.25}$$

Recalling the expression for the optical field interaction part of the Hamiltonian, $H_L = -E(t) \cdot \mu$, we can write $\rho^{(n)}(t)$ as:

$$\begin{aligned} \rho^{(n)}(t) = \left(\frac{i}{\hbar}\right)^n \int_{-\infty}^{t} dt_n \int_{-\infty}^{t_n} dt_{n-1} \cdots \int_{-\infty}^{t_2} dt_1\, E(t_n)E(t_{n-1}) \cdots E(t_1) \\ \times [\mu(t_n), [\mu(t_{n-1}), \cdots [\mu(t_1), \rho(t_0)] \cdots]] \\ \times\ e^{(i\omega_0 + \gamma)(t_1 - t_2 + t_3 - t_4 + \cdots \pm t_n - t)} \\ \times\ e^{(i\omega_0 + \Gamma)(t_2 - t_3 + t_4 - t_5 + \cdots \mp t_n - t)} \end{aligned} \tag{2.3.26}$$

In order to use this perturbative expansion approach to solve the OBE, we need to take help from some fundamental ideas from nonlinear optics.

2.3.3 Polarization in nonlinear optics

We know that the macroscopic polarization induced in a material as a result of optical excitation can be written as a Taylor expansion in the excitation electric field as:

$$P = \epsilon_0\chi^{(1)}E + \epsilon_0\chi^{(2)}E^2 + \epsilon_0\chi^{(3)}E^3 + \text{ higher order terms} \tag{2.3.27}$$

The macroscopic polarization can also be expressed as the expectation value of the dipole operator:

$$P(t) = Tr\{\mu\rho(t)\} \tag{2.3.28}$$

So, the *n-th* order polarization can be written as:

$$P^{(n)}(t) = Tr\{\mu\rho^{(n)}(t)\} \tag{2.3.29}$$

We can combine equations 2.3.26 and 2.3.29 to express the *n-th* order polarization as:

$$\begin{aligned} P^{(n)}(t) = \left(\frac{i}{\hbar}\right)^n \int_{-\infty}^{t} dt_n \int_{-\infty}^{t_n} dt_{n-1} \cdots \int_{-\infty}^{t_2} dt_1\, E(t_n)E(t_{n-1})\cdots \\ \cdots E(t_1)\cdot S(t_1, t_2, t_3, \cdots t_n, t) \end{aligned} \tag{2.3.30}$$

where the *n-th* order response function $S(t_1, t_2, t_3, \cdots t_n, t)$, is given by:

$$\begin{aligned} S(t_1, t_2, t_3, \cdots t_n, t) = \left(\frac{i}{\hbar}\right)^n \langle [\mu(t_n), [\mu(t_{n-1}), \cdots [\mu(t_1), \rho(t_0)]\cdots]] \\ \times\ e^{(i\omega_0 + \gamma)(t_1 - t_2 + t_3 - t_4 + \cdots \pm t_n - t)} \\ \times\ e^{(i\omega_0 + \Gamma)(t_2 - t_3 + t_4 - t_5 + \cdots \mp t_n - t)} \rangle \end{aligned} \tag{2.3.31}$$

Here, $\langle\cdots\rangle$ represents the expectation value. This expression for the *n-th* order macroscopic nonlinear polarization demonstrates how the interaction at different times $t = t_1, t_2, t_3, \cdots t_n$ generates a non-equilibrium density matrix and off diagonal matrix elements, causing an emission of a light field followed by the last interaction at $t = t_n$.

As mentioned before, FWM is a third order nonlinear response of a two level system under excitation by optical field. In other words, the response of the system

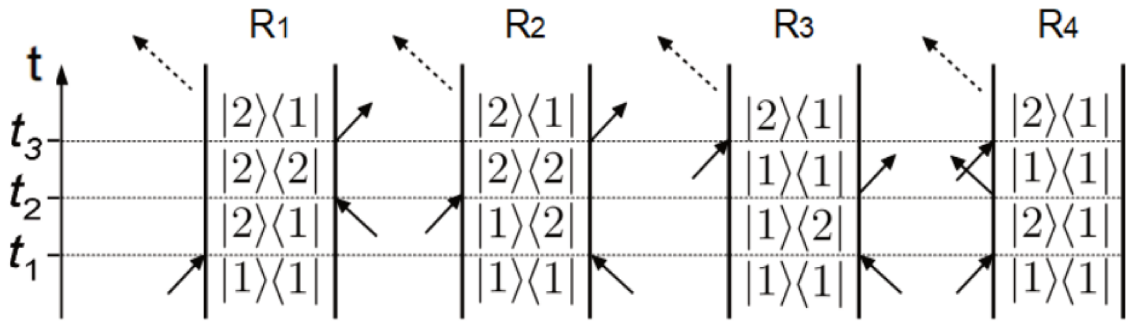

Figure 2.2: Feynman diagram showing the interactions between a two level system and excitation optical field, at different points in time from t_1 to t_3. Each arrow represents an interaction on the ket or bra of the density operator, with the last dotted arrow representing emission of light due to third order polarization of the system [74]

.

corresponding to $\epsilon_0\chi^{(3)}E^3$ in equation 2.3.27 or $n = 3$ in equation 2.3.29 contains the FWM signal measured in FWM spectroscopy. The response for $n = 3$, $S(t_1, t_2, t_3, t)$ will be a sum of 8 terms in total. 4 terms among these are complex conjugates of the other 4 terms. It is then enough to consider only 4 terms (denoted as R_1, R_2, R_3, R_4) to understand the third order response. The Feynman diagram representation of these terms is particularly helpful in visualizing and understanding the interaction involved in each term. Figure 2.2 shows the Feynman diagrams corresponding to each of these terms. In the diagrams, the evolution of the ket and bra of the density operator is represented by the left and right vertical lines, respectively. The arrows represent the interaction with the optical field, with a right (left) pointing arrow corresponding to electric field with phase factor $e^{-i(\omega t-kr)}$ ($e^{i(\omega t-kr)}$). An arrow pointing towards (away) the vertical line denotes excitation (de-excitation) of the system. The last dashed arrow represents the third order nonlinear response emission from the system.

We can express the third order macroscopic polarization by using $n = 3$ in equation 2.3.30 and write:

$$P^{(3)}(t) = \int_{-\infty}^{t} dt_3 \int_{-\infty}^{t_2} dt_2 \int_{-\infty}^{t_1} dt_1 \, E(t_3)E(t_2) \times E(t_1)S(t_1, t_2, t_3, t) \tag{2.3.32}$$

We consider the case where the excitation optical field is composed of three mode locked laser pulses. The electric field of each pulse has the general form:

$$E(t) = E_0 f(t) \Big[\, e^{-i(\omega t - \boldsymbol{k}\cdot\boldsymbol{r})} + \, e^{i(\omega t - \boldsymbol{k}\cdot\boldsymbol{r})} \Big] \tag{2.3.33}$$

where E_0 is the field amplitude and $f(t)$ represents the pulse envelope. Using this form of the electric field, we can write the total field $E(t_3)$ at time $t = t_3$, as the sum of the fields corresponding to each pulse:

$$\begin{aligned} E(t_3) &= E_1(t_3) + E_2(t_3) + E_3(t_3) \\ &= E_{10} f(t_3) \Big[\, e^{-i(\omega t_3 - \boldsymbol{k}\cdot\boldsymbol{r})} + \, e^{i(\omega t_3 - \boldsymbol{k}\cdot\boldsymbol{r})} \Big] \\ &\quad + E_{20} f(t_3) \Big[\, e^{-i(\omega t_3 - \boldsymbol{k}\cdot\boldsymbol{r})} + \, e^{i(\omega t_3 - \boldsymbol{k}\cdot\boldsymbol{r})} \Big] \\ &\quad + E_{30} f(t_3) \Big[\, e^{-i(\omega t_3 - \boldsymbol{k}\cdot\boldsymbol{r})} + \, e^{i(\omega t_3 - \boldsymbol{k}\cdot\boldsymbol{r})} \Big] \end{aligned} \tag{2.3.34}$$

Developing the products in equations 2.3.32 and 2.3.34, we see that the third order response contains 864 terms. In order to simplify and reduce the number of terms to a manageable number, a few assumptions are necessary.

2.3.4 Simplified analytical solution

The first assumption in order to simplify the expression for the third order response is to consider strict time ordering of the excitation pulses. We can take the first pulse to be centered at $t = t_1 = 0$. The second pulse, delayed by τ, arrives at time $t = t_2$ and the third pulse is delayed from the second pulse by T, arriving at time $t = t_3$, as shown in figure 2.3. We assume that the temporal width of the pulse is considerably smaller than the delays between the pulses and they do not overlap with each other. This assumption allows us to state that the interaction at $t = t_1$ corresponding to $\mu(t_1)$ results only from $E_1(t_1)$, not the other two pulses. Same consideration will apply for the second and third interaction originating from $E_2(t_2)$ and $E_3(t_1)$ only, respectively. Applying this assumption on equation 2.3.34, will result in the envelope functions ($f(t_3)$) being replaced by delta functions ($\delta(t_3)$).

The second assumption we can make is to consider the pulse width to be very short compared to any decay timescale of the system. This enables us to represent the electric field of the pulses as Delta functions with a phase factor containing the ap-

propriate frequency and wavevector. This is known as the "semi-impulse limit". This approximation is particularly relevant for confined systems where the decay timescale is generally much longer than the pulse duration. This allows for the development of exact and analytical approaches to the optical Bloch equations [78]. Since we are mostly working with 2D excitons in this thesis, such pulse approximations need to be discussed and adapted, which will be addressed in the next section.

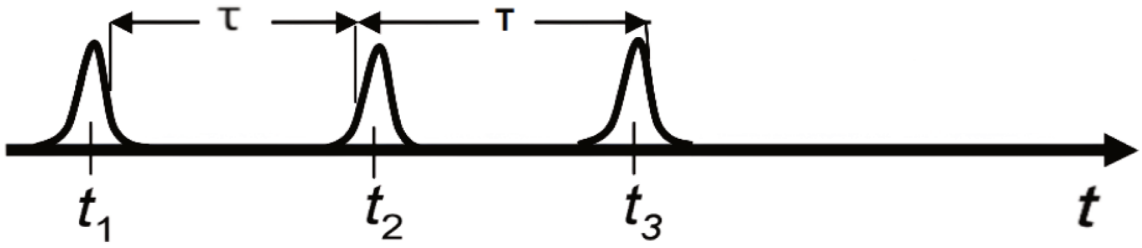

Figure 2.3: Visual representation of three mode locked laser pulses. Pulse 1 arrives at times $t = t_1 = 0$. Pulse 2 arrives at a delay of τ at time $t = t_2$, while pulse 3 has an additional delay of T, arriving at time $t = t_3$ [74]

.

The last assumption is known as the "Rotating wave approximation" (RWA). Evaluating the third order response $P^{(3)}$, using the electric field expression from equation 2.3.33, leads to integrals with phase factors like: $e^{\pm i(\omega-\omega_0)t}$ and $e^{\pm i(\omega+\omega_0)t}$. For near resonance condition ($\omega \approx \omega_0$), the RWA allows us to consider only the factor $e^{\pm i(\omega-\omega_0)t}$, since the integral with the rapidly oscillating term $e^{\pm i(\omega+\omega_0)t}$, quickly averages out to 0.

In addition to these three assumptions, it is worth examining the definition of the time origin in our discussion. So far we have worked with a time origin defined as the arrival time of the first pulse. Speaking from an experimental point of view, it is more convenient to define the time axis origin as the time of arrival of the third pulse, since this is really the time when the third order polarization signal is emitted and this is when the measurement starts. If we combine the time ordering of pulses, semi-impulse limit, RWA and the new time origin definition, we can write the electric field terms from equation 2.3.32 under resonant condition ($\omega = \omega_0$), in the following simplified form:

$$E(t_3)E(t_2)E(t_1) = A_2 E_{30}\delta(t_3)\mathrm{e}^{-i\omega_0 t_3} \\ \times E_{20}\ \delta(t_2+T)\mathrm{e}^{-i\omega_0(t_2+T)} \times E_{10}\ \delta(t_1+T+\tau)\mathrm{e}^{i\omega_0(t_1+T+\tau)} \tag{2.3.35}$$

where all the time independent factors have been absorbed into A_2.

Selection of the FWM signal

Before reaching the simplified solution to the OBE, one more important consideration remains regarding the selection of the FWM signal among the the third order response. Addressing this will allow us to express the third-order response function in equation 2.3.32 in a simplified form. Let's consider three excitation pulses with different wavevectors $\boldsymbol{k}_1, \boldsymbol{k}_2, \boldsymbol{k}_3$ or or modulation frequencies $\Omega_1, \Omega_2, \Omega_3$ (added to the main optical frequencies). Considering different wavevectors and frequencies for the three pulses, the term $E(t_3)E(t_2)E(t_1)$ in equation 2.3.32, will have exponents with different combinations of signs of $\boldsymbol{k}_{1,2,3}$ and $\Omega_{1,2,3}$: $\pm\boldsymbol{k_1} \pm \boldsymbol{k_2} \pm \boldsymbol{k_3}$, $\pm\Omega_1 \pm \Omega_2 \pm \Omega_3$. The third order response stemming from a particular type of interaction, giving rise to specific sequence of evolution of density matrix elements, is emitted at a particular direction given by the wavevector sign combination or at a particular frequency. The FWM signal corresponds to the responses R_1 and R_2 in the Feynman diagram (figure 2.2). The wavevector (frequency) corresponding to R_1 and R_2 are: $\boldsymbol{k} = \boldsymbol{k}_1 + \boldsymbol{k}_3 - \boldsymbol{k}_2$ ($\Omega = \Omega_1 + \Omega_3 - \Omega_2$) and $\boldsymbol{k} = \boldsymbol{k}_2 + \boldsymbol{k}_3 - \boldsymbol{k}_1$ ($\Omega = \Omega_2 + \Omega_3 - \Omega_1$) respectively. So, by adjusting the detection geometry of the experiment or the detection frequency, it is possible to detect only one response among among all the possible responses shown in the Feynman diagram. In most traditional FWM spectroscopy, the detector is placed in the direction $\boldsymbol{k}_2 + \boldsymbol{k}_3 - \boldsymbol{k}_1$, to choose the response corresponding to R_2. This is referred to as directional selection or spatial phase selection. However, in our experimental setup, we work in a colinear geometry and use frequency or temporal phase selection to detect the response R_2, at frequency $\Omega_2 + \Omega_3 - \Omega_1$. The reason behind designing our experiment based on temporal phase selection will be described in more detail later in this chapter.

Using the expression for n-th order response function (equation 2.3.31), the specific FWM response, R2 can be written as:

$$S(t_1, t_2, t_3, t) = A_1 \times e^{(-i\omega_0 + \gamma)(t_1 - t_2)} \times e^{(i\omega_0 + \Gamma)(t_2 - t_3)} \times e^{(i\omega_0 + \gamma)(t_3 - t)} \tag{2.3.36}$$

where A_1 contains the time independent terms. The first exponential factor in this equation takes into account the phase reversal of the polarization induced by the first order pulse.

Finally, Using equation 2.3.36 and 2.3.35, we can evaluate the result of the triple integral from equation 2.3.32. The three integrals will have the following form:

$$\int_{-\infty}^{t} E_{30}\ \delta(t_3) e^{-i\omega_0 t_3} \times e^{(i\omega_0 + \gamma)(t_3 - t)}\, dt_3 = E_{30}\ \Theta(t)\ e^{-i\omega_0 t - \gamma t} \tag{2.3.37}$$

$$\int_{-\infty}^{t_3} E_{20}\ \delta(t_2 + T) e^{i\omega_0 (t_2 + T)} \times e^{(i\omega_0 + \Gamma)(t_2 - t_3)}\, dt_2 = E_{20}\ \Theta(T)\ e^{-i\omega_0 T - \Gamma T} \tag{2.3.38}$$

$$\int_{-\infty}^{t_2} E_{10}^{*}\ \delta(t_1 + T + \tau) e^{-i\omega_0 (t_1 + T + \tau)} \times e^{(i\omega_0 + \gamma)(t_1 - t_2)}\, dt_1 = E_{10}^{*}\ \Theta(\tau)\ e^{i\omega_0 \tau - \gamma \tau} \tag{2.3.39}$$

where, $\Theta(t)$, $\Theta(T)$ and $\Theta(\tau)$ are heaviside functions. By combining all the time-independent terms into B, we can write the third order polarization emission emitted at frequency $\Omega_3 + \Omega_2 - \Omega_1$ in the following simplified form:

$$P^{(3)}(\omega_0, t, \tau, T) = B\ \Theta(t)\Theta(T)\Theta(\tau)\ e^{-i\omega_0 (t + T - \tau)} \times e^{-\gamma (t + \tau)} \times e^{-\Gamma T} \tag{2.3.40}$$

As mentioned before, $\gamma = \frac{1}{T_2}$ and $\Gamma = \frac{1}{T_1}$ are the coherence and population decay rate. Equation 2.3.40 expresses the third order polarization emission from a two level system or an ensemble of homogneously broadened two level systems (the spectral inhomogeneity of the ensemble is not considered at this step).

The physical mechanism described by this equation can be summarized as follows, keeping in mind the relevant Feynman diagram (R_2 in figure 2.2): The first pulse

generates an off diagonal density matrix element ρ_{12} (first order polarization). The off diagonal element oscillates and starts to relax because of dephasing, at a rate given by γ, in what is known as "Free Polarization Decay". The second pulse (after a delay τ), generates a diagonal density matrix element ρ_{22}. In other words, the second pulse generates a second order population from the remaining first order polarization. The population also starts to relax with a rate given by Γ, until the third pulse arrives, delayed from the second pulse by T. The third pulse generates the off diagonal element ρ_{21} and triggers the emission from third order polarization. The strength of the third order polarization depends on the population decay by the time of arrival of the third pulse. This emission is the signal that is detected in the FWM experiment.

2.3.5 2 pulses vs 3 pulses configuration: Detecting coherence or population decay

In the description presented above, there are two control parameters τ and T, allowing for two types of measurements. If we fix the time delay τ between the first two pulses, then the FWM amplitude will be proportional to the two level system population. So, the FWM signal evolution with varying T, will give us a measurement of the population dynamics of the system (characterized by $\Gamma = \frac{1}{T_1}$). The generated second order population will be maximum if τ is set to 0. On the other hand, if we fix the time delay T between pulse 2 and pulse 3 and detect the FWM signal as a function of τ, we can measure the coherence dynamics of the system characterized by $\gamma = \frac{1}{T_2}$. Setting $T = 0$ allows for the maximum of the third order polarization signal. For this measurement, instead of considering three pulses with different frequency and delay between them, we can consider two pulses with frequency Ω_1 and Ω_2. This effectively allows us to consider the second pulse interacting with the system twice. For this two pulse FWM microscopy scheme, the third order response will be emitted at frequency ($\Omega = 2\Omega_2 - \Omega_1$) and the expression for the polarization becomes:

$$P^{(3)}_{2p}(\omega_0, t, \tau) = B\ \Theta(t)\Theta(\tau)\ e^{-i\omega_0(t-\tau)} \times\ e^{-\gamma(t+\tau)} \tag{2.3.41}$$

where the heaviside functions $\Theta(t)$ and $\Theta(\tau)$ dictates that the third order signal is present only for positive time (after the arrival of the second pulse) and for positive delay τ between the two pulses. Referring to R_2 in figure 2.2 again, it is worth

noticing the difference between the off diagonal terms generated by the first and the third interaction. Pulse 1 generates ρ_{12} which oscillates with phase $e^{i\omega_0 t}$, while pulse 3 generates ρ_{21}, oscillating with a reversed phase $e^{-i\omega_0 t}$. Since for two pulse FWM technique, there is no time delay between the second and third interaction, it can be seen as the second pulse causing a phase flip of the polarization generated by the first pulse. This phase flip has important consequences if we consider FWM measurement on an ensemble of two level systems with inhomogeneous broadening, which will be described in detail in the next section.

2.3.6 Solution for inhomogeneously broadened systems

In the description presented so far, what has been referred to as coherence decay rate $\gamma = \frac{1}{T_2}$, represents the "Free Polarization Decay" of a system as a response to excitation by optical field. This can be considered as a system's inherent property. However, in the case of an ensemble of two level systems, if there is a spatial distribution of transition frequencies, then this induces a dephasing between the different polarizations or coherences associated with each individual system. In linear spectroscopy, such dephasing leads to a damping of the coherences, and the average of the individual decoherence times cannot be retrieved. In FWM microscopy, this is no longer the case, both homogeneous and inhomogeneous contributions can be evaluated. This is one of the key advantages of this experimental approach. In order to truly determine the dynamics of excitons in an ensemble with considerable inhomogeneity, the contribution of inhomogeneous broadening needs to taken into account. We can approximate this contribution in the ensemble of N systems with a Gaussian distribution of resonant frequencies with a standard deviation σ:

$$\mathcal{G}(\omega_0) = \frac{1}{\sqrt{2\pi}\sigma}\, e^{-\frac{(\omega_0 - \omega_{0c})^2}{2\sigma^2}} \tag{2.3.42}$$

where, ω_{0c} is the center of the Gaussian distribution. In order to take the inhomogeneous broadening into account, we integrate $P^{(3)}$ from equation 2.3.40 over the Gaussian distribution of transition frequencies:

$$
\begin{aligned}
P_{2p}^{(3)}(t,\tau) &= \int_{-\infty}^{\infty} P^{(3)}(\omega_0,t,\tau) N\mathcal{G}(\omega')\, d\omega' \\
&= NA\ \Theta(t)\Theta(\tau)\ e^{-\gamma(t+\tau)} \\
&\quad \times \frac{1}{\sqrt{2\pi}\sigma} \int_{-\infty}^{\infty} e^{\left[\left(-\frac{\omega_0^2}{2\sigma^2} - \omega_0(it - i\tau - \frac{\omega_{0c}}{\sigma^2}) - \frac{\omega_{0c}^2}{2\sigma^2}\right)\right]} d\omega_0
\end{aligned}
\tag{2.3.43}
$$

The result of the integral is as follows:

$$
\begin{aligned}
P_{2p}^{(3)}(t,\tau) &= NB\Theta(t)\Theta(\tau)\ e^{-i\omega_{0c}(t-\tau)}\ e^{-\gamma(t+\tau)} e^{-\frac{\sigma^2}{2}(t-\tau)^2} \\
&= N\ P^{(3)}(\omega_{0c},t,\tau)\ e^{-\frac{\sigma^2}{2}(t-\tau)^2}
\end{aligned}
\tag{2.3.44}
$$

This equation expresses the time and delay dependent third order polarization or FWM amplitude for an ensemble of two level systems, considering both the effect of homogeneous and inhomogeneous broadening. The time evolution of the third order polarization for such an ensemble is determined by the product of two decay contributions: $e^{-\gamma(t+\tau)}$ and $e^{-\frac{\sigma^2}{2}(t-\tau)^2}$, stemming from homogeneous broadening and inhomogeneous broadening of the systems, respectively.

This equation represents an important physical mechanism in the ensemble of two level systems. In two pulse FWM technique, the second pulse flips the phase of the coherence generated by the first pulse. For an ensemble of two level systems, after the first interaction, the coherence generated in all the systems starts to evolve, oscillating in phase initially. In the presence of inhomogeneity, their coherence oscillate with different phases. As a result, the macroscopic polarization quickly approaches 0 even though individually, the coherence of the systems have not completely decayed yet. The second pulse flips all of their phases and subsequently their phases evolve in the opposite way. After a delay of τ from the arrival of the second pulse, the coherence of the systems in the ensemble are in phase again. Looking at equation 2.3.44, for $t = \tau$, $P^{(3)}(t,\tau) = N\ P^{(3)}(\omega_{0c},t,\tau)$ or in other words, the third order polarization signal is N times stronger than the polarization of a single system. This is known as photon echo.

In FWM microscopy experiment, we do not directly measure the time domain

signal. The detector records the time integrated, frequency resolved FWM signal. If we Fourier transform equation 2.3.44, from time domain to frequency domain, we get:

$$\begin{aligned} P_{2p}^{(3)}(\omega,\tau) &= NB\Theta(\tau)\ e^{-\gamma\tau - \frac{\sigma^2\tau^2}{2} + i\omega_{0c}\tau} \\ &\int_0^\infty e^{-\gamma t - \frac{\sigma^2 t^2}{2} + \sigma^2 t\tau - i(\omega_{0c}-\omega)t}\, dt \\ &= NB\ e^{i\omega\tau}\ e^{\frac{i\gamma(\omega_{0c}-\omega)}{\sigma^2}}\ e^{-\frac{(\omega_{0c}-\omega)^2}{2\sigma^2}}\ e^{-2\gamma\tau + \frac{\gamma^2}{2\sigma^2}} \\ &\times erfc\left[\frac{\gamma}{\sqrt{2}\sigma} - \frac{\tau\sigma}{\sqrt{2}} + \frac{i(\omega_{0c}-\omega)}{\sqrt{2}\sigma}\right] \end{aligned} \tag{2.3.45}$$

Here, $erfc$ represents the complementary error function and ω can be considered as the detection frequency in the experiment. After absorbing all the constants and the oscillating term into A and considering the detected signal at the central frequency ω_0 ($\omega = \omega_0$), the final expression can be written in a simplified way:

$$P_{2p}^{(3)}(\tau) = A\ \Theta(\tau)\ \ e^{\left[-2\gamma\tau + \frac{\gamma^2}{2\sigma^2}\right]}\, erfc\left[\frac{\gamma}{\sqrt{2}\sigma} - \frac{\tau\sigma}{\sqrt{2}}\right] \tag{2.3.46}$$

This is the expression for time integrated FWM signal amplitude for an ensemble of two level systems considering both homogeneous and inhomogeneous broadening.

2.3.7 Beyond the semi-impulse limit

One of the key assumptions we made in order to reach this expression, was the semi-impulse limit, whereby we considered the excitation laser pulses as delta pulses. In practice of course, laser pulses have finite temporal width. The semi impulse limit assumption is still fully valid for systems with characteristic decay times that are orders of magnitude longer than the pulse temporal width. However, for systems with decay times comparable to the laser pulse width, we can not rely completely on the semi impulse limit. In this thesis, the excitation laser pulse width is $\approx 100fs$ and the characteristic decay timescale of 2D excitons in vdW materials can range between hundreds of femtoseconds to a few nanoseconds. For measurements on such systems, the effect of the pulse width needs to be taken into account. The laser

pulses are well approximated by a Gaussian profile. So, ideally, three Gaussian pulse-shape should be used to express the electric field terms to evaluate the triple integral for $P^{(3)}$ in equation 2.3.32. Then, the response function needs to be convoluted with each Gaussian pulse-shape, which becomes quite challenging in complexity [77]. A good compromise between this computationally heavy task and accuracy is to make a convolution of one Gaussian profile with the expression for $P_{2p}^{(3)}$ in equation 2.3.46, which delivers reasonably accurate results. Equation 2.3.46 convoluted with a Gaussian function, was used to fit the majority of the FWM amplitude decay results presented in the subsequent chapters, as the accuracy of the method has been well established [28, 30, 79].

It is usual practice in time resolved spectroscopy to designate the excitation pulses as pump or probe pulse. For two pulse FWM microscopy, we will refer to pulse 1 and 2 as pump and probe pulse, respectively. In this experiment, the FWM intensity is detected for a set of different delays between pump and probe pulses and the decay of the FWM signal amplitude as a function of delay is used to infer the coherence dynamics of the systems.

2.3.8 Expression for population dynamics

For population dynamics, probed in the three pulse configuration, the pulses are designated as pump-1, pump-2 and probe pulse. We detect the FWM signal as a function of the the delay τ_{23} between the two last pulses. In this configuration, the inhomogeneous broadening contribution does not depend on τ_{23}. Therefore, we can derive an analytical formula of the following form:

$$P_{3p}^{(3)}(\tau_{23}) = C\ e^{\left[\frac{1}{2}\left(\frac{T_p}{T_1}\right)^2 - \frac{\tau_{23}}{T_1}\right]}\left[1 + erf\left(\frac{\tau_{23}}{T_p} - \frac{T_p}{2T_1}\right)\right] \tag{2.3.47}$$

where, T_p is the temporal width of the pulse, erf is the error function, C contains all the constants. This equation is used as the basis for fitting the population dynamics data in this thesis.

2.4 FWM microscopy experimental setup

In this section, the FWM microscopy experimental setup developed in this thesis will be described in details, keeping in mind the theoretical framework and requirements discussed so far. The description of the experiment will be divided into three distinct segments. First, the beam preparation part will focus on how the excitation beams are generated with the necessary properties, such as: (*i*) achieving the minimum pulse duration at the location of the sample, and (*ii*) a well-defined phase modulation to enable the frequency selection scheme. The second segment will depict how the sample and the microscope objective are housed inside a cryostat with the piezostages. Finally, the last part will outline the complexities of detecting the FWM signal. Heterodyne dual balanced detection technique and Fourier transform spectral interferometry (FTSI) will be explained in details.

2.4.1 Preparation of input beams

The laser source used for the FWM microscopy experiment is a Ti:Sapph (Titanium doped Sapphire), mode locked pulsed laser, with pulse duration of ≈ 100 fs, repetition rate of 80 MHz and output power ≈ 2 W. It is tunable in wavelength within a range of 690 nm - 1090 nm (1.14 - 1.79 eV). There are two crucial elements necessary for beam preparation in this experiment: pulse compressor and Acousto-optic modulators (AOM). In order to understand the layout of the setup, the functionality of these elements need to be discussed.

Prism pulse compressor

Pulse temporal spreading or pulse broadening is an inevitable and undesirable effect that occurs in every experiment that utilizes pulsed laser. When light wave consisting of different frequency components travel through a material, they experience different refractive index and attain different velocities, leading to delays in travel time relative to each other. This effect, known as Group delay dispersion (GDD), leads to the temporal spreading of the pulse. Considering a laser pulse with different frequency components, GDD causes some frequency components to "lead" and others to "lag", which is another way of saying that the pulse becomes stretched or broadened or chirped in time. In a pulse, if the lower frequency components travel faster than the

higher frequency components (which is generally the case in any material), then the pulse is referred to as "positively chirped". Pulse broadening is almost always an inconvenience in spectroscopy. Moreover, GDD introduced by each transmission of the pulse through an optics accumulate. It can limit the highest achievable temporal resolution. The effects become particularly severe for advanced spectroscopic experimental setup with a high number of transmission optics and sub-ps laser pulses which have a relatively broad spectrum.

The way to deal with this issue is to use a "Pulse compressor": a device that can introduce negative GDD to the pulse. When the pulse travels through the pulse compressor, the lower frequency components travel a longer path compared to the higher frequency components. Prisms can be used for this purpose. However, the prism material can introduce angular and spatial dispersion of its own and also cause pulse-front tilt. These extra unwanted effects can be nullified by placing in the beam path, another prism anti-parallel to the first one and then an additional identical couple of prisms, leading then to a set of four prisms. This four prism pulse compressor yields the primary desired effect of negating pulse broadening and this design has been used traditionally in spectroscopy. But, it has some drawbacks as well. In addition to this design being bulky, tuning GDD imposes very strict alignment conditions since it requires very small precise rotations in all four prisms and maintaining equal distances between the prisms. Small imperfections in the alignment in such a configuration can lead to residual spatio-temporal distortion and magnification of the laser beam.

An alternative to the four prism pulse compressor is to use two prisms with two passes through each prism. This design replaces the last two prisms in the original four prism compressor with a roof mirror which sends the beam back towards the only two prisms at a different height for second passes through them. This achieves the desired negative GDD, but it still exhibits, though to a lesser extent, the drawbacks of the four-prism design. Fortunately, this idea of cutting down the number of prisms by allowing more than one pass through them can be extended one step further. The best known way to design a prism pulse compressor with minimal spatio-temporal distortion and magnification is to use one prism only [80]. This is the option that we used in our experiemntal setup and is presented in the following paragraphs.

Figure 2.4 demonstrates a single prism pulse compressor, highlighting the integral parts: prism, retroreflector and roof mirror. In this design, after the beam passes through the prism once, it is inverted and send back for the second pass at a different

height by a retroreflector. A roof mirror is placed on the opposite side of the prism which reflects back the beam for the third pass and finally, the retro-reflector sends back the beam one more time for the fourth pass through the prism. Once this device is implemented, aligned and the retroreflector position is fixed, tuning it with changing wavelength of the laser requires only the rotation of one prism. This rotation does not change the alignment and the direction of the output beam of the compressor at all. It has a much more convenient GDD tuning procedure as well, since it only involves the translation of one prism (into or out of the beam path) or the translation of the retroreflector relative to the prism. The condition of maintaining equal distance between prisms in the previous designs are automatically fulfilled here.

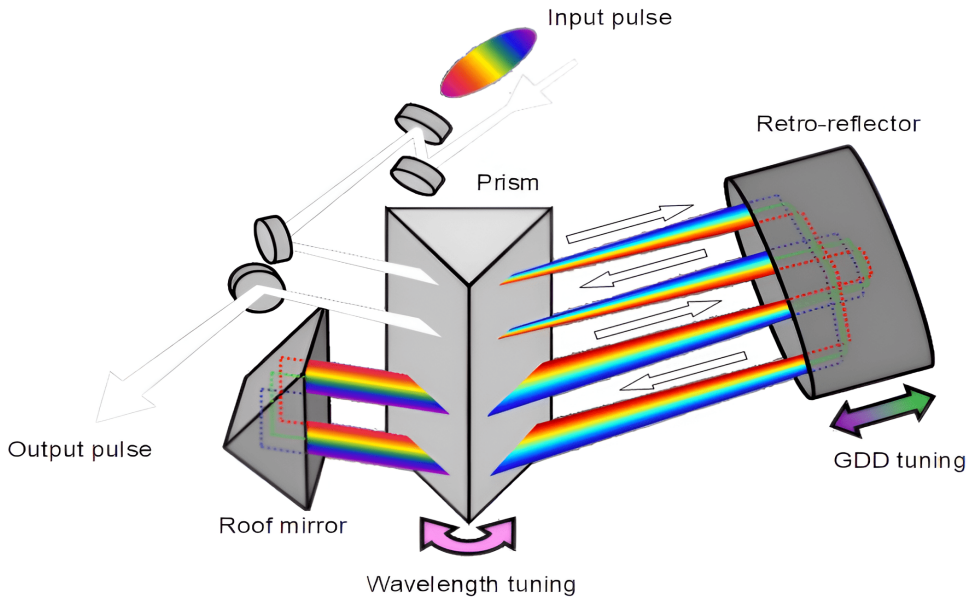

Figure 2.4: Schematic diagram of a single prism pulse compressor highlighting the four passes of the beam through the prism. The crucial components are: prism, retroreflector and roof mirror [80]

Beside compensating for pulse broadening, the one prism compressor does not introduce any residual unwanted effect on the beam. For example: the magnification experienced by the beam on the first pass (M_1) is reversed on the second pass. In other words, the beam experiences de-magnification by the same amount on the second pass. Since the same scenario is applicable for the third and fourth pass, we can write: $M_1 = \frac{1}{M_2} = M_3 = \frac{1}{M_4}$, where M_2, M_3 and M_4 are the magnifications in

the second, third and fourth pass, respectively. The overall magnification M given by the product of the magnifications in each pass, is equal to 1. Then the angular dispersion in a one prism compressor can ideally be reduced to zero. The one prism pulse compressor fulfills the role of introducing negative GDD, with minimum residual effects on the beam and the least amount of restrictions on the alignment needed for its operation, while ffering spatial compactness [80].

Before implementing the pulse compressor in the experimental setup, simulation of the device is necessary. There are two key considerations in the design of the compressor: incidence angle of the beam and distance between the prism and the retro-reflector. The incidence angle, i on the prism should ideally be equal to the Brewster's angle for a given wavelength to ensure minimum polarization induced loss. i should also be equal to the incidence angle for minimum deviation to ensure maximum dispersion. Commercially available "Brewster prisms" have the property that the Brewster angle for a range of wavelengths matches the incidence angle for minimum deviation with a reasonable degree of accuracy. Such a Brewster prism made of highly dispersive glass (N-SF66) is used to design the pulse compressor. The well known Sellmier equation of refractive index allows the calculation of the refractive index of the prism material as a function of wavelength between 690 nm and 1090 nm (emission range of the laser source):

$$n^2(\lambda) = 1 + \frac{B_1\lambda^2}{\lambda^2 - C_1} + \frac{B_2\lambda^2}{\lambda^2 - C_2} + \frac{B_3\lambda^2}{\lambda^2 - C_3} \tag{2.4.1}$$

The coefficients B_1, B_2, B_3, C_1, C_2 and C_3 are material specific empirical parameters that are available from the prism manufacturer datasheet. Once the refractive indices are obtained, the incidence angle for minimum deviation is calculated for the same wavelength range with the equation:

$$i = \sin^{-1}\left(n \sin\left(\frac{A}{2}\right)\right) \tag{2.4.2}$$

where A is the apex angle of the prism. Calculating the incidence angles provides us with a quantification of the rotation angle of the prism necessary for tuning the pulse compressor with changing wavelength. Figure 2.5a shows the calculated incidence angle for minimum deviation for varying laser wavelength. The total GDD introduced by the pulse compressor can be expressed by the following equation:

$$\mathrm{GDD_{pr}} = \frac{\lambda^3}{2\pi c^2}\left[4l\left(\frac{d^2n}{d\lambda^2} + \left(2n - \frac{1}{n^3}\right)\left(\frac{dn}{d\lambda}\right)^2\right)\sin\beta - 2\left(\frac{dn}{d\lambda}\right)^2\cos\beta + 4\left(\frac{d^2n}{d\lambda^2}\right)\left(2D_{\frac{1}{e^2}}\right)\right] \tag{2.4.3}$$

Here, l is the separation between the prism and the retrorelfector. $D_{\frac{1}{e^2}}$ is the beam diameter. β can be referred to as the spreading angle. It is defined as the difference in the exit angles out of the prism on the first pass, between the highest wavelength component and the lowest wavelength component of the light being dispersed. β can be estimated as:

$$\beta = -2\frac{dn}{d\lambda}\delta\lambda \tag{2.4.4}$$

where, $\delta\lambda$ is the range of wavelength being dispersed [81].

Figure 2.5b shows how the GDD introduced by the pulse compressor changes rapidly with varying prism-retroreflector separation, for a laser center wavelength of 930 nm. As it is demonstrated, the introduced GDD goes from positive to negative and keeps increasing in the negative direction with increasing separation.

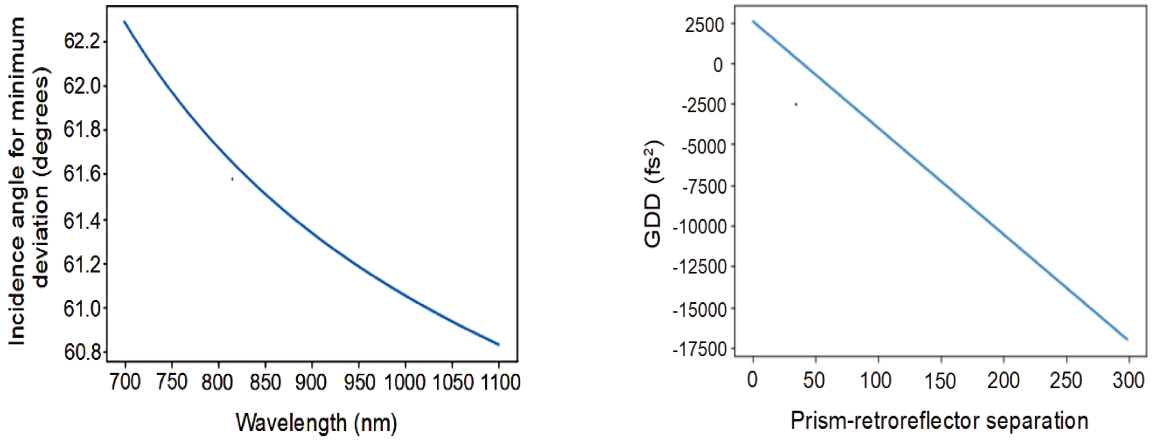

(a) (b)

Figure 2.5: (a) change of incidence angle for minimum deviation as a function of laser wavelength (b) Group delay dispersion (GDD) introduced by the one prism pulse compressor vs prism-retroreflector separation, for laser center wavelength of 930 nm.

The prism-retroreflector separation, l is determined by checking the pulse duration for different l and making sure that l is enough to introduce enough compensating

negative GDD in the pulse compressor for the minimum (690 nm) and maximum (1090 nm) operating wavelength of the laser. Afterwards, the translation of the prism is used to fine tune the GDD to obtain the minimum possible pulse duration. Subsequently, rotation of the prism to tune the incidence angle for varying wavelength, is tested to make sure that the minimum pulse duration is achievable for the full operating wavelength range without changing the alignment. Typically, we reduce the temporal spreading of the pulse at the sample location from $\approx$ 400 fs to $\approx$ 100 fs.

Temporal phase (frequency) selection

In section 2.3.4 of the theoretical background for FWM, we discussed the possibility of detecting FWM signal using either spatial phase (wavevector) selection or temporal phase (frequency) selection. The spatial phase selection scheme is only achievable for a macroscopic system or a very large ensemble of two level systems, where the characteristic lengthscale (l) is much larger than the wavelength of the optical field (λ). This technique is not applicable when $l \approx \lambda$. For such sub-wavelength sized systems, the translational invariance is broken and the emission is isotropic. In such a case, spatial phase selection is no longer possible, and this is where temporal phase selection comes into play. The principle is as follows: the exciting beams pass through an AOM, which adds an additional radio-frequency component Ω_i ($\approx$ 110 MHz), to the optical frequency, with i= 1, 2, 3 for the first, second and third pulse, respectively. For each beam, the value of Ω_i is slightly different. The collinear beams are all focused on the sample via a microscope objective. Then, the coherent FWM response emitted by the system carries the corresponding radio-frequency combination, Ω_d (for example, $\Omega_d = \Omega_3 + \Omega_2 - \Omega_1$ for R2 in figure 2.2).

In order to detect this FWM response, the signal, along with other exciting beams (the details of the detection method will be provided in the section "FWM signal detection"), passes through a final AOM, driven at the response frequency Ω_d, and is mixed with a reference beam. This is known as heterodyne detection. The FWM microscopy experimental setup developed in this thesis operates based on temporal phase selection and heterodyne detection. In this context, precise phase control is essential for both the excitation pulses and the detection of the FWM signal. In the following section, we will discuss how this is achieved.

Acousto-Optic Modulators

We use AOM in order to control the temporal phase of the excitation pulses and also to detect the FWM signal. These devices play an extremely crucial role in our experiment. The working principle of an AOM is described here. In simple terms, AOM is a crystal with an attached piezoelectric transducer. Applying a voltage to the transducer generates acoustic wave which travels through the crystal. As a result, periodic compression and expansion leading to a periodic change of refractive index is generated in the crystal. Any incident light interacts with this grating like structure and one part of the beam gets or diffracted while the other part is transmitted. Additionally, The diffracted beam can experience an up-shift or down-shift in their frequency. Figure 2.6a shows a schematic of an AOM, with the wavevector (frequency) of the input/transmitted beam, the acoustic wave and the first order diffracted beam, denoted as $\boldsymbol{k_0}(\omega_0)$, $\boldsymbol{K}(\Omega)$ and $\boldsymbol{k_{-1}}(\omega_0 - \Omega)$, respectively. The interaction between laser and the AOM acoustic wave can be better understood as the interaction between photons and phonons. Applying momentum and energy conservation to the interaction, we can write:

$$\hbar \boldsymbol{k_{-1}} = \hbar \boldsymbol{k_0} - \hbar \boldsymbol{K} \tag{2.4.5}$$

$$\hbar \omega_{-1} = \hbar \omega_0 - \hbar \Omega \tag{2.4.6}$$

This diffracted beam is the first order down-shifted beam or order -1 beam. Up-shifted beam (order $+1$) is produced similarly and follows similar expressions as shown above. Figure 2.6b and 2.6c shows order -1 and order $+1$ diffracted beams, respectively, both satisfying the phase matching condition. It is evident that the angle at which the first order of diffraction will be most efficient can be written as:

$$\theta_{\mathrm{Br}} = \sin^{-1}\left(\frac{K}{2k_0}\right) = \sin^{-1}\left(\frac{\lambda}{2\Delta}\right) \tag{2.4.7}$$

where, $K = \mid \boldsymbol{K} \mid$, $k_0 = \mid \boldsymbol{k_0} \mid$ and λ is the wavelength of the input laser [82, 83].

In our FWM microscopy setup, AOMs made of Tellurium dioxide (TiO_2) crystal, with an operating wavelength range of 690 nm - 1064 nm and driving frequency range of 85 - 135 MHz were used. A programmable Radio frequency (RF) generator was used to provide the driving acoustic wave for the AOM. Using equation 2.4.7, the Bragg angle θ_{Br} for laser wavelength $\approx$ 700 nm, was found to be $\approx 1.2°(0.02$ rad).

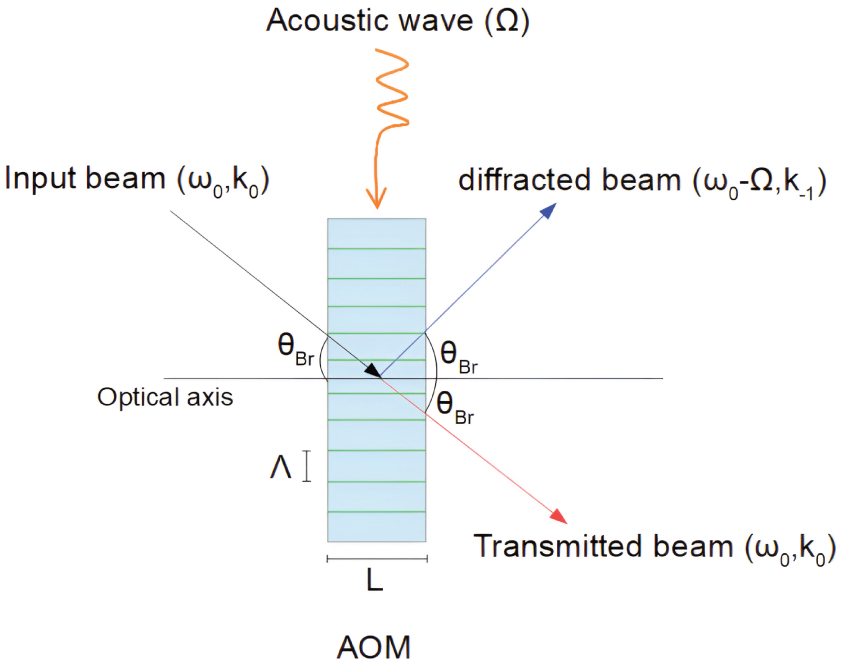

(a)

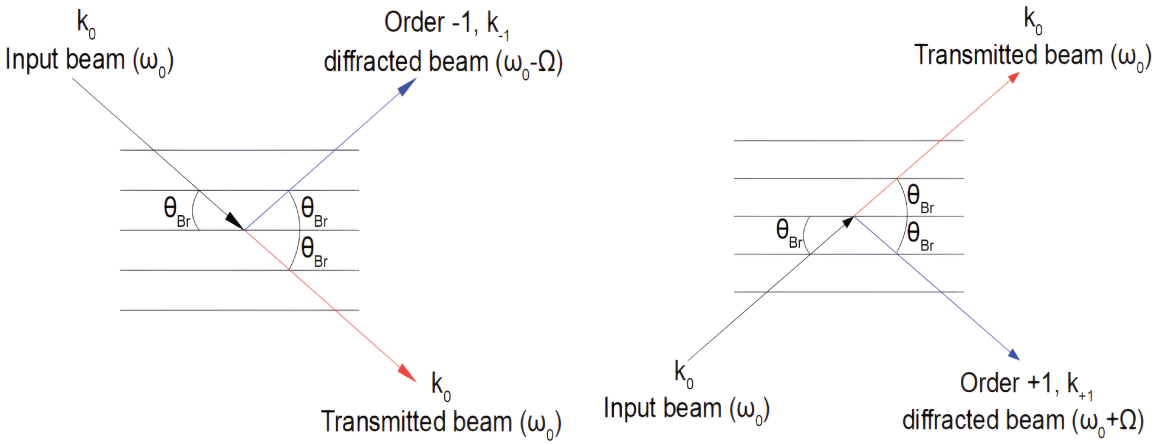

(b) (c)

Figure 2.6: (a)Schematic diagram of Acousto-optic modulator (AOM). θ_{Br}: Bragg angle, L: interaction length, Δ: Acoustic wavelength, $K(\Omega)$: $k_0(\omega_0)$: wavevector (frequency) of the input / transmitted beam, $K(\Omega)$: wavevector (frequency) of the acoustic wave, $k_{-1}, \omega_0 - \Omega$: wavevector (frequency) of the first order diffracted beam (b) order -1 diffracted beam (c) order $+1$ diffracted beam [82].

Towards the sample

Figure 2.7 shows a simplified schematic diagram of the beam preparation part of the FWM microscopy experimental setup. After the laser beam exits its source, it passes through a waveplate and a polarizer. The output power of the laser source is $\approx$ 2W, which is extremely high compared to what is usually needed (hundreds of nW to hundreds of μW) for FWM microscopy measurement on excitonic systems. The waveplate-polarizer combination enables a degree of control over the laser power as well. They are shown together as "polarization optics" in the schematic.

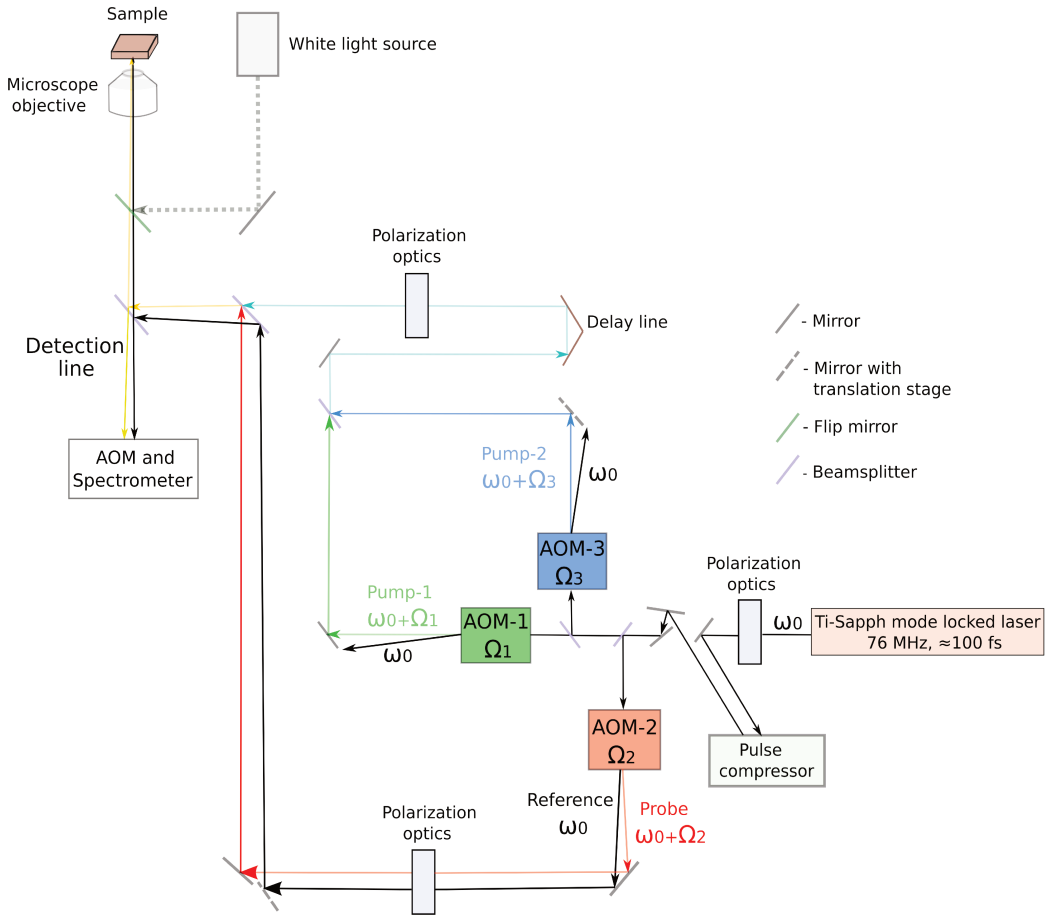

Figure 2.7: Schematic diagram of beam preparation for FWM microscopy. ω_0: laser frequency, AOM: Acousto-optic modulator, $\Omega_1, \Omega_2, \Omega_3$: driving frequencies of the respective AOMs. The reflected pump, probe and the FWM signal beam (black) and the reference beam (yellow), passing into the detection line, are also indicated.

The beam is then sent into the pulse compressor. Once the beam exits the compressor, it is split into two parts by a beamsplitter. One part of the beam goes to AOM-2 driven at frequency Ω_2. The transmitted part of the output of AOM-2 acts as the reference beam for heterodyne detection subsequently, while the up-shifted 1st order diffracted part of the output is used as the probe beam with frequency $\omega_0 + \Omega_2$, where ω_0 is the laser frequency. The other part of the laser beam from the beamsplitter is split once more and sent to AOM-1 and AOM-3, driven at Ω_1 and Ω_3. The up-shifted 1st order diffracted beams from AOM-1 and AOM-3 form two pump beams, denoted as pump-1 and pump-2 with frequency $\omega_0 + \Omega_1$ and $\omega_0 + \Omega_3$, respectively. Before they are combined to propagate together, pump-2 is reflected from a mirror mounted on a translation stage. This stage allows the control of the delay of pump-2 with respect to pump-1 within a small range (few fs, should ideally be reduced to zero for population measurements). The pump beams and the probe-reference beams go through separate polarization optics. Finally, the probe and the two pumps are combined in a beamsplitter in the same spatial mode. From this point, all the beams travel using the same optics. Until this point, the setup is protected with plexi-glass cover to prevent airflow from causing any relative phase fluctuation among the beams. The reference beam propagates parallel to the probe beam, but at a different height. This geometrical configuration is crucial for the detection of the FWM signal and as such, it will explained in detail later on in this chapter.

2.4.2 Coupling to the sample: Microscope objective

As the name "FWM microscopy" conveys, coupling the beams to the microscope objective is an integral part of the experiment. After the beams are prepared and recombined (pump-probe beams in the same spatial mode and reference beam at a different height), they are directed into the objective aperture using a beamsplitter with a high transmission coefficient ($\approx 90\%$). As a result, only $\approx 10\%$ of the input beam intensity is actually directed towards the sample. The choice of transmission coefficient is based on the fact that the FWM signal is exceedingly weak compared to the reflected pump and probe beams from the sample, which are collinear with the FWM signal. So, it is necessary to allow as much transmission as possible for the FWM signal. The microscope objective focuses the laser beam onto the sample into

a diffraction limited spot. The diameter (FWHM) of the focused laser beam spot depends on the numerical aperture (NA) and can be written as:

$$r_m = \frac{1.22\ \lambda}{NA} \tag{2.4.8}$$

Figure 2.8a shows how a objective focuses light onto the sample plane. The angle α is the angular admittance of the objective. It is used to define the numerical aperture as: $NA = nsin\alpha$, where n is the refractive index of the material in which the objective is placed in [83]. In our experiment, $n \approx 1$, since the objective is placed in air. We use objective with different NA, from 0.25 upto 0.9, depending on the type of measurement. For the FWM measurements presented in this thesis, 0.9 NA objective was used, which leads to a resolution of $\approx 1\ \mu m$, for laser wavelength 800 nm.

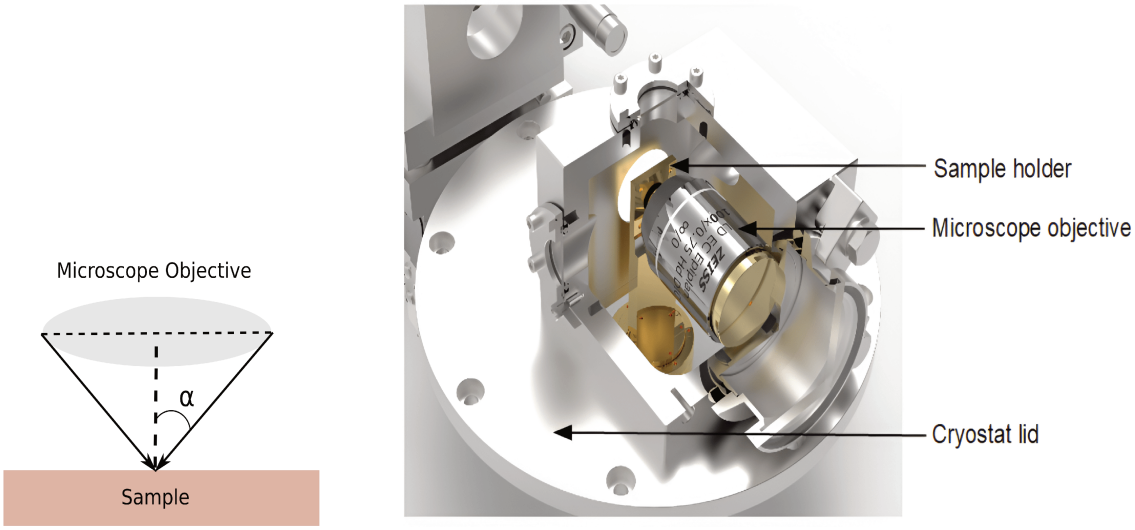

(a) (b)

Figure 2.8: (a) Visual representation of laser beam focused on the sample plane by the microscope objective. α: angular admittance of the objective [83]. (b) Cross sectional schematic of microscope objective and the sample holder, inside the cryostat [provided by Nicolas Beyer from IPCMS].

The sample itself can be glued to a piece of metal that can be screwed on a metallic sample holder. The holder sits on top of the piezostages, that allows movement of the sample with nm accuracy. The sample holder and the piezostages are housed inside a cryostat, that allows control over the temperature of the sample between $4K$ and

room temperature. The suitable coolant (Nitrogen or Helium in liquid form) is flown from a reservoir into the cryostat, where a thermal exchanger, placed very close to the sample cools it down. Then the coolant (in gaseous form at this point) is extracted out of the cryostat for recovery. Using a high NA objective becomes challenging in this configuration, since the working distance becomes too small (1 mm working distance for 0.9 NA objective). To circumvent this, the lid of the cryostat was customized in a way that allows for the objective to be mounted inside the cryostat. Figure 2.8b shows a cross sectional view of the objective and sample holder inside the cryostat.

2.4.3 FWM signal detection

The technique used to detect FWM signal in this experiment can be referred to as heterodyne spectral interferometry (HSI). It combines aspects of two well known techniques: Heterodyne detection and Fourier transform spectral interferometry (FTSI). In addition to these, a dual balanced scheme is used to cancel out the background that copropagates with the signal. The following description will cover each of these aspects and also some other relevant optical components involved in the detection of the signal.

The FWM signal is detected through interference with a reference pulse. To optimize the interference contrast, the reference pulse should follow the same optical path as the excitation and collection beams. However, the reference pulse must not participate in the excitation process. Therefore, in the beam preparation section, the reference and probe beams emerge from AOM-2, where the transmitted beam is taken as reference and the diffracted beam acts as the probe beam. Then they are directed to propagate at a different angle. As a result, the beams are focused on different locations on the sample.

Figure 2.9 shows a simplified schematic diagram of the detection part of the FWM microscopy experimental setup. The FWM signal that is emitted by the excitonic system is collected by the microscope objective. In reflection geometry, the FWM signal is superimposed on the reflected probe and pump beams and the reference beam propagates at a different height. All the beams are taken to the detection path through the beamsplitter that was used to send the excitation beams. The beams are then sent into an AOM (detection AOM) driven at frequency Ω_d, using a dual lens system (L2, L3). Ω_d depends on the type of measurement and needs to match exactly

the frequency of the FWM signal. For two pulse FWM measurement (coherence dynamics), $\Omega_d = 2\Omega_2 - \Omega_1$ and for three pulse FWM measurements (population dynamics), $\Omega_d = \Omega_2 + \Omega_3 - \Omega_1$ (the choice of detection frequency and heterodyne detection is provided in the next section). The output beams from the AOM is focused by lens L4, for imaging onto the slit of a monochromator. The spectrally resolved beams are then detected by charged couple device (CCD) cameras. Two pinholes with very small apertures (≈ 200 μm), positioned at the focusing plane of lens L2, spatially filters the beams. These pinholes ensures that we collect the beams coming from the location of interest on the sample and also block out any scattered light.

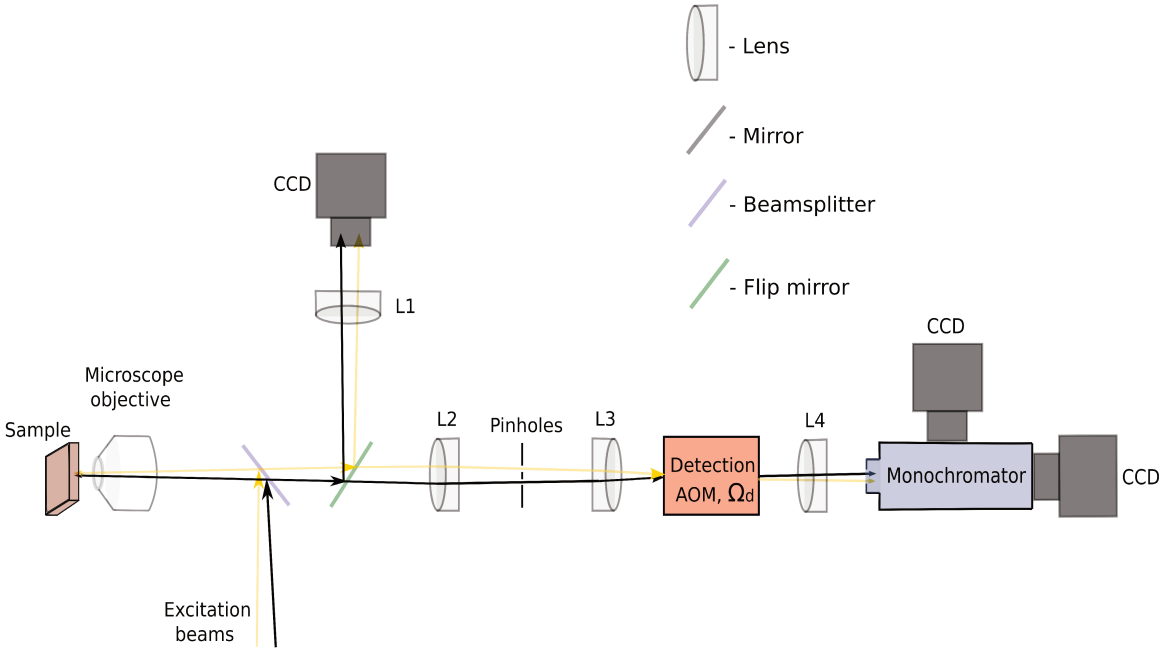

Figure 2.9: Schematic diagram of FWM signal detection. ω_0: laser frequency, AOM: Acousto-optic modulator, $\Omega_1, \Omega_2, \Omega_3$: driving frequencies of the respective AOMs

The primary purpose of the detection AOM is to mix the weak FWM signal with the reference beam and recover the signal from the resulting interference, in a process referred to as Heterodyne Spectral Interferometry (HSI) [75, 83]. Several aspects of this technique will be described below. The description will start with how the choice of driving frequencies of the beam preparation AOMs and detection AOM play a crucial role in choosing the desired third order response from the system. This will

be followed by a discussion on the specific geometry of the beams at the detection AOM. Lastly, the method to extract FWM signal amplitude and phase from the detected signal will be stated. Although the discussion will focus on two pulse FWM signal detection, it is equally applicable to three pulse FWM measurements as well.

Choice of AOM driving frequencies

A pulsed laser beam can be thought of in time domain as a superposition of short pulses with center frequency ω_0, envelope $A(t)$ and a repetition rate of $T_{rep} = \frac{2\pi}{\Omega_{rep}}$. Using this notation, the reference beam $E_r(t)$ can be written as:

$$E_r(t) = \mathcal{E}_r(t) + c.c. \tag{2.4.9}$$

where

$$\mathcal{E}_r(t) = e^{-i\omega_0 t} \sum_n A_r(t - n\tau_{rep}) \tag{2.4.10}$$

Here, n is an integer. The third order signal from the two level system can be labelled as $\mathcal{E}_s^{l_1,l_2}$. The values of l_1 and l_2 determine which third order response is being considered. For example: $l_1 = -1$ and $l_2 = +2$ refers to the two pulse FWM signal of interest to us. Considering the frequency shift of the detection AOM driven at Ω_d, the FWM signal field $\mathcal{E}_s^{l_1,l_2}(t)$ can be expressed as:

$$\mathcal{E}_s^{l_1,l_2}(t) = e^{-i\omega_0(l_1+l_2)t} \sum_n e^{-i(l_1\Omega_1 + l_2\Omega_2 - \Omega_d)n\tau_{rep}} A_s^{l_1,l_2}(t - n\tau_{rep}) \tag{2.4.11}$$

where Ω_1 and Ω_2 are the pump and probe AOM driving frequencies. At this point, we need to divert our attention for a moment to the response of the spectrometer. If a signal $\mathcal{E}(t)$ is sent as input to a spectrometer, the monochromator diffracts the signal and depending on the spectral resolution $\Delta\omega$, introduces a time spreading $\tau_m \approx \frac{5.6}{\Delta\omega}$ [75]. So, the spectrally resolved output of the monochromator can be written as:

$$\mathcal{E}(\omega, t) = \int_{t-\tau_m}^{t} \mathcal{E}(t') e^{-i\omega(t-t')}\, dt' \tag{2.4.12}$$

The signal intensity detected in the CCD, $I(\omega, t)$ can be written as:

$$
\begin{aligned}
I(\omega,t) &= \left[\mathcal{E}_r(\omega,t) + \mathcal{E}_s(\omega,t) + \text{c.c.}\right]^2 \\
&= 2\left[|\mathcal{E}_r(\omega,t)|^2 + |\mathcal{E}_s(\omega,t)|^2 + 2\mathcal{R}\left(\mathcal{E}_r^*(\omega,t)\mathcal{E}_s(\omega,t)\right)\right]
\end{aligned}
\tag{2.4.13}
$$

where we ignored the terms oscillating at high frequency 2ω. The last term in this equation contains $I_{int} = \mathcal{E}_r^*(\omega,t)\mathcal{E}_s(\omega,t)$. This is the interference term, which is of relevance for detecting the FWM signal. Since the pulse duration of the reference and the signal is much smaller than the repetition period of the laser τ_{rep}, only contributions from the same value of n in equation 2.4.10 and 2.4.11 takes part in interference in the spectrometer. The interference signal is integrated in the CCD over an exposure time T_e (usually between hundreds of μs to a hundreds of ms). The number of repetitions within T_e can then be given by: $N = \frac{T_e}{\tau_{rep}}$. Taking these considerations in mind and using equation 2.4.10 and 2.4.11, the time integrated interference intensity can be written as:

$$
\begin{aligned}
I_{int}^{l_1,l_2}(\omega) &= \int_0^{T_e} I_{int}^{l_1,l_2}(\omega,t)\,dt \\
&= I_{single}^{l_1,l_2}(\omega)\sum_{n=0}^{N-1} e^{i\omega_0(1-l_1-l_2)n\tau_{rep}} e^{-i(l_1\Omega_1+l_2\Omega_2-\Omega_d)n\tau_{rep}}
\end{aligned}
\tag{2.4.14}
$$

where,

$$
\begin{aligned}
I_{single}^{l_1,l_2}(\omega) = &\int_{-\infty}^{\infty} dt' \int_{t'-\tau_m}^{t'} e^{i\omega(t'-t_r)}\,dt_r \\
&\int_{t'-\tau_m}^{t'} dt_s e^{i\omega(t'-t_s)} A_r^*(t_r) A_s^{l_1,l_2}(t_s) e^{i\omega_0[t_r-(l_1+l_2)t_s]}
\end{aligned}
\tag{2.4.15}
$$

We can deduce from these two expressions, that signal fields with $l_1 + l_2 = 1$ are the only ones contributing to the time integrated interference term. Fields with frequencies other than the reference frequency ω_0 (second harmonics from example), oscillates with multiples of ω_0 frequency and averages out to 0. Under this condition, the summation term in equation 2.4.14 can be simplified as:

$$
\sum_{n=0}^{N-1} e^{-in\phi_0} = \frac{sin(\frac{N\phi_0}{2})}{sin(\frac{\phi_0}{2})} e^{\frac{-i(N-1)\phi_0}{2}} \tag{2.4.16}
$$

where, $\phi_0 = (l_1\Omega_1 + l_2\Omega_2 - \Omega_d)\tau_{rep} = \Omega_i\tau_{rep}$. This is the same expression as the far field diffraction of N slits. The maxima of this function is at $\phi_0 = 2\pi m$, which

translates into $\Omega_i = m\Omega_{rep}$, where m is an integer and $\Omega_{rep} = \frac{2\pi}{\tau_{rep}}$. Around the maxima, the expression of the sum has the form of the sinc function: $\frac{sin(x)}{x}$, with $x = \frac{T_e(\Omega_i - m\Omega_{rep})}{2}$. It is clear that, the signal gets heavily suppressed for $\Omega_i - m\Omega_{rep} > \frac{4}{T_e}$, .

The total interference term is a sum of all possible responses $I_{int}^{l_1',l_2'}$. Since the pulse duration of the beams T_p ($\approx 100\ fs$) is much smaller than the repetition period of the laser τ_{rep} ($80\ MHz$), the interference has sidebands with separation Ω_{rep} between them. As a result, Ω_i is only defined modulo Ω_{rep}. The driving frequencies of the beam preparation AOMs, Ω_1 and Ω_2 can be chosen in the hundred of MHz range. Hence, Ω_i corresponding to different l_1, l_2 combination can be made to differ in MHz range. This frequency separation between the responses is large enough for the desired response to be isolated and collected. By choosing the driving frequency of the detection AOM $\Omega_d = l_1\Omega_1 + l_2\Omega_2$, we can make sure that only the interference contribution $I_{int}^{l_1,l_2}$, corresponding to a particular l_1, l_2 survives and all other contribution is suppressed by a factor $T_e\Omega_i' > 10^6$. For the detection of two pulse FWM signal described in the theoretical background section of this chapter, we need to take $l_1 = -1, l_2 = +2$ or $\Omega_d = 2\Omega_2 - \Omega_1$. If the detection AOM is driven at the pump frequency Ω_1 or the probe frequency Ω_2, then we can detect only the pump and the probe, respectively, while canceling out all other signals [75, 84].

Dual balanced detection

Referring to equation 2.4.13, the square terms $|\mathcal{E}_r(\omega,t)|^2$ and $|\mathcal{E}_s(\omega,t)|^2$ are detected by the spectrometer, along with the interference term. In order to detect only the weak interference term, it is imperative to cancel out the non-interfering terms and any remaining unwanted background signal. The geometry of the beams at the detection AOM is specifically designed to achieve this.

The focusing of the pump-probe and reference beams at different locations on the sample leads to an angular dependence at the detection AOM. It is done in a precise way to make the pump-probe-FWM signal beams and the reference beam incident on the AOM at Bragg angle, but incident from opposite sides of the optical axis. In other words, if the incidence angle for pump-probe-FWM signal beams is θ_{Br}, the incidence angle for the reference beam can be written as $-\theta_{Br}$. This geometry results in the FWM signal experiencing a frequency down-shift by Ω_d and an up-shift by the same amount for the reference. We know that initially the FWM signal

with ω_0 center frequency is modulated at frequency $2\Omega_2 - \Omega_1$ for two pulse FWM and the reference beam carries just the optical frequency ω_0 without modulation. If $\Omega_d = 2\Omega_2 - \Omega_1$, then the Bragg angle geometry results in the diffracted part of the FWM signal with frequency ω_0 becoming superimposed on the transmitted part of the reference with the same frequency. At the same time, the diffracted part of the reference (modulated at frequency $2\Omega_2 - \Omega_1$) becomes superimposed with the transmitted part of the FWM signal with the same frequency. So, in the CCD image, there will be two interferograms vertically shifted from each other. Any other signal fields with different frequencies (linear reflections and so on) do not contribute to the interference. An example of such heterodyning leading to the selection of an interfering signal is shown in figure 2.10, where the interference is provided by the probe and reference and the detected at the probe frequency Ω_2. Using the case where the probe is being detected at the detection AOM aids significantly in the visualisation of the intricacies of the technique. Subsequent description and figures related to the detection process are equally applicable for detecting the FWM signal, probe and pump beam.

In figure 2.10, I_U is the "upper" interferogram, resulting from the mixing of the diffracted probe signal and the transmitted reference. The "lower" interferogram I_L is the result of the mixing of transmitted probe signal and diffracted reference signal. The key aspect to notice here is that the interferograms I_U and I_L contain order -1 and $+1$ diffracted beams from the AOM and as such has a phase difference of π between them. By a simple subtraction of I_L from I_U, we can cancel out most of the non-interfering signals and get the interferogram $I = I_U - I_L$.

Since I_U and I_L are imaged at different locations on the CCD, any inhomogeneity in the CCD response can lead to inefficient background cancellation. In order to address this issue, the phase of the driving signal of the AOM can be manipulated. As mentioned before, the FWM signal can be exceedingly weak compared to the background signals that co-propagates along with it. A large number of exposures (each of time T_e) need to be taken to achieve a good signal to noise ratio of FWM signal. Let's consider the case where an offset phase (ϕ) is introduced in the driving RF signal of the detection AOM and cycled between 0 and π, for successive exposures. We can denote the upper and lower interferogram for $\phi = 0$ as I_U^+, I_L^+ and for $\phi = \pi$ as I_U^- and I_L^-, respectively. In a given measurement, for the first exposure with $\phi = 0$, the first subtraction (as shown in figure 2.10) will give us $I^+ = I_U^+ - I_L^+$.

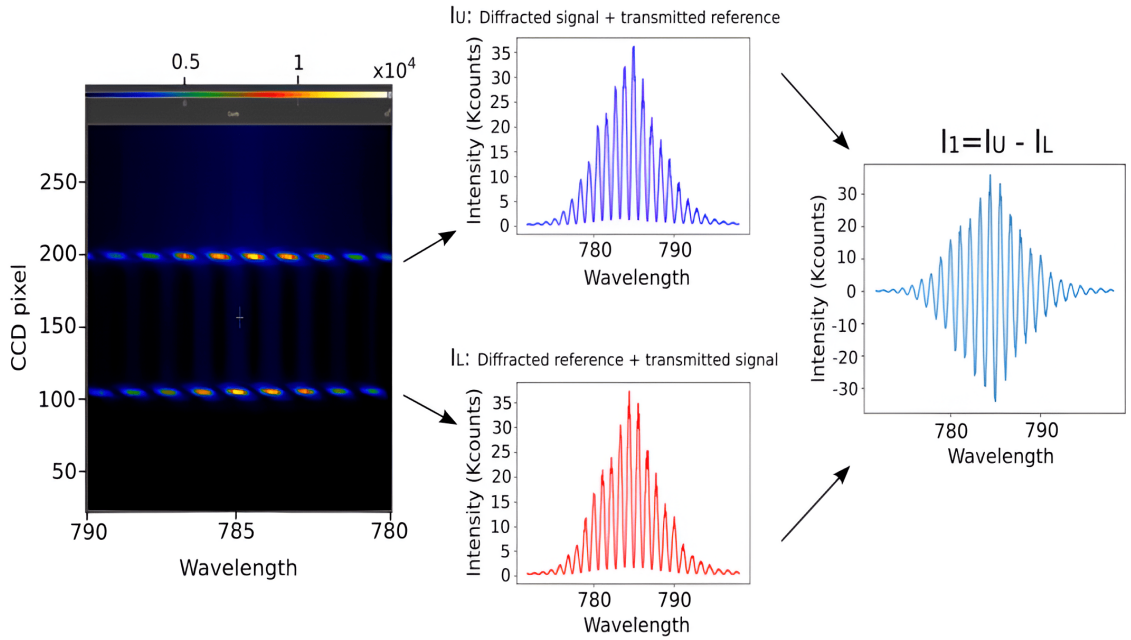

Figure 2.10: CCD image of two interferograms coming out of the detection AOM driven at the probe frequency Ω_2, followed by the interference spectra. The color scale shows the intensity in the CCD image. I_U : interferogram resulting from the mixing of diffracted probe and transmitted reference. I_L : interferogram from diffracted reference and transmitted probe. $I_1 = I_U - I_L$: the interferogram resulting from the subtraction of I_L from I_U.

For the second exposure with $\phi = \pi$, we will have $I^- = I_U^- - I_L^-$. The resultant interferograms I^+ and I^- will have a π phase difference as well. This will allow us to subtract I^- from I^+ and get a double subtracted interferogram $I_d = I^+ - I^-$. This is referred to as dual balanced detection. The output interferogram I_d will be free of any non-interfering beams co-propagating with the FWM signal and also cancel out any unwanted effect stemming from an inhomogeneous response of the CCD. Such procedure is repeated a large number of times and a series of double subtracted interferograms, I_d are obtained. Summing these interferograms will deliver a high signal to noise ratio. This sum can be expressed as: $I_d^s = \sum_{e=1}^{P} I_{de}$, where P is the number of pairs of measurements. In the next section, the procedure to extract the

FWM signal amplitude and phase from the interferograms will be described. This procedure can be applied directly on the sum I_d^s. Alternatively, it can be applied on the interferograms I_{de} from each pair of exposures and the signal can be summed subsequently. As will be discussed, treating the interferograms I_d individually before summing them can provide an opportunity to correct for any effect stemming from unwanted fluctuations in the relative phases of the laser beams [75, 83].

FWM amplitude and phase extraction

The FWM signal amplitude and phase extraction from double subtracted interferograms is done using Fourier transform spectral interferometry (FTSI). As mentioned before, this process is applicable on I_{de} or I_d^s. Figure 2.11a shows an example of a double subtracted interferogram obtained from the interference of probe and reference beams.

Referring to the beam preparation section, the reference beam is leading the probe by a delay of $\tau_r \approx 2$ ps. Since the signal is emitted as soon as the probe arrives on the sample, the reference keeps the same phase difference with the FWM signal as it does with the probe, resulting from the delay ($e^{-i\omega_0\tau_r}$). Considering this phase shift, the spectral interference I_{de} can be written as:

$$I_{de}(\omega) = 2\mathcal{R}\ (\mathcal{E}_r(\omega)\mathcal{E}_s(\omega))e^{i\omega\tau_r} \tag{2.4.17}$$

Inverse Fourier transforming this expression into the time domain, we get:

$$F^{-1}[I_{de}(\omega)] = f(t-\tau_r) + f(-t-\tau_r) \tag{2.4.18}$$

where, $f(t)$ is the correlation product of the reference field and the FWM signal field. So, the inverse Fourier transform result is the sum of two correlation products, one centered at $t = \tau_r$ and the other at $t = -\tau_r$. Figure 2.11b demonstrates the inverse Fourier transform of the interferogram from figure 2.11a. We can argue that the signal field obeys the causality principle, meaning it is only emitted after the arrival of the excitation pulses. Considering the center of the last exciting pulse as the time origin, if τ_r is a few times greater than the exciting pulse duration (T_p), then the two correlation terms will not overlap in time. The presence of these two components in time domain is a consequence of the symmetric nature of Fourier transformation. The peak at $t = \tau_r$ represents the interference between the FWM signal and the

reference beam delayed by τ_r, corresponding to real measurement condition, whereas the component at $t = -\tau_r$, is a mirrored artifact. The frequency domain interference is the result of the overlap of these two peaks. The phase of the FWM signal can not be extracted correctly if this artifact is not removed. Multiplying 2.4.18 with a heaviside function $\Theta(t)$ will allow us to extract the relevant term $f(t - \tau_r)$ and a subsequent Fourier transform can deliver the desired complex FWM signal field. Such extraction of both the amplitude and phase of the third order response of a system is in sharp contrast with traditional pump-probe spectroscopy where only the intensity of the nonlinear response is extracted [75].

Additionally, such an analysis in the spectral domain opens possibilities to improve the signal-to-noise ratio. However, instead of using a simple heaviside function, we can apply more than one modified heaviside functions based on appropriate conditions that will improve the signal to noise ratio.

We can introduce a limitations on the heaviside function in a way that only the part of the time domain result that has FWM signal is chosen and the part which contains only noise is filtered out. This will filter out any part of the result at positive time, which contains only noise. We can write this modified heaviside function as:

$$\Theta_1(t) = \begin{cases} 1, & \text{if } t > \tau_r - d_1 T_p \text{ and } t < \tau_r + d_2 T_p \\ 0, & \text{otherwise} \end{cases} \tag{2.4.19}$$

Here, d_1 and d_2 are integers, the values of which can be chosen such that the FWM signal decay at positive time is covered completely. In the second step, we can apply what could be considered a noise filter $\Theta_2(t)$ on the result $I_{\Theta_1}(t) = \Theta_1(t)|F^{-1}I_{de}(\omega)|$. The definition of $\Theta_2(t)$ is done in the following steps: first, a mean value μ of the result $I_{\Theta_1}(t)$ is calculated and any $I_{\Theta_1}(t)$ value greater than μ is discarded. This process is repeated again. The mean value μ and the standard deviation σ of this new data set is used to calculate the second heaviside function as:

$$\Theta_2(t) = \begin{cases} 1, & \text{if } I_{\Theta_1}(t) > \mu + s\sigma \\ 0, & \text{otherwise} \end{cases} \tag{2.4.20}$$

where s is an integer that can be fixed at a value that delivers a good signal to noise ratio. The result obtained after applying the second heaviside function: $\Theta_2(t)I_{\Theta_1}(t)$ or $\Theta_1(t)\Theta_2(t)F^{-1}[I_{de}(\omega)]$ can be Fourier transformed back into the frequency domain

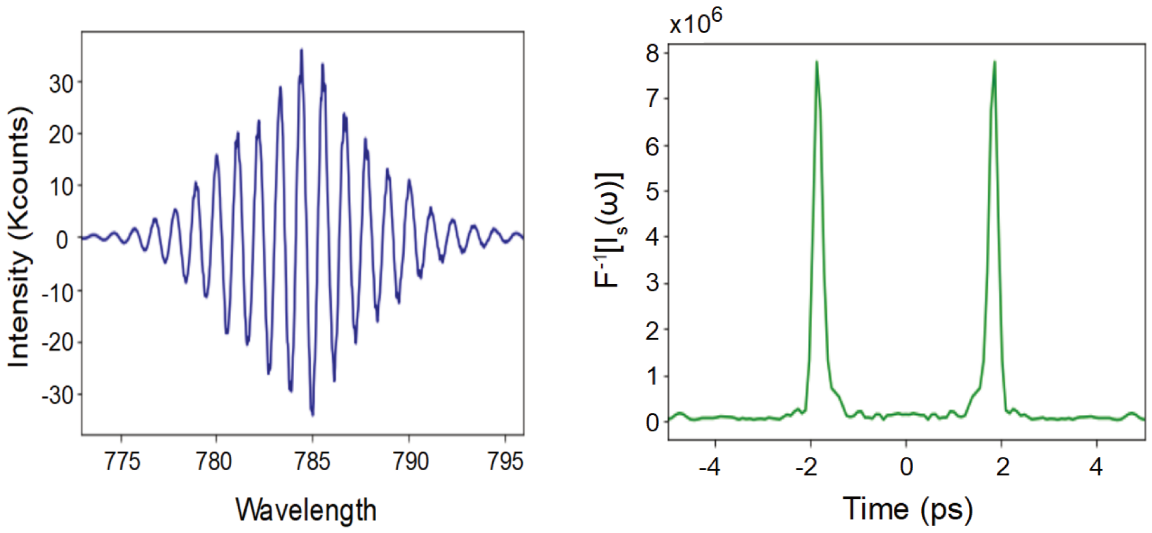

(a)

(b)

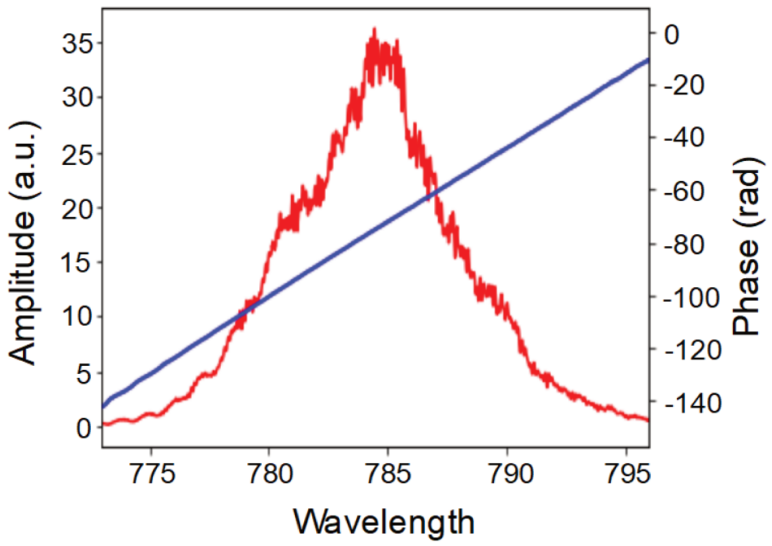

(c)

Figure 2.11: (a) Example interferogram obtained by driving the detection AOM at probe frequency Ω_2 and after performing double subtraction to cancel out the background. (b) Time domain signal: result of Fourier transformation of the frequency domain interferogram. The two components are centered at $t = \tau_r$ and $t = -\tau_r$. For this example, $\tau_r = 2\ ps$ (c) Amplitude and phase of the probe signal extracted after Fourier transforming the time domain component centered at $t = \tau_r$.

and the complex FWM signal can be retrieved completely as:

$$\mathcal{E}_s(\omega) = \frac{F[\Theta_1(t)\Theta_2(t)F^{-1}I_{de}(\omega)]e^{-i\omega\tau_r}}{\mathcal{E}_r^*(\omega)} \tag{2.4.21}$$

The complex FWM signal field $\mathcal{E}_{se}$ extracted from an interferogram I_{de} can be written in the following form:

$$\mathcal{E}_{se} = C_e e^{i\phi_e} \tag{2.4.22}$$

where C_e and ϕ_e are the FWM amplitude and phase, respectively. Figure 2.11c shows the amplitude and phase extracted from the time domain data from figure 2.11b. The phase factor ϕ_e can vary between the interferograms I_{de} for different e or different pairs of measurements.

As described in the beam preparation part of the setup, the beams travel separately through different sets of optics, before recombining in a beamsplitter. This can lead to random changes in the path length of the beams and cause fluctuation in their relative phase, which results in the aforementioned fluctuation in the FWM signal phase ϕ_e. If this effect is strong enough, adding I_{de} for different e directly, without taking into considering the phase fluctuation will lead to a significant decrease in the signal to noise ratio. Since the phase ϕ_e corresponding to each interferogram I_{de} is extracted as described above, their relative phase difference can be corrected. It should be remembered that the absolute value of ϕ is arbitrary and in principle, any absolute value can be imposed on the phases ϕ_e of all I_{de}. If the phase corresponding to the interferogram I_{d1} for $e = 1$ is denoted as ϕ_1, we can correct the phase corresponding to any I_{de}, by multiplying equation 2.4.22 with the factor $e^{i(\phi_1-\phi_e)}$. This phase correction can be done in a similar way in the time domain as well [75, 83, 85]. For most of the data presented in this thesis, phase correction was not necessary, as the phase fluctuation was minimal. However, the phase analysis of the FWM could contain specific information on the system under study (chapter 3 and 4) and it is also the core of the well-known 2D spectroscopy [75, 85, 86].

We will conclude this chapter with an important note regarding the two main decay times that characterize exciton coherence dynamics: the free polarization decay time T_2, associated with homogeneous broadening, and an additional decay rate T_2^*, related to inhomogeneous broadening. For simplicity in this chapter, the decay rates corresponding to homogeneous and inhomogeneous broadening were denoted as $\gamma =$

$\frac{1}{T_2}$ and $\sigma = \frac{1}{T_2^*}$. However, the characterization of homogeneous and inhomogeneous broadening in energy is done by defining the corresponding full width at half maximum (FWHM) as $\gamma = \frac{2\hbar}{T_2}$ for a Lorentzian decay, and $\sigma = \frac{\hbar\sqrt{8\ln 2}}{T_2^*}$ for a Gaussian decay. From this point on, we will adopt this definition of γ and σ.

3 Dynamics of anisotropic excitons in rhenium disulfide (ReS_2)

3.1 Introduction

In this chapter, the FWM microscopy experimental results obtained from excitons in Rhenium disulfide (ReS_2), will be described. Some of the fundamental properties of ReS_2 were introduced in Chapter 1. This group-7 Transition Metal Dichalcogenide (TMD) has a strong in-plane anisotropic structure stemming from its distorted octahedral phase (1T′) and reduced symmetry. The Jahn-Teller like structural distortion, along with a zigzag Re-Re chain-like structure along the crystallographic axis (b-axis), give rise to a pair of anisotropic excitons within the 2D plane of the ReS_2 lattice. These excitons naturally exhibit quasi-one-dimensional features without the need for strain engineering [20, 22–24, 65, 66, 87, 88]. The anisotropic characteristics of ReS_2 remain stable under ambient conditions, in contrast to other anisotropic materials like black phosphorus, which degrades under similar conditions [25,26]. This stability makes ReS_2 an interesting candidate for polarization-sensitive optoelectronic applications [27, 89]. Furthermore, unlike traditional MX_2 compounds that exhibit direct bandgap exciton transitions only in the monolayer limit [59, 90], ReS_2 demonstrates a persistent excitonic optical response even as the number of layers increase. This is due to the weak interlayer coupling, which ensures that the band structure remains largely independent of the number of layers, resulting in a monolayer-like electronic structure even in bulk ReS_2 Yet, the fundamental question of whether the gap is truly direct or indirect is the subject of active debate to date [68, 69]. Similarly, the origin of the anisotropic properties in ReS_2 continues to be under investigation, specifically whether the excitonic species originate from a single high-symmetry point of the Brillouin zone or from two different valleys related by space inversion [67–69]. In this context, time-resolved experiments can provide valuable insights. Earlier reports with time-resolved photoluminescence (PL) or non-resonant pump-probe measurements have identified exciton population decay timescale within 10 - 100 ps [70, 91–93], but these methods are limited by their temporal resolution or the involvement of charge relaxation pathways that lead to exciton formation, which may obscure the observa-

tion of intrinsic excitonic dynamics. Moreover, excitonic linewidths in bare MX_2 are largely dominated by inhomogeneous contributions [28, 50, 94]. Even after hexagonal boron nitride (hBN) encapsulation, local disorder in MX_2 still persists owing to their nanoscale strain gradients, dielectric disorder, unintentional doping or atomic reconstruction [29–31]. The extent to which such disorder contributes to the excitonic linewidth in ReS_2 is still an open question. Similarly, the coherence properties have not been explored for low-dimensional anisotropic semiconductors including ReS_2. To address all these questions, resonant four-wave mixing (FWM) spectroscopy is particularly suitable [28, 50], which provides direct pathway to investigate the dynamics of exciton coherence and population by resonantly exciting specific optical transitions. Since the exciton anisotropy varies with the orientation (b-axis) and thickness of each ReS_2 flakes [27, 64, 67, 95], a microscopic approach is also essential.

Using FWM microscopy, we explored the coherence and population dynamics of anisotropic excitons in ReS_2, with respect to several environmental conditions, including temperature, excitation power, flake location, and thickness. Our study found that the coherence time (T_2) for excitons in ReS_2 is on the order of hundreds of femtoseconds. Notably, this coherence time remains remarkably robust despite variations in temperature and excitation power. The excitonic linewidth is primarily homogeneously broadened, suggesting a minimal level of disorder in bare ReS_2. These characteristics distinguish ReS_2 from other layered semiconductors. Furthermore, the population dynamics of anisotropic excitons in ReS_2 display a complex decay behavior, with multiple exponential components that range from approximately 150 femtoseconds to several nanoseconds. This kind of population dynamics arise from scattering between bright and dark excitons states. These results underscore the unique properties of ReS_2, making it a promising candidate for ultrafast optoelectronic applications and advanced photonic devices, where both stability and low disorder are critical for performance. Importantly, these intrinsic dynamics are consistent with a direct bandgap, regardless of the number of ReS_2 layers.

3.2 Sample description and initial characterization

The ReS_2 sample under consideration here, was fabricated using a traditional bottom-up approach. We selected a commercially available quasi-transparent flat Sapphire substrate, which was first cleaned using Argon plasma for two minutes to ensure a

pristine surface before proceeding with the sample preparation. The ReS_2 flakes were mechanically exfoliated from commercially available bulk crystal (purchased from "2D semiconductor"), using standard scotch tape. After obtaining many flakes of varying thickness (from a few layer to bulk), these flakes were directly transferred onto the cleaned sapphire substrate. This transfer method ensures that the ReS_2 maintains its structural integrity and uniformity.

Following the transfer process, the ReS_2 flakes went through a detailed identification and thickness characterization process. We used a white light optical microscope to initially identify the flakes and assess their overall quality. For precise thickness measurements, we used an atomic force microscope (AFM), which provided accurate topographical information and gave us an estimation of the number of layers for the flakes of interest. This meticulous preparation and characterization process ensured that the ReS_2 samples were suitable for subsequent experiments.

Initial characterization before proceeding to FWM measurement on ReS_2 excitons, started with extensive white light imaging of the sample. An are of the sample was chosen for measurement that contained flakes with different contrast which suggests different thickness. Subsequent Atomic Force Microscopy imaging revealed the thickness of the flakes in that area accurately. Figure 1.1a shows the white light image of the flakes chosen for measurement. Six different flakes of varying thickness are marked with dotted line and designated as flake-1 to flake-6. The AFM image of the same area is demonstrated in figure 1.1b, with the height profiles represented by the color scale. The flakes vary in thickness from bulk-like (Flake-1) to monolayer (Flake-6). The thickness data extracted from AFM measurement for flake-1 to 6, allowed their classification as bulk-like (green), multilayers (black), few-layers (blue), 3-4 layered (brown), 2-3 layered (yellow), and 1-2 layered (pink) flakes, respectively.

The optical emission from these layered ReS_2 flakes is primarily dominated by excitonic transitions. The exciton resonances were initially identified through hyperspectral photoluminescence (PL) imaging (figure 1.1c) of the area shown in the white light and AFM images. An example spectrum from this PL map (flake-2) is presented in figure 1.1d, which highlights two prominent peaks. These peaks correspond to the anisotropic excitons denoted as EX1 and EX2, observed at approximately 1.54 eV and 1.57 eV, respectively. Such PL spectra were collected from all the six flakes shown in figure 3.1a. A comparison of these PL spectra are demonstrated in figure 3.2a.

Next, once EX1 and EX2 were characterized by PL, we performed FWM mi-

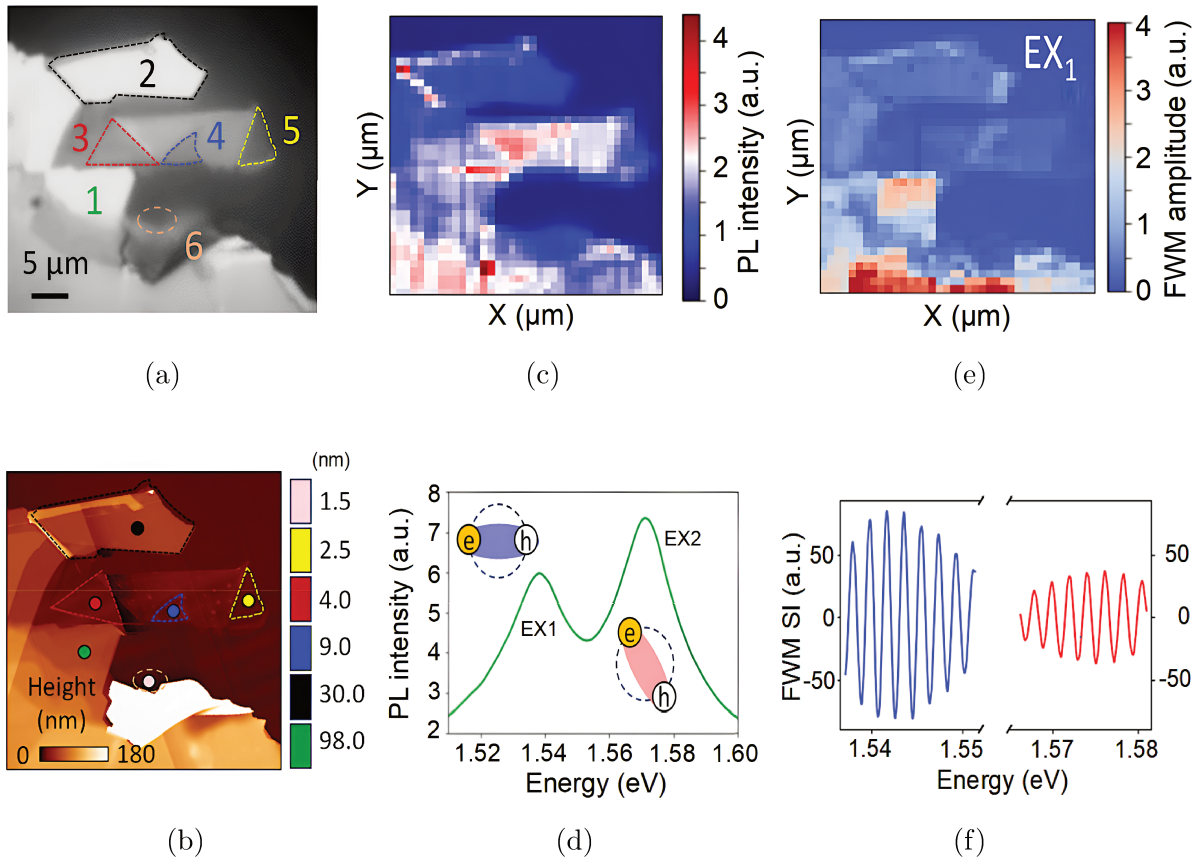

Figure 3.1: Basic morphological and optical characterizations of layered ReS_2. (a) White light image of mechanically exfoliated ReS_2 flakes with different thickness marked as flake-1 to flake-6. (b) Atomic force micrograph of the ReS_2 flake locations with corresponding colour bar denoting height profiles of individual flakes marked with individual colours (vertical) and overall height profiles (horizontal). (c) Hyperspectral PL map (77 K) of the same flakes with the associated colour scale. The step size is 1 μm. (d) Typical PL spectrum (flake-2) highlighting the two lowest energy optically bright excitons (EX1 and EX2) with schematic representation in the inset. (e) Hyperspectral map of FWM amplitude of the ReS_2 flakes at $\tau_{12} \approx 0$ for EX1 (f) Example of FWM signal: spectral interferograms for EX1 (blue line) and EX2 (red line) obtained at resonant excitonic energies recorded for $\tau_{12} \approx 0$.

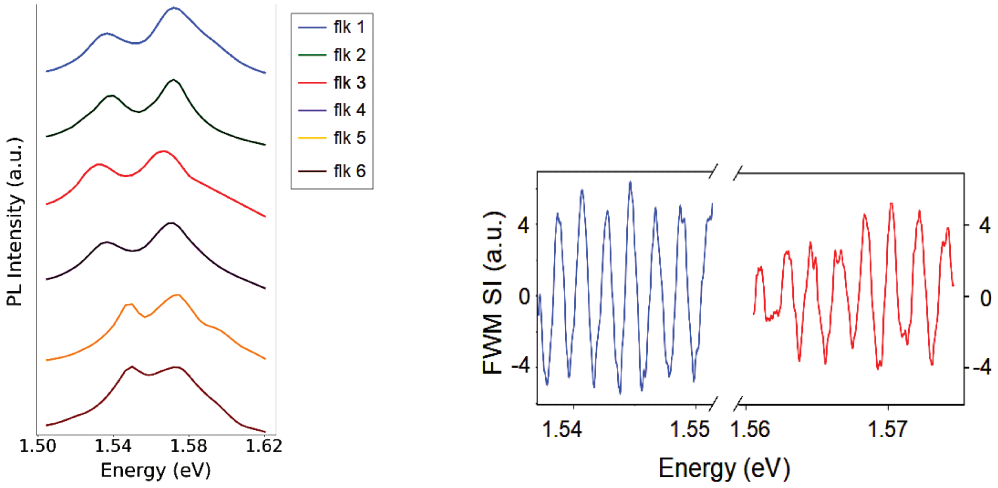

(a) (b)

Figure 3.2: (a) Comparison of PL spectra among the six flakes on the sample: flake-1 (bulk-like) to flake-6 (monolayer). (b) Example of FWM signal for flake 6 (monolayer): spectral interferograms for EX1 (blue line) and EX2 (red line) obtained at resonant excitonic energies recorded for $\tau_{12} \approx 0$.

croscopy (details in chapter 2) to investigate their coherent dynamics. Similar to the hyperspectral PL map, a hyperspectral FWM (two pulse) amplitude map is shown in figure 1.1e. For this map, the FWM signal was measured resonantly at pump-probe delay $\tau_{12} = 0$, over the chosen flakes. The FWM amplitude for each point on the map, is obtained by integrating over the linewidth of each exciton and shown with the corresponding colour scale. Example of FWM spectral interference (dual balanced) detected from EX1 and EX2 in flake-2, is presented in figure 1.1f. A similar example for flake-6 is demonstrated in figure 3.2b.

The FWM signal strength from the excitons in ReS_2 is dependent on the linear polarization orientation of the excitation beams, as a result of the in-plane aniostropy in ReS_2. To optimize the FWM signal for each exciton, we first analyzed the linear polarization resolved FWM signal in the two-pulse configuration at $\tau_{12} = 0$, and determined the local dipole orientations under resonant conditions for EX1 and EX2. The FWM amplitude as a function of the excitation polarization angle is demonstrated in figure 3.3a, for both excitons. In this figure, the blue and red dots represent the FWM amplitude for EX1 and EX2, respectively. The signal exhibits a $\cos^4(\theta - \theta_0)$ behaviour, where θ is the excitation polarization angle. This behavior is due to the

FWM amplitude scaling with the third-order nonlinear susceptibility (χ^3) and the fourth power of the projection of the signal with the reference beam field. We observe a difference of about 70° in the orientation of the two linear dipoles, consistent with prior findings [19].

3.3 Coherence dynamics

Following the initial characterization and optimization of FWM signal, the measurement of the excitonic coherence dynamics will now be presented, as a function of pump-probe delay τ_{12}. Decoherence occurs as a result of the inherent homogeneous broadening of the excitonic transition, as well as inhomogeneous broadening stemming from disorder in the local environment, characterized by the linewidths γ and σ, respectively. FWM microscopy provides a rather unique opportunity to decipher the contributions from these mechanisms. In order to determine if the inhomogeneous contribution is significant with respect to its homogeneous counterpart, we look at the ratio $\frac{\sigma}{\gamma}$, at 10 K temperature where it is expected to be the highest. This ratio can be determined from the evolution of FWM amplitude as a function of real time variable t and the pump-probe delay τ_{12}. This 2D plot is obtained by Fourier transforming the detected interference between the FWM signal from the excitons and the reference beam (details of the detection scheme is provided in chapter 2). Strong inhomogeneous broadening would manifest itself as a clear signature of photon echo in the $t-\tau_{12}$ plot, i.e., maximum FWM amplitude would follow the diagonal line $t = \tau_{12}$. Figure 3.3d and 3.3e show such plots at 10 K for EX1 and EX2, respectively, for the multilayer flake-2. Remarkably, we do not observe photon echo formation for either exciton (no diagonal FWM amplitude), as demonstrated. Instead, the signal evolves as free induction decay, indicating a weak inhomogeneous contribution to coherence decay and satisfying the condition $\sigma \ll \gamma$. Next, we estimate an upper bound for the value of σ, that can be used in the fitting of FWM amplitude vs τ_{12} data and extract the decoherence time, T_2. For this purpose, equation 2.3.44 (chapter 2) was used to simulate the FWM amplitude 2D plots, corresponding to the experimental data and roughly determine σ. This equation assumes the delta pulse condition. The simulated plots for EX1 and EX2, corresponding to figure 3.3d and 3.3e are shown in figure 3.3g and 3.3h, respectively, along with the obtained value of γ and σ. As is evident, the simulations confirm the validity of the assumption $\sigma \ll \gamma$. Figure

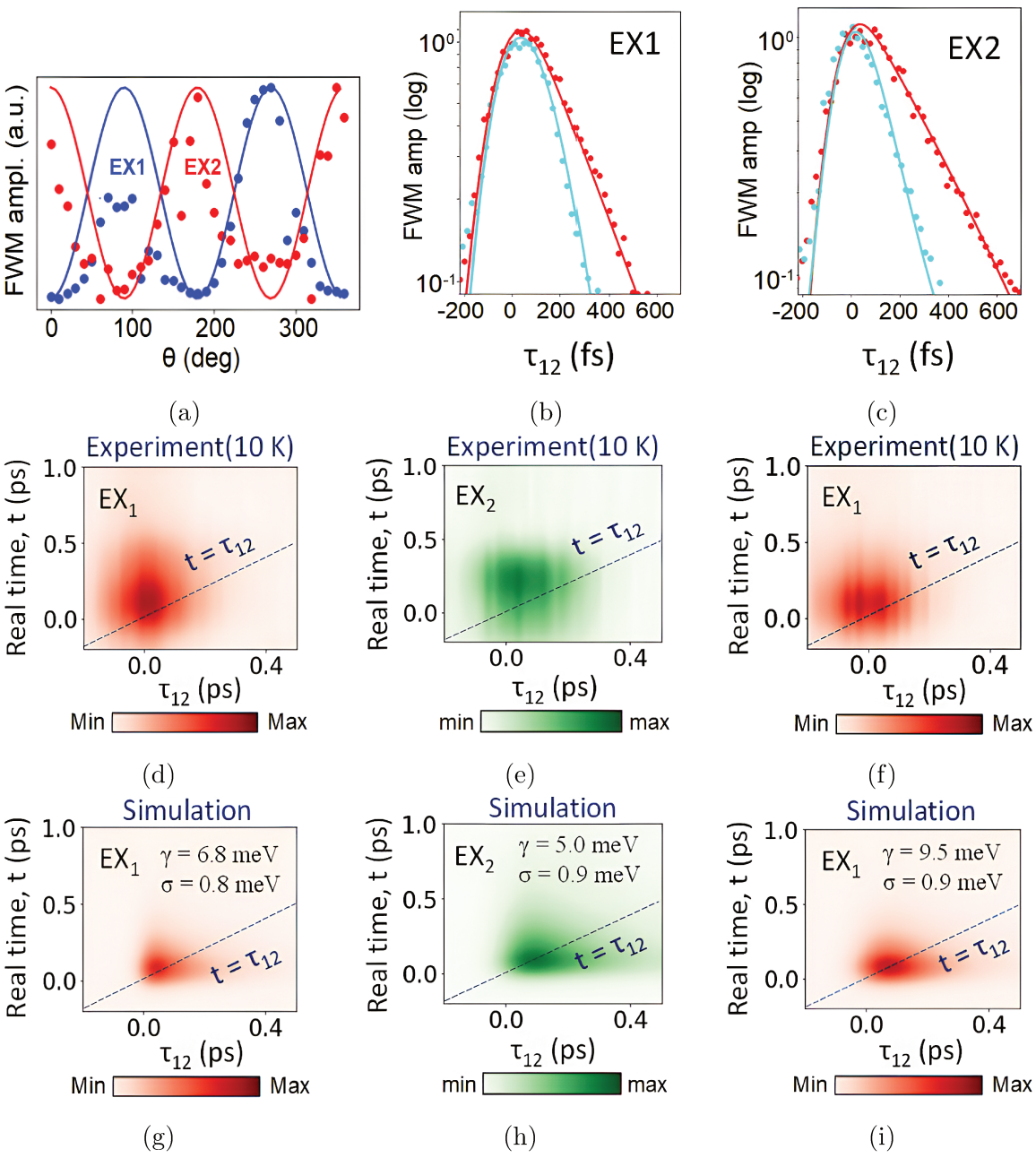

Figure 3.3: (a) FWM amplitude, at $\tau_{12} = 0$, as a function of linear polarization angle (identical for pump-probe) for both EX1 (blue dots) and EX2 (red dots) with the corresponding fits (solid lines). Examples of FWM amplitudes versus τ_{12} presented for (b) EX1 and (c) EX2 at 10 K temperature and ≈ 64 W/cm^2 pump power density along with the corresponding fits (solid lines) for monolayer (cyan) and multilayer (red) ReS_2 flake. Measured FWM amplitude as a function of real time t and delay τ_{12} for (d) EX1 flake-2 and (e) EX2 flake-2 (f) Ex1 flake-6, respectively. The corresponding simulations for these three cases are shown in (g), (h) and (i), respectively.

3.3f and 3.3i displays the experimentally obtained and simulated FWM amplitude 2D plots, respectively for EX1 in flake-6, which is the flake of lowest thickness in the sample. It is clear that σ remains negligible and independent of flake thickness, with an upper bound of $\sigma \leq 1$ meV.

The FWM amplitude vs τ_{12} data was fitted with the convolution of equation 2.3.46 (chapter 2), with a Gaussian pulse shape and considering the upperbound of σ. Figure 3.3b and 3.3c demonstrate examples of such fitting for EX1 and EX2, respectively, where, the red (cyan) color corresponds to multilayer flake-2 (monolayer flake-6). The validity of the upper bound of σ was confirmed by the consistent fit quality. The homogeneous linewidth γ extracted from the fit for both excitons are ≈ 5 meV and ≈ 8 meV, for flake-2 and flake-6, respectively, with $\sigma \leq 1$ meV. In contrast, conventional MX2 exhibits such behavior only when fully encapsulated in thick hBN [30, 31]. Comparatively, in bare monolayer MoSe2 [30], σ ranges between 7 to 15 meV.

Evolution of γ with environmental parameters

Now that γ is extracted reliably from the two pulse FWM data, we can discuss about the detailed evolution of γ as a function of various environmental conditions, as summarized in figure 3.4. We examine the behavior of γ with respect to temperature, excitation power, flake locations, and flake thickness. The first noticeable aspect is the resilience of the excitonic coherence with respect to sample temperature (T) and the resulting increase in exciton-phonon interaction. Examples of FWM dynamics on multilayer flake-2 with respect to temperature variation for EX1 and EX2, are shown in figure 3.3a and 3.3b, respectively, while $\gamma(T)$ for these excitons are presented in figure 3.3c and 3.3d. Remarkably, the coherence dynamics remain discernible, although approaching our time resolution ($\approx$ 100 fs) even at room temperature. This contrasts sharply with MX_2 systems, where the dynamics becomes unresolveable above approximately 120 K, measured with similar temporal resolution [28–31]. This highlights a particular robustness of the excitons in ReS_2 against temperature-induced decoherence. The thermal broadening of homogeneous linewidth, $\gamma(T)$ can be analyzed in detail using the follwing expression:

$$\gamma(T) = \gamma_0 + \alpha T + \beta \left(\exp\left(\frac{E_0}{K_B T} \right) - 1 \right)^{-1} \tag{3.3.1}$$

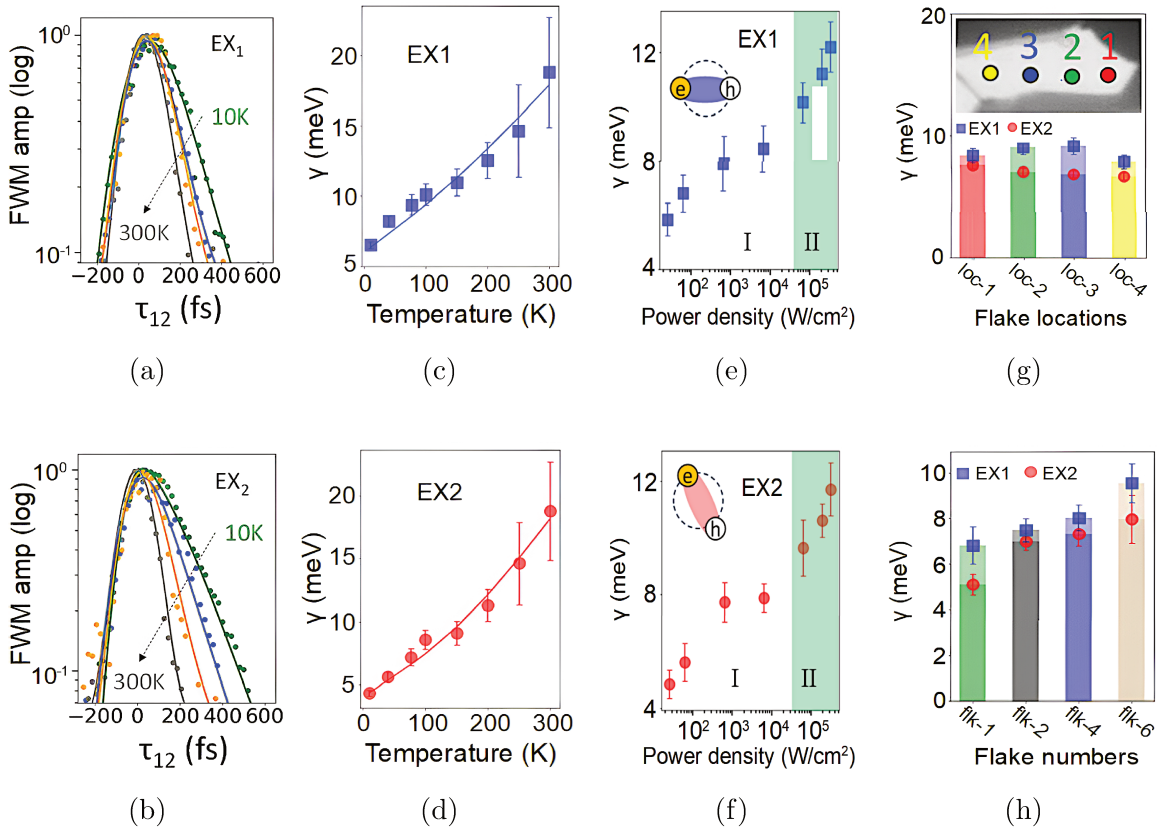

Figure 3.4: Coherent dynamics of anisotropic excitons in layered ReS_2. (a) EX1 and (b) EX2 FWM amplitude vs τ_{12} presented for several temperatures from 10 K to 300 K, along with the corresponding fits (solid lines) on flake-2. Variation of homogeneous linewidth, γ with corresponding fits for (c, e) EX1 and (d, f) EX2 in function of temperature and power density, respectively. Temperature dependent measurements shown in figure (c and d) are performed at fixed $\approx$ 64 W/cm^2 pump power density. Solid lines denote temperature induced dephasing fits. Power dependent measurements shown in figure (e and f) were performed at fixed temperature: 10 K. Region I (white shaded area) and II (green shaded area) show two distinct linear behaviour with different slope. Inset of (e and f): schematic images of in-plane anisotropic excitons in ReS_2 with different dipolar orientations. (g) Distribution of γ for different locations on flake-2 along with the inset showing different locations of measurement on flake-2 that matches with the colour codes of corresponding bars. (h) Homogeneous linewidth (γ) for EX1 (blue) and EX2 (red) in function of flake numbers at 10 K and $\approx$ 64 W/cm^2 pump power density.

where γ_0 is the homogeneous linewidth limit at zero temperature, E_0 is the thermal activation energy and K_B is the Boltzman constant ($1.38\times$ 10^{-23} J/K). The 2nd and 3rd terms in this expression represent the contributions of low-energy acoustic phonons and high-energy optical phonons, characterized by the corresponding scattering coefficients α and β, respectively. Equation 3.3.1 describes how increasing temperature causes homogeneous linewidth broadening or faster coherence decay as a result of the exciton-phonon scattering. The linear dependence of γ on T for acoustic phonons stems from the assumption that the energies of interacting acoustic phonons, constrained by momentum conservation, are less than the thermal energy k_BT. As is shown from figure 3.3c and 3.3d, $\gamma(T)$ exhibits an exceptionally linear behavior even up to room temperature. The extracted value of γ_0 is 5.8 ± 0.9 meV and $\approx 3.9 \pm 0.8$ meV for EX1 and EX2, respectively. For both EX1,2, the value of the acoustic-phonon scattering coefficient α is extracted to be $\approx 33 \pm 15$ μeV/K. The pronounced linear behavior of $\gamma(T)$ in ReS_2 is noticeably different from the well-reported parabolic trend of $\gamma(T)$ in MX_2 [28–31].

On the other hand, the optical phonon contribution to homogeneous linewidth broadening can be fitted with several pairs of E_0 and β, with E_0 varying from 50 meV to 200 meV and β ranging from a few meV to 2 eV. Based on a recent estimation of E_0 [18], we limited E_0 at around 50 meV and, from fitting, extracted it to be 61 (44) meV, with β being 5.0 ± 2.6 (6.3 ± 1.1) meV for EX1(2). The extracted value of the optical phonon coupling (β) in ReS_2 is approximately 30 times lower than in $MoSe_2$ and WSe_2 monolayers [28,30] for similar activation energy and acoustic phonon coupling strength, demonstrating once again the robustness of ReS_2 excitonic coherence against an increase in temperature. The pronounced linear behavior of $\gamma(T)$ observed for ReS_2, caused by relatively weak optical phonon coupling, is surprisingly similar to what has been reported for single-walled carbon nanotube systems exhibiting exciton-phonon scattering within one-dimensional framework [96,97]. To further understand this unique behavior in the two-dimensional ReS_2, one possible approach of interpreting this behavior ia to consider the quasi-one-dimensional characteristics of the Rhenium (Re) chains in the crystal structure. These chains, a result of the material's strong structural anisotropy, might contribute to the observed exciton-phonon interactions in a manner akin to what occurs in true one-dimensional systems [20,65].

Exciton density is an important parameter that can influence γ. This parameter is controlled directly by the pump power density, P. An increase in P leads to higher

exciton density, which leads to more exciton-exciton and cause excitation induced dephasing (EID) [31, 50]. Studies with power dependent FWM meeasurments have consistently reported a linear trend in $\gamma(P)$ within $10^2 - 10^3$ W/cm^2 for bare and hBN encapsulated MX_2 monolayers [31, 50]. In our measurements for ReS_2, up to 2.5×10^5 W/cm^2, $\gamma(P)$ displays two distinct quasi-linear characteristics, as shown in figure 3.3e and 3.3f, for EX1 and EX2, respectively. This rather unusual behaviour was analyzed, in each region, using a power-law model: $\gamma(P) = \gamma_{P0} + A \times P$, where γ_{P0} is the zero-power linewidth and A is a coefficient which quantifies the strength of exciton-exciton interaction. Under low power conditions (Region-I), A is extracted to be $\approx 5 \times 10^{-4}$ meVcm^2/W at 10 K temperature for both excitons, which is an order of magnitude smaller compared to MX_2 [65], measured with similar pulse length and repetition rate, indicating reduced EID in ReS_2. Similar measurements done at 77 K temperature also exhibit similar behavior, highlighting robust coherence characteristics of EX1,2 against an increase in optical density. We conclude the study of exciton coherence by exploring the variation in γ depending on the measurement location. Figure 3.3g displays γ for both EX1,2 over multiple locations on Flake-2 spanning approximately 10 μm. The extracted γ values exhibit very weak spatial dispersion, demonstrating uniform exciton coherence dynamics behavior across the flake, which once again confirms the measured negligible inhomogeneous broadening (σ). Figure 3.3h demonstrates a comparison of γ for EX1, EX2 in four flakes: flake-1, 2, 4 and 6. As is shown, γ does not change significantly as the flake thickness changes from monolayer (flake-6) to multilayer (flake-2). This once again implies a distinct robustness of the excitonic coherence dynamics in ReS_2.

3.4 Population dynamics

Following the trails of the study of coherent dynamics, a three-pulse resonant excitation scheme (pulses denoted as $P_1,\ P_2,\ P_3$), is employed to examine the population dynamics of excitons EX1 and EX2. When the delay between P_1 and P_2, τ_{12} is set at ≈ 0, the polarization-selective resonant pumping generates an initial population of anisotropic excitons within the light cone. The generated excitons then relax through both radiative and non-radiative channels.

A schematic illustrating these processes is provided in Figure 3.5. To identify the relevant relaxation channels for excitons in ReS_2 and explore the interactions

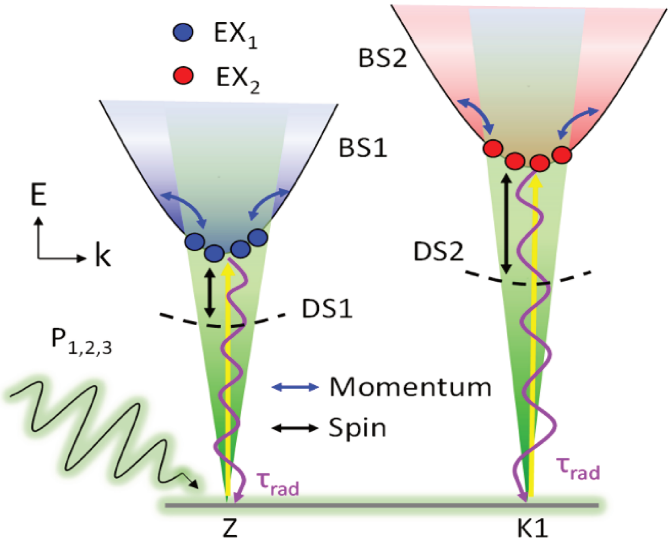

Figure 3.5: Schematic of the energy level dispersion (E, k), including optical transition and scattering processes, under the hypothesis of the two valleys (Z and K1) in ReS_2. BS1,2 refers to the spin-allowed excitonic transition bands comprising the excitonic bright states EX1,2 (red and blue dots), which lie within the light cones (green shaded areas) and are split by 30 meV (see Fig. 1.e). DS1,2 designates the spin-dark states (no direct optical transition allowed), which, according to Ref [68], are located 13 meV (20 meV) below EX1,2. The resonant optical excitations of EX1,2 are depicted as yellow solid lines. From the light cone, EX1,2 excitons can radiatively recombine (purple curved arrow), scatter to momentum-dark states outside the light cone (blue solid line), or scatter to spin-dark states DS1,2 (black solid line).

among them, the population dynamics is analyzed under varying conditions, including different power density, temperature, and flake thicknesses. Figures 3.6c and 3.6d present examples of the population dynamics of EX1 as functions of temperature and power, respectively, over a timescale up to 800 fs. Figures 3.6e and 3.6f show similar data for the full time window of measurement, spanning upto $\approx$ 280 ps. The observed decays suggest that EX1 and EX2 exhibit multi-timescale population dynamics, ranging from hundreds of femtoseconds to nanoseconds. In contrast to MX_2 [39, 98, 99], where transient phase modulations are significant, the population dynamics in ReS_2 show negligible transient phase effects. The population dynamics can be fitted using the equation 2.3.47 (chapter 2), which is derived from a multi-

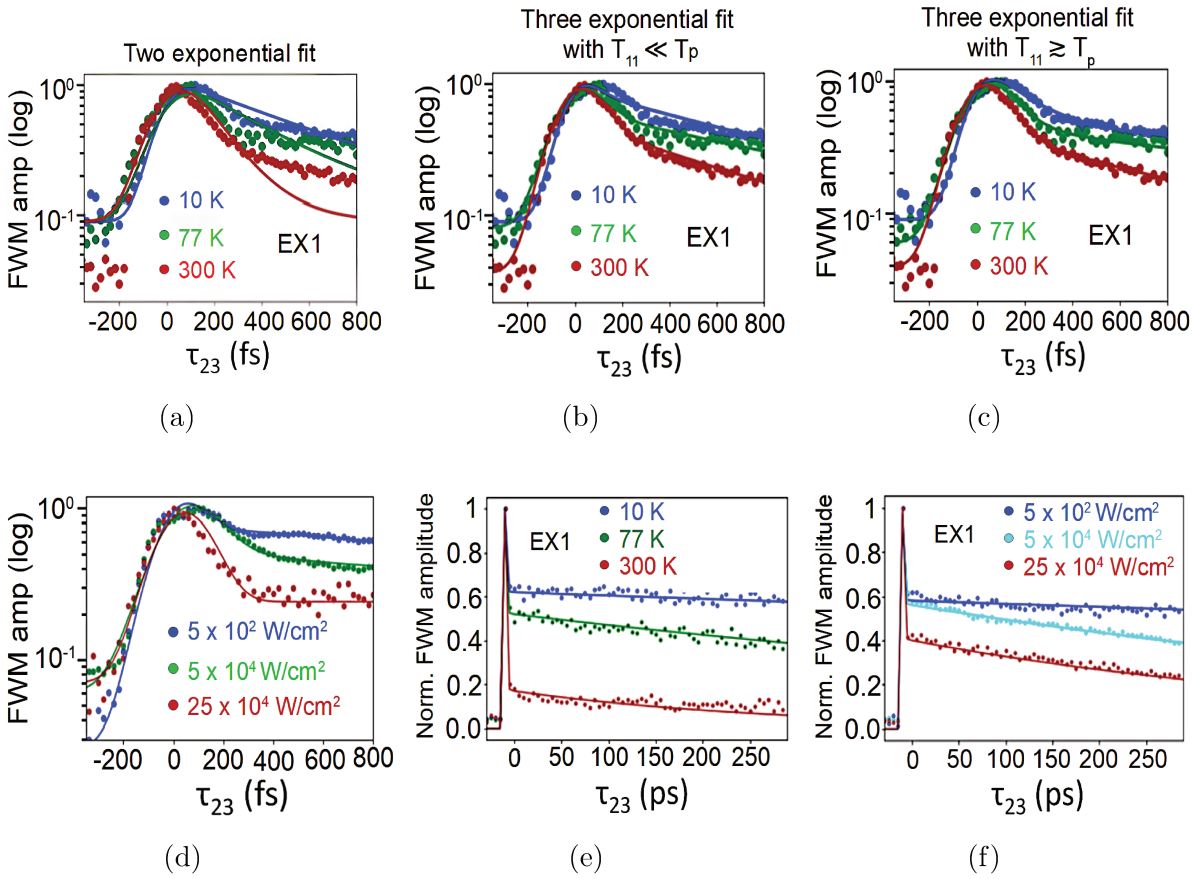

Figure 3.6: Temperature dependent normalized FWM field amplitude data in function of the P_2, P_3 delay τ_{23} (upto 800 fs) for EX1 (flake-2) fitted (solid lines) with three different models: (a) two-exponential fitting, (b) three-exponential fitting, in which the characteristic time of the first component, T_{11} is assumed to be negligible compared to the pulse duration T_p ($T_{11} \ll T_p$) resulting in a Dirac-like response component in FWM amplitude decay vs τ_{23} and finally (c) three-exponential fitting with resolvable first decay component ($T_{11} \gtrsim T_p$). When comparing different fittings, it highlights the accuracy of the three-exponential fits which is applied in subsequent analysis. (d) FWM amplitude vs τ_{23} (upto 800 fs) as a function of excitation power density (P_1). Note that, the last decay component in the population dynamics data extends well-beyond the 1 ps short-range experimental delay window, and contributed as a quasi-constant amplitude term in the fit. This component is precisely determined from the experiments with a large delay range upto ($\approx$ 280 ps). Examples of such FWM amplitude decay is shown as a function of (e) temperature and (f) excitation power density.

exponential transient response function $R(\tau_{23}) \propto \sum_{n=1}^{3} A_n \theta(\tau_{23}) e^{-\frac{\tau_{23}}{T_{1n}}}$, convoluted with a Gaussian pulse, where $\Theta(\tau_{23})$ is the Heaviside function.

The fitting analysis allows for the extraction of three distinct lifetime components: T_{11}, T_{12}, and T_{13}, as well as their corresponding relative amplitudes $\frac{A_1}{A}$, $\frac{A_2}{A}$ and $\frac{A_3}{A}$, where $A = A_1 + A_2 + A_3$, for both excitons. The longest decay component, approximately in the nanosecond range, is accurately determined from experiments with extended delay ranges, as shown in figures 3.6e and 3.6f. To ensure clarity in short-time-scale analysis, alternative fitting methods were also employed: i) fitting with only two measurable decay times (figure 3.6a), and ii) fitting with three decay times while assuming the first decay time is instantaneous relative to the experimental resolution or $T_{11} \ll T_p$ (figure 3.6b). These alternative approaches resulted in poor fitting quality, underscoring the necessity of analyzing with a model with three resolvable decay channels, as demonstrated in figure 3.6c.

The three lifetime components and their corresponding relative amplitudes across different temperature, power density and flake number, for both EX1 and EX2 are presented in figure 3.7 and 3.8, respectively. We see an extremely fast initial decay channel, T_{11} with a characteristic time of approximately 150 fs, for both excitons. This decay time changes slightly depending on temperature, excitation power, and flake thickness. The second decay component, T_{12} can vary between 0.5 to 1.0 ps. the relative amplitudes of these two components are similar ($\frac{A_1}{A} \approx \frac{A_2}{A}$). The third decay component (T_{13}) can be between hundreds of ps to few ns, both excitons, with higher relative amplitude ($\frac{A_3}{A} \approx 2 \times \frac{A_1}{A}$) at low power and temperature. The 150 fs ultrafast decay timescale, is similar to what has been widely reported for dynamics measurement under resonant optical excitation, in different MX_2 systems [29, 30, 98, 100]. However, our result sharply contrasts with non-resonant studies on ReS_2, which was able to only measure dynamics in the range of $10 - 100$ ps [70, 91–93]. It is worth mentioning that the population dynamics, including the lifetime components and their relative amplitudes, remain largely unaffected by variations in flake thickness. This observation suggests that the band structure remains consistent regardless of the number of layers present and again confirms the known property of weak interlayer coupling in ReS_2 [67].

Population dynamics vs bandgap structure

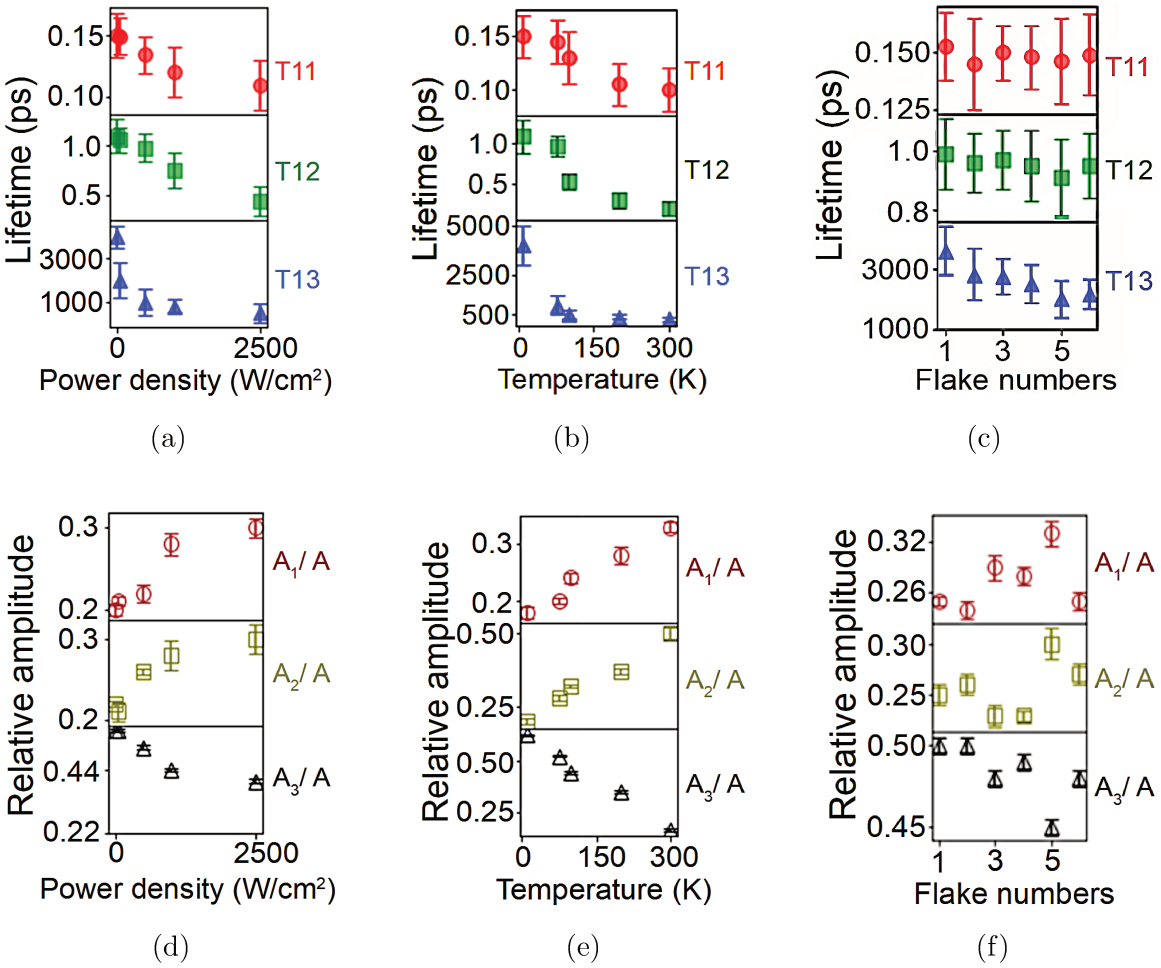

Figure 3.7: Transient FWM population dynamics fitting lifetimes for EX1 (flake-2) with corresponding errors represented as error bars as a function of different parameters: (a) power density, (b) temperature and (c) flake numbers. The corresponding relative amplitudes for the three lifetime components are shown as a function of the same parameters in (d), (e) and (f), respectively.

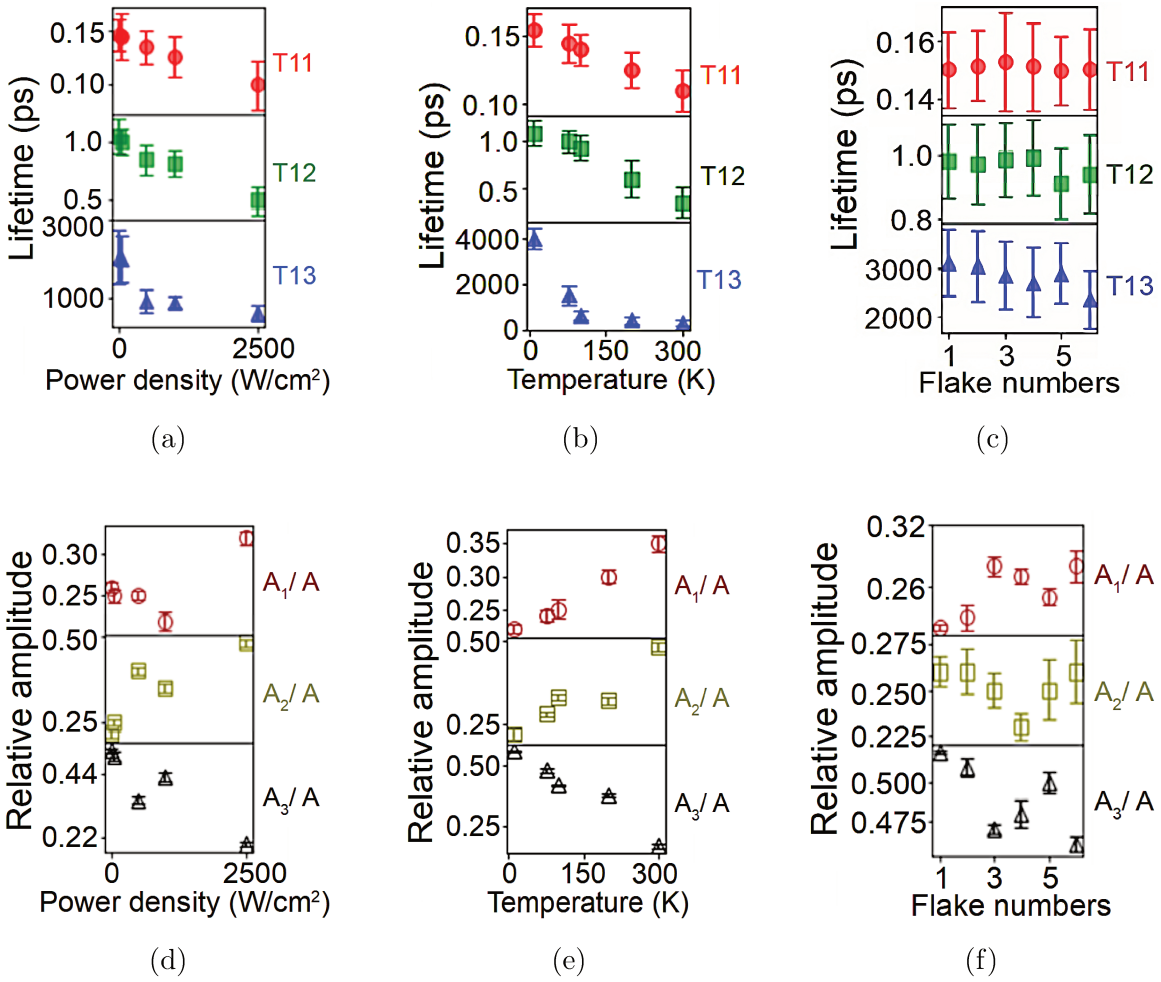

Figure 3.8: Transient FWM population dynamics fitting lifetimes for EX2 (flake-2) with corresponding errors represented as error bars as a function of different parameters: (a) power density, (b) temperature and (c) flake numbers. The corresponding relative amplitudes for the three lifetime components are shown as a function of the same parameters in (d), (e) and (f), respectively.

Our results show that all three time components decrease as optical power and temperature increase. Additionally, we observe a change in the relative contribution of these components: the weight of the third channel ($\frac{A_3}{A}$) decreases, while the contribution of the second channel ($\frac{A_2}{A}$) increases, eventually becoming dominant at room temperature. Such multiscale dynamics indicate a strong interplay between bright states and dark states reservoirs [18, 28, 39, 68, 100]. TMDs possess relatively large exciton mass, the broad exciton linewidth and the small conduction band splitting, which makes exciton scattering in these materials highly efficient [59,90]. Hence, a significant fraction of exciton population can scatter out of the light cone, into the dark state reservoir through non-radiative process. These can include exciton-phonon scattering, exciton-exciton scattering and also Auger scattering process which has shown a particularly high efficiency in WSe_2 monolayers [100]. With increasing temperature and excitation density, non-radiative exciton-phonon and exciton-exciton scattering increase, respectively and eventually become the dominant process in the population dynamics. The dark states can be: (i) excitons with in-plane momentum outside the light cone of the dispersion branch, and (ii) spin-forbidden dark states, which lie tens of meV below the bright states and emerge from structural anisotropy-induced exchange interaction, as revealed in recent magneto-PL studies on ReS_2 [68]. The complex exciton population dynamics, with varying decay times, can be attributed to a combination of the characteristic times of scattering processes in excited states and irreversible decay processes into the fundamental state. In this framework, a combination of radiative decay into the fundamental state and exciton scattering into the dark states gives rise to the first ultrafast component (T_{11}). The longer second (T_{12}) and third components (T_{13}) are associated with the decay of the dark excitons, primarily due to the return of the population into the light cone via secondary scattering. It should be noted that the population dynamics of EX1 and EX2 are very similar across different temperatures and excitation densities. This similarity, particularly at low temperatures despite the 30 meV exciton energy splitting, indicates that inter-valley EX1-EX2 scattering plays a negligible role compared to the other scattering mechanisms discussed above.

Our results show that T_1 and T_2 values for layered ReS_2 are similar to what has been reported for excitons in MX_2 monolayers [28–31, 39, 50, 94, 100], which possess direct band gap characteristics. In contrast, indirect gap bilayer $MoSe_2$ [99] exhibits ultrashort T_1 (60 fs and 800 fs) and T_2 (50 fs) values at 30 K temperature. This

decrease by one order of magnitude stems from interlayer coupling causing a complex indirect bandstructure for bilayer $MoSe_2$, which provides multiple ultrafast scattering pathways for excitons. The enhancement of exciton-photon scattering times due to the indirect band gap was estimated to be around 10 fs in WS_2 bilayers [101]. Therefore, our findings on ReS_2 suggest an electronic structure featuring direct band gap regardless of layer thickness, which was predicted earlier using angle-resolved (k-space) photoemission spectroscopy on bulk [20] and atomically thin ReS_2 [32].

3.5 Conclusion

In summary, we investigated the intrinsic T_2 and T_1 characteristic times of excitons in anisotropic ReS_2 layered systems using ultrafast four-wave mixing microscopy under resonant conditions. We found that the excitonic linewidth has negligible contribution from inhomogeneous broadening, while the population dynamics T_1 is primarily dominated by ultrafast non-radiative processes. We found T_2 to show a weak dependence on layer thickness, whereas T_1 remains almost independent of it. Compared to the excitonic coherence in MX_2 TMDs, few-layer ReS_2 displays remarkable robustness against optical density and temperature, enabling room-temperature quantum features. The largescale spatial homogeneity of T_2 and the negligible inhomogeneous contribution indicate a particularly low level of excitonic disorder in exfoliated flakes. Our findings thus provide fundamental insights into low-dimensional anisotropic layered ReS_2, highlighting that it offers the advantage of MX_2 monolayer-like direct band excitonic properties combined with the robustness provided by the multilayer structure.

4 Dynamics of excitons in $MoSe_2$-graphene heterostructure

4.1 Introduction

$MoSe_2$ is one the most prominent and extensively studied vdW materials. In its monolayer form, this material exhibits a direct bandgap and hosts bright excitons with exceptionally high binding energies [8, 12–16]. Furthermore, the vdW properties of $MoSe_2$ allow stacking of monolayers or thin layers of this material, with other vdW materials to form heterostructures. Although the excitonic properties in bare $MoSe_2$ have been studied extensively, significant opportunities remain for exploring and engineering novel excitonic properties in $MoSe_2$ based vdW heterostructures. These advanced structures could induce new phenomenon at the interface or add new degrees of freedom over the excitons [9, 12, 13, 33]. In this chapter, we investigate the exciton dynamics in a $MoSe_2$-graphene heterostructure.

In our study, we work with a sample prepared by our collaborators at IPCMS, University of Strasbourg (Stephane Berciaud's group), consisting of a $MoSe_2$ monolayer encapsulated in hBN and deposited on a Si/SiO_2 substrate. Our sample also contains regions with a heterostructure of monolayer $MoSe_2$ and graphene. The electronic and optical properties of this heterostructure can be heavily influenced by any phenomena occurring at the interface, due to the atomic nature of the constituent monolayers and the sub-nm interlayer distance [5]. In this study, we attempt to uncover the effect of the coupling between graphene and $MoSe_2$, on the excitonic properties, particularly on exciton dynamics. We aim to determine the timescale and the nature of the dominant coupling mechanism. The interaction between excitons in $MoSe_2$ and graphene can be static, occurring as soon as the two materials come into contact, or dynamic, driven by photoexcitation. Studies on heterostructures composed of graphene and various Group 6 TMDs ($MoSe_2$, WSe_2, WS_2) have discussed two possible dynamic processes in this context: net charge transfer and energy transfer [5, 33–36]. Regardless of the nature of the dynamic process, the presence of graphene is expected to introduce a non-radiative decay channel (timescale denoted by τ_G) for excitons in the heterostructure. Previous studies have discussed the nature and timescale of this decay channel

and hypothesized contribution from both an energy transfer process [5, 33, 35] and a net charge transfer process [34, 36]. Notably, our collaborators, using time-resolved photoluminescence (TRPL), investigated the same sample studied in this work, estimating the energy transfer timescale to graphene, to be approximately 2.5 ps [5]. This timescale roughly aligns with reports in other studies [33–35]. However, the long rise times (on the order of several ps) observed due to the nonresonant excitation used in these studies obscure the exciton dynamics at ultrafast timescales (less than 1 ps). Therefore, in this context, we question the role of graphene on the intrinsic characteristic decay time of excitons. In our study, using FWM microscopy with resonant excitation, we determine the timescale (τ_G) of photoinduced dynamic transfer process into graphene and question the nature of this transfer process. We also show that graphene imparts an unpredicted and remarkable effect on the exciton dynamics, by increasing the inhomogeneous broadening with higher excitation power density, leading to a confinement effect and a subsequent increase in exciton lifetime.

4.2 Sample description and initial characterization

The sample under investigation here is an hBN-encapsulated Graphene-$MoSe_2$ heterostructure, prepared via mechanical exfoliation and transfer (details in Chapter 2) on a Si/SiO_2 substrate. The sample features several regions with distinct heterostructure configurations, from which we selected three areas for measurement. The first area contains only a monolayer of $MoSe_2$ encapsulated in hBN, with no Graphene present. The second and third areas consist of monolayer and bilayer Graphene, respectively, stacked on top of monolayer $MoSe_2$, with the entire structure encapsulated in hBN. For ease of description, these regions will be referred to as the reference region, Gr-1L region, and Gr-2L region, respectively. The results obtained from the reference region serve as a baseline for comparison with those from the Gr-1L and Gr-2L regions. This comparison allows us to assess the influence of Graphene on the excitonic dynamics in monolayer $MoSe_2$. Figure 4.1 shows an optical microscopy image of the sample with all three chosen regions marked for clarity.

As seen in Figure 4.1, even the smallest region exceeds an area of 10 μm^2. Given the spatial resolution of our experiment ($\leq$ 1 μm), it is essential to select a precise spot within each region for focused measurement, ensuring accuracy and consistency throughout the comparative analysis. Hyperspectral PL mapping facilitated

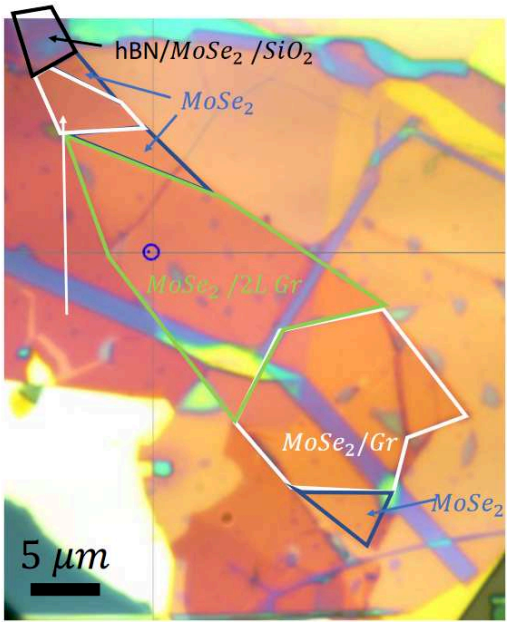

(a)

Figure 4.1: White light image of $MoSe_2$-graphene heterostructure sample under investigation. The regions containing $MoSe_2$, $MoSe_2$-1 layer graphene and $MoSe_2$-2 layer graphene are marked in blue, white and green, respectively. The image was taken from our collaborators [5].

the identification of three optimal locations that exhibited clean PL signatures, free from structured background. Figures 4.2a, 4.2b, and 4.2c display the white light (gray-scale) images of the reference, Gr-1L, and Gr-2L regions, respectively, with the chosen measurement locations highlighted by circles. The PL spectra from these locations are shown in figures 4.2d, 4.2e, and 4.2f (taken at 15 K temperature and ≈ 255 W/cm^2 power density). The reference region demonstrates a typical $MoSe_2$ monolayer PL spectrum, with the exciton peak at 1.65 eV and the red-shifted charged exciton (trion) peak at 1.62 eV. In contrast, the spectrum from the Gr-1L location shows no signature of the trion. Additionally, there is a significant quenching (decrease) of the exciton intensity by almost a factor of 15 and a small red-shift in exciton energy (10 meV) compared to the reference location. For the Gr-2L spectrum, the trion peak is absent as well. The exciton intensity here is further quenched, and the exciton peak is red-shifted relative to the Gr-1L location by 7 meV. The PL spectra for the three locations are shown together (zoomed on the exciton) in figure 4.2g, which highlights

the PL quenching and the red-shift in exciton energy, in the presence of graphene.

The observations mentioned so far: the absence of trion, red-shift of the exciton peak, and PL quenching, have all been reported in previous studies on TMD-Graphene heterostructures [5,6,33–37]. The explanations regarding these observations will be summarized below, after reminding some relevant properties of Graphene. Graphene has semimetallic properties, with exceptionally high electron mobility and cone-shaped energy dispersion (Dirac cones). The Dirac point of Graphene is located within the bandgap of most group-6 TMDs, making it an ideal acceptor of charge carriers [5, 33]. Most of the effects on the static and dynamic properties of excitons observed in TMD-Graphene heterostructures can be traced back to this capability of Graphene to accept charge carriers.

In this context, we can start discussing our observations beginning with the absence of trions in the presence of Graphene. Thin layers of TMD usually contain a considerable amount of native doping, regardless of the fabrication technique. These extra charges give rise to the formation of charged excitons or trions. When a monolayer TMD ($MoSe_2$ in this case) is brought into contact with Graphene, because of the band offset, the native doping from $MoSe_2$ crosses over to Graphene. This static charge transfer process happens without photo-excitation and effectively makes the TMD monolayer charge neutral, leading to the absence of charged exciton or trion emission in the PL spectrum observed in this study [5, 6, 33]. The red-shift in the exciton peak can also be attributed to a static effect, although not to static charge transfer. The exceptionally high binding energy of excitons in monolayer TMD is due to the lack of dielectric screening around the excitons. In a heterostructure, Graphene provides extra screening, causing a reduction in the binding energy. At the same time, the mismatch between the Fermi levels between $MoSe_2$ and Graphene causes a reduction in the electronic bandgap in $MoSe_2$. The interplay between these two effects lead to an overall small decrease of ≈ 10 meV in the exciton transition energy [34, 37].

The last effect we will discuss, namely PL quenching of excitons in $MoSe_2$ (and other group-6 TMD by extension), can not be explained by a static process. Photoexcited dynamic transfer process (energy transfer or net charge transfer) opens up a non-radiative decay channel for the excitons and leads to significant PL quenching in the presence of graphene. The precise characteristic timescale of these processes are still a matter of active studies. This aspect of TMD-graphene heterostructures

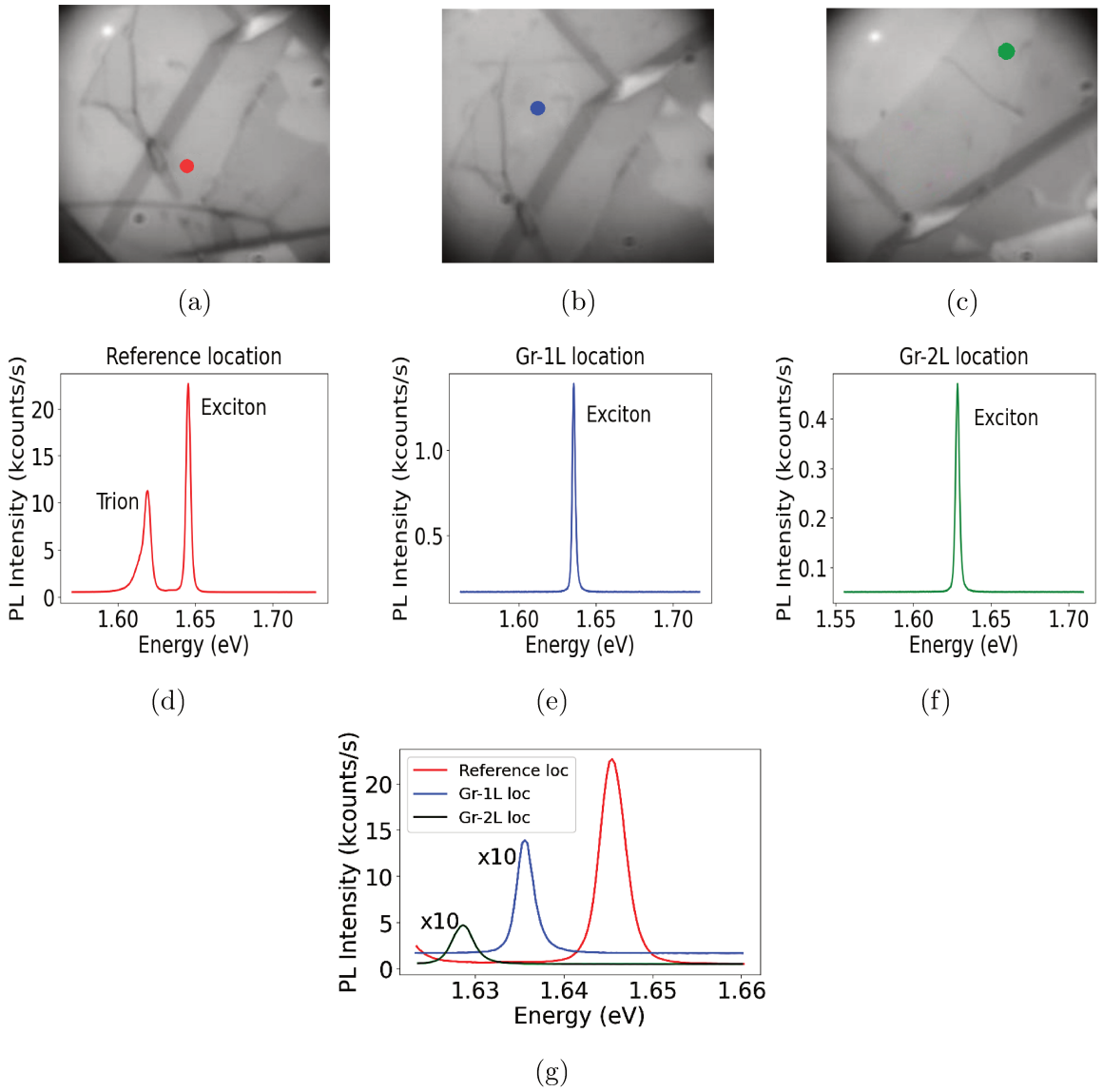

Figure 4.2: White light image (grayscale) of the three regions of the heterostructure sample: (a) $MoSe_2$ (b) $MoSe_2$-1 layer graphene and (c) $MoSe_2$-2 layer graphene. The measurement locations are marked with red, blue and green circle, respectively. The PL spectrum corresponding to the (d) reference location, (e) Gr-1L location and (f) Gr-2L location. The PL measurement was done at 15 K temperature and $\approx$ 255 W/cm^2 power density. (g) A comparison of the PL spectra from the three locations (zoomed on the exciton peak). The PL spectrum for the Gr-1L and Gr-2L locations are multiplied by a factor of 10 for clarity.

will become more relevant in section 4.4, where we look into the population dynamics of excitons.

Following the PL characterization, we proceed to perform FWM microscopy to study the exciton dynamics, as a function of excitation power and temperature. In order to deliver a more consistent description of our results and the corresponding interpretations, the coherence dynamics results will be divided into two parts: inhomogeneous and homogeneous broadening. First, our observations regarding the inhomogneneous broadening of excitons in this sample will be discussed and the method we followed to extract the inhomogeneous linewidth (σ). This will be accompanied by a comparison of the evolution of σ with different environmental parameters, across the three locations. Subsequently, the exciton population dynamics results will be presented. The corresponding explanations directly follow the trend observed in the evolution of σ. Finally, the behavior of the homogeneous linewidth (γ) of excitons in this sample will be described and explained using the population dynamics results.

4.3 Inhomogeneous broadening

Inhomogeneous broadening can play a crucial role in determining the overall coherence dynamics of excitons, particularly when there is non-negligible disorder in the host material. Accurately evaluating σ can provide valuable insight into the material's properties, for instance, how the disorder is influenced by the stacking of two layered materials. More particularly, in this study, inhomogeneous broadening plays a specific role, and its evolution with power and temperature governs the changes in the coherence and population decay of the excitons. The FWM measurements and data analysis, used to extract the inhomogeneous linewidth σ and homogeneous linewidth γ, follow similar methodology outlined in Chapter 3. We perform two pulse FWM measurement with excitation energy resonant with the exciton energy extracted from PL measurements. We use circularly polarized excitation, to ensure the selective formation of excitons in a single valley of $MoSe_2$. We Fourier transform the spectral interference of the two-pulse FWM signal from the excitons and the reference beam to obtain the FWM amplitude as a function of real time, t, and the pump-probe delay τ_{12}. The presence of notable inhomogeneous broadening, leading to a photon echo signature, manifests itself in the 2D $t - \tau_{12}$ plot as high FWM amplitude along the $t = \tau$ diagonal line.

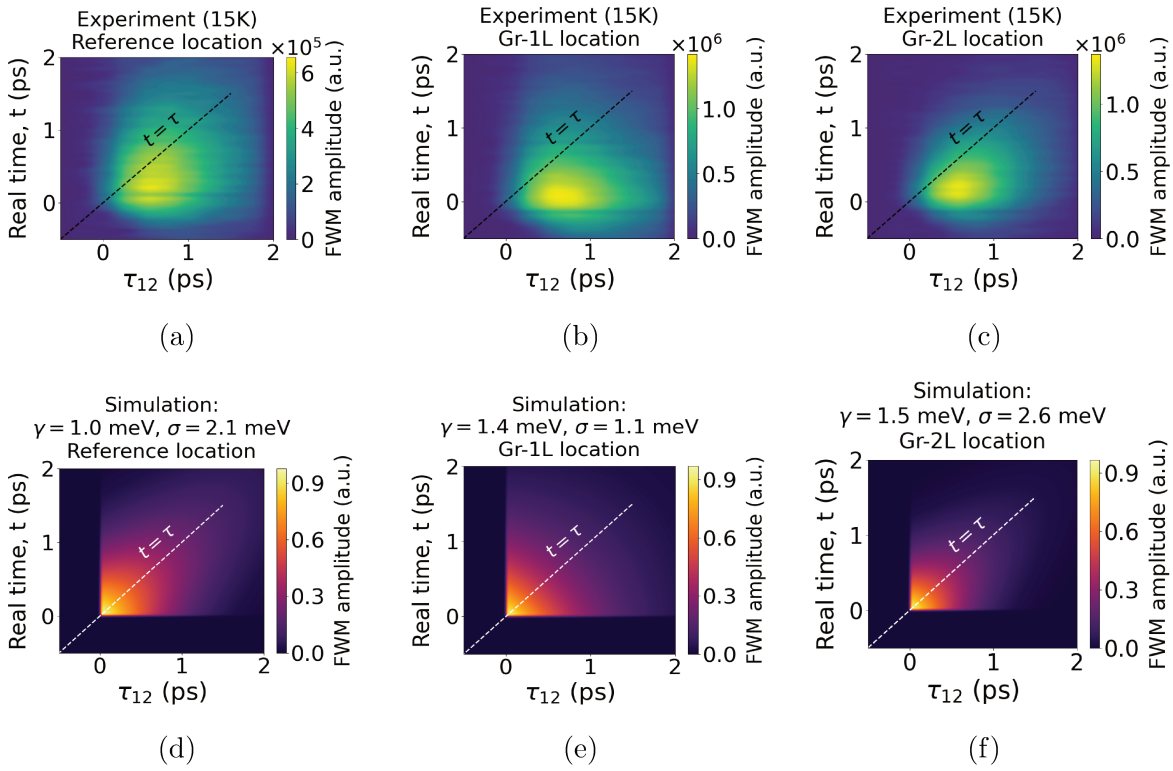

Figure 4.3: 2D $t - \tau_{12}$ plots showing the measured FWM amplitude vs real time, t and pump-probe delay τ_{12}, for the (a) reference location (b) Gr-1L location and (c) Gr-2L location. The measurements were performed at 15 K temperature and with $\approx$ 32 W/cm^2 pump power density. The corresponding simulations, along with the used values of γ and σ, are shown in (d), (e) and (f), respectively.

Figures 4.3a, 4.3b, and 4.3c show the 2D plot obtained from the reference, Gr-1L, and Gr-2L locations, respectively (15 K temperature and $\approx$ 32 W/cm^2 pump power density). The corresponding simulations (using equation 2.3.44 from Chapter 2, which assumes the delta pulse condition), with the values of γ and σ, are shown in Figures 4.3d, 4.3e, and 4.3f. As demonstrated, there is a sign of photon echo visible in the 2D plots, particularly for the reference location and Gr-2L location. We estimate a broad range of σ from the simulation. This allows us to accurately fit the FWM amplitude vs pump-probe delay (τ_{12}) data (using equation 2.3.46) and extract the values of γ and σ from the fit. Figures 4.4a, 4.4b and 4.4c show one example of FWM amplitude vs τ_{12} data fit, from each of the three locations. It should be mentioned that these figures shows noticeable FWM amplitude at negative delay τ_{12}. This is

due to the nonlinear local field effect [102] and does not play a significant role in determining the FWM amplitude decay for positive delay. The decay timescale can be reliably extracted without taking this effect into account.

Additionally, for the sake of comparison with PL data, we calculated the exciton linewidth (full width at half maximum, FWHM) using γ and σ, extracted from two-pulse four-wave mixing (FWM) measurements at low power (where the exciton density regime can be comparable). In this calculation, we considered the exciton lineshape obtained from FWM, as a convolution of a Lorentzian of FWHM given by γ and a Gaussian lineshape of FWHM given by σ. We compared this to the exciton linewidth obtained from the PL spectra. Table 4.1 shows a comparison between the linewidths calculated by using the two methods described above. As demonstrated, the linewidths calculated from FWM measurements (from 6.4 W/cm^2 to 31.8 W/cm^2 pump power density) match closely with the ones obtained from PL spectra (at 255 W/cm^2) excitation power density). At higher pump power density, the FWM linewidth diverges away from the PL linewidth, due to excitation induced effects.

	Pump power density (W/cm^2)	**Reference location**	**Gr-1L location**	**Gr-2L location**
FWM linewidth (meV)	6.4	2.57 ± 0.31	1.85 ± 0.16	3.19 ± 0.21
	12.7	2.46 ± 0.19	1.87 ± 0.14	2.93 ± 0.89
	31.8	2.46 ± 0.22	2.04 ± 0.07	3.39 ± 0.19
PL linewidth (meV)	Excitation power: 255 W/cm^2	2.82	1.95	2.46

Table 4.1: Comparison between exciton linewidth at the three measurement locations, obtained from 2 pulse FWM and PL measurement

We will look into the behavior of the extracted homogeneous linewidth γ later in this chapter. For now, we focus on how σ evolves with two environmental parameters: excitation power density (pump power density, P) and temperature (T).

Figures 4.5a and 4.5b show the evolution of σ as a function of P and T, respectively, for the three measurement locations. The power dependent measurements were performed at a temperature of 15 K, while the temperature-dependent measurements were conducted with P $\approx$ 255 W/cm^2. The choice of the pump power density was made to ensure that enough FWM signal to noise ratio is achieved even at high temperature, where exciton oscillator strength is expected to decrease [12].

For the reference location, σ only shows a slight decrease with increasing P. In stark contrast, for the Gr-1L and Gr-2L locations, σ exhibits a clear trend of increasing with higher values of P. On the other hand, for all three locations, σ increases

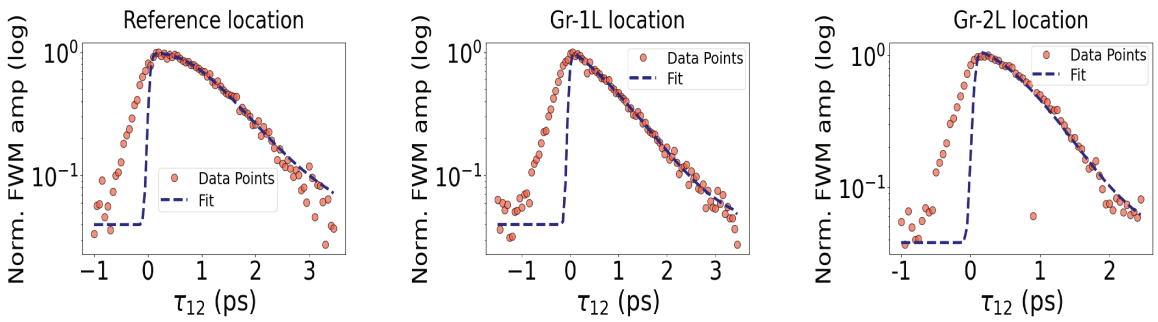

(a) (b) (c)

Figure 4.4: Examples of coherence dynamics FWM data (FWM amplitude vs pump-probe delay τ_{12}), with corresponding fit, for (a) reference location (b) Gr-1L location and (c) Gr-2L location. All the data shown here were taken at 15 K temperature and $\approx$ 13 W/cm^2 pump power density. The energy of the laser pulse was set at the exciton energy, obtained from PL spectrum for each location, with optimization of $\pm$ 2 meV to maximize FWM signal intensity

as T increases from 15 K to 95 K. A complete model of the behavior of σ is beyond the scope of this study. Nonetheless, we can point out some overall considerations that can qualitatively address the difference in the trend of σ in the three locations as a function of P. Inhomogeneous broadening is an effect on the excitonic transition of local disorder in a material. Hence, σ is heavily influenced by the dielectric environment surrounding the excitons, including factors such as strain, flake deformities, impurities, defects, or local potential traps and the nature of the interface that the host material experiences [28, 30, 38]. The inhomogeneous broadening linewidth, σ can also change significantly from one location to another on the same 2D layer [30], highlighting the various spatial scales of excitonic disorder. For the reference location, $MoSe_2$ monolayer is interfaced with the encapsulating hBN layers. Whereas, for Gr-1L and Gr-2L locations, $MoSe_2$ monolayer is in contact with monolayer and bilayer Graphene, respectively. The presence of Graphene provides a significantly different local environment to the monolayer $MoSe_2$, with potentially different density of defects and free carrier concentration [30]. Higher excitation density leads to photodoping or generation of excess charge carriers [103], impacting the local environment. More specifically, a hypothesis can be suggested based on the photodoping effect. Indeed, several studies have reported efficient photodoping in $MoSe_2$ [103], graphene , and

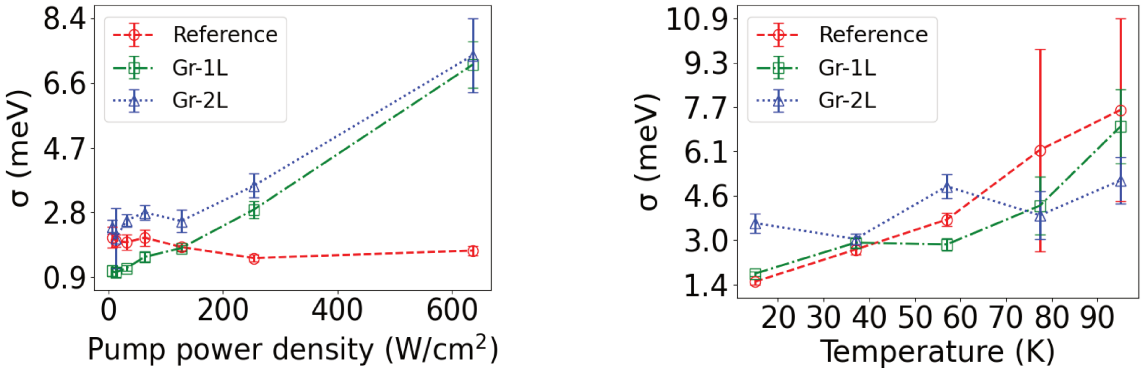

(a) (b)

Figure 4.5: Evolution of inhomogeneous broadening linewidth σ, for the three measurement locations, as a function of (a) pump power density, P and (b) temperature, T. The power dependent measurements were performed at a temperature of 15 K, while the temperature-dependent measurements were conducted with pump power density ≈ 255 W/cm^2.

graphene-heterostructures [104, 105], with efficiency enhanced due to unique band alignments and interlayer interactions. This photodoping naturally follows the intensity of excitation, and the resulting excess of charge carriers can impact the local environment and increase the excitonic disorder level. Therefore, we can propose a hypothesis that a combined photodoping effect in the $MoSe_2$-graphene structures, capable of leading to significant inhomogeneous broadening, accounts for the differences in sigma behavior between the reference location and the two $MoSe_2$-graphene locations.

In order to understand the trend of σ with higher temperature (T), two relevant consequences need to be considered. First, with increasing T, the excess thermal energy can activate more local disorder centers in the environment. Secondly, The density of phonon modes increases with higher T. The interaction of electron and phonon can cause broadening of the energy bands and a change in the bandgap as well. The electron-phonon coupling can vary considerably among different locations across the sample. With increasing T, the magnitude of this effect increases as well [106]. Hence, the combined effect of the two consequences mentioned above result in an increase in the inhomogeneous linewidth, σ, for all three locations, as T increases.

In the next two sections, we will see how the behavior of σ (particularly σ vs P)

heavily influences the evolution of population decay and homogeneous lineiwdth γ. As will be discussed, these rather unexpected observations lead to a remarkable effect of graphene on the excitons in $MoSe_2$.

4.4 Population dynamics

Next we discuss the population dynamics of excitons in this sample. A three-pulse FWM scheme (details in chapter 2) was used to measure the population dynamics. The FWM amplitude vs pump-probe delay (τ_{23}) data suggests the presence of multiple decay mechanisms with different decay timescales interacting with each other. Similar to figure 4.4, we notice considerable FWM amplitude at negative delay τ_{23}, due to nonlinear local field effect [102], which does not play a significant role in determining the population decay timescales. The population dynamics data was fitted with equation 2.3.47, which allows us to separate the contribution of different timescales involved in shaping the dynamics. To accurately determine the number of decay components in the dynamics, we compared the fit using two exponentials with the fit using three exponentials. The results for both cases, across the three locations, are shown in Figure 4.6. To ensure clarity, we analyzed the fits in both short and long time windows. We present the short window fit (up to 10 ps) in Figures 4.6a, 4.6b, 4.6c and the long window fit (up to 190 ps) in Figures 4.6d, 4.6e, 4.6f. As demonstrated, the two exponential model resulted in poor fitting quality. In order to quantify the error in these two fitting methods, we calculate the relative sum error (σ_{err}) as:

$$\sigma_{err} = \frac{\sqrt{\frac{1}{N}\sum_{i=1}^{N}(x_i^{\text{data}} - x_i^{\text{fit}})^2}}{\langle |x_i^{\text{data}}| \rangle} \tag{4.4.1}$$

where, N is the number of FWM amplitude data points, x_i^{data} denotes the experimentally obtained FWM amplitude for a certain delay τ_{23} and x_i^{fit} represents the fit value corresponding to the same delay. The extracted σ_{err} for three exponential component fit for reference, Gr-1L and Gr-2L location are 0.0.05, 0.02 and 0.02, respectively. Whereas, σ_{err} values for two component fit are 0.14, 0.48 and 0.55, respectively. The higher values of σ_{err}, for the two component fit highlights the necessity of using three exponentials to accurately model the population dynamics data.

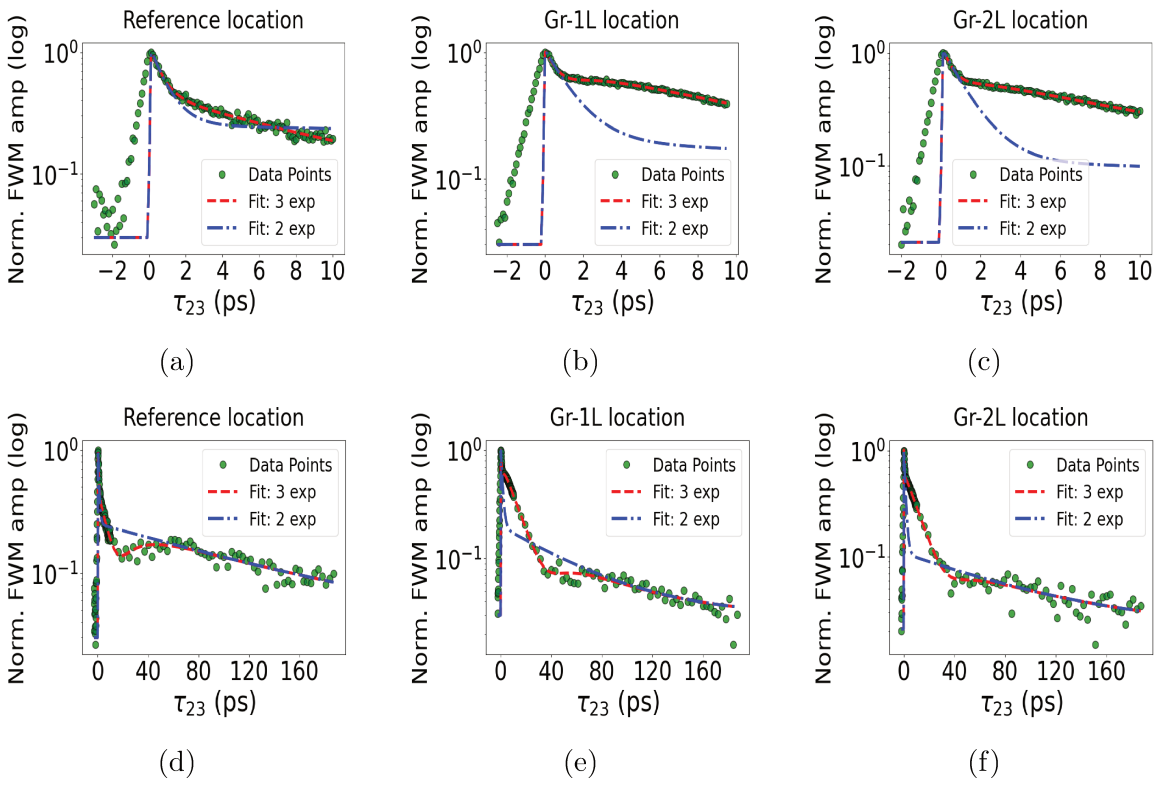

Figure 4.6: Comparison between population dynamics FWM data (FWM amplitude vs pump-probe delay τ_{23}) fitting with two decay components and three components, for the three measurement locations. For clarity, the fitting comparison upto 10 ps are shown in figures (a), (b) and (c). The corresponding fits for the full measurement delay window are shown in (d), (e) and (f) respectively. All the data shown here were taken at 15 K temperature and $\approx$ 13 W/cm^2 pump power density.

Using this method of fitting, we were able to extract three decay timescales T_{11}, T_{12}, and T_{13} for each data set, along with their corresponding phases (ϕ_1, ϕ_2, ϕ_3) and amplitudes (A_1, A_2, A_3). The shortest of the three decay components, T_{11}, ranges from approximately 370 fs to 1.5 ps, depending on the environmental conditions. The longer components, T_{12} and T_{13}, span from approximately 5 ps to 30 ps and 50 ps to 830 ps, respectively. The extracted population decay timescales for the reference location are systematically in agreement with similar measurements conducted on $MoSe_2$ monolayer excitons. [28,31,38,39]. The phases related to the decay timescales play a crucial role in determining the shape of the population dynamics data. Particularly, the FWM amplitude vs τ_{23} in the full measurement time window (figures 4.6d, 4.6e,

4.6f), shows that the FWM amplitude does not decrease monotonically with τ_{23} and can even rise again after an initial drop. These types of features can not be fitted with just a sum of multiple exponentials. Rather, this can be explained by considering that population decay is a coherent process and the interaction of the phases of the decay timescales can lead to such features in the dynamics [30, 38]. Hence, the inclusion of the phases in the fitting equation is required to get a good fit of the population dynamics data and determine the decay timescales accurately.

Following the extraction of the decay timescales, we now look at how they evolve with different excitation power density (pump-1 power density, P) and temperature (T). These results are summarized in Figure 4.7. With increasing P, we observe a decrease in T_{11} for the reference location (Figure 4.7a), whereas it increases for Gr-1L and Gr-2L locations. Figure 4.7c shows a similar trend for T_{12}. On the other hand, T_{13} increases with higher P, for all three locations (Figure 4.7e). It is noticeable that the value of T_{13} at any given P for the reference location is significantly higher (approximately by a factor of 2), compared to the values for the Gr-1L and Gr-2L locations. Figures 4.7b, 4.7d, and 4.7f show the evolution of the decay components with increasing T. For all three locations, as T rises, we observe a slight decrease in T_{11} and T_{12}, along with a general increase in T_{13}. Apart from a singular effect (that we attribute to a fluctuation in the experimental conditions) resulting in a high T_{13} value at temperature T= 57 K, the rate of increase of T_{13} as a function of T is higher for the reference location compared to Gr-1L and Gr-2L locations.

We will start the interpretation of the population dynamics results by discussing the likely origin of each of the decay components and then proceed to explain the differences that we observe in the dynamics as a result of the presence of graphene. The decay components can be described in a somewhat similar way as the components observed for ReS_2 excitons (chapter 3). The fastest component T_{11} most likely stems from a combined effect of the radiative decay of the exciton into the fundamental state and scattering into the dark states. There is no general consensus about the precise origin of the two longer components (T_{12} and T_{13}), but they have been associated with the decay of the dark excitons, primarily due to the return of the population into the light cone via secondary scattering [28, 38]. These states can be momentum dark states (momentum out of the light cone) or spin forbidden states [28].

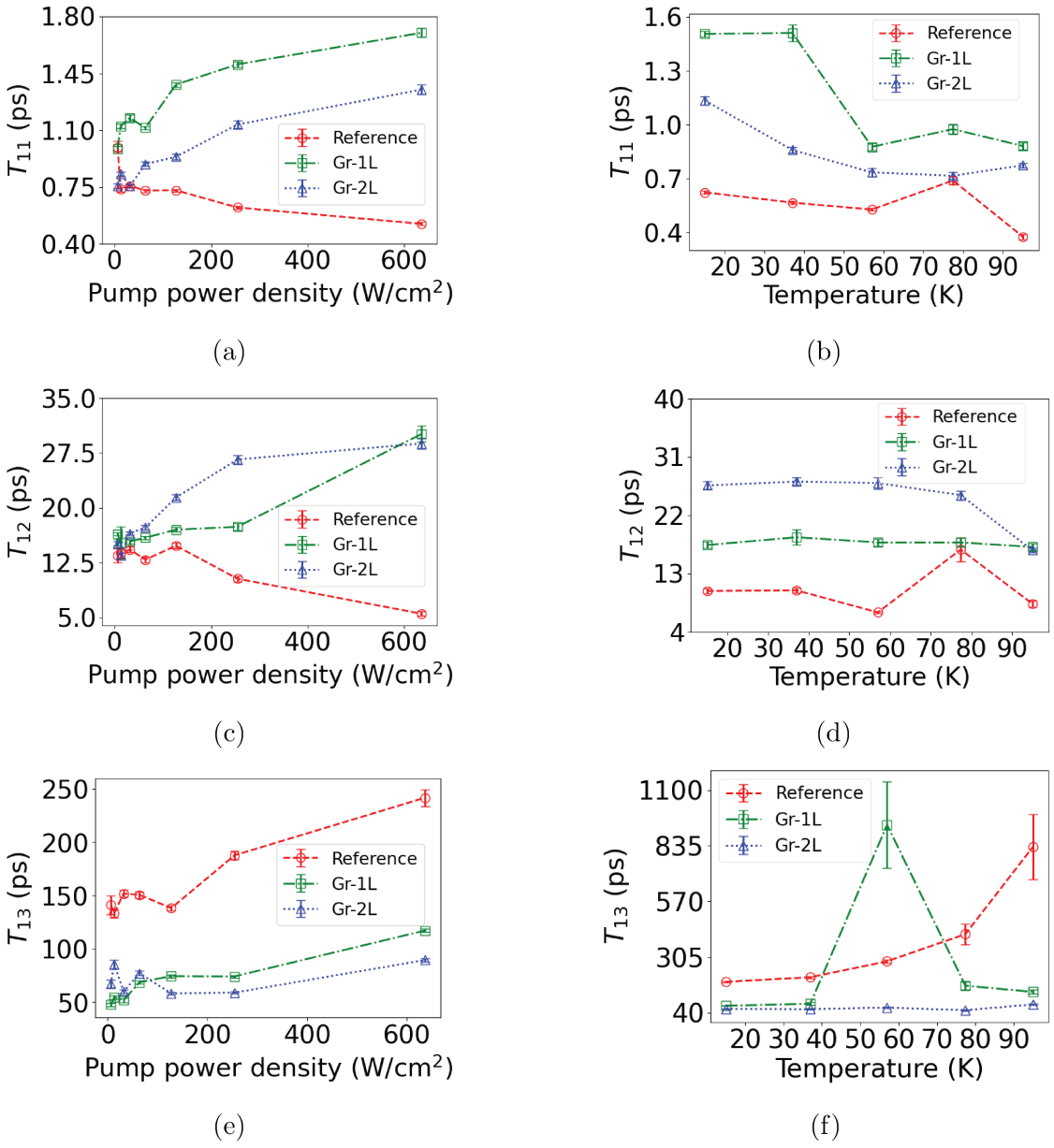

Figure 4.7: Evolution of the three extracted population dynamics timescales T_{11}, T_{12} and T_{13} as a function of (a), (c), (e) pump power density and (b), (d) and (f) temperature. The power dependent dynamics data were taken at 15 K temperature, whereas the temperature dependent FWM measurements were performed with ≈255 W/cm^2 pump power density. The value of T_{13} at Gr-1L location, for 57 K temperature shows a significant increase compared to the other two locations. This value is a sharp departure from an otherwise clear trend in T_{13}. We consider this value as an anomalous fluctuation and disregard it in our analysis.

Coupling with graphene

As presented in Figure 4.7, the evolution of the population decay timescales in $MoSe_2$, with P and T show clear differences when graphene is present in the environment. The most notable change with the introduction of graphene is observed for T_{13} in our results, which decreases by a factor of ≈ 2, compared to the reference location. The extracted values of T_{11} and T_{12} do not show any appreciable reduction in Gr-1L and Gr-2L location compared to the reference location, at low power density and at any temperature of measurement. Hence, our results do not highlight a distinguishable signature of a dynamic transfer process (whether energy or net charge) into graphene in few-ps timescale, as estimated by previous studies using non-resonant excitation, on similar heterostructures [5, 33–35, 40]. On the other hand, the observed reduction of T_{13} in the presence of graphene highlights a coupling mechanism on a long timescale, largely distinct from of T_{11} and T_{12}. From the measurements, we can estimate an approximate value of the transfer timescale, by comparing T_{13} between the reference location and Gr-1L location, at a lower power of 12.7 W/cm^2 where the power induced effect is minimized. By considering the decay rate for Gr-1L ($\Gamma_{13G} = 1/T_{13G}$), as a sum of the decay rate at the reference location ($\Gamma_{13r} = 1/T_{13r}$) and the decay rate corresponding to transfer timescale into graphene ($\Gamma_G = 1/\tau_G$), we estimate τ_G to be approximately 100 ps.

Now that, in the low excitaion density regime, a long timescale of the exciton-graphene coupling has been highlighted, the origin of such a mechanism should be questioned. If there is a transfer of one type of charge carrier (either electron or hole) into graphene, an expected outcome would be an increase in doping of graphene, which would lead to an increase in its Fermi energy E_F. This would cause a measureable shift in the Raman peak energy of Graphene. We refer to this process as net charge transfer. The earlier studies referred to so far [5,33–35,40], used Raman spectroscopy to monitor the doping level in graphene. They found no significant signature of doping in the Raman line of graphene within the time resolution of their experiment ($>$ 1 ps). They hypothesized that the dynamic carrier transfer process into graphene is dominated by either a dipole-dipole interaction between charge carriers in graphene and $MoSe_2$ or simultaneous tunneling of electron and hole into graphene. The authors refer to both situations as energy transfer, as no net charge differences are induced in

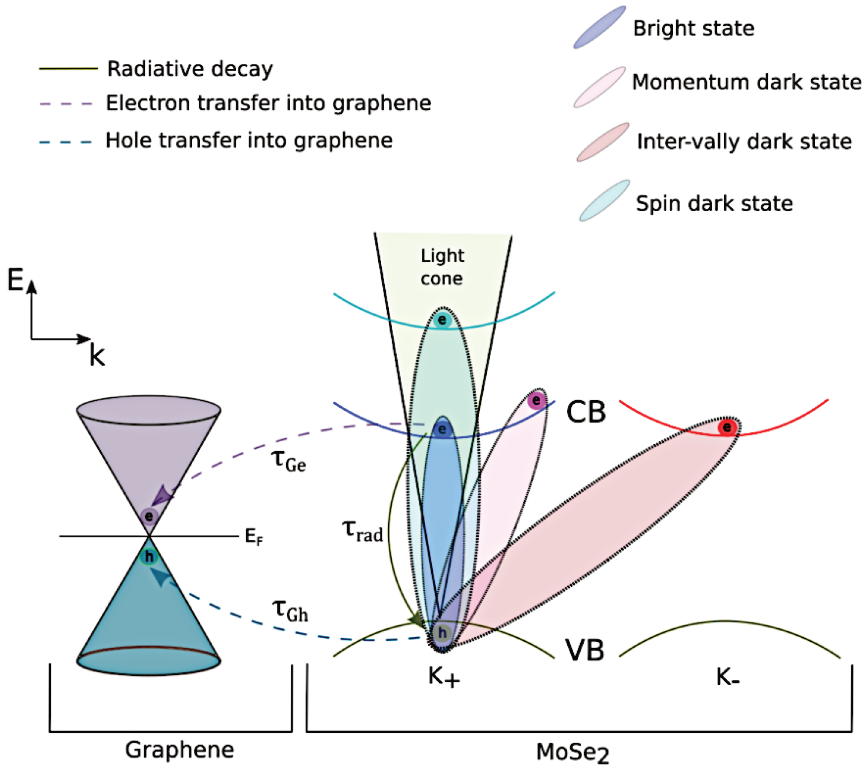

Figure 4.8: Schematic of the different scattering channels for resonantly excited excitons in $MoSe_2$ - graphene heterostructure. For $MoSe_2$, both K_+ and K_- valleys are shown. In this study, bright excitons are selectively formed at K_+ valley by excitation with σ^+ circularly polarized light. The bright exciton can scatter into the inter-valley dark state, momentum dark state and spin dark state (highlighted with ellipses of different color). Through inter-valley scattering processes, the K_+ bright exciton can scatter into the bright exciton state of K_- valley, as well as the family of dark states of K_- valley (not shown). All the abovementioned states can participate in the processes of electron and hole transfer into graphene (highlighted with dashed arrows). The electron and hole transfer timescales are represented by τ_{Ge} and τ_{Gh}, respectively. τ_{rad} represents the radiative decay timescale of the exciton.

the graphene. It is important to note that these earlier studies [5, 33–35, 40], utilized time-resolved photoluminescence (TRPL), with non-resonant excitation, to infer few-picosecond transfer timescales and attributed them to energy transfer occurring both with "hot excitons" during their relaxation and with "cold exciton" at the funda-

mental transition level. The mechanism of coupling highlighted in our study differs strongly from the earlier studies. We can suggest that the coupling mechanism responsible for the observations in our study, originates from net charge transfer, which is expected to occur on a timescale much longer than energy transfer. This hypothesis could be further verified by performing resonant Raman spectroscopy on similar heterostructures and monitoring the doping level in graphene, focusing on the tens of picoseconds timescale.

However, this raises a very interesting question: Why are fast decays, attributed to transfer to graphene, not decipherable in our resonant experiments? Conversely, why have longer timescales of decay not been observed in TRPL experiments? The answer may lie, as mentioned above, in the conditions of the experiments. In resonant experiments, hot excitons and free electron-hole pairs are not involved; only bound fundamental excitons, which are more difficult to dissociate, are present. Additionally, with off-resonant excitation, the quenching of the photoluminescence attributed to transfer process into graphene during hot exciton relaxation, leads to a severe reduction in the density of excitons at the fundamental level. This results in a distinct regime of excitation between resonant and off-resonant experiments. This latter point suggests that exciton scattering mechanisms, such as exciton-exciton interactions, are more efficient in the regime of resonant excitation, leading to faster decay components in the population dynamics and hindering the short-time coupling mechanisms with graphene. Moreover, with off-resonant excitation, hot excitons can decay and populate several dark exciton states, in stark contrast to resonant experiments, where only the bright excitons are primarily excited, resulting in different initial conditions for the population dynamics. A schematic showing the possible dark state scattering channels for the resonantly excited bright exciton in the studied heterostructure is presented in figure 4.8.

Evolution of T_{11} with excitation power density

We now focus on another important observation regarding the fastest decay timescale T_{11}. The evolution of T_{11} with increasing P (figure 4.7a) bears a remarkable resemblance to the trend observed for σ in Figure 4.5a), i.e., T_{11} decreases with higher P for the reference location and in contrast it increases with higher P for Gr-1L and Gr-2L locations. This can be explained by the following hypothesis. An increase in

the localization of the excitons would lead to longer radiative decay [41]. Since, T_{11} is attributed to a combined effect of radiative decay and scattering into dark states, increasing exciton localization would manifest itself as an increase in T_{11}. Localization of excitons can be strongly influenced by local disorder, leading to inhomogeneous broadening [41]. With an increase in σ, due to higher local disorder in the sample, exciton center of mass localization length decreases. This enhanced exciton localization results in a slower radiative recombination of the excitons (increase in T_{11}). This is precisely what is observed for T_{11} vs P for the graphene 1L and 2L locations, consistent with the increase of σ with P. On the other hand, the exact opposite scenario plays out for the reference location, where we observe a decrease in σ with higher P. This leads to lower disorder in the sample, larger exciton localization length (more delocalization), leading to faster radiative decay component leading to an overall decrease in T_{11}. This hypothesis was also used in ref [30] to explain a correlation between varying σ, depending on the measurement location and population lifetime for excitons in another group-6 TMD material, $MoSe_2$.

We also observe T_{12} following a similar trend as T_{11} with P. Without precisely identifying the origin of T_{12}, it is difficult to formulate a proper hypothesis.

4.5 Homogeneous broadening

After discussing the population dynamics, We can now go back and finish the analysis regarding the role of the graphene interface on the coherence dynamics of excitons in MoSe2. As described in section 4.3, we use the 2D $t - \tau_{12}$ plots to determine a broad range of inhomogeneous linewidth σ, which allows us to fit FWM amplitude vs τ_{12} data to extract the homogeneous linewidth γ ($= \frac{2\hbar}{T_2}$), using equation 2.3.46. To conclude the analysis, we look at the evolution of γ as a function of P and T in the three locations, as presented in Figure 4.9. With higher P and T, we see an overall increase in γ for all three locations. However, for the reference location, γ increases at a faster rate (almost linearly) with respect to P compared to Gr-1L and Gr-2L locations.

In order to understand the difference in the behavior of γ among the three locations, we meed to correlate it with our results regarding σ and T_{11}, presented in the previous sections. Now, let's first focus on the reference location. We have observed that with increasing power P, σ decreases at the reference location, and as a result,

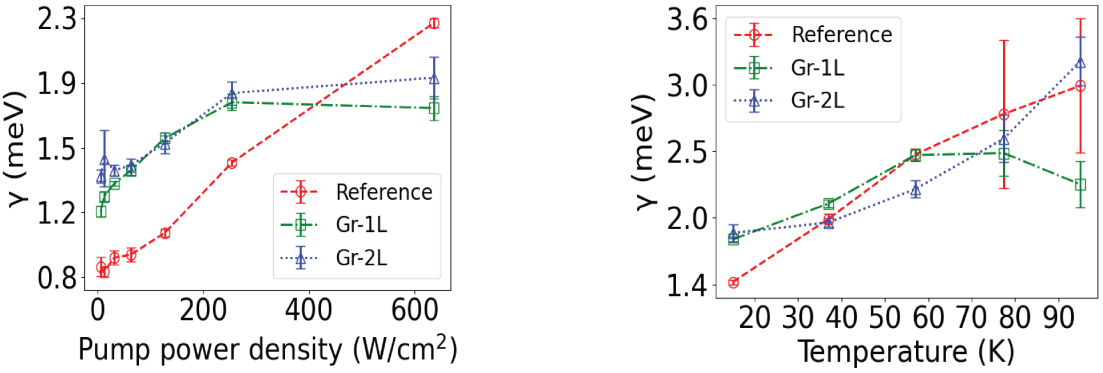

(a) (b)

Figure 4.9: Evolution of homogeneous broadening linewidth γ, for the three measurement locations, as a function of (a) pump power density and (b) temperature. The power dependent data were taken at 15 K temperature and the temperature dependent FWM measurements were performed with $\approx$ 255 W/cm^2 pump power density.

T_{11} also decreases (figures 4.5a, 4.7a). This leads us to question whether the increase in the homogeneous linewidth γ (decrease of the decoherence time T_2) with excitation power density is due to the reduction in the lifetime or not. In other words, is the decoherence rate primarily limited by energy dissipation, leading to $T_2 \approx 2T_1$. In our results, the population dynamics comprise different components. However, we can restrict the analysis to the fastest component T_{11} and draw a first conclusion by examining the ratio between T_2 and T_{11}, as shown in table 4.2 (for comparison, the ratios for Gr-1L and Gr-2L locations have also been included). As demonstrated, this ratio is considerably higher at the reference location compared to the other two locations at any given P. Particularly, from 12.7 W/cm^2 to 127.3 W/cm^2, T_2 is almost equal to $2T_{11}$, i.e., lifetime limited. So, for the reference location, T_2 decreases (γ increases), following the decrease in T_{11}. On the other hand, for the Gr-1L and Gr-2L locations, as T_{11} increases with higher P, it is clear from the ratios ($\frac{T_2}{T_{11}}$) that energy dissipation is not responsible for the increase in γ. Instead, other mechanisms leading to pure dephasing are playing the dominant role in the coherence dynamics.

Concerning the increase in γ with temperature, the trend is common to all three locations and has been regularly observed in semiconductors [75,107,108] and TMDs [28, 30, 50]. As temperature increases, the phonon population rises, leading to more probable scattering events between phonons and excitons. The enhanced scattering leads

Pump power density (W/cm^2)	T_2/T_{11}		
	Reference location	Gr-1L location	Gr-2L location
6.4	1.5	1.1	1.2
12.7	2	0.9	1.04
31.8	1.83	0.82	1.2
63.7	1.88	0.79	1
127.3	1.7	0.85	0.89
254.6	1.4	0.46	0.6
636.6	1.12	0.41	0.48

Table 4.2: Ratio of decoherence time T_2 to population decay component T_{11} for different pump power density and measurement locations.

to faster dephasing and rising γ. Since we don't see any noticeable difference in the behavior of γ a sa function of T, among the three locations, we can conclude that the graphene layers and their phonon contributions, do not appear to play a crucial role in $MoSe_2$ exciton coherence with temperature.

4.6 Conclusion

In this study, we employed resonant four-wave mixing (FWM) microscopy to investigate the coherence and population dynamics of excitons in hBN-encapsulated $MoSe_2$-graphene heterostructure. A comparative analysis was conducted between regions containing $MoSe_2$ with and without graphene. The most significant influence of graphene was observed in the longest population dynamics timescale, T_{13}, which exhibited a reduction by approximately a factor of 2. In contrast, no similarly strong effect was seen in the other two population decay components, T_{11} and T_{12}. From this observation, we established a lower bound for the charge carrier transfer timescale from $MoSe_2$ to graphene of approximately 100 ps. We proposed several possibilities to explain this result. Additionally, we observed a distinct variation in the behavior of the inhomogeneous broadening linewidth (σ) across different measurement locations. Notably, the increase in σ with optical density at the $MoSe_2$-graphene location clearly correlates with an increase in T_{11}, suggesting that the presence of graphene enhances exciton localization under optical excitation. This new graphene-induced effect, in addition to its fundamental characteristics, could have interesting implications for photodetector applications, where maximizing the lifetime is essential for enabling

efficient electron-hole dissociation.

This study is the first to employ resonant excitation with ≈ 100 fs time resolution combined with phase-sensitive detection on a $MoSe_2$-graphene heterostructure. Our results offer new insights into the dynamics of excitons in this type of advanced vdW heterostructures, laying the groundwork for the development of a comprehensive model to quantitatively describe exciton-graphene interactions in these systems.

5 Statistical analysis of defect emission in hBN: spectral families

The results presented in this chapter are considerably different in nature compared to the previous three chapters. This chapter focuses not on 2D systems, but rather on zero dimensional (0D) confined systems. This study relies on a static (PL) analysis of the optical properties of 0D systems, which is not only a self-contained investigation but also a prerequisite for exploring more advanced spectroscopy techniques on these types of systems. The work presented here is based on the findings published in our article [109]. Single photon emitters (SPE) or Quantum emitters (QE) in two-dimensional (2D) layered materials are rapidly emerging as building blocks for next generation quantum technologies, including Quantum sensing and quantum communication [45,110–116].These optically active defects inherit remarkable properties from their 2D host materials, such as: high mechanical flexibility, easy integration into photonic chips and the ability to be stacked with other 2D materials leading to a plethora of heterostructures. Another interesting feature of these quantum emitters is their proximity to interfaces due to the atomically thin nature of their host material, which significantly enhances photon extraction efficiency. Moreover, this characteristic paves the way to advanced defect engineering including deterministic placement of emitters and the ability to fine-tune their optoelectronic properties on demand [43, 117].

Among the different types of quantum emitters found in 2D materials, atomic-like defects in hexagonal boron nitride (hBN) are particularly promising. hBN is a wide bandgap semiconductor. In its bulk form, it has a 5.9 eV bandgap with VBM at K point and CBM at M point of the first Brillouin zone. If the number of layers are reduced down to a monolayer, it becomes a direct bandgap semiconductor (M point) with 7.25 eV bandgap. It is electrically insulating (small dielectric constant), thermally conductive, mechanically rigid and possess high thermal and chemical stability. hBN has a graphene like hexagonal crystal structure. In an individual layer of hBN, Boron (B) and Nitrogen (N) atoms are arranged in hexagonal pattern, with polarized and strong covalent bond (sp^2 hybridization) between them. Successive layers of hBN are held together by weak Van der Waals force [45,118,119]. Because of its insulating

properties, small lattice mismatch with graphene and resistance to oxidation hBN has long been used for encapsulation and as a barrier material for 2 dimensional heterostructures and quantum well [120]. Atomically thin hBN has also been found to be highly transparent over a broad wavelength range (250 nm-900 nm) [121].

In the recent years, hBN has come to prominence as a host of bright photostable single photon emitters at room temperature [111, 122–124], with emission spread over a large wavelength range [111, 123–129], including ultraviolet [130–132] and near-infrared ranges [133]. To date, very few materials have shown such exceptional property. Examples include mostly wide bandgap materials like diamond, silicon carbide and more recently carbon nanotubes [111]. hBN being a wide bandgap material (5.9 eV in bulk hBN) has the ability to host localized defect states deep within its bandgap and are well preserved from coupling with the continuous energy bands and therefore exhibits single photon emission even at room temperature [111]. The versatility of hBN-based quantum emitters is further underscored by recent breakthroughs demonstrating resonant excitation [134], Rabi oscillation [135], ultrafast coherent control [136], and optical spin orientation [137–139]. These studies have demonstrated the potential of hBN defects as a robust platform for both fundamental scientific exploration and the development of next-generation quantum technologies. However, to fully harness the potential of these emitters and bring them to the forefront of application in quantum technologies, a deep understanding of the atomic composition and structural characteristics of these defects is essential.

One of the primary difficulties in uncovering the origin of these defects is the strong dispersion in emission wavelength, particularly in the visible range. This topic remains under active debate. Theoretical studies have consistently shown that the hBN can accommodate a wide variety of quantum defects, making it more difficult to identify any single type of defect using their emission signature [140–143]. Multiple hypotheses have been proposed so far, particularly regarding emissions in the $1.6 - 2.2$ eV optical range. Some studies hypothesized Carbon substitutions as a critical factor in defect emission [144–149], while others suggest that formation of donor-acceptor pairs may explain the sharp luminescence lines observed at low temperature [150].

Beyond these, other possibilities like dangling bonds at surfaces or grain boundaries [151], naturally occurring vacancies or antisites [152–155], and oxygen substitutions [156] have also been put forward as possible explanations. The complexity

involved in identifying the exact origin of these defects in hBN is made worse by the absence of precise experimental spectral assignments for the defect emission lines. Several factors contribute to this difficulty: i) The potential coexistence of different defects located spatially close together and with similar spectral features. ii) The complex nature of the defect emission spectrum, which includes a main transition line known as the zero phonon line (ZPL), usually accompanied by one or more phonon sidebands (PSBs). iii) Changes in the spectral features induced by local environmental factors, such as strain [157] or electric field from trapped charges and surrounding dielectric environment. Some studies have reported histograms of ZPL spectral occurrences based on a sample size of of 40-100 emission lines at room temperature [111,158]. These histograms showed a broad distribution of ZPL occurrences within the $1.6-2.2\ eV$ range, suggesting that ZPL emission is distributed apparently continuously across this spectral range. More detailed studies at cryogenic temperature [123, 159] involving larger sample sizes of 340 and 627 ZPL occurrences have shown a similar continuous distribution of ZPL emissions, albeit with four distinct clusters. The presence of these clusters provide an opportunity for optical assignment of defect emission lines. These findings underscore the importance of studying a large number of defects to obtain statistically significant results. Addressing the apparent randomness of spectral properties in hBN requires a comprehensive approach, involving extensive data collection and analysis.

In this chapter, we address the challenges associated with the spectral identification of defect emission families in liquid exfoliated hBN nanoflakes at room temperature. The liquid exfoliation process is cost-effective, scalable and offer diverse configurations in terms of flake size, flake agglomeration, and local environmental conditions. This diversity allows an opportunity to fabricate representative samples with various defect species, possessing different spectral properties. Our comprehensive investigation takes into account a vast dataset of 87421 photoluminescence (PL) spectra, which collectively yield 8307 zero phonon lines (ZPLs). This extensive sampling allows us to construct ZPL occurrence histograms with a spectral binning of $2\ meV$, offering a high-resolution view of the ZPL spectral distribution. This enables the identification of narrow sets of possible defect clusters. In order to analyze such a large number of spectra, we developed a peak detection algorithm that determines the emission energy and linewidth of ZPLs and corresponding PSBs. As such, 11 distinct spectral ZPL emission clusters or families within the $1.6-2.2\ eV$ range are clearly

idenified. Each of these families has a well resolved emission energy center, indicating a sharp discretization of the ZPL energy distribution. This finding challenges the prevailing hypothesis of a broad and continuous distribution of defect energies and the associated spectral randomness.

The precision in identifying these emission families can play a crucial role in uncovering the microscopic origins of the emitters in hBN hosts. Given that density functional theory (DFT) calculations often lack the accuracy needed to determine absolute transition energies, the spectral spacing between these families serves as a more reliable parameter, which could help significantly to identify the chemical composition of the defects. In addition to spectral identification, our statistical approach provides valuable insights into the coupling constants between defects and lattice vibrations across a large dataset. On top of this, we present a pioneering exploration of how the morphology of hBN nanoflakes influences the formation of different defect species. We examine the relationship between defect occurrences and both the size of the nanoflake building blocks and the type of their agglomerations. We demonstrate that the formation of specific defect families can be precisely controlled by adjusting these morphological parameters. This level of control offers a new avenue for tailoring the properties of hBN-based quantum emitters. Reproducing one certain type of defect with a specific emission energy is crucial for performing advanced time resolved spectrocopy (FWM microscopy for example) measurements on these single systems.

5.1 Sample description and initial characterization

The hBN nanoflake samples for this study were prepared via the following steps. First, the liquid exfoliated layered (1-5 layers) hBN nanoflakes suspended in 1:1 ethanol/water solution, were purchased from Graphene Supermarket. 20 ml of the suspended hBN solution was sonicated for 30 minutes in an ultrasonic bath to break down any flake cluster formed due to sample aging. Following this, the hBN solution was centrifuged at 8000 rpm for 30 minutes. Both the supernatant solution (upper part of the centrifuged solution) and the complimentary precipitate solution can lead to unique sample configuration in terms of flake size distribution and surface morphology.

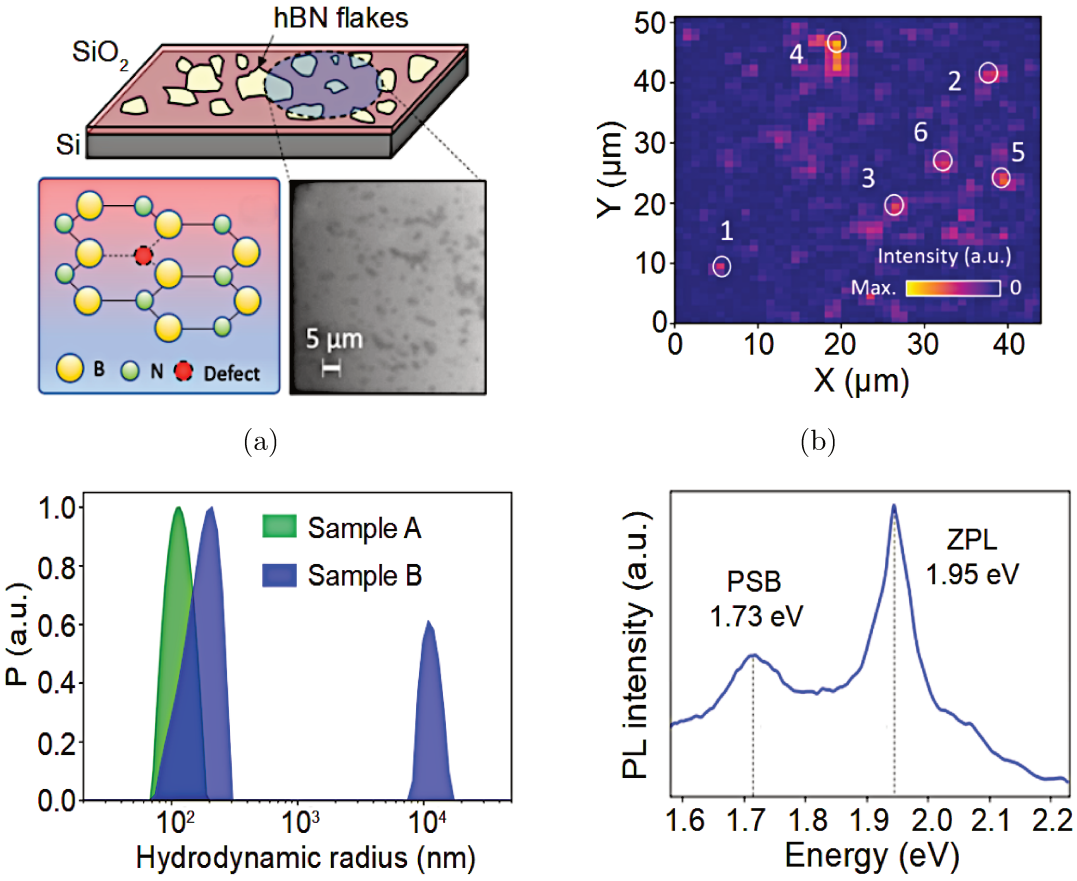

Figure 5.1: Initial characterization of hBN samples. (a) Schematic representations of a hBN nanoflake sample, with the inset showing a white light image of a typical area on the sample. A hBN lattice with a Nitrogen vacancy (NV) defect is also demonstrated. (b) An example of a hyperspectral PL map obtained from a typical hBN flake sample area. (c) Intensity weighted size distribution P of hBN flakes for samples A (green) and sample B (blue) obtained from DLS measurement (d) An example of a defect PL spectrum, with a ZPL at 1.95 eV and PSB at 1.73 eV.

A commercial dynamic light scattering (DLS) setup (ALV / CGS-3) was used to characterize the nanoflake size distribution for these two parts of the centrifuged solution. The acquisition is performed at a scattering angle of 90°, under illumination at 633 nm. The intensity correlation function is computed in a homodyne mode, and is then inverse Laplace transformed using a CONTIN algorithm [160]. This allows us to obtain the intensity weighted distribution of relaxation times, from which

the distribution of translation diffusion coefficients and subsequently of nanoflakes hydrodynamics radii are determined. The experiments are performed at low system concentrations, guaranteeing that the resulting distributions remain unaffected by concentration levels. Two samples were prepared from the centrifuged solution. Sample A was processed from the supernatant part, containing small flakes with sizes distributed from 80 to 160 nm (FWHM boundaries), as shown in the DLS measurement result (figure 5.1c). Whereas, sample B was obtained from the complementary precipitate part of the solution and contains larger hBN flakes with two distinct size distributions: One spanning from 130 to 250 nm, while the other extending from 9 to 14 μ m. The second size distribution is broader in width by two orders of magnitude and implies that, in sample B, the hBN flakes predominantly reside within this distribution of larger flakes, centered around 11 μm.

Next, these hBN solutions were drop casted onto 1:1 O_2/Ar plasma treated (2 minutes), 300 nm thick SiO_2/Si substrates. The controlled plasma treatment of the substrate was critical in accomplishing a high surface area coverage of the flakes and desired morphologies. Afterwards, the prepared samples were annealed at 850°C for 3 hours in a tube furnace under atmospheric pressure. It is important to mention that the large agglomerations were mainly formed during deposition and drying of nanoflakes on the substrates. Following the sample preparation, extensive white light imaging was done to identify locations on the samples with different surface morphology of hBN flakes. Figure 5.1a shows a schematic view of hBN flakes deposited on the substrate, with a white light image of a typical area on the sample shown in the inset. It also demonstrates an example of a structural defect in hBN: Nitrogen vacancy (NV defect). All the samples prepared for this study were also characterized by a scanning electron microscope (SEM) to explore different morphologies of hBN nanoflakes distribution over the substrates, in section 5.6.

A home-built confocal micro-PL setup (0.6 NA, 50× objective) was used for characterizing the hBN samples by obtaining hyperspectral PL maps. A continuous-wave 532 nm laser was used to excite the samples. With such sub-hBN-bandgap excitation, we probe the defect induced emissions ranging between 1.6 eV and 2.2 eV. A schematic of the setup and a detailed description of the experimental method is presented in chapter 2. The PL emission spectrum ($I_\lambda(\lambda)$) were collected using a spectrometer with a spectral resolution of 0.15 nm over the 555-785 nm (1.58-2.23 eV) range. We convert the spectrum into energy by using the conversion, $I_E = I_\lambda(\lambda)\frac{hc}{E}$. The spec-

tral lineshape is determined as: $L_E(E) = \frac{I_E}{E^3}$. Indeed, if one wants to compare it to any model or quantities related to the fraction of light emitted into the zero-phonon line (ZPL) with respect to the phonon sideband (PSB), it should be estimated based on the lineshape (or population) $L(E)$ and not on the PL intensity distribution I_E, where the latter scales with E^3 due to the spontaneous emission process. We kept the excitation power at 2 mW for all the PL measurements. This power is above the saturation power for the majority of emitters and allowed us to work with the most robust ones. The hyperspectral maps have a step size of 1 μm. The combination of such a step size and the confocal detection allowed us to ensure that the same emitter is not detected multiple time. Figure 5.1b shows a representative example of a hyperspectral map obtained from one of the fabricated samples. A typical spectrum obtained from a defect, corresponding to one pixel in a hyperspectral map, is presented in figure 5.1d, clearly highlighting the ZPL at 1.95 eV and PSB at 1.72 eV. We performed extensive hyperspectral mapping of our hBN samples and obtained 87421 PL spectra in total. The methodology for accurately analyzing this massive number of spectra is presented in the next section.

5.2 Peak detection algorithm

Accurate identification of zero phonon lines (ZPLs) in photoluminescence (PL) spectra is particularly challenging, given that the majority of detected spectra contain multiple peaks. These multiple peaks within a single spectrum can represent several possibilities: they might correspond to multiple ZPLs from closely located defects within the same laser spot, or they could be a combination of a ZPL and its associated phonon sidebands (PSBs) from a single defect [126, 146, 161, 162]. Recently, Hoese et al. [134] demonstrated that two-photon correlation measurements can reliably distinguish between ZPLs and PSBs in a PL spectrum of hBN defects. However, this method is impractical for analyzing large number of PL spectra such as the case in our study. We approach the data analysis with the hypothesis that each PL emission line is associated with an emitted ZPL, and that no isolated phonon-assisted transitions—such as those resulting from forbidden transitions, made allowed by strong vibronic coupling—occur independently [142]. Based on this assumption, we have developed an algorithm that relies on the well-established physical properties of defect emission spectra in hBN to differentiate between ZPLs and PSBs.

Our algorithm is informed by research that has shown that, at room temperature, PSBs in hBN defect PL spectrum primarily arise from three distinct phonon modes. These modes are red-shifted by approximately 166, 175, and 200 meV from the ZPL [132, 134, 163–165]. Additionally, PSBs are characterized by significantly lower PL intensity and broader linewidths compared to the ZPL. To automatically and unequivocally determine whether a peak in a given spectrum is a ZPL or a PSB, the algorithm proceeds as follows. The PL spectrum at each coordinate of a hyperspectral map is taken as input. In a spectrum, peaks are identified under the condition that its prominence (height relative to its lowest contour line) is 3 times the noise standard deviation (σ_{noise}). The algorithm puts more emphasis on the prominence of a peak rather than its absolute intensity. This allows for a very accurate comparison of peak intensities and disregard the effect of spectrally shaped background and overlap of multiple peaks. For a single peak spectrum (SPS), the algorithm considers the peak as a ZPL. In case of a multiple peaks spectrum (MPS), it considers two peaks at a time and compares them in terms of its emission energy and prominence. As example: in a spectrum with n peaks ($I_1, I_2, I_3, ...I_n$), the algorithm first considers all of them as ZPL and then compares the highest energy peak I_1 with each subsequent peaks I_{1+p}, from highest to lowest energy.

In such a comparison, the sorting of these into ZPL and PSB is done based on the two following criteria: i) the energy difference between the two peaks under comparison matches the energy of one of the three known phonon modes mentioned above and ii) the red-shifted peak has smaller prominence and larger linewidth compared to the other peak. If these two conditions are met, then the red-shifted peak I_{1+p} is stored as a PSB and not as a ZPL. The algorithm then moves on to the next unsorted peak and repeats similarly. Since our measurement is limited to the spectral window of 1.58 - 2.23 eV, PSBs involving two phonon interaction can only be detected for ZPLs at $\approx$ 2 eV. Hence, multi-phonon PSBs are not considered in this algorithm. After filtering all the peaks, for each peak chosen as ZPL, the algorithm stores the peak energy E_{00}, its linewidth δE_{00} and the energy shift of the corresponding PSBs relative to the ZPL. In addition to this selection process, we also impose an absolute limit of 30 meV on the linewidth of a peak in order for it to be considered as a ZPL. This condition is based on numerous previous studies reporting the linewidth of defects in hBN. To minimize the ZPL identification errors, we adopt a non-restrictive condition on the phonon energy range (ZPL-PSB redshift) using a uniform interval of 135 to

215 meV. This allows the algorithm to tolerate small fluctuations of phonon modes due to local strain and layer thickness [166–168]. Figure 5.2 shows the selection of ZPL and PSB by the algorithm, for four spectrum of different shapes as examples.

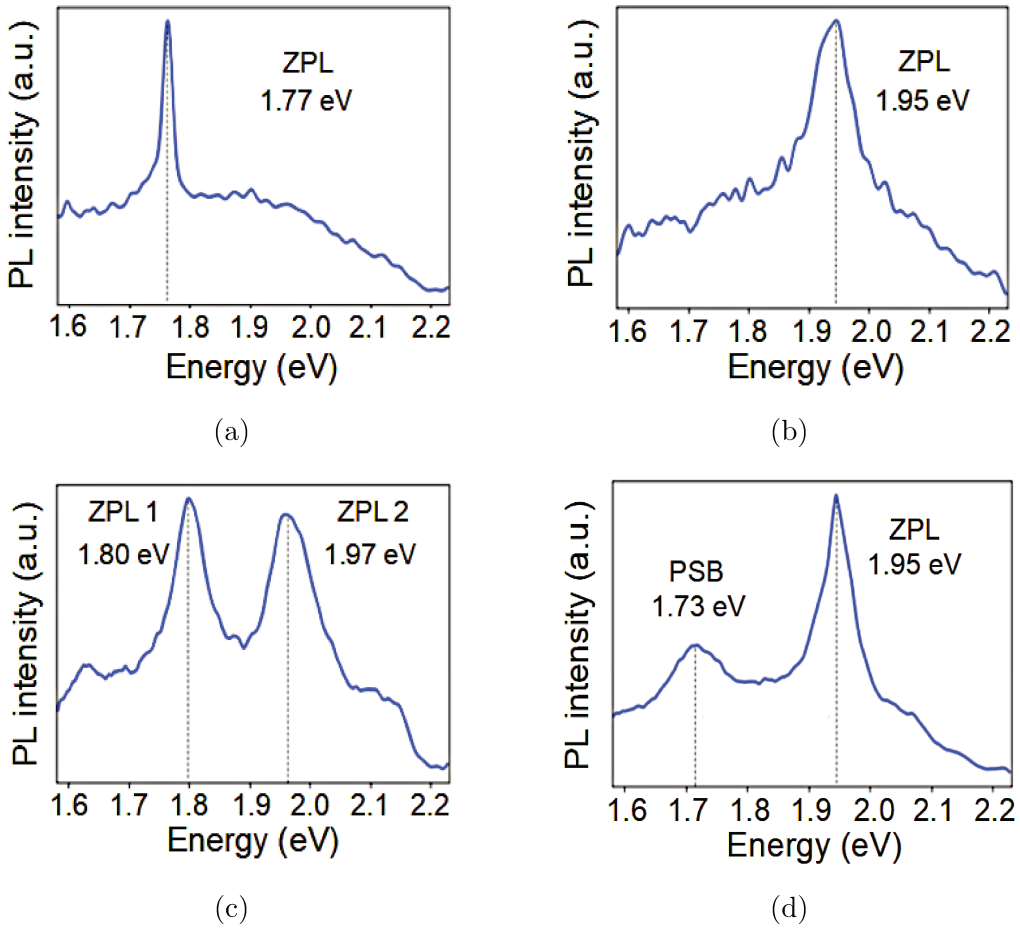

Figure 5.2: Examples of PL spectra peak sorting by the algorithm. (a) and (b) SPS inputs: The algorithm chooses the peaks in both spectra as ZPLs: (a) narrow linewidth peak at 1.77 eV and (b) broad linewidth peak at 1.95 eV. (c) MPS input: The algorithm chooses the two detected peaks: one at 1.97 eV and a red-shifted peak at 1.80 eV, as ZPLs. (d) MPS input: The algorithm chooses the peak at 2.01 eV as ZPL and the red-shifted peak at 1.72 eV as the corresponding PSB.

The developed algorithm unequivocally identifies the ZPLs from the spectra it analyzes. By automating a reliable ZPL identification process, we greatly enhance the accuracy and rapidity of PL characterization of our samples. A potential drawback

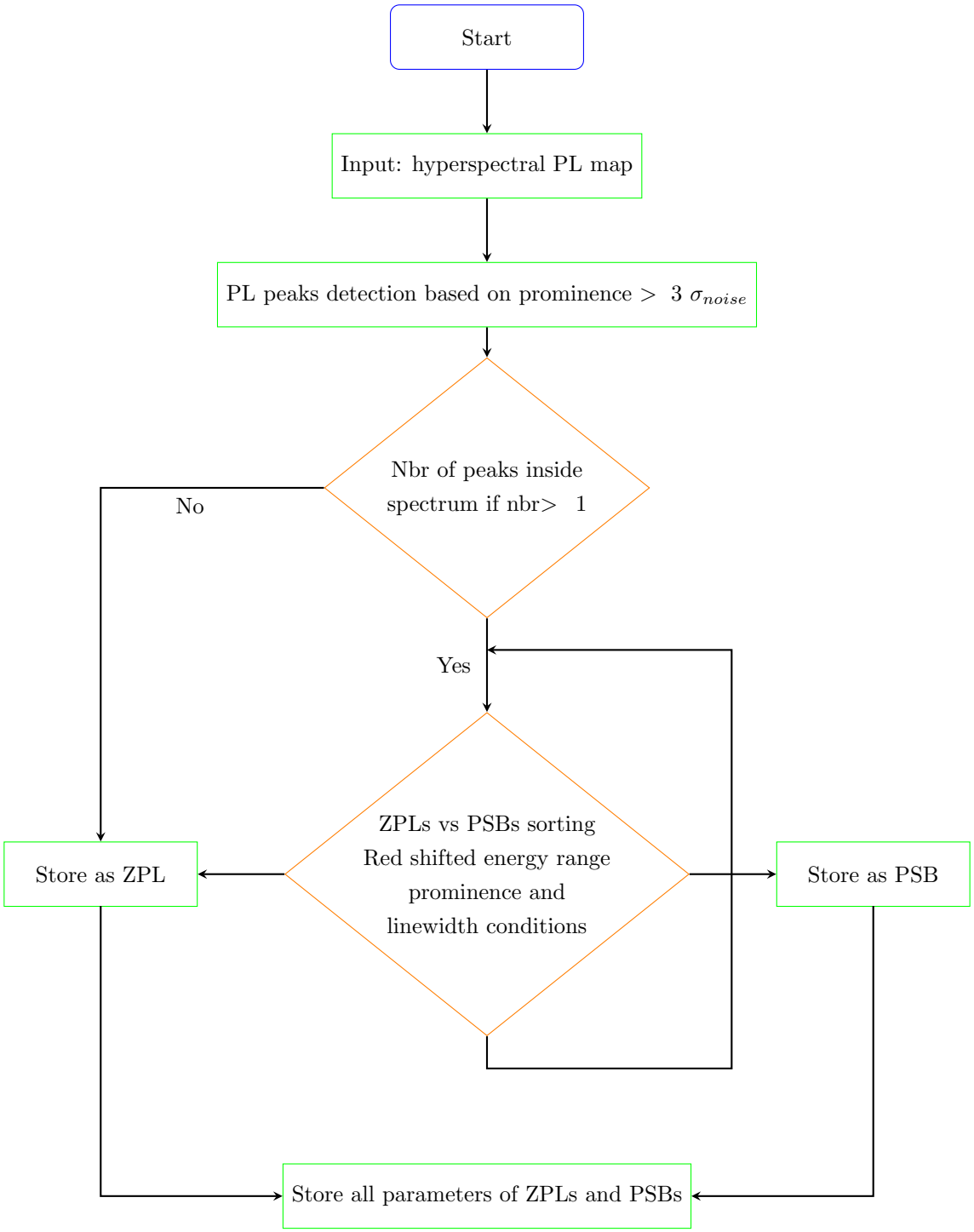

Figure 5.3: Flowchart illustrating the peak detection algorithm for ZPL and PSB identification from a PL spectrum.

is the possibility of underestimating the number of ZPLs in case of a weaker ZPL spectrally positioned in the considered PSB red-shift range of a higher prominence ZPL. However, the linewidth limit and the prominence condition placed in the algorithm can prevent these instances of misidentification of ZPL as PSB. Figure 5.3 summarizes this algorithm using a flowchart. In the next sections, the hyperspectral PL data analysis results obtained by using the algorithm is presented.

5.3 Spectral families

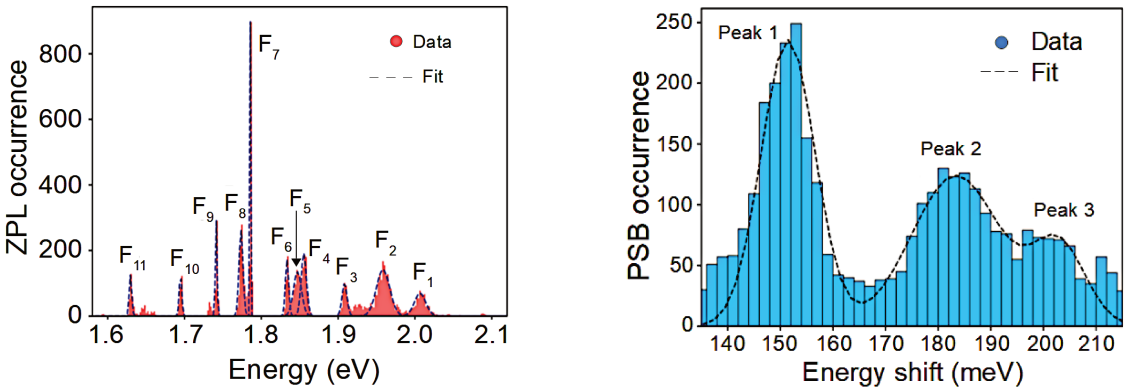

(a) (b)

Figure 5.4: (a) Histogram (red colored, number of total ZPLs: 8307) of total ZPL occurrences collected from both samples A and B, fitted by the sum of 11 Gaussian functions (dashed line), identifying 11 defect families (F1-to-F11). (b)Histogram (cyan colored) of 3501 PSBs detected from MPS. The dashed lines represent a fit comprising the sum of three Gaussian functions, revealing three distinct peaks.

The algorithm presented in the previous section was applied on 21 hyperspectral maps containing 87421 spectra in total and among them it identified 8307 ZPLs. Histogram of the peak positions of the ZPLs was then constructed with a spectral binning of 2 meV. The total ZPL spectral distribution obtained in this way is presented in figure 5.4a. Remarkably, the ZPL energy distribution does not seem continuous rather it shows clear separation into discrete sets, that we refer to as "spectral families". We clearly identify 11 such families in the spectral range 1.6 - 2.2 eV and denote them as F_1 to F_{11}. The histogram was fitted with a sum of 11 Gaussian distributions. The fit demonstrated that the families possess well defined energy center (c_i) and Half width

Defect family	**ZPL center, c_i and width, w_i (HWHM) of peak energy distribution**		**Mean ZPL HWHM linewidth (meV)**	**Relative abundance (%) with respect to total detected ZPL**	
	c_i (eV)	w_i (meV)		**Sample A**	**Sample B**
F_1	2.01	14.8	10.2	10.7	N/A
F_2	1.96	16.8	11.3	20.2	0.4
F_3	1.91	5.8	10.5	N/A	6.9
F_4	1.86	6.4	9.3	13.6	N/A
F_5	1.85	9.8	10.8	N/A	14.4
F_6	1.83	3.8	9.9	5.5	N/A
F_7	1.79	0.2	3.6	9.4	2.1
F_8	1.77	5.2	8.7	N/A	6.3
F_9	1.74	0.2	7.8	3.2	0.9
F_{10}	1.69	3.4	10.1	2.8	0.3
F_{11}	1.63	3.4	9.2	3.3	N/A

Table 5.1: Summary of ZPL parameters for each defect family

at half maximum (HWHM) width (w_i) ranging between 0.2 to 16.8 meV (listed in table 5.1). This suggests that the defects are robust against any inhomogeneity in the sample like flake orientation, thickness, strain and fluctuation in dielectric environmental conditions. The residual sum of squares over the full spectral range was found to be 6344, with a residual standard error of 4.4 occurrences. The high accuracy indicates that almost all the detected ZPLs fall under one of the discrete families.

It is noteworthy that the families F_1 and F_2 are the most predominant with respect to number of ZPLs that constitute them. These two families, with center $c_i \approx 2$ eV, contain $\approx 30\%$ of all the ZPLs. It should be mentioned that defect ZPLs centered around ≈ 2 eV are the most commonly reported hBN defects in the literature. The family F_7 on the other hand, has a remarkably narrow dispersion of energy ($w_i \approx$ 0.2 meV). The ZPLs of this family also exhibits very narrow spectral linewidth, with a mean ZPL HWHM linewidth $< \delta E_{00} >_7 = 3.6$ meV, as mentioned in table 5.1 (alongside the $< \delta E_{00} >$ of all other families). The narrow linewidth and the high occurrence of this family suggests exceptional decoupling of this type of defect from local environment in ambient conditions.

Defect family	**PSB** ΔE_{01} **(eV)**	**PSB shift** Δ_{PSB} **(meV)**	**Proportion of ZPL with PSB** (%)	**Mean DWF** f_{ZPL} (%)	**Mean DWF** f^{l}_{ZPL} **estimated from lineshape** (%)
F_1	1.85	160	22.4	65.3	57.4
F_2	1.78	180	96.1	67.7	55.1
F_3	1.73	180	7.4	54.7	44.4
F_4	1.69	170	66.1	55.8	48.1
F_5	1.70	150	55.5	52.4	46.8
F_6	1.63	200	95.6	73.7	61.7
F_7	1.60	190	91.2	67.3	58.6

Table 5.2: Summary of defect-phonon coupling characteristic parameters for each defect family

5.4 Defect-phonon coupling parameters

We use our statistical approach to extract and report some parameters related to the coupling between defects and lattice vibrations. Figure 5.4b shows a histogram of PSB energy shift with respect to their corresponding ZPLs, for 3898 spectra where PSB was identified. The histogram shows three peaks which match the three well known phonon modes energy in hBN. This further strengthens the reliability of the developed algorithm. Table 5.2 lists the extracted parameters characteristic of defect-phonon coupling for the families for which PSBs were detectable, i.e, F_1 to F_7. For the rest of the families, the spectral window of measurement did not cover the spectral position of their corresponding PSB. The parameters reported in table 5.2 include PSB energy centers ΔE_{01}, energy shifts $\Delta_{PSB} = \Delta E_{00} - \Delta E_{01}$ and percentage of ZPL which has a corresponding PSB. In terms of understanding the interaction of defects with the crystallographic environment, one important parameter is the reorganisation energy. It can be understood as the energy required to reorganise the local crystal structure around a defect following emission or absorption processes. An exact measurement of this parameter is beyond the scope of this study. However, this reorganization energy could be related to the energy shift between the ZPL energy and the mean energy estimated from the lineshape spectrum [142], which is presented in table 5.2.

In this table, we also list the Debye-Waller factor (DWF) for the defects, which is defined as the fraction of the total emission from a defect emitted into the ZPL. This factor characterizes the strength of electron-phonon coupling and is related to the Huang-Rhys factor (HRF) as: $DWF = e^{-(HRF)}$. Beside being a key aspect in exploring the microscopic origin of defects, the DWF is instrumental in determining the applicability of a defect in quantum technology [144,145,151,153,154]. In order to compare with previous studies, relying sometimes on PL spectra and not on lineshape, the DWF is estimated here in two ways: i) using the energy spectrum, $I_E = I_\lambda(\lambda)\frac{hc}{E}$ or ii) the lineshape spectrum $L_E(E = \frac{I_E}{E_3}$. The DWF values calculated by using both of these methods (denoted as f_{ZPL} and f^L_{ZPL}, respectively) are included in table 5.2. As is shown, f_{ZPL} can vary from 52% to 74%, while f^L_{ZPL} ranges from 44% to 62%.

5.5 SPS vs MPS

As mentioned in the previous section, the analyzed spectra in this study can be classified into two types, based on the number of peaks in a spectrum: single peak spectrum (SPS) and multiple peaks spectrum (MPS). Examples of each type are shown in figure 5.5a and 5.5b, respectively. A comparison between the ZPL energy histograms of these two types of spectra can provide new insights into the spectral families. It can also be a test of the reliability of ZPL identification by the algorithm. The histograms corresponding to SPS and MPS are presented in figure 5.5c and 5.5d, respectively. The extracted energy centers c_i for each family are listed in table 5.3. Although most of the detected ZPLs in this study are from MPS, clear discretization can be seen in both histograms. This combined with the consistency in the energy centers between SPS and MPS confirm that the presence of spectral families and the spectral assignment associated with them are independent of spectral features. Having said that, there are a few differences between the SPS and MPS ZPL energy distributions. The relative weight of the families are different between the histograms and particularly, families F_9 and F_{11} are only visible in the MPS histogram. Since each spectrum is collected from an area of 1 μ m^2, multiple peaks correspond to high density regions with more than one optically active defects in an area less than 1 μm^2. This assumption is supported by ref [157], where the authors reported the presence of multiple defects localized in a $\approx$ 35 nm region.

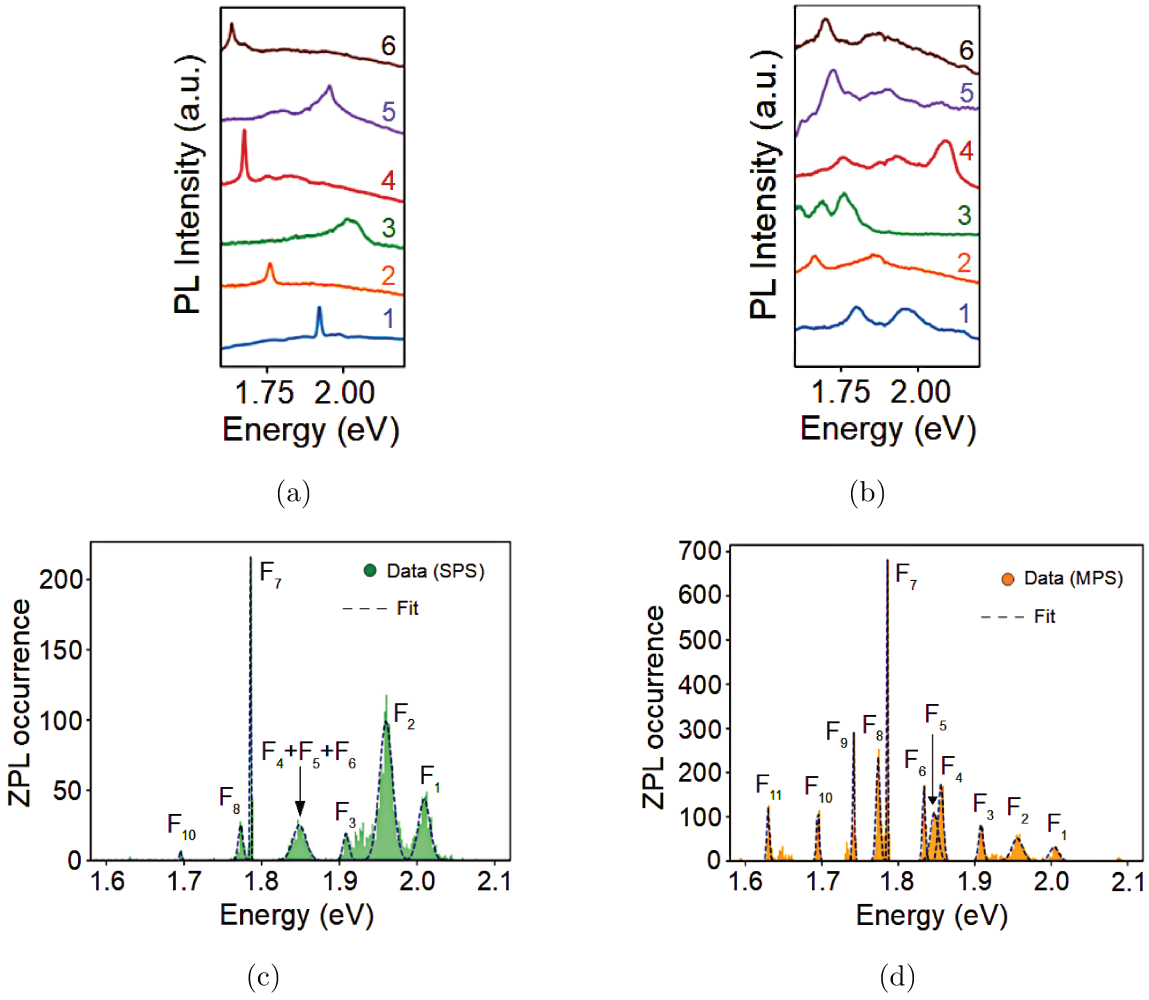

Figure 5.5: Stack plot showing 6 typical PL spectra in hBN, with offsets along normalized intensity, for (a) SPS and (b) MPS. (c) Histogram (green colored) of SPS based on 2564 ZPLs. (d) Histogram (orange colored) of MPS based on 5743 ZPLs. All defect families are identified with multi-Gaussian fits.

Defect family	Energy center, c_i (eV)					
	Spectrum type		Agglomeration type		Flakes building block size	
	SPS	MPS	Small	Large	Sample A (100 nm)	Sample B (10 μm)
F_1	2.01	2.00	2.01	2.01	2.01	N/A
F_2	1.96	1.96	1.96	1.96	1.96	N/A
F_3	1.91	1.91	N/A	N/A	N/A	1.91
F_4	1.85	1.86	N/A	1.86	1.86	N/A
F_5		1.85	N/A	N/A	N/A	1.8
F_6		1.83	N/A	1.83	1.83	N/A
F_7	1.79	1.79	1.79	1.79	1.79	N/A
F_8	1.77	1.77	N/A	N/A	N/A	1.77
F_9	N/A	1.74	N/A	1.74	1.74	N/A
F_{10}	1.70	1.69	N/A	1.70	1.70	N/A
F_{11}	N/A	1.63	N/A	1.61	1.63	N/A

Table 5.3: Summary of optical characteristics for defect families. Defect families (F1 to F11) with corresponding defect center energies in eV, through the use of multi-Gaussian fits. The centers are presented based on the size of building blocks flakes, agglomeration (agg.) type, and spectrum type, which encompasses both multiple peak spectra (MPS) and single peak spectra (SPS).

We can form the following hypothesis to explain the differences between the histograms for SPS and MPS. In dense regions, multiple closely located defects can interact to form a complex defect. For example: defects with opposite charges can pair through Coulomb interaction over a nanometric scale. Elastic interactions and covalent bond formation can also lead to defect pairing, although it requires close atomic separation to be efficient. Clustered defects like these have different electronic structure compared to a single defect, which can lead to small differences in ZPL center energies, between the two cases.

5.6 Effect of flake morphology and size distribution

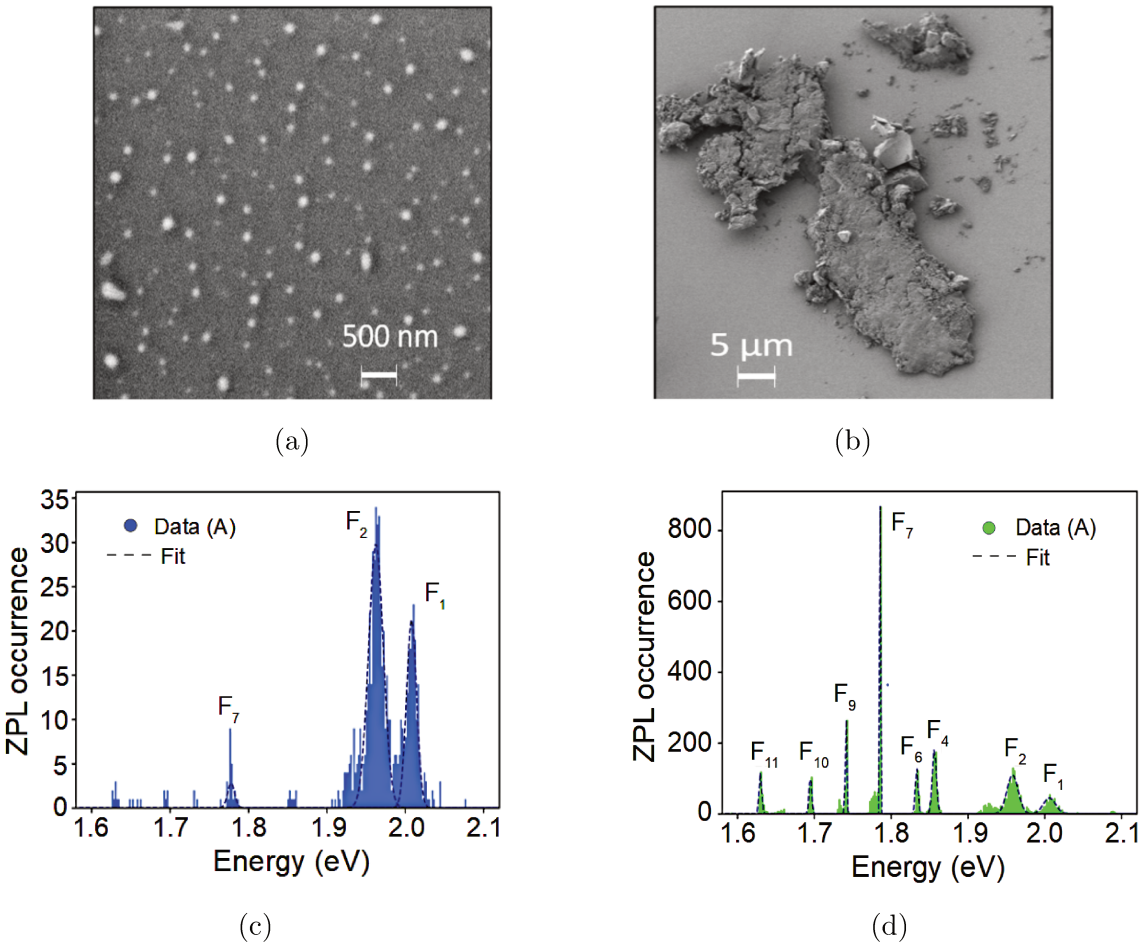

Figure 5.6: Impact of hBN agglomeration types. Representative scanning electron microscopy images of (a) small and (b) large hBN agglomerations in sample A. (c) Histogram of ZPLs (blue colored, number of ZPLs: 783) and corresponding fits (dashed line) for small hBN agglomerations in sample A. (d) Histogram of ZPLs (lime colored, number of ZPLs: 4839) and corresponding fits (dashed line) for large hBN agglomerations in sample A

After identifying the spectral families and extracting some key parameters, we turn our attention to the possibility of controlling the formation of defect families, by using the surface morphology of hBN flakes. The flakes can be deposited on the substrate via simple drop casting or spin coating. Whichever process is followed, the flakes

tend to cluster together horizontally and vertically in apparently random ways. The formation of such agglomeration seems to be unavoidable and leads to nonuniform hBN flake density across the substrate. By comparing the contrast profiles of white-light images and scanning electron microscopy (SEM) micrographs, we classified the PL probed areas on the sample into two flake arrangement morphologies: i) small agglomeration: isolated flakes, with flake agglomeration size typically below 1 μm ii) large agglomeration: flake agglomeration size above 5 μm. SEM images of both of these types of agglomeration are presented as example in figure 5.6a and 5.6b, respectively. Here, we are considering only sample A, which was prepared from supernatant solution containing a single narrow nanoflake size distribution centered around 100 nm. Analyzing the ZPL energy distribution of this sample will allow us to isolate the effect of flake morphology, excluding the effect of flake size. The ZPL energy histogram for small and large agglomeration for sample A are shown n figure 5.6c and 5.6d, respectively.

There are significant differences in terms of the spectral family occurrence between the two histograms. Small agglomeration flakes predominantly show only two families F_1 and F_2, with F_7 barely visible. Whereas, all the families except for F_3, F_5 and F_8 appear in large agglomeration flakes. Although a complete understanding of these differences are beyond the scope of our study, we can however, propose a line of thought. We know that flake edges play a significant role in the formation of defects. Not only defects appear preferentially near flake edges, the electronic structure of the defect has been shown to be linked to the nature of the edge as well. Different chemical groups can be attached to the flake edges; in particular, terminations made of nitrogen dangling bonds passivated by hydrogen were identified experimentally [169]. It has also been shown theoretically that for Boron [153, 155, 170] and Nitrogen [170] vacancy defects, such a Hydrogen passivation induces a symmetry lowering and lattice distortions, leading to significant changes in the ZPL energy. Sample A, containing small flakes, has a high density of edges. When individual flakes agglomerate, the edges and terminations can become modified. The structure and symmetry of the edges can be reconfigured. The reactive sites of the edges can become passivated or bonded to develop new type of termination. Agglomeration can also cause multiple defects to interact and form complex defects [171–173]. Besides these effects, agglomeration can cause changes in the dielectric environment around a defect. Overall, these arguments present a plausible explanation for the broader range of defects seen

in large agglomerations as opposed to small ones.

5.7 Defect families vs building blocks

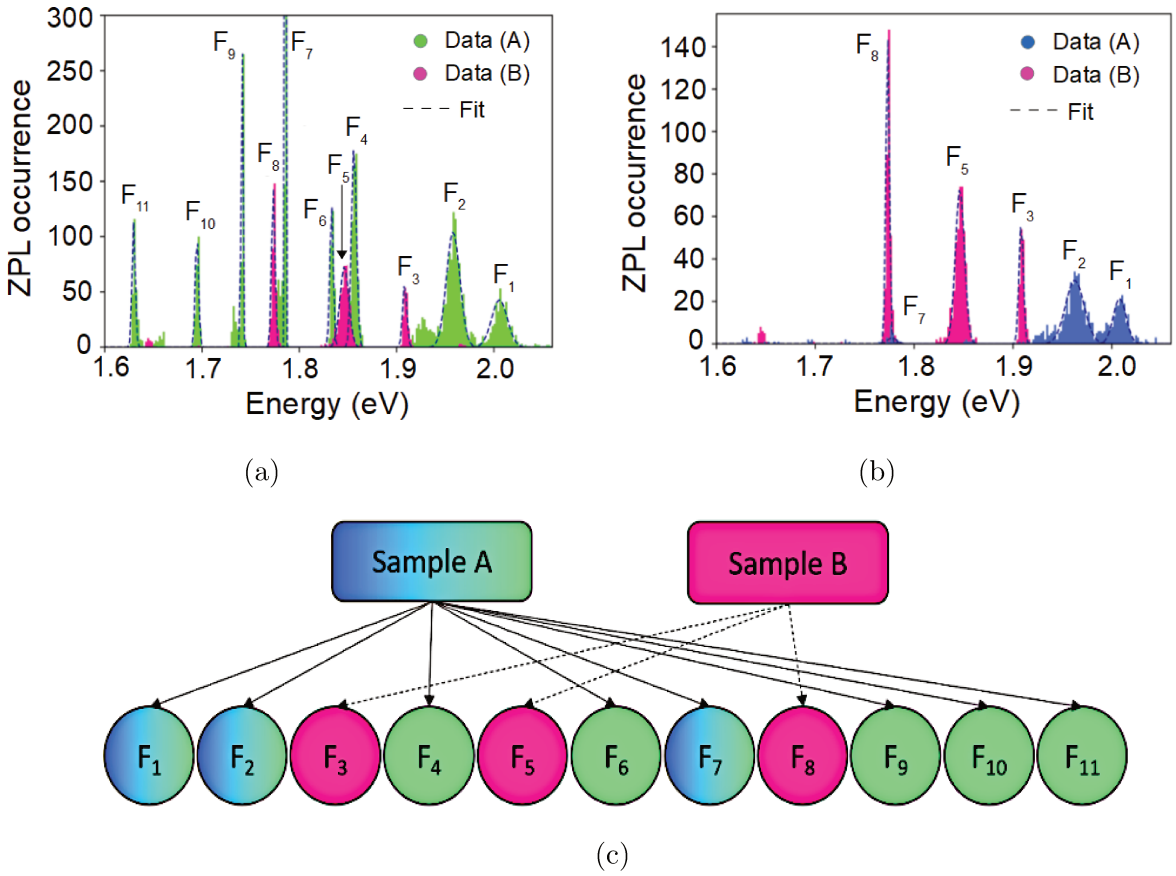

Figure 5.7: Impacts of hBN building blocks. (a) Comparative histogram profiles and corresponding fits (dashed line) as a function of large agglomeration for samples A (lime-colored histogram, number of ZPL: 4839) and B (pink colored histogram, number of ZPL: 991). Value of ZPL peak maxima for F7 is 846. (b) Comparative histograms and corresponding fits (dashed line) of defect families for two extremely distinct morphological cases: small hBN agglomeration from sample A (royal-blue-colored histogram, number of ZPLs: 783) vs large hBN agglomeration from sample B (deep-pink-colored histogram, number of ZPLs: 991). (c) Schematic summary showcasing the presence of different defect families for samples A and B.

We now turn our attention towards the influence of flake size on the occurrences of defect families. In order to do that, we compare the results obtained from sample A, prepared with small flakes a with mean size of 100 nm, with sample B, fabriacted with larger flakes with two size distributions centered at 210 nm and 11 μ m (figure 5.1c). We refer to the size selected flakes used to prepare the samples as "building block flakes". We focus only on large agglomerations in both samples. The small agglomerations are not taken into consideration as they do not contain large sized flakes. In contrast, the large agglomerations in sample B predominantly consist of larger flakes of mean size 11 μm. Comparing the ZPL energy histograms between the large agglomeration areas between sample A and B allows us to shed light on the effect of flake size only, as shown in figure 5.7a. Only 3 families (F_3, F_5 and F_8 are present in the ZPL histogram of sample B (large flakes). On the other hand, sample A shows all the other families except for these aforementioned three families, displaying the occurrence of complimentary set of defect families in these two types of hosts. It is clear that the flake size has a significant effect on the type of defect formation. Once again, we can provide a initial hypothesis in response to this observation. We know that the hBN surface to volume ratio is lower compared to small flakes [168]. So, the density of defects lying close to edges or surfaces will be significantly low in large flakes of ≈ 10 μ m. In addition to this, The position of a defect relative to edges can alter their electronic and optical properties. Hence, large hBN flakes should host deeper defects, which are less effected by edges, leading to distinct types of defects compared to small flakes.

The observations that hBN flake morphology and flake size, both allow some degree of control over the formation of defect families, raised the question: how much control over defect formation can we achieve using the the two aforementioned parameters. To answer this, we compare the ZPL energy histograms between small agglomerations (isolated flakes) flakes from sample A and large agglomerations from sample B (figure 5.7b). These two extreme cases reveal a clear spectral discrepancy. The "edge defects" from sample A (F_1) and F_2) shows a notable blue-shift compared to the "deeper defects" from sample B (F_3, F_5 and F_8). It is also worth noting that the edge defects exhibit the widest spectral width distribution (w_i in table 5.1), among all other types of defects. This strengthens the assignment of these defects as "edge defects", since their atomically thin local environment makes them susceptible to more fluctuation. The dependence of defect families on the morphological parameters

of flakes presents an opportunity to easily control the spectral occurrences of hBN defects. By carefully selecting the sizes of hBN building blocks and using precise spin-coating techniques, one can either prevent or encourage agglomeration, offering a simple method to customize the spectral properties of defects in hBN hosts.

5.8 Defect density vs morphology

We wrap up our study by analyzing the global density of defects with respect to hBN flake morphology. Reaching a suitable density of defects would be a desirable aspect of potential hBN defect based devices. We consider two types of defect density. First, we define the global density of defects as the total number of defects divided by the total area probed by PL. On the other hand, we define the effective density of defects as the total number of detected defects divided by the area covered by hBN flakes. The method we used to calculate the effective density is as follows. We determined the total PL probed area for small agglomeration and large agglomeration to be $7 \times 10^4 \mu m^2$ and $2 \times 10^4 \mu m^2$, respectively. To determine the effective surface area coverage by hBN, we analyzed the gray scale contrast profile of the white light and SEM images of the measurement areas. The pixels of the images where the contrast was more than two times higher than the background were considered to be covered by hBN and were taken into account when calculating the effective density. This caused occasional exclusion of very low contrast hBN nanoflake areas, leading to slight underestimation of effective hBN coverage area. The average percentage of hBN coverage per mapped area was found to be 9% for small agglomeration and 68% for large agglomeration. The calculated effective and global densities for different morphologies are provided in table 5.4. We observe somewhat similar effective density (from 0.26 to $0.53 \mu m$) for all cases. This is despite the difference in host thickness between small agglomeration in sample A (isolated few layer flakes) and large agglomeration in sample B. This is an indication that most of the defects appear in the first few layers near the surface, regardless of the flake morphology. Our observation supports a hypothesis presented in ref [174], which used a different sample preparation protocol, but involved high temperature annealing similar to our study. It is worth noting that the annealing process leads to the migration of defects, potentially resulting in their formation at the surfaces and edges. In addition, our achieved defect density is comparable to one of the highest reported hBN defect densities, observed in mechanically exfoliated

	Effective (global) defect density ($/\mu m^2$)	
Flake morphology	Sample A	Sample B
Small agglomeration	0.26 (0.03)	N/A
Large agglomeration	0.53 (0.37)	0.48 (0.32)

Table 5.4: Summary of the average effective density of defects as a function of hBN flake morphologies

samples treated with advanced thermal processing [175]. This highlights that the morphological control of defects is compatible with achieving a high defect density.

5.9 Conclusion and perspective

We conducted an extensive statistical analysis involving a large dataset of hBN defect PL emission lines, totaling over 10000 instances. Through this comprehensive sampling, we identified 11 distinct spectral families of defects, each with well defined emission centers within the spectral range of 1.6 to 2.2 eV. Our result challenges previous hypotheses that suggested spectral randomness in defect emission, leading to a broad, continuous energy distribution. Utilizing our statistical approach, we also extracted important defect parameters, including emission linewidths, spatial defect density, phonon sidebands (PSBs), and Franck-Condon factors.

Our findings provide valuable insights for determining the microscopic origins of emitters in hBN hosts. Notably, the spectral spacing between defect families could serve as a critical parameter for theoretical studies, as opposed to relying on absolute energy values, which are difficult to determine with sufficient precision and complicate the identification of the chemical nature of defects. Additionally, we demonstrated that the morphology of hBN hosts significantly influences the spectral occurrence of defect families. We have demonstrated that it is possible to selectively generate a variety of defects while maintaining a high defect density, by controlling the size and

arrangement of flakes. This was achieved through simple methods such as centrifugation and drop casting, offering a practical and scalable alternative to expensive defect engineering techniques.

Although we have put forward several hypotheses, this study does not fully explain the underlying physical mechanisms. Therefore, the newfound flexibility provided by controlling flake morphology clearly merits further exploration to enhance our understanding of defect formation and to fully leverage its potential for precise spectral control of defects in hBN.

One of the key motivations of this work was to reproduce defects with consistent emission energies, enabling resonant FWM microscopy measurements on these defects. For FWM microscopy to be successfully applied, several practical requirements must be met. In our experimental setup, the pulsed laser source operates within an emission range of 1.1 eV to 1.8 eV, imposing a strict limitation on the types of defects compatible with the system. Additionally, any significant adjustment in the laser energy (greater than 20 meV) necessitates a complete realignment of the setup—a complex and time-consuming process. Consequently, if the defect emission energies vary over a broad range, conducting measurements on a large number of defects becomes impractical. Furthermore, FWM microscopy demands that the system under investigation exhibit high oscillator strength, as well as temporal and spectral stability. The results presented in this chapter contributed to our ability to reproduce defects with suitable emission energies.

We have attempted FWM microscopy measurment on defect families with emission energies below 1.8 eV, but these efforts have thus far been unsuccessful. There are several factors that may account for this. First, the temporal and spectral stability of the defects can be improved. Second, the long defect lifetimes in hBN, which have been reported to reach up to 18 μs at room temperature [176], lead to a reduced oscillator strength, making it exceedingly difficult to detect an FWM signal from such systems. Finally, Many types of defects in hBN have been demonstrated to be charged defects with more than two levels involved in the defect transition, making it impossible to excite these systems resonantly. Further studies, building upon the findings in this chapter, could help engineer a very narrow set of families with high temporal and spectral stability. Furthermore, coupling these defects to photonic structures like cavity [177] or metamaterial [178], could help reduce the defect lifetime and enhance their emission. These steps would greatly increase the likelihood of

successfully measuring FWM signal from these defects, enabling the demonstration of ultrafast coherent control on these systems and bringing them to the forefront of quantum information technologies.

6 Conclusion

This thesis aimed to investigate the dynamic properties of excitons VdW materials and assess potential methods for engineering some of the excitonic properties. The majority of the work in this thesis centered around TMDs and advanced vdW structures incorporating TMDs. To this purpose, we developed a state of the art FWM microscopy experimental setup, combining a diffraction limited spatial resolution, ultrafast time resolution ($\approx$ 100 femtosecond) and $\approx 300\mu\ eV$ spectral resolution.

Using this experiment, we studied the coherence and population dynamics of anisotropic excitons in ReS_2. Our findings revealed homogeneously limited coherence dynamics for excitons in this material and population dynamics characterized by three decay timescales (from 150 fs to several ns). These results showcase the potential of excitons in ReS_2 as a promising candidate for optoelectronic and photonic devices.

We have studied an advanced vdW structure based on $MoSe_2$. This $MoSe_2$-graphene heterostructure enabled us to investigate the impact of graphene on the dynamic properties of excitons in $MoSe_2$ monolayer. Our approach highlights the existence of a long-time scale process of photo-induced dynamic charge carrier transfer in graphene, occurring over 100 ps. We also discovered a novel effect of graphene on the excitons, manifesting as a change in inhomogeneous broadening with excitation power density, leading to a change of the population decay timescale. Several hypotheses were proposed to explain these findings and to address the difference with earlier studies.

In addition to investigating the dynamic properties of excitons in vdW structures, we conducted an extensive statistical analysis of quantum defect emission energy in hBN using μ-PL spectroscopy. Our analysis revealed a clear discretization of emission energy distribution in histograms of spectral occurrences, built from 8307 zero phonon lines (ZPLs). This finding challenges the previous hypothesis of a spectrally random distribution of defect ZPLs in hBN. We also uncovered the role of hBN flake surface morphology and size in determining defect formation. Our results could potentially help to decipher the microscopic origin of defects and demonstrate a scalable approach for selectively fabricating defects with a narrow emission energy distribution.

7 Perspective

In this last section, we will take a look at how the work presented in this thesis opens up numerous opportunities for future research. The developed FWM experimental setup can be applied to study the dynamic properties of excitonic systems in various semiconductor structures and vdW materials. We will discuss two major ongoing research efforts in our lab.

7.1 Electric gate control of excitons in $MoSe_2$

A 2D system like $MoSe_2$ monolayer presents an excellent platform for investigating the influence of static electric field largely due to the high binding energy of the excitons. A large number of studies have reported a quadratic red-shift in exciton energy (referred to as "Quantum confined stark effect"), as a result of out of plane electric field in both quantum well structures [179–182] and TMDs [183–185]. Studies on the effect of applied in-plane electric field in quantum well have shown two competing effects on the exciton energy: a red-shift due to quadratic stark shift and a blue-shift arising from the electron and hole being pushed in opposite directions [179, 186–188]. Additionally, there is a significant broadening of the exciton linewidth [179, 186, 187]. Such effects have not been clearly highlighted so far with TMDs. Indeed, to highlight the intrinsic electric field effect on the exciton, particular care must be taken in the heterostructure design to avoid change of the doping level with the applied fields. Such changes could lead to variations in the exciton energy, thereby potentially masking the intrinsic effect of the applied field [49, 184, 189]. Moreover, in stark contrast to quantum wells (QWs), only a few studies have been conducted on TMDs in dynamic regimes [49, 190, 191], and these are not free from the doping effects discussed above. Therefore, the intrinsic influence of the electric field, in various configurations, on lifetime and coherence time of excitons remains to be explored. In contrast, the sample we are studying relies on a specific design with dual gates, allowing us to uncover the effects of both in-plane and out-of-plane electric fields on excitons and exciton dynamics, while potentially minimizing the impact of significant changes in doping levels

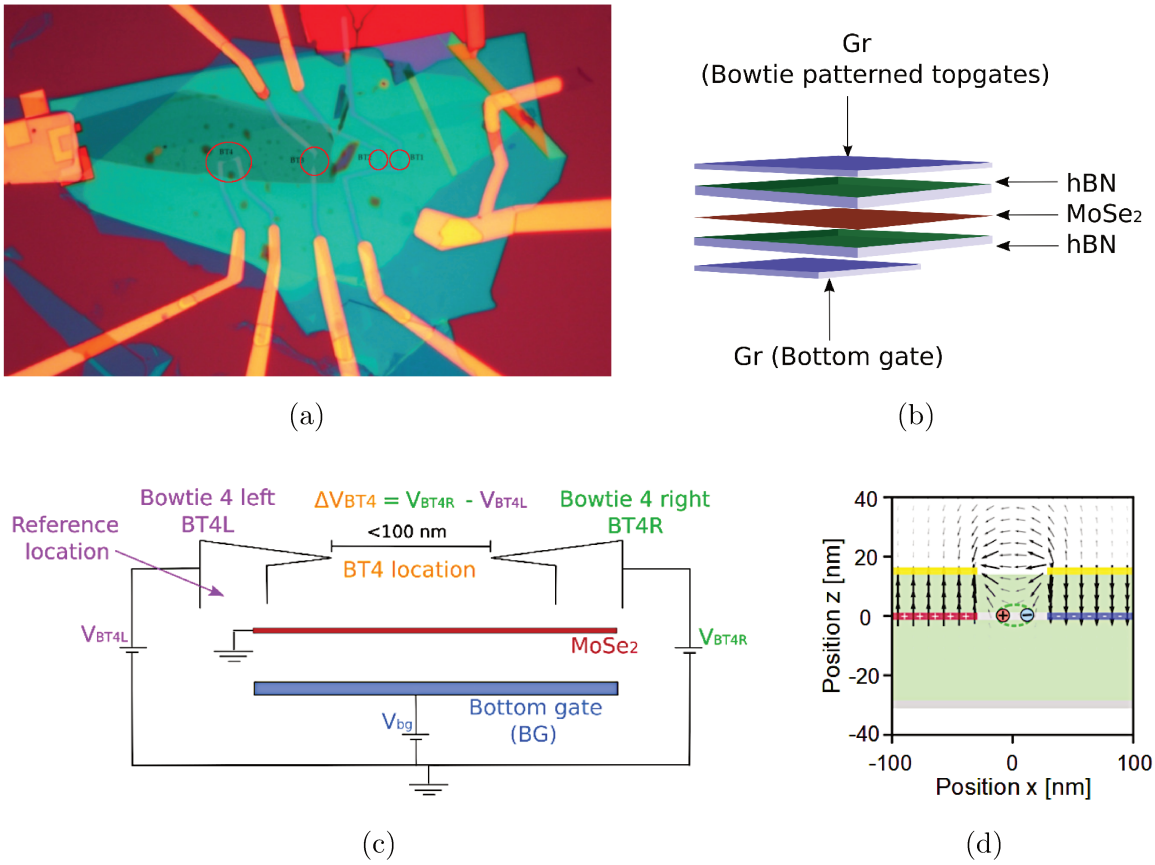

Figure 7.1: (a) Color image of hBN encapsulated $MoSe_2$ sample with bottom gate and bowtie gates. The locations with the bowtie gates are marked with red color circles [192].(b) Schematic showing the stacking of $MoSe_2$, hBN and graphene used in the sample. (c) Schematic of the gate circuit in the sample under investigation, showing the bowtie 4 left (BT4L) and right (BT4R) arms, with the corresponding voltages. The BT4 location and the reference location are also demonstrated. (d) Side view (xz) schematic of the electric field at a vertical cut along y = 0. The schematic shows two bowtie arms (in gold color) and the corresponding electric field lines. This image was taken from our collaborators [192]

We received the sample under investigation, from our collaborator Thibault Chervy, working in NTT reserach (Sunnyvale, USA). It contains a $MoSe_2$ monolayer, encapsulated in hBN and is contacted with gate electrodes made of graphene. Figures 7.1a and 7.1b show a color image of the sample, the stacking of different layers in the sample, respectively. As mentioned, this specific sample design and contacts allow for

the application of electric fields in different directions based on the sample location: a transverse electric field (referred to as the reference location, situated below the arm of the bow-tie, see figure 7.2b) and an in-plane electric field (referred to as the BT4 location situated between the bowtie, see figure 7.2a). Figure 7.1c and 7.1d show a schematic of the bowtie gate circuit and a sideview of the electric field lines.

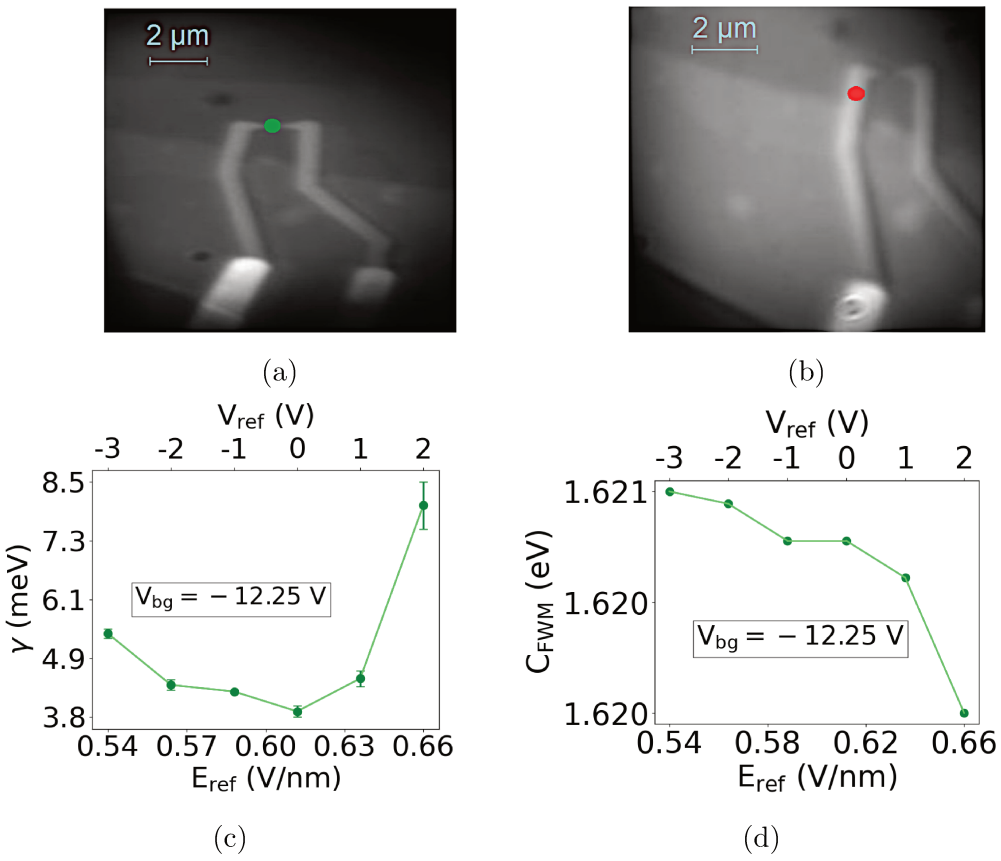

Figure 7.2: (a) White light image of bowtie 4 (BT4) location, marked with a green circle. (b) White light image of the reference location, marked with a red circle. Evolution of (c) homogeneous broadening linewidth γ and (d) FWM peak energy, C_{FWM}, for the reference location, as a function of V_{ref} and E_{ref}, under charge neutrality. The measurements were performed at 7 K temperature and ≈223 W/cm^2 pump power density.

In our study, we used the resonant four-wave mixing (FWM) microscopy experimental setup to explore the coherent dynamics of excitons as a function of the applied electric field in both directions. First, we identified the voltage regime where the dop-

ing changes induced by the difference of voltage could be minimized (figure 7.2b), allowing us to explore more intrinsic effects of the applied transverse electric field. We confirmed this by observing a gradual redshift in the exciton transition (figure 7.2d), in contrast to the blueshift caused by increased doping. Additionally, the study of coherence dynamics showed an increase in the homogeneous broadening with the electric field (figure 7.2c), though to a lesser extent compared to previous coherence studies [49], suggesting that doping increase may not be the dominant mechanism of decoherence.

Conversely, at the BT4 location (figure 7.2a), we were also able to observe features of the coherent dynamics due to the in-plane component of the electric field. Importantly, the specific experimental setup we employed, based on dual-balanced detection and optical heterodyne technique, allowed us to finely monitor the exciton resonance energy shift. This revealed a signature of a blueshift caused by the in-plane electric field in contrast to the redshift observed with the transverse field. This effect is likely due to a different mechanism, such as the reduction in exciton binding energy resulting from the electric field pushing the electron and hole in opposite directions [179, 186–188].

However, at this stage, deciphering all the contributions (doping, inhomogeneity of the electric field, heating, and intrinsic effects of the electric field on the exciton wavefunction) to the coherent dynamics, exciton energy shift, and lifetime processes is still premature, and further studies are needed. In particular, to completely eliminate the influence of doping changes, we propose two configurations for future measurements on this sample: i) using compensating gate voltage combinations to maintain a constant doping level [183], and ii) removing the sample ground contact and operating in a floating gate configuration, thereby avoiding any charge transfer from the electrode to the 2D layer. These measurements should open up new perspectives for understanding and controlling exciton energy and dynamics through applied electric fields, without the influence of doping changes, which have tended to dominate previous studies.

7.2 Toward confined systems

Electric field-controlled samples, such as the one described in the previous section also open novel breakthrough perspectives for shaping the dimensionality and ge-

ometry of excitonic wavefunctions, including 1D, ring, and 0D excitons [192]. The investigation of the dynamics of such shaped excitons, from 1D excitonic systems to confined 0D systems is another intriguing avenue of research being pursued in our group. Other 0D systems of interest include defects in hBN [45, 142, 150, 193] and bound excitons in TMDs [43, 112, 115, 117]. These single-photon emitters hold immense potential as foundational components for next-generation quantum technologies. Challenges for FWM measurements on these systems include weak oscillator strength, long lifetime and the possibility of these systems possessing metastable states. Integrating these confined systems into photonic structures, such as cavities, metamaterials or nanoplasmonic stuctures could significantly enhance their interaction with light and potentially reduce their lifetime, allowing then to perform more advanced spectroscopies. [177, 178, 194]. Additionally, the results from this thesis regarding the understanding of quantum defects in hBN could be used and developed towards a narrow and selective formation of quantum defects, making the feasibility of FWM measurements on such systems easier. Such measurements could reveal intriguing fundamental properties of these systems and for instance, a demonstration of ultrafast coherent control on 0D systems could propel them into the forefront of quantum information technologies.

References

[1] Gang Hee Han, Dinh Loc Duong, Dong Hoon Keum, Seok Joon Yun, and Young Hee Lee. van der waals metallic transition metal dichalcogenides. *Chemical Reviews*, 118(13):6297–6336, 2018. PMID: 29957928.

[2] Andrea Splendiani, Liang Sun, Yuanbo Zhang, Tianshu Li, Jonghwan Kim, Chi-Yung Chim, Giulia Galli, and Feng Wang. Emerging Photoluminescence in Monolayer MoS_2. *Nano Letters*, 10(4):1271–1275, 2010. PMID: 20229981.

[3] Yi Zhang, Tay-Rong Chang, Bo Zhou, Yong-Tao Cui, Hao Yan, Zhongkai Liu, Felix Schmitt, James Lee, Rob Moore, Yulin Chen, et al. Direct observation of the transition from indirect to direct bandgap in atomically thin epitaxial $MoSe_2$. *Nature nanotechnology*, 9(2):111–115, 2014.

[4] Gerardo G. Naumis. 5 - electronic properties of two-dimensional materials. In Eui-Hyeok Yang, Dibakar Datta, Junjun Ding, and Grzegorz Hader, editors, *Synthesis, Modeling, and Characterization of 2D Materials, and Their Heterostructures*, Micro and Nano Technologies, pages 77–109. Elsevier, 2020.

[5] Luis Enrique Parra Lopez. *Tailoring the luminescence of atomically-thin semiconductors with sub-nanometer resolution.* PhD thesis, Université de Strasbourg, 2021.

[6] Guillaume Froehlicher. *Optical spectroscopy of two-dimensional materials: graphene, transition metal dichalcogenides and van der Waals heterostructures.* PhD thesis, Université de Strasbourg, 2016.

[7] Akanksha R Urade, Indranil Lahiri, and KS Suresh. Graphene properties, synthesis and applications: a review. *Jom*, 75(3):614–630, 2023.

[8] Manish Chhowalla, Hyeon Suk Shin, Goki Eda, Lain-Jong Li, Kian Ping Loh, and Hua Zhang. The chemistry of two-dimensional layered transition metal dichalcogenide nanosheets. *Nature chemistry*, 5(4):263–275, 2013.

[9] Gang Hee Han, Dinh Loc Duong, Dong Hoon Keum, Seok Joon Yun, and Young Hee Lee. van der waals metallic transition metal dichalcogenides. *Chemical reviews*, 118(13):6297–6336, 2018.

[10] Qing Hua Wang, Kourosh Kalantar-Zadeh, Andras Kis, Jonathan N Coleman, and Michael S Strano. Electronics and optoelectronics of two-dimensional transition metal dichalcogenides. *Nature nanotechnology*, 7(11):699–712, 2012.

[11] Alexey Chernikov, Timothy C Berkelbach, Heather M Hill, Albert Rigosi, Yilei Li, Özgur B Aslan, David R Reichman, Mark S Hybertsen, and Tony F Heinz. Excitons in atomically thin transition-metal dichalcogenides. In *2014 Conference on Lasers and Electro-Optics (CLEO)-Laser Science to Photonic Applications*, pages 1–2. IEEE, 2014.

[12] Gang Wang, Alexey Chernikov, Mikhail M Glazov, Tony F Heinz, Xavier Marie, Thierry Amand, and Bernhard Urbaszek. Colloquium: Excitons in atomically thin transition metal dichalcogenides. *Reviews of Modern Physics*, 90(2):021001, 2018.

[13] Sophia Helmrich. *Optical properties of quasiparticles in monolayer and bilayer TMDCs*. PhD thesis, Technische Universitaat Berlin (Germany), 2020.

[14] Ursula Wurstbauer, Bastian Miller, Eric Parzinger, and Alexander W Holleitner. Light–matter interaction in transition metal dichalcogenides and their heterostructures. *Journal of Physics D: Applied Physics*, 50(17):173001, 2017.

[15] Marco Manca. *Study of the optoelectronic properties of atomically thin WSe2*. PhD thesis, INSA de Toulouse, 2019.

[16] Tanushree H Choudhury, Xiaotian Zhang, Zakaria Y Al Balushi, Mikhail Chubarov, and Joan M Redwing. Epitaxial growth of two-dimensional layered transition metal dichalcogenides. *Annual Review of Materials Research*, 50:155–177, 2020.

[17] Ching-Hwa Ho and Zhan-Zhi Liu. Complete-series excitonic dipole emissions in few layer ReS_2 and $ReSe_2$ observed by polarized photoluminescence spectroscopy. *Nano Energy*, 56:641–650, 2019.

[18] Avijit Dhara, Devarshi Chakrabarty, Pritam Das, Aswini K Pattanayak, Shreya Paul, Shreyashi Mukherjee, and Sajal Dhara. Additional excitonic features and momentum-dark states in res 2. *Physical Review B*, 102(16):161404, 2020.

[19] Burak Aslan, Daniel A Chenet, Arend M Van Der Zande, James C Hone, and Tony F Heinz. Linearly polarized excitons in single-and few-layer res_2 crystals. *ACS Photonics*, 3(1):96–101, 2015.

[20] D Biswas, Alex M Ganose, R Yano, JM Riley, L Bawden, OJ Clark, J Feng, L Collins-Mcintyre, MT Sajjad, W Meevasana, et al. Narrow-band anisotropic electronic structure of res_2. *Physical Review B*, 96(8):085205, 2017.

[21] CH Ho, YS Huang, Kwong-Kau Tiong, and PC Liao. Absorption-edge anisotropy in res 2 and rese 2 layered semiconductors. *Physical Review B*, 58(24):16130, 1998.

[22] K Friemelt, M-Ch Lux-Steiner, and E Bucher. Optical properties of the layered transition-metal-dichalcogenide ReS_2: Anisotropy in the van der Waals plane. *Journal of applied physics*, 74(8):5266–5268, 1993.

[23] CH Ho, PC Liao, YS Huang, Tzuen-Rong Yang, and Kwong-Kau Tiong. Optical absorption of res 2 and rese 2 single crystals. *Journal of applied physics*, 81(9):6380–6383, 1997.

[24] CM Fang, GA Wiegers, C Haas, and RA De Groot. Electronic structures of, and in the real and the hypothetical undistorted structures. *Journal of Physics: Condensed Matter*, 9(21):4411, 1997.

[25] Joshua O Island, Gary A Steele, Herre SJ van der Zant, and Andres Castellanos-Gomez. Environmental instability of few-layer black phosphorus. *2D Materials*, 2(1):011002, 2015.

[26] Sruthi Kuriakose, Taimur Ahmed, Sivacarendran Balendhran, Vipul Bansal, Sharath Sriram, Madhu Bhaskaran, and Sumeet Walia. Black phosphorus: ambient degradation and strategies for protection. *2D Materials*, 5(3):032001, 2018.

[27] Erfu Liu, Yajun Fu, Yaojia Wang, Yanqing Feng, Huimei Liu, Xiangang Wan, Wei Zhou, Baigeng Wang, Lubin Shao, Ching-Hwa Ho, et al. Integrated digital inverters based on two-dimensional anisotropic ReS_2 field-effect transistors. *Nature communications*, 6(1):1–7, 2015.

[28] Tomasz Jakubczyk, Valentin Delmonte, Maciej Koperski, Karol Nogajewski, Clément Faugeras, Wolfgang Langbein, Marek Potemski, and Jacek Kasprzak. Radiatively limited dephasing and exciton dynamics in $MoSe_2$ monolayers revealed with four-wave mixing microscopy. *Nano letters*, 16(9):5333–5339, 2016.

[29] Tomasz Jakubczyk, Karol Nogajewski, Maciej R Molas, Miroslav Bartos, Wolfgang Langbein, Marek Potemski, and Jacek Kasprzak. Impact of environment on dynamics of exciton complexes in a WS_2 monolayer. *2D Materials*, 5(3):031007, 2018.

[30] Tomasz Jakubczyk, Goutham Nayak, Lorenzo Scarpelli, Wei-Lai Liu, Sudipta Dubey, Nedjma Bendiab, Laëtitia Marty, Takashi Taniguchi, Kenji Watanabe, Francesco Masia, et al. Coherence and density dynamics of excitons in a single-layer MoS_2 reaching the homogeneous limit. *ACS nano*, 13(3):3500–3511, 2019.

[31] Caroline Boule, Diana Vaclavkova, Miroslav Bartos, Karol Nogajewski, Lukas Zdražil, Takashi Taniguchi, Kenji Watanabe, Marek Potemski, and Jacek Kasprzak. Coherent dynamics and mapping of excitons in single-layer mose 2 and wse 2 at the homogeneous limit. *Physical Review Materials*, 4(3):034001, 2020.

[32] Mathias Gehlmann, Irene Aguilera, Gustav Bihlmayer, Slavomiir Nemsak, Philipp Nagler, Pika Gospodaric, Giovanni Zamborlini, Markus Eschbach, Vitaliy Feyer, Florian Kronast, et al. Direct observation of the band gap transition in atomically thin ReS_2. *Nano letters*, 17(9):5187–5192, 2017.

[33] Etienne Lorchat, Luis E Parra López, Cédric Robert, Delphine Lagarde, Guillaume Froehlicher, Takashi Taniguchi, Kenji Watanabe, Xavier Marie, and Stéphane Berciaud. Filtering the photoluminescence spectra of atomically thin semiconductors with graphene. *Nature nanotechnology*, 15(4):283–288, 2020.

[34] Guillaume Froehlicher, Etienne Lorchat, and Stéphane Berciaud. Charge versus energy transfer in atomically thin graphene-transition metal dichalcogenide van der waals heterostructures. *Physical Review X*, 8(1):011007, 2018.

[35] Jiaqi He, Nardeep Kumar, Matthew Z Bellus, Hsin-Ying Chiu, Dawei He, Yongsheng Wang, and Hui Zhao. Electron transfer and coupling in graphene–tungsten disulfide van der waals heterostructures. *Nature communications*, 5(1):5622, 2014.

[36] Etienne Lorchat, Stefano Azzini, Thibault Chervy, Takashi Taniguchi, Kenji Watanabe, Thomas W Ebbesen, Cyriaque Genet, and Stéphane Berciaud. Room-temperature valley polarization and coherence in transition metal dichalcogenide–graphene van der waals heterostructures. *ACS photonics*, 5(12):5047–5054, 2018.

[37] Archana Raja, Andrey Chaves, Jaeeun Yu, Ghidewon Arefe, Heather M Hill, Albert F Rigosi, Timothy C Berkelbach, Philipp Nagler, Christian Schüller, Tobias Korn, et al. Coulomb engineering of the bandgap and excitons in two-dimensional materials. *Nature communications*, 8(1):15251, 2017.

[38] Tomasz Jakubczyk, Miroslav Bartos, Karol Nogajewski, Lorenzo Scarpelli, Wolfgang Langbein, Marek Potemski, and Jacek Kasprzak. Dynamics of resonantly excited excitons in mose _2 and ws _2 single-layers monitored with four-wave mixing. *arXiv preprint arXiv:2002.01720*, 2020.

[39] Lorenzo Scarpelli, Francesco Masia, EM Alexeev, F Withers, AI Tartakovskii, KS Novoselov, and W Langbein. Resonantly excited exciton dynamics in two-dimensional mose 2 monolayers. *Physical Review B*, 96(4):045407, 2017.

[40] Carino Ferrante, Giorgio Di Battista, Luis E Parra López, Giovanni Batignani, Etienne Lorchat, Alessandra Virga, Stéphane Berciaud, and Tullio Scopigno. Picosecond energy transfer in a transition metal dichalcogenide–graphene heterostructure revealed by transient raman spectroscopy. *Proceedings of the National Academy of Sciences*, 119(15):e2119726119, 2022.

[41] Sabrine Ayari, Adlen Smiri, Aida Hichri, Sihem Jaziri, and Thierry Amand. Radiative lifetime of localized excitons in transition-metal dichalcogenides. *Physical Review B*, 98(20):205430, 2018.

[42] K. S. Novoselov, A. K. Geim, S. V. Morozov, D. Jiang, Y. Zhang, S. V. Dubonos, I. V. Grigorieva, and A. A. Firsov. Electric field effect in atomically thin carbon films. *Science*, 306(5696):666–669, 2004.

[43] Mehran Kianinia, Zai-Quan Xu, Milos Toth, and Igor Aharonovich. Quantum emitters in 2d materials: Emitter engineering, photophysics, and integration in photonic nanostructures. *Applied Physics Reviews*, 9(1), 2022.

[44] Raul Perea-Causin, Daniel Erkensten, Jamie M Fitzgerald, Joshua JP Thompson, Roberto Rosati, Samuel Brem, and Ermin Malic. Exciton optics, dynamics, and transport in atomically thin semiconductors. *APL Materials*, 10(10), 2022.

[45] Akbar Basha Dhu-al-jalali-wal-ikram Shaik and Penchalaiah Palla. Optical quantum technologies with hexagonal boron nitride single photon sources. *Scientific reports*, 11(1):12285, 2021.

[46] Wenjing Zhang, Chih-Piao Chuu, Jing-Kai Huang, Chang-Hsiao Chen, Meng-Lin Tsai, Yung-Huang Chang, Chi-Te Liang, Yu-Ze Chen, Yu-Lun Chueh, Jr-Hau He, et al. Ultrahigh-gain photodetectors based on atomically thin graphene-MoS_2 heterostructures. *Scientific reports*, 4(1):3826, 2014.

[47] David Tebbe, Marc Schütte, Kenji Watanabe, Takashi Taniguchi, Christoph Stampfer, Bernd Beschoten, and Lutz Waldecker. Tailoring the dielectric screening in WS_2–graphene heterostructures. *npj 2D Materials and Applications*, 7(1):29, 2023.

[48] Samuel Brem. *Microscopic theory of exciton dynamics in two-dimensional materials*. PhD thesis, Chalmers Tekniska Hogskola (Sweden), 2020.

[49] Aleksander Rodek, Thilo Hahn, James Howarth, Takashi Taniguchi, Kenji Watanabe, Marek Potemski, Piotr Kossacki, Daniel Wigger, and Jacek Kasprzak. Controlled coherent-coupling and dynamics of exciton complexes in a $MoSe_2$ monolayer. *2D Materials*, 10(2):025027, 2023.

[50] Galan Moody, Chandriker Kavir Dass, Kai Hao, Chang-Hsiao Chen, Lain-Jong Li, Akshay Singh, Kha Tran, Genevieve Clark, Xiaodong Xu, Gunnar Berghäuser, et al. Intrinsic homogeneous linewidth and broadening mechanisms

of excitons in monolayer transition metal dichalcogenides. *Nature communications*, 6(1):8315, 2015.

[51] Christopher L Smallwood and Steven T Cundiff. Multidimensional coherent spectroscopy of semiconductors. *Laser & Photonics Reviews*, 12(12):1800171, 2018.

[52] A. H. Castro Neto, F. Guinea, N. M. R. Peres, K. S. Novoselov, and A. K. Geim. The electronic properties of graphene. *Rev. Mod. Phys.*, 81:109–162, Jan 2009.

[53] Jean-Noel Fuchs and Mark Oliver Goerbig. Introduction to the physical properties of graphene. *Lecture notes*, 10(11), 2008.

[54] Damien Voiry, Aditya Mohite, and Manish Chhowalla. Phase engineering of transition metal dichalcogenides. *Chemical Society Reviews*, 44(9):2702–2712, 2015.

[55] Yung-Chang Lin, Dumitru O Dumcenco, Ying-Sheng Huang, and Kazu Suenaga. Atomic mechanism of the semiconducting-to-metallic phase transition in single-layered MoS_2. *Nature nanotechnology*, 9(5):391–396, 2014.

[56] Ke Wang, Yu Zhou, Lixun Cheng, Dongdong Li, Zhihao Hu, Shuangming Chen, Chuanqiang Wu, Li Song, and Binghui Ge. Engineering phase transition from 2H to 1T in $MoSe_2$ by W cluster doping toward lithium-ion battery. *Inorganic Chemistry*, 62(51):21257–21264, 2023.

[57] Ivan Pelant and Jan Valenta. *Luminescence spectroscopy of semiconductors*. OUP Oxford, 2012.

[58] Chihiro Hamaguchi and C Hamaguchi. *Basic semiconductor physics*, volume 9. Springer, 2010.

[59] Alexey Chernikov, Timothy C Berkelbach, Heather M Hill, Albert Rigosi, Yilei Li, Burak Aslan, David R Reichman, Mark S Hybertsen, and Tony F Heinz. Exciton binding energy and nonhydrogenic rydberg series in monolayer ws 2. *Physical review letters*, 113(7):076802, 2014.

[60] Pierluigi Cudazzo, Ilya V Tokatly, and Angel Rubio. Dielectric screening in two-dimensional insulators: Implications for excitonic and impurity states in graphane. *Physical Review B—Condensed Matter and Materials Physics*, 84(8):085406, 2011.

[61] Dong Sun, Jia-Wei Lai, Jun-Chao Ma, Qin-Sheng Wang, and Jing Liu. Review of ultrafast spectroscopy studies of valley carrier dynamics in two-dimensional semiconducting transition metal dichalcogenides. *Chinese Physics B*, 26(3):037801, 2017.

[62] Andor Kormányos, Guido Burkard, Martin Gmitra, Jaroslav Fabian, Viktor Zólyomi, Neil D Drummond, and Vladimir Fal'ko. k· p theory for two-dimensional transition metal dichalcogenide semiconductors. *2D Materials*, 2(2):022001, 2015.

[63] Di Xiao, Gui-Bin Liu, Wanxiang Feng, Xiaodong Xu, and Wang Yao. Coupled spin and valley physics in monolayers of mos 2 and other group-vi dichalcogenides. *Physical review letters*, 108(19):196802, 2012.

[64] Yung-Chang Lin, Hannu-Pekka Komsa, Chao-Hui Yeh, Torbjorn Bjorkman, Zheng-Yong Liang, Ching-Hwa Ho, Ying-Sheng Huang, Po-Wen Chiu, Arkady V Krasheninnikov, and Kazu Suenaga. Single-layer res_2: two-dimensional semiconductor with tunable in-plane anisotropy. *ACS nano*, 9(11):11249–11257, 2015.

[65] Beom Seo Kim, WS Kyung, JD Denlinger, Changyoung Kim, and SR Park. Strong one-dimensional characteristics of hole-carriers in ReS_2 and $ReSe_2$. *Scientific reports*, 9(1):2730, 2019.

[66] Joanna M Urban, Michał Baranowski, A Kuc, A Surrente, Y Ma, D Włodarczyk, Andrzej Suchocki, Dmitry Ovchinnikov, Thomas Heine, Duncan Kennedy Maude, et al. Non equilibrium anisotropic excitons in atomically thin res_2. *2D Materials*, 6(1):015012, 2018.

[67] Sefaattin Tongay, Hasan Sahin, Changhyun Ko, Alex Luce, Wen Fan, Kai Liu, Jian Zhou, Ying-Sheng Huang, Ching-Hwa Ho, Jinyuan Yan, et al. Monolayer behaviour in bulk res_2 due to electronic and vibrational decoupling. *Nature communications*, 5(1):1–6, 2014.

[68] P Kapuściński, J Dzian, AO Slobodeniuk, C Rodríguez-Fernández, J Jadczak, L Bryja, C Faugeras, DM Basko, and M Potemski. Exchange-split multiple Rydberg series of excitons in anisotropic quasi two-dimensional ReS_2. *2D Materials*, 9(4):045005, 2022.

[69] Robert Oliva, Magdalena Laurien, Filip Dybala, Jan Kopaczek, Ying Qin, Sefaattin Tongay, Oleg Rubel, and Robert Kudrawiec. Pressure dependence of direct optical transitions in ReS_2 and $ReSe_2$. *npj 2D Materials and Applications*, 3(1):20, 2019.

[70] Qiannan Cui, Jiaqi He, Matthew Z Bellus, Mirzojamshed Mirzokarimov, Tino Hofmann, Hsin-Ying Chiu, Matthew Antonik, Dawei He, Yongsheng Wang, and Hui Zhao. Transient absorption measurements on anisotropic monolayer res_2. *Small*, 11(41):5565–5571, 2015.

[71] Fang Liu, Xin Zhao, Xiao-Qing Yan, Junfang Xie, Wangwei Hui, Xiufeng Xin, Zhi-Bo Liu, and Jian-Guo Tian. Ultrafast nonlinear absorption and carrier relaxation in ReS_2 and $ReSe_2$ films. *Journal of Applied Physics*, 125(17), 2019.

[72] Kostya S Novoselov, Da Jiang, F Schedin, TJ Booth, VV Khotkevich, SV Morozov, and Andre K Geim. Two-dimensional atomic crystals. *Proceedings of the National Academy of Sciences*, 102(30):10451–10453, 2005.

[73] Wolfgang Langbein and Brian Patton. Transient coherent nonlinear spectroscopy of single quantum dots. *Journal of Physics: Condensed Matter*, 19(29):295203, 2007.

[74] Peter Hamm. Principles of nonlinear optical spectroscopy: A practical approach or: Mukamel for dummies. *University of Zurich*, 41(5):77, 2005.

[75] W Langbein. Coherent optical spectroscopy of semiconductor nanostructures. *La Rivista del Nuovo Cimento*, 33(5):255–312, 2010.

[76] Robert W Boyd, Alexander L Gaeta, and Enno Giese. Nonlinear optics. In *Springer Handbook of Atomic, Molecular, and Optical Physics*, pages 1097–1110. Springer, 2008.

[77] Christopher L Smallwood, Travis M Autry, and Steven T Cundiff. Analytical solutions to the finite-pulse bloch model for multidimensional coherent spectroscopy. *JOSA B*, 34(2):419–429, 2017.

[78] F Fras, Q Mermillod, G Nogues, C Hoarau, C Schneider, M Kamp, Sven Höfling, W Langbein, and J Kasprzak. Multi-wave coherent control of a solid-state single emitter. *Nature Photonics*, 10(3):155–158, 2016.

[79] Lorenzo Scarpelli. *Optical spectroscopy of excitons confined in two-dimensional materials and semiconductor heterostructures*. PhD thesis, Cardiff University, 2019.

[80] Selcuk Akturk, Xun Gu, Mark Kimmel, and Rick Trebino. Extremely simple single-prism ultrashort-pulse compressor. *Optics express*, 14(21):10101–10108, 2006.

[81] RL Fork, OE Martinez, and JP Gordon. Negative dispersion using pairs of prisms. *Optics letters*, 9(5):150–152, 1984.

[82] Dennis T Gies and Ting-Chung Poon. Measurement of acoustic radiation pattern in an acousto-optic modulator. In *Proceedings IEEE SoutheastCon 2002 (Cat. No. 02CH37283)*, pages 441–445. IEEE, 2002.

[83] Brian Patton. *Non-linear Optical Spectroscopy of Single Quantum Dots*. PhD thesis, Technische Universitat Dortmund, 2020.

[84] Wolfgang Langbein and Brian Patton. Heterodyne spectral interferometry for multidimensional nonlinear spectroscopy of individual quantum systems. *Opt. Lett.*, 31(8):1151–1153, Apr 2006.

[85] L Lepetit, G Chériaux, and M Joffre. Linear techniques of phase measurement by femtosecond spectral interferometry for applications in spectroscopy. *JOSA B*, 12(12):2467–2474, 1995.

[86] Gabriela S. Schlau-Cohen, Akihito Ishizaki, and Graham R. Fleming. Two-dimensional electronic spectroscopy and photosynthesis: Fundamentals and applications to photosynthetic light-harvesting. *Chemical Physics*, 386(1):1–22, 2011.

[87] Arslan Usman, M Adel Aly, Hilary Masenda, Joshua JP Thompson, Surani M Gunasekera, Marcin Mucha-Kruczyński, Samuel Brem, Ermin Malic, and Martin Koch. Enhanced excitonic features in an anisotropic res 2/wse 2 heterostructure. *Nanoscale*, 14(30):10851–10861, 2022.

[88] Florian Dirnberger, Jonas D Ziegler, Paulo E Faria Junior, Rezlind Bushati, Takashi Taniguchi, Kenji Watanabe, Jaroslav Fabian, Dominique Bougeard, Alexey Chernikov, and Vinod M Menon. Quasi-1d exciton channels in strain-engineered 2d materials. *Science Advances*, 7(44):eabj3066, 2021.

[89] Junyong Wang, Yong Justin Zhou, Du Xiang, Shiuan Jun Ng, Kenji Watanabe, Takashi Taniguchi, and Goki Eda. Polarized light-emitting diodes based on anisotropic excitons in few-layer ReS_2. *Advanced Materials*, 32(32):2001890, 2020.

[90] Kin Fai Mak, Keliang He, Changgu Lee, Gwan Hyoung Lee, James Hone, Tony F Heinz, and Jie Shan. Tightly bound trions in monolayer MoS_2. *Nature materials*, 12(3):207–211, 2013.

[91] Sangwan Sim, Doeon Lee, Jekwan Lee, Hyemin Bae, Minji Noh, Soonyoung Cha, Moon-Ho Jo, Kyusang Lee, and Hyunyong Choi. Light polarization-controlled conversion of ultrafast coherent–incoherent exciton dynamics in few-layer ReS_2. *Nano letters*, 19(10):7464–7469, 2019.

[92] Xiaofan Wang, Keisuke Shinokita, Hong En Lim, Nur Baizura Mohamed, Yuhei Miyauchi, Nguyen Thanh Cuong, Susumu Okada, and Kazunari Matsuda. Direct and indirect exciton dynamics in few-layered ReS_2 revealed by photoluminescence and pump-probe spectroscopy. *Advanced Functional Materials*, 29(6):1806169, 2019.

[93] Jiaqi He, Lu Zhang, Dawei He, Yongsheng Wang, Zhiyi He, and Hui Zhao. Ultrafast transient absorption measurements of photocarrier dynamics in monolayer and bulk rese 2. *Optics Express*, 26(17):21501–21509, 2018.

[94] Prasenjit Dey, Jagannath Paul, Zefang Wang, CE Stevens, Cunming Liu, AH Romero, Jie Shan, DJ Hilton, and Denis Karaiskaj. Optical coherence in atomic-monolayer transition-metal dichalcogenides limited by electron-phonon interactions. *Physical review letters*, 116(12):127402, 2016.

[95] Daniel A Chenet, Burak Aslan, Pinshane Y Huang, Chris Fan, Arend M Van Der Zande, Tony F Heinz, and James C Hone. In-plane anisotropy in mono- and few-layer ReS_2 probed by Raman spectroscopy and scanning transmission electron microscopy. *Nano letters*, 15(9):5667–5672, 2015.

[96] DT Nguyen, C Voisin, Ph Roussignol, C Roquelet, Jean-Sébastien Lauret, and Guillaume Cassabois. Phonon-induced dephasing in single-wall carbon nanotubes. *Physical Review B—Condensed Matter and Materials Physics*, 84(11):115463, 2011.

[97] Kohei Yoshikawa, Ryusuke Matsunaga, Kazunari Matsuda, and Yoshihiko Kanemitsu. Mechanism of exciton dephasing in a single carbon nanotube studied by photoluminescence spectroscopy. *Applied Physics Letters*, 94(9), 2009.

[98] Karolina Ewa Połczyńska, Simon Le Denmat, Takashi Taniguchi, Kenji Watanabe, Marek Potemski, Piotr Kossacki, Wojciech Pacuski, and Jacek Kasprzak. Coherent imaging and dynamics of excitons in mose 2 monolayers epitaxially grown on hexagonal boron nitride. *Nanoscale*, 15(15):6941–6946, 2023.

[99] Sophia Helmrich, Kevin Sampson, Di Huang, Malte Selig, Kai Hao, Kha Tran, Alexander Achstein, Carter Young, Andreas Knorr, Ermin Malic, et al. Phonon-assisted intervalley scattering determines ultrafast exciton dynamics in mose 2 bilayers. *Physical review letters*, 127(15):157403, 2021.

[100] Christoph Pöllmann, Philipp Steinleitner, Ursula Leierseder, Philipp Nagler, Gerd Plechinger, Michael Porer, R Bratschitsch, Christian Schüller, Tobias Korn, and Rupert Huber. Resonant internal quantum transitions and femtosecond radiative decay of excitons in monolayer WSe_2. *Nature materials*, 14(9):889–893, 2015.

[101] Archana Raja, Malte Selig, Gunnar Berghauser, Jaeeun Yu, Heather M Hill, Albert F Rigosi, Louis E Brus, Andreas Knorr, Tony F Heinz, Ermin Malic, et al. Enhancement of exciton–phonon scattering from monolayer to bilayer WS_2. *Nano letters*, 18(10):6135–6143, 2018.

[102] Thilo Hahn, Jacek Kasprzak, Paweł Machnikowski, Tilmann Kuhn, and Daniel Wigger. Influence of local fields on the dynamics of four-wave mixing signals from 2d semiconductor systems. *New Journal of Physics*, 23(2):023036, 2021.

[103] Andreij C Gadelha, Alisson R Cadore, Lucas Lafeta, Ana M De Paula, Leandro M Malard, Rodrigo G Lacerda, and Leonardo C Campos. Local photodoping in monolayer MoS_2. *Nanotechnology*, 31(25):255701, 2020.

[104] Hongyu Tang, Sergey G Menabde, Tarique Anwar, Junhyung Kim, Min Seok Jang, and Giulia Tagliabue. Photo-modulated optical and electrical properties of graphene. *Nanophotonics*, 11(5):917–940, 2022.

[105] Long Ju, Jairo Velasco, Edwin Huang, Salman Kahn, Casey Nosiglia, Hsin-Zon Tsai, Wei Yang, Takashi Taniguchi, Katsutoshi Watanabe, Yi Zhang, et al. Photoinduced doping in heterostructures of graphene and boron nitride. *Nature nanotechnology*, 9(5):348–352, 2014.

[106] Alejandro Molina-Sánchez, Maurizia Palummo, Andrea Marini, and Ludger Wirtz. Temperature-dependent excitonic effects in the optical properties of single-layer mos 2. *Physical Review B*, 93(15):155435, 2016.

[107] Steven T Cundiff. Coherent spectroscopy of semiconductors. *Optics express*, 16(7):4639–4664, 2008.

[108] Paola Borri, W Langbein, Jørn Märcher Hvam, and F Martelli. Well-width dependence of exciton-phonon scattering in in x ga 1- x a s/g a a s single quantum wells. *Physical Review B*, 59(3):2215, 1999.

[109] Md Samiul Islam, Rup Kumar Chowdhury, Marie Barthelemy, Loic Moczko, Pascal Hebraud, Stephane Berciaud, Alberto Barsella, and Francois Fras. Large-scale statistical analysis of defect emission in hbn: Revealing spectral families and influence of flake morphology. *ACS nano*, 18(32):20980–20989, 2024.

[110] Igor Aharonovich, Dirk Englund, and Milos Toth. Solid-state single-photon emitters. *Nature photonics*, 10(10):631–641, 2016.

[111] Toan Trong Tran, Kerem Bray, Michael J Ford, Milos Toth, and Igor Aharonovich. Quantum emission from hexagonal boron nitride monolayers. *Nature nanotechnology*, 11(1):37–41, 2016.

[112] Maciej Koperski, K Nogajewski, Ashish Arora, V Cherkez, Paul Mallet, J-Y Veuillen, J Marcus, Piotr Kossacki, and M Potemski. Single photon emitters in exfoliated WSe_2 structures. *Nature nanotechnology*, 10(6):503–506, 2015.

[113] Yu-Ming He, Genevieve Clark, John R Schaibley, Yu He, Ming-Cheng Chen, Yu-Jia Wei, Xing Ding, Qiang Zhang, Wang Yao, Xiaodong Xu, et al. Single quantum emitters in monolayer semiconductors. *Nature nanotechnology*, 10(6):497–502, 2015.

[114] Carmen Palacios-Berraquero and Carmen Palacios-Berraquero. Atomically-thin quantum light emitting diodes. *Quantum confined excitons in 2-dimensional materials*, pages 71–89, 2018.

[115] Philipp Tonndorf, Stefan Schwarz, Johannes Kern, Iris Niehues, Osvaldo Del Pozo-Zamudio, Alexander I Dmitriev, Anatoly P Bakhtinov, Dmitry N Borisenko, Nikolai N Kolesnikov, Alexander I Tartakovskii, et al. Single-photon emitters in gase. *2D Materials*, 4(2):021010, 2017.

[116] Igor Aharonovich and Milos Toth. Quantum emitters in two dimensions. *Science*, 358(6360):170–171, 2017.

[117] Steffen Michaelis de Vasconcellos, Daniel Wigger, Ursula Wurstbauer, Alexander W Holleitner, Rudolf Bratschitsch, and Tilmann Kuhn. Single-photon emitters in layered van der waals materials. *physica status solidi (b)*, 259(4):2100566, 2022.

[118] Soumyabrata Roy, Xiang Zhang, Anand B Puthirath, Ashokkumar Meiyazhagan, Sohini Bhattacharyya, Muhammad M Rahman, Ganguli Babu, Sandhya Susarla, Sreehari K Saju, Mai Kim Tran, et al. Structure, properties and applications of two-dimensional hexagonal boron nitride. *Advanced Materials*, 33(44):2101589, 2021.

[119] N Ooi, V Rajan, J Gottlieb, Y Catherine, and JB Adams. Structural properties of hexagonal boron nitride. *Modelling and Simulation in Materials Science and Engineering*, 14(3):515, 2006.

[120] HX Jiang and Jing Yu Lin. Hexagonal boron nitride epilayers: growth, optical properties and device applications. *ECS Journal of Solid State Science and Technology*, 6(2):Q3012, 2016.

[121] Li Song, Lijie Ci, Hao Lu, Pavel B Sorokin, Chuanhong Jin, Jie Ni, Alexander G Kvashnin, Dmitry G Kvashnin, Jun Lou, Boris I Yakobson, et al. Large scale

growth and characterization of atomic hexagonal boron nitride layers. *Nano letters*, 10(8):3209–3215, 2010.

[122] Sumin Choi, Toan Trong Tran, Christopher Elbadawi, Charlene Lobo, Xuewen Wang, Saulius Juodkazis, Gediminas Seniutinas, Milos Toth, and Igor Aharonovich. Engineering and localization of quantum emitters in large hexagonal boron nitride layers. *ACS applied materials & interfaces*, 8(43):29642–29648, 2016.

[123] Nicholas R Jungwirth, Brian Calderon, Yanxin Ji, Michael G Spencer, Michael E Flatté, and Gregory D Fuchs. Temperature dependence of wavelength selectable zero-phonon emission from single defects in hexagonal boron nitride. *Nano letters*, 16(10):6052–6057, 2016.

[124] LJ Martínez, Thomas Pelini, V Waselowski, JR Maze, Bernard Gil, Guillaume Cassabois, and Vincent Jacques. Efficient single photon emission from a high-purity hexagonal boron nitride crystal. *Physical review B*, 94(12):121405, 2016.

[125] Toan Trong Tran, Christopher Elbadawi, Daniel Totonjian, Charlene J Lobo, Gabriele Grosso, Hyowon Moon, Dirk R Englund, Michael J Ford, Igor Aharonovich, and Milos Toth. Robust multicolor single photon emission from point defects in hexagonal boron nitride. *ACS nano*, 10(8):7331–7338, 2016.

[126] Annemarie L Exarhos, David A Hopper, Richard R Grote, Audrius Alkauskas, and Lee C Bassett. Optical signatures of quantum emitters in suspended hexagonal boron nitride. *ACS nano*, 11(3):3328–3336, 2017.

[127] Xiangzhi Li, Gabriella D Shepard, Andrew Cupo, Nicolas Camporeale, Kamran Shayan, Yue Luo, Vincent Meunier, and Stefan Strauf. Nonmagnetic quantum emitters in boron nitride with ultranarrow and sideband-free emission spectra. *ACS nano*, 11(7):6652–6660, 2017.

[128] Nicholas R Jungwirth and Gregory D Fuchs. Optical absorption and emission mechanisms of single defects in hexagonal boron nitride. *Physical review letters*, 119(5):057401, 2017.

[129] Gabriele Grosso, Hyowon Moon, Benjamin Lienhard, Sajid Ali, Dmitri K Efetov, Marco M Furchi, Pablo Jarillo-Herrero, Michael J Ford, Igor Aharonovich,

and Dirk Englund. Tunable and high-purity room temperature single-photon emission from atomic defects in hexagonal boron nitride. *Nature communications*, 8(1):1–8, 2017.

[130] Luc Museur, Eduard Feldbach, and Andrei Kanaev. Defect-related photoluminescence of hexagonal boron nitride. *Physical Review B—Condensed Matter and Materials Physics*, 78(15):155204, 2008.

[131] Romain Bourrellier, Sophie Meuret, Anna Tararan, Odile Stéphan, Mathieu Kociak, Luiz HG Tizei, and Alberto Zobelli. Bright uv single photon emission at point defects in h-bn. *Nano letters*, 16(7):4317–4321, 2016.

[132] TQP Vuong, Guillaume Cassabois, Pierre Valvin, Abdelkarim Ouerghi, Yannick Chassagneux, Christophe Voisin, and Bernard Gil. Phonon-photon mapping in a color center in hexagonal boron nitride. *Physical review letters*, 117(9):097402, 2016.

[133] Robin Camphausen, Loris Marini, Sherif Abdulkader Tawfik, Toan Trong Tran, Michael J Ford, and Stefano Palomba. Observation of near-infrared sub-poissonian photon emission in hexagonal boron nitride at room temperature. *APL Photonics*, 5(7), 2020.

[134] Michael Hoese, Prithvi Reddy, Andreas Dietrich, Michael K Koch, Konstantin G Fehler, Marcus W Doherty, and Alexander Kubanek. Mechanical decoupling of quantum emitters in hexagonal boron nitride from low-energy phonon modes. *Science advances*, 6(40):eaba6038, 2020.

[135] Kumarasiri Konthasinghe, Chitraleema Chakraborty, Nikhil Mathur, Liangyu Qiu, Arunabh Mukherjee, Gregory D Fuchs, and A Nick Vamivakas. Rabi oscillations and resonance fluorescence from a single hexagonal boron nitride quantum emitter. *Optica*, 6(5):542–548, 2019.

[136] Johann A Preuss, Daniel Groll, Robert Schmidt, Thilo Hahn, Paweł Machnikowski, Rudolf Bratschitsch, Tilmann Kuhn, Steffen Michaelis De Vasconcellos, and Daniel Wigger. Resonant and phonon-assisted ultrafast coherent control of a single hbn color center. *Optica*, 9(5):522–531, 2022.

[137] Andreas Gottscholl, Mehran Kianinia, Victor Soltamov, Sergei Orlinskii, Georgy Mamin, Carlo Bradac, Christian Kasper, Klaus Krambrock, Andreas Sperlich, Milos Toth, et al. Initialization and read-out of intrinsic spin defects in a van der waals crystal at room temperature. *Nature materials*, 19(5):540–545, 2020.

[138] Hannah L Stern, Qiushi Gu, John Jarman, Simone Eizagirre Barker, Noah Mendelson, Dipankar Chugh, Sam Schott, Hoe H Tan, Henning Sirringhaus, Igor Aharonovich, et al. Room-temperature optically detected magnetic resonance of single defects in hexagonal boron nitride. *Nature communications*, 13(1):618, 2022.

[139] Angela Haykal, Rana Tanos, Noel Minotto, Alrik Durand, Florentin Fabre, Jiahan Li, JH Edgar, Viktor Ivady, Adam Gali, Thierry Michel, et al. Decoherence of vb- spin defects in monoisotopic hexagonal boron nitride. *Nature Communications*, 13(1):4347, 2022.

[140] L Weston, D Wickramaratne, M Mackoit, A Alkauskas, and CG Van de Walle. Native point defects and impurities in hexagonal boron nitride. *Physical Review B*, 97(21):214104, 2018.

[141] Ali Sajid, Jeffrey R Reimers, and Michael J Ford. Defect states in hexagonal boron nitride: Assignments of observed properties and prediction of properties relevant to quantum computation. *Physical Review B*, 97(6):064101, 2018.

[142] A Sajid, Michael J Ford, and Jeffrey R Reimers. Single-photon emitters in hexagonal boron nitride: a review of progress. *Reports on Progress in Physics*, 83(4):044501, 2020.

[143] Chanaprom Cholsuk, Sujin Suwanna, and Tobias Vogl. Tailoring the emission wavelength of color centers in hexagonal boron nitride for quantum applications. *Nanomaterials*, 12(14):2427, 2022.

[144] Sherif Abdulkader Tawfik, Sajid Ali, Marco Fronzi, Mehran Kianinia, Toan Trong Tran, Catherine Stampfl, Igor Aharonovich, Milos Toth, and Michael J Ford. First-principles investigation of quantum emission from hbn defects. *Nanoscale*, 9(36):13575–13582, 2017.

[145] A Sajid and Kristian S Thygesen. Vncb defect as source of single photon emission from hexagonal boron nitride. *2D Materials*, 7(3):031007, 2020.

[146] Noah Mendelson, Dipankar Chugh, Jeffrey R Reimers, Tin S Cheng, Andreas Gottscholl, Hu Long, Christopher J Mellor, Alex Zettl, Vladimir Dyakonov, Peter H Beton, et al. Identifying carbon as the source of visible single-photon emission from hexagonal boron nitride. *Nature materials*, 20(3):321–328, 2021.

[147] Maciej Koperski, Diana Vaclavkova, Kenji Watanabe, Takashi Taniguchi, Kostya S Novoselov, and Marek Potemski. Midgap radiative centers in carbon-enriched hexagonal boron nitride. *Proceedings of the National Academy of Sciences*, 117(24):13214–13219, 2020.

[148] Philipp Auburger and Adam Gali. Towards ab initio identification of paramagnetic substitutional carbon defects in hexagonal boron nitride acting as quantum bits. *Physical Review B*, 104(7):075410, 2021.

[149] Cesar Jara, Tomas Rauch, Silvana Botti, Miguel AL Marques, Ariel Norambuena, Raul Coto, JE Castellanos-Águila, Jeronimo R Maze, and Francisco Munoz. First-principles identification of single photon emitters based on carbon clusters in hexagonal boron nitride. *The Journal of Physical Chemistry A*, 125(6):1325–1335, 2021.

[150] Qinghai Tan, Jia-Min Lai, Xue-Lu Liu, Dan Guo, Yongzhou Xue, Xiuming Dou, Bao-Quan Sun, Hui-Xiong Deng, Ping-Heng Tan, Igor Aharonovich, et al. Donor–acceptor pair quantum emitters in hexagonal boron nitride. *Nano Letters*, 22(3):1331–1337, 2022.

[151] Mark E Turiansky, Audrius Alkauskas, Lee C Bassett, and Chris G Van de Walle. Dangling bonds in hexagonal boron nitride as single-photon emitters. *Physical review letters*, 123(12):127401, 2019.

[152] Mehdi Abdi, Jyh-Pin Chou, Adam Gali, and Martin B Plenio. Color centers in hexagonal boron nitride monolayers: a group theory and ab initio analysis. *ACS Photonics*, 5(5):1967–1976, 2018.

[153] Jeffrey R Reimers, Jun Shen, Mehran Kianinia, Carlo Bradac, Igor Aharonovich, Michael J Ford, and Piotr Piecuch. Photoluminescence, pho-

tophysics, and photochemistry of the vb- defect in hexagonal boron nitride. *Physical Review B*, 102(14):144105, 2020.

[154] Viktor Ivády, Gergely Barcza, Gergő Thiering, Song Li, Hanen Hamdi, Jyh-Pin Chou, Örs Legeza, and Adam Gali. Ab initio theory of the negatively charged boron vacancy qubit in hexagonal boron nitride. *npj Computational Materials*, 6(1):41, 2020.

[155] Yifeng Chen and Su Ying Quek. Photophysical characteristics of boron vacancy-derived defect centers in hexagonal boron nitride. *The Journal of Physical Chemistry C*, 125(39):21791–21802, 2021.

[156] Song Li and Adam Gali. Identification of an oxygen defect in hexagonal boron nitride. *The Journal of Physical Chemistry Letters*, 13(41):9544–9551, 2022.

[157] Fariah Hayee, Leo Yu, Jingyuan Linda Zhang, Christopher J Ciccarino, Minh Nguyen, Ann F Marshall, Igor Aharonovich, Jelena Vučković, Prineha Narang, Tony F Heinz, et al. Revealing multiple classes of stable quantum emitters in hexagonal boron nitride with correlated optical and electron microscopy. *Nature materials*, 19(5):534–539, 2020.

[158] Yongliang Chen, Mika T Westerhausen, Chi Li, Simon White, Carlo Bradac, Avi Bendavid, Milos Toth, Igor Aharonovich, and Toan Trong Tran. Solvent-exfoliated hexagonal boron nitride nanoflakes for quantum emitters. *ACS Applied Nano Materials*, 4(10):10449–10457, 2021.

[159] Andreas Dietrich, M Bürk, Elena S Steiger, Lukas Antoniuk, Trong Toan Tran, Minh Nguyen, Igor Aharonovich, Fedor Jelezko, and Alexander Kubanek. Observation of fourier transform limited lines in hexagonal boron nitride. *Physical Review B*, 98(8):081414, 2018.

[160] Stephen W Provencher. Contin: a general purpose constrained regularization program for inverting noisy linear algebraic and integral equations. *Computer Physics Communications*, 27(3):229–242, 1982.

[161] Noah Mendelson, Marcus Doherty, Milos Toth, Igor Aharonovich, and Toan Trong Tran. Strain-induced modification of the optical characteris-

tics of quantum emitters in hexagonal boron nitride. *Advanced Materials*, 32(21):1908316, 2020.

[162] Alexander Bommer and Christoph Becher. New insights into nonclassical light emission from defects in multi-layer hexagonal boron nitride. *Nanophotonics*, 8(11):2041–2048, 2019.

[163] Matthew A Feldman, Alex Puretzky, Lucas Lindsay, Ethan Tucker, Dayrl P Briggs, Philip G Evans, Richard F Haglund, and Benjamin J Lawrie. Phonon-induced multicolor correlations in hbn single-photon emitters. *Physical Review B*, 99(2):020101, 2019.

[164] Daniel Wigger, Robert Schmidt, Osvaldo Del Pozo-Zamudio, Johann A Preuß, Philipp Tonndorf, Robert Schneider, Paul Steeger, Johannes Kern, Yashar Khodaei, Jaroslaw Sperling, et al. Phonon-assisted emission and absorption of individual color centers in hexagonal boron nitride. *2D Materials*, 6(3):035006, 2019.

[165] P Khatri, IJ Luxmoore, and AJ Ramsay. Phonon sidebands of color centers in hexagonal boron nitride. *Physical Review B*, 100(12):125305, 2019.

[166] G Kern, G Kresse, and JJPRB Hafner. Ab initio calculation of the lattice dynamics and phase diagram of boron nitride. *Physical Review B*, 59(13):8551, 1999.

[167] Liang Wang, Yayun Pu, Ai Kah Soh, Yuping Shi, and Shuangyi Liu. Layers dependent dielectric properties of two dimensional hexagonal boron nitride-nanosheets. *AIP Advances*, 6(12), 2016.

[168] Aideen Griffin, Andrew Harvey, Brian Cunningham, Declan Scullion, Tian Tian, Chih-Jen Shih, Myrta Gruening, John F Donegan, Elton JG Santos, Claudia Backes, et al. Spectroscopic size and thickness metrics for liquid-exfoliated h-bn. *Chemistry of Materials*, 30(6):1998–2005, 2018.

[169] Rick W Dorn, Matthew J Ryan, Tae-Hoon Kim, Tian Wei Goh, Amrit Venkatesh, Patrick M Heintz, Lin Zhou, Wenyu Huang, and Aaron J Rossini. Identifying the molecular edge termination of exfoliated hexagonal boron nitride

nanosheets with solid-state nmr spectroscopy and plane-wave dft calculations. *Chemistry of Materials*, 32(7):3109–3121, 2020.

[170] A Sajid, Kristian S Thygesen, Jeffrey R Reimers, and Michael J Ford. Edge effects on optically detected magnetic resonance of vacancy defects in hexagonal boron nitride. *Communications Physics*, 3(1):153, 2020.

[171] Jacques Bourgoin. *Point defects in Semiconductors II: Experimental aspects*, volume 35. Springer Science & Business Media, 2012.

[172] Tengyuan Hao, Tousif Ahmed, Rownak Jahan Mou, Justin Xu, Shane Brown, and Zubaer M Hossain. Critical inter-defect distance that modulates strength and toughness in defective 2d sp2-lattice. *Journal of Applied Physics*, 127(20), 2020.

[173] Derek S Wang, Christopher J Ciccarino, Johannes Flick, and Prineha Narang. Hybridized defects in solid-state materials as artificial molecules. *ACS nano*, 15(3):5240–5248, 2021.

[174] Tobias Vogl, Marcus W Doherty, Ben C Buchler, Yuerui Lu, and Ping Koy Lam. Atomic localization of quantum emitters in multilayer hexagonal boron nitride. *Nanoscale*, 11(30):14362–14371, 2019.

[175] Yongliang Chen, Chi Li, Simon White, Milad Nonahal, Zai-Quan Xu, Kenji Watanabe, Takashi Taniguchi, Milos Toth, Toan Trong Tran, and Igor Aharonovich. Generation of high-density quantum emitters in high-quality, exfoliated hexagonal boron nitride. *ACS Applied Materials & Interfaces*, 13(39):47283–47292, 2021.

[176] Wei Liu, Nai-Jie Guo, Shang Yu, Yu Meng, Zhi-Peng Li, Yuan-Ze Yang, Zhao-An Wang, Xiao-Dong Zeng, Lin-Ke Xie, Qiang Li, et al. Spin-active defects in hexagonal boron nitride. *Materials for Quantum Technology*, 2(3):032002, 2022.

[177] Tobias Vogl, Ruvi Lecamwasam, Ben C Buchler, Yuerui Lu, and Ping Koy Lam. Compact cavity-enhanced single-photon generation with hexagonal boron nitride. *Acs Photonics*, 6(8):1955–1962, 2019.

[178] Dylan Lu, Jimmy J Kan, Eric E Fullerton, and Zhaowei Liu. Enhancing spontaneous emission rates of molecules using nanopatterned multilayer hyperbolic metamaterials. *Nature nanotechnology*, 9(1):48–53, 2014.

[179] David AB Miller, DS Chemla, TC Damen, AC Gossard, W Wiegmann, TH Wood, and CA Burrus. Electric field dependence of optical absorption near the band gap of quantum-well structures. *Physical Review B*, 32(2):1043, 1985.

[180] TH Wood, CA Burrus, DAB Miller, DS Chemla, TC Damen, AC Gossard, and W Wiegmann. High-speed optical modulation with gaas/gaalas quantum wells in ap-i-n diode structure. *Applied Physics Letters*, 44(1):16–18, 1984.

[181] Yuan-Ping Feng and HN Spector. Exciton energies as a function of electric field in quantum wells finite potential barrier case. *physica status solidi (b)*, 190(1):211–217, 1995.

[182] DA Broido. Excitonic spectrum of an undoped quantum well in electric field. *Superlattices and Microstructures*, 3(1):13–16, 1987.

[183] Ivan Verzhbitskiy, Daniele Vella, Kenji Watanabe, Takashi Taniguchi, and Goki Eda. Suppressed out-of-plane polarizability of free excitons in monolayer WSe_2. *ACS nano*, 13(3):3218–3224, 2019.

[184] Jonas G Roch, Nadine Leisgang, Guillaume Froehlicher, Peter Makk, Kenji Watanabe, Takashi Taniguchi, Christian Schonenberger, and Richard J Warburton. Quantum-confined Stark effect in a MoS_2 monolayer van der Waals heterostructure. *Nano letters*, 18(2):1070–1074, 2018.

[185] Julian Klein, Jakob Wierzbowski, Armin Regler, Jonathan Becker, Florian Heimbach, K Muller, Michael Kaniber, and Jonathan J Finley. Stark effect spectroscopy of mono-and few-layer MoS_2. *Nano letters*, 16(3):1554–1559, 2016.

[186] DAB Miller. Electric field dependence of optical properties of quantum well structures. In *Electro-optic and Photorefractive Materials: Proceedings of the International School on Material Science and Technology, Erice, Italy, July 6–17, 1986*, pages 35–49. Springer, 1987.

[187] Yoshihiro Hamakawa, FA Germano, and Paul Handler. Interband electro-optical properties of germanium. i. electroabsorption. *Physical Review*, 167(3):703, 1968.

[188] Frank L Lederman and John D Dow. Theory of electroabsorption by anisotropic and layered semiconductors. i. two-dimensional excitons in a uniform electric field. *Physical Review B*, 13(4):1633, 1976.

[189] Alexey Chernikov, Arend M Van Der Zande, Heather M Hill, Albert F Rigosi, Ajanth Velauthapillai, James Hone, and Tony F Heinz. Electrical tuning of exciton binding energies in monolayer ws 2. *Physical review letters*, 115(12):126802, 2015.

[190] Prasenjit Dey, Luyi Yang, Cedric Robert, Gang Wang, Bernhard Urbaszek, Xavier Marie, and Scott A Crooker. Gate-controlled spin-valley locking of resident carriers in wse 2 monolayers. *Physical review letters*, 119(13):137401, 2017.

[191] Anran Wang, Yuhan Wang, Jianfei Li, Ning Xu, Songlin Li, Xinran Wang, Yi Shi, and Fengqiu Wang. Controlling relaxation dynamics of excitonic states in monolayer transition metal dichalcogenides ws2 through interface engineering. *Applied Physics Letters*, 118(12), 2021.

[192] Jenny Hu, Etienne Lorchat, Xueqi Chen, Kenji Watanabe, Takashi Taniguchi, Tony F Heinz, Puneet A Murthy, and Thibault Chervy. Quantum control of exciton wave functions in 2d semiconductors. *Science Advances*, 10(12):eadk6369, 2024.

[193] Maciej Koperski, Karol Nogajewski, and Marek Potemski. Single photon emitters in boron nitride: More than a supplementary material. *Optics Communications*, 411:158–165, 2018.

[194] Minh Nguyen, Sejeong Kim, Toan Trong Tran, Zai-Quan Xu, Mehran Kianinia, Milos Toth, and Igor Aharonovich. Nanoassembly of quantum emitters in hexagonal boron nitride and gold nanospheres. *Nanoscale*, 10(5):2267–2274, 2018.

Université de Strasbourg

Md Samiul Islam

Coherent ultrafast spectroscopy of excitons in Van der Waals materials

Résumé

Dans cette thèse, basée sur un développement original de microscopie de mélange à quatre ondes ultrarapide, la première mesure directe de la dynamique de cohérence excitonique dans le disulfure de rhénium a été obtenue. Ces résultats ont démontré une robustesse unique de la cohérence excitonique par rapport à d'autres matériaux dichalcogénures de métaux de transition (TMD). Le potentiel de contrôle des propriétés intrinsèques des excitons dans les matériaux van der Waals (vdW) a été exploré dans des assemblages bidimensionnels innovants. En particulier, l'impact du graphène sur l'environnement excitonique d'une hétérostructure et sur les propriétés dynamiques de ces excitons a été étudié. Enfin, une avancée significative vers la compréhension et l'ingénierie des propriétés optiques des défauts émetteurs de photons uniques dans le nitrure de bore hexagonal (hBN) a été réalisée.

Mots clés : Spectroscopie ultrarapide, Microscopie à mélange à quatre ondes, matériaux de Van der Waals, Dichalcogénure de métal de transition, Disulfure de rhénium, hétérostructure, exciton, cohérence

Résumé en anglais

In this thesis, based on an original development of ultrafast four wave mixing microscopy, the first direct measurement of excitonic coherence dynamics in rhenium disulfide was obtained. These results demonstrated a unique robustness of excitonic coherence compared to other Transition metal dichalcogenide (TMD) materials. The potential for controlling the intrinsic properties of excitons in van der Waals (vdW) materials was explored in innovative two-dimensional assemblies. In particular, the impact of graphene in the excitonic environment of a heterostructure on the dynamic properties of these excitons has been investigated. Finally, a significant step towards understanding and engineering the optical properties of single photon emitting defects in hBN has been achieved.

Keywords : Ultrafast spectroscopy, Four wave mixing microscopy, van der Waals materials, Transition metal dichalcogenide, Rhenium disulfide, heterostructure, exciton, coherence